Digital Comprehensive Summaries of Uppsala Dissertations
from the Faculty of Science and Technology 2436

Mining Nature's Platinum

Discovery, Characterization, and Optimization of Hydrogenases for Green H_2 Applications

PRINCESS R. CABOTAJE

ACTA UNIVERSITATIS
UPSALIENSIS
2024

ISSN 1651-6214
ISBN 978-91-513-2206-3
urn:nbn:se:uu:diva-536472

UPPSALA
UNIVERSITET

Dissertation presented at Uppsala University to be publicly examined in room 2001, Ångströmlaboratoriet, Lägerhyddsvägen 1, Uppsala, Tuesday, 8 October 2024 at 13:00 for the degree of Doctor of Philosophy. The examination will be conducted in English. Faculty examiner: Professor Stephen W. Ragsdale (Department of Biological Chemistry, University of Michigan, Ann Arbor, Michigan, United States).

Abstract

Cabotaje, P. R. 2024. Mining Nature's Platinum. Discovery, Characterization, and Optimization of Hydrogenases for Green H_2 Applications. *Digital Comprehensive Summaries of Uppsala Dissertations from the Faculty of Science and Technology* 2436. 179 pp. Uppsala: Acta Universitatis Upsaliensis. ISBN 978-91-513-2206-3.

Establishing a sustainable hydrogen (H_2) economy requires developing catalysts that are not reliant on rare and expensive metals like platinum. As summarized in **Chapter 1**, microorganisms utilize hydrogenases to harness molecular H_2 for their metabolic processes. Remarkably, these ancient gas-processing enzymes rely on earth-abundant metals to reach activities on par with platinum. Investigating the biodiversity and understanding the mechanism of these enzymes offer a promising route to develop sustainable catalysts for H_2-processing.

This thesis employed a multidisciplinary approach, including bioinformatics, biochemistry, synthetic chemistry, and biophysics, to investigate two hydrogenase superfamilies, namely [FeFe] and [NiFe] hydrogenases. Key methods are outlined in **Chapter 2**. The main aim was to provide insights into their evolution, diversity, structure, function, and potential for green H_2 applications.

Chapter 3 challenges the prevailing view of [FeFe] hydrogenase domain distribution by revealing their presence and activity in diverse archaeal lineages, including DPANN, Asgard, and Thermoplasmata, which notably host [NiFe]-[FeFe] hybrids. The study provides a new minimal size requirement for functional hydrogenase and contests the notion of evolutionary independence between the two hydrogenase superfamilies.

Chapter 4 identifies a distinct proton transfer pathway in the putatively sensory Group D [FeFe] hydrogenases, diverging from the well-characterized pathway in the catalytic Group A enzymes. The study supports the critical role of proton transfer in controlling overall enzymatic function and provides insights for engineering catalysts that integrate both proton transfer and redox chemistry.

Chapter 5 demonstrates how rational engineering approaches informed by evolutionary insights can enhance both H_2 production and O_2 tolerance in a Group D [FeFe] hydrogenase, *Tam*HydS. This work reveals the synergistic impact of protein scaffold modifications on catalytic performance and highlights the potential of integrating phylogenetic information and protein engineering for developing robust and efficient biocatalysts.

Chapter 6 elucidates the mechanism by which Huc, an isolated O_2-tolerant [NiFe] hydrogenase, is able to efficiently oxidize trace atmospheric H_2. This exceptional capability arises from the intrinsic properties of the enzyme, particularly its high affinity for H_2 and elevated overpotential, rather than being dependent on the cellular context. The insights gained from this study provide valuable guidance for the design and engineering of (a)biotic catalysts capable of operating under ambient conditions.

Keywords: hydrogen, iron, nickel, hydrogenase, redox catalysis, enzyme catalysis, archaea, substrate transport, rational design

Princess R. Cabotaje, Department of Chemistry - Ångström, Molecular Biomimetics, Box 523, Uppsala University, SE-75120 Uppsala, Sweden.

ISSN 1651-6214
ISBN 978-91-513-2206-3
URN urn:nbn:se:uu:diva-536472 (http://urn.kb.se/resolve?urn=urn:nbn:se:uu:diva-536472)

To the Filipino dreamer

List of Papers

This thesis is based on the following papers, which are referred to in the text by their Roman numerals.

I. Greening[#], C., **Cabotaje, P. R.**[#], Alvarado, L. E. V., Leung, P. M.[#], Land, H.[#], Rodrigues-Oliveira, T., Ponce-Toledo, R. I., Senger, M., Klamke, M. A., Milton, M., Lappan, R., Mullen, S., West-Roberts, J., Mao, J., Song, J., Schoelmerich, M., Stairs, C. W., Schleper, C., Grinter, R., Spang, A., Banfield, J. F., Berggren, G.[#] (2024) Minimal and hybrid hydrogenases are active from archaea. *Cell*, 187(13): 3357–3372.E19

[#]Inventors: Patent App. No. 2023902336, filed on July 21, 2023

Author's contributions: Contributed to experimental design. Performed H_2 production tests on artificially matured lysates. Performed EPR whole cell, lysate, and isolate sample preparation, and participated in EPR analysis. Expressed, isolated, reconstituted, and artificially matured select hydrogenases. Performed electrochemical experiments and analysis. Contributed to FTIR sample preparation. Co-wrote the manuscript, designed, and prepared figures with support from other authors.

II. **Cabotaje, P. R.**, Walter, K., Zamader, A., Huang, P., Ho, F., Land, H., Senger, M., Berggren, G. (2023) Probing Substrate Transport Effects in Enzymatic Hydrogen Catalysis - An Alternative Proton Transfer Pathway in Putatively Sensory [FeFe] Hydrogenase. *ACS Catalysis,* 13(15): 10435–10446

Author's contributions: Contributed to the planning of the project and the interpretation of the results. Contributed to *in silico* work and analysis. Performed site-directed mutagenesis. Expressed, isolated, reconstituted, and artificially matured the variants. Performed H_2 production and oxidation assays. Performed EPR sample preparation and participated in EPR analysis. Contributed to FTIR sample preparation, measurements, and analysis. Supervised K.W. in characterizing the variants. Wrote the manuscript, designed, and prepared figures with support from other authors.

III. **Cabotaje, P. R.**, Sekretareva, A., Senger, M., Huang, P., Walter, K., Redman, H. J., Croy, N., Stripp, S. T., Land, H., Berggren, G. Probing the influence of the protein scaffold on H-cluster reactivity via gain-of-function studies - Improved H_2 evolution and O_2 tolerance through rational design in [FeFe] hydrogenase. *In preparation for resubmission.*

Author's contributions: Contributed to the planning of the project. Contributed to *in silico* work and analysis. Performed site-directed mutagenesis. Expressed, isolated, reconstituted, and artificially matured the variants. Performed H_2 production and oxidation assays. Performed electrochemical experiments and analysis. Performed EPR sample preparation and participated in EPR analysis. Contributed to FTIR sample preparation, measurements, and analysis. Supervised K.W. in isolating a variant. Wrote the manuscript, designed, and prepared figures with support from other authors.

IV. Grinter, R., Kropp, A., Venugopal, H., Senger, M., Badley, J., **Cabotaje, P. R.**, Jia, R., Duan, Z., Huang, P., Stripp, S. T., Barlow, C. K., Belousoff, M., Shafaat, H. S., Cook, G. M., Schittenhelm, R. B., Vincent, K. A., Khalid, S., Berggren, G., Greening, C. (2023) Structural basis for bacterial energy extraction from atmospheric hydrogen. *Nature*, 615(7952): 541–547

Author's contributions: Performed electrochemical experiments and analysis. Performed EPR sample preparation and participated in EPR analysis. Contributed to manuscript writing, designed, and prepared figures with support from other authors.

First and co-first authors are underlined in the author list.

Reprints were made with permission from the respective publishers.

Other publications not included in this thesis

During the PhD, contributions were made to the following publications, not included in the thesis.

V. Welsh, C., **Cabotaje, P. R.**, Marcelino, V. R., Watts, T. D., Kountz, D. J., Gould, J. A., Doan, N. Q., Lingford, J. P., Solari, J., D'Adamo, G. L., Huang, P., Bong, N., Gulliver, E. L., Young, R. B., Walter, K., Wolf, P. G., Ridlon, J. M., Gaskins, H. R., Giles, E. M., Lyras, D., Lappan, R., Berggren, G., Forster, S. C., Greening, C. A widespread hydrogenase drives fermentative growth of gut bacteria in healthy people.
Submitted. doi.org/10.1101/2024.08.15.608110
Author's contributions: Contributed to experimental design. Performed H_2 production tests on artificially matured lysates. Performed EPR whole cell sample preparation, and participated in EPR analysis. Contributed to manuscript writing, designed and prepared figures with support from other authors.

VI. Senger, M., Schumann, C., **Cabotaje, P. R.**, Zamader, A., Land, H., Berggren, G. Indications for a universal hydrogen catalysis mechanism in [FeFe]-hydrogenases of different phylogenetic groups. *Resubmitted*
Author's contributions: Expressed, isolated, reconstituted, and artificially matured the hydrogenase. Supervised C. S. in isolating the hydrogenase. Contributed to FTIR sample preparation. Contributed to manuscript writing, designed, and prepared figures with support from other authors.

VII. Voloshyn, I., Schumann, C., **Cabotaje, P. R.**, Zamader, A., Land, H., Senger, M. Secondary structure changes as the potential H_2 sensing mechanism of Group D [FeFe]-hydrogenases. *Resubmitted.*
Author's contributions: Expressed, isolated, reconstituted, and artificially matured the hydrogenase. Supervised C. S. in isolating the hydrogenase. Contributed to manuscript writing, designed, and prepared figures with support from other authors.

VIII. Cheng, F., Pavliuk, O., Hardt, S., Hunt, L. A., Cai, B., Kubart, T., Hammarström, L., Plumeré, N., Berggren, G., Tian, H. (2024) Embedding biocatalysts in a redox polymer enhances the performance of dye-sensitized photocathodes in bias-free photoelectrochemical water splitting. *Nature Communications,* 15(1): 3202
Author's contributions: Contributed to experimental design and sample preparation for electrochemical experiments. Performed H_2 production tests on *Cr*HydA1.

Contents

Abbreviations

$E^0_{2H^+/H_2}$	thermodynamic potential of $2H^+/H_2$ couple
$[2Fe]^{ADT}$	$[2Fe]_H$ subsite mimic with amine ($-NH_2-$) as bridgehead
$[2Fe]_H$	diiron subsite of the H-cluster
$[2Fe]^{PDT}$	$[2Fe]_H$ subsite mimic with methylene ($-CH_2-$) as bridgehead
$[4Fe\text{-}4S]_H$	four iron-four sulfur subsite of the H-cluster
[FeFe]	iron-iron
[NiFe]	nickel-iron
ΔE	energy difference
ΔiscR	deletion of the gene encoding for the IscR transcription factor
μ_B	Bohr magneton = 9.274×10^{-24} J·T^{-1}
μCO	bridging carbon monoxide
μH	bridging hydride
ADT	azadithiolate
Ag/AgCl	silver/silver chloride reference electrode
ATP	adenosine triphosphate
ATR	Attenuated total reflection
B_0	external magnetic field
BV	benzyl viologen
Csd(A)	cysteine desulfurase
CV	cyclic voltammetry
DET	direct electron transfer
e^-	electron
E	non-standard reduction potential
E^0	standard reduction potential
E_{app}	applied potential
E_{atm}	reduction potential of $2H^+/H_2$ couple at atmospheric condition
E_{eq}	equilibrium potential
E_{onset}	onset potential
EPR	Electron Paramagnetic Resonance spectroscopy
ET	electron transfer
EY	Eosin Y
F	Faraday's constant = 96,485 C mol^{-1}
Fd	ferredoxin
Fe_d	distal iron
Fe_p	proximal iron

FLP	frustrated Lewis pair
FTIR	Fourier-transformed infrared spectroscopy
g_e	g-value of electron in its "free" state ≈ 2.0023
GTP	guanosine triphosphate
H^-	hydride
h	Planck's Constant = 6.626 x 10^{-34} J·s
H^+	proton
HER	hydrogen evolution reaction
*Hyd*A	catalytic subunit of [FeFe] hydrogenases
HydE	H-cluster maturation rSAM enzyme
HydF	H-cluster maturation GTP-binding enzyme
HydG	H-cluster maturation rSAM enzyme
IPTG	isopropyl β-D-1-thiogalactopyranoside
ISC	iron-sulfur cluster
IscR	iron-sulfur cluster regulator
k_{cat}	catalytic constant
k_{cat}/K_m	specificity constant
kDa	kilodalton
K_m	Michaelis' constant
L	orbital angular momentum
LUCA	last universal common ancestor
MAG	metagenome-assembled genome
MB	methylene blue
MD	molecular dynamics
MET	mediated electron transfer
MJ/L	megajoule per liter
MJ/m^2	megajoule per square meter
MQ	menaquinone
m_s	magnetic moment
MV	methyl viologen
n	number of moles of electrons transferred
N_2	molecular nitrogen
NADH	nicotinamide adenine dinucleotide
NaDT	sodium dithionite
OCP	open circuit potential
OCS	open coordination site
OD_{600}	optical density at 600 nm
OXP	oxidative phosphorylation
PAS	Per-Arnt-Sim signaling domain
PCET	proton-coupled electron transfer
PCR	polymerase chain reaction
PEM	proton exchange membrane
PFE	protein film electrochemistry
PGE	pyrolytic graphite edge

pH_2	partial pressure of H_2
pKa	acid dissociation constant
pO_2	partial pressure of O_2
PTP	proton transfer pathway
R	universal gas constant = 8.314 J K^{-1} mol^{-1}
RMSD	root mean square deviation
ROS	reactive oxygen species
rpm	rotations per minute
rSAM	radical *S*-adenosylmethionine
S	spin angular momentum
SDS-PAGE	sodium dodecyl sulfate–polyacrylamide gel electrophoresis
SHE	standard hydrogen electrode
SLP	substrate level phosphorylation
STH	solar-to-hydrogen efficiency
T	temperature
$t_{1/2}$	half-life value
TEA	terminal electron acceptor
TEOA	triethanolamine
TOF	turnover frequency
U/mg	one unit of activity per milligram of enzyme
ν	frequency
V_{max}	maximum velocity
y. a.	years ago
η	overpotential

Chapter 1, Introduction

Advancements in renewable energy: The role of H_2-based systems

The growing concerns about climate change underscore the urgency of transitioning to clean energy systems. Renewable energy (such as solar, wind, hydroelectric, tidal, and wave power) represents a promising frontier in this regard. Yet, to be harnessed effectively, these energy sources typically require conversion into usable forms like electricity or heat. A single hour's worth of solar radiation (≈ 5 MJ/m^2) could power the world for an entire year (demand ≈ 1 MJ/m^2), but its intermittency and the lack of a robust global infrastructure (*e.g.,* for extraction or conversion) limit its widespread use.[1]

Beyond electricity, society heavily relies on chemical fuels for energy transport. Producing chemical fuels from non-hydrocarbon energy sources or their derived electricity is, thus, inevitable. In this context, molecular hydrogen (H_2) stands out as a highly promising chemical fuel due to its high energy output per unit mass in the form of heat (120−142 MJ/kg), surpassing that of conventional fossil fuels such as oil, natural gas, and coal (30−60 MJ/kg).[2] In 2022, global H_2 consumption reached 95 million metric tons (Mt).[3] Of this total, 53 Mt were utilized in the chemical industry, with 60% allocated for ammonia production. The projected H_2 demand for 2030 is expected to exceed the combined utilization for fuel and power generation applications.

Hydrogen's versatility is evident in its storage and transportation options: it can be stored in cryogenic liquid, insulated tanks, metal hydride materials via thermal adsorption/desorption, compressed gas cylinders, or underground reservoirs and caverns. It can be transported via pipelines, trucks, and rails as highly compressed gas or as a liquid through shipping routes. The oxidation of H_2 theoretically results in zero carbon emissions. Given its high energy content, zero-emission combustion, and adaptability, coupled with its large-scale storage and transportation capabilities, H_2 emerges as a compelling energy carrier.[4]

While H_2-based systems offer promising prospects, several obstacles hinder their large-scale implementation.[5] The challenges include the low volumetric energy density of hydrogen (8 MJ/L for H_2 as liquid vs 32 MJ/L for gasoline[2]), high pressure requirement for liquefaction, the risk of pipeline structural failures leading to explosive gas leaks, and the high costs linked to

the entire harvesting-to-distribution chain. Global H_2 demand is rising, but it remains largely fossil-fuel dependent.[3] Mature technologies produce H_2 from hydrocarbons (steam reforming and pyrolysis) or coal (gasification) as feedstocks.[6] These approaches, however, contradict the "hydrogen economy" vision, advocating large-scale, carbon-neutral H_2 production to displace our existing fossil fuel-based power economy.

Water (H_2O), an abundant and accessible resource, offers a carbon-neutral pathway for hydrogen production when split into H_2 and O_2.[7] The primary method, electrolysis, utilizes an electrical current to dissociate water molecules into its constituent gases.[8] This process boasts a high production purity, with electrolytic H_2 concentration exceeding 99.5%, surpassing the 97–98% concentration typically obtained from fossil fuel-based sources.[9, 10] When harnessed in fuel cells, H_2 serves as a clean energy medium—completing the cycle by generating electricity with water as the primary by-product.

Electrocatalysts play a pivotal role in enhancing the efficiency of water-splitting technologies. Noble metals such as in the platinum group excel as electrocatalysts due to their high efficiency. However, even these robust materials face challenges in the acidic conditions inherent to proton exchange membrane (PEM) cells, which can lead to electrode deterioration over time. Moreover, the scarcity and the uneven geographical distribution of noble metals impede their global application and risk exacerbating social inequalities, especially in regions that are already disproportionately affected by the climate crisis.[11]

To address these limitations, research has sought alternative materials. Catalysts derived from more abundant metals like cobalt and nickel have emerged as potential substitutes, though they have yet to match the efficiency of their noble metal counterparts.[12, 13] For instance, platinum in hydrogen evolution reaction (HER) can achieve (faradaic) efficiencies up to 92%, setting a high benchmark for substitute materials.

What if we could learn from Nature, which has mastered harnessing H_2 for billions of years, by using earth abundant metals like nickel and iron, without compromising rates, stability, efficiency, and selectivity?

Hydrogenases drive Nature's H_2 economy

Molecular hydrogen (H_2)—the most abundant element in the universe—has been fuelling life on Earth since time immemorial. While we, humans, only recently realized its potential to power our future, microbes have been harnessing H_2 long before us (predicted to be ≈ 4 billion years ago).[14-17] This ancient fuel is pivotal in how living organisms acquire and transform energy to perform biological or cellular processes. It serves diverse roles in microbial physiology, from disposal of excessive reductant during fermentation to respiration, energy conservation, and carbon fixation.

Theorised as the primordial electron donor, H_2 has maintained its indispensability in evolutionary history as an energy source and a diffusible electron sink.[16] The founding lineages of both archaea and bacteria are predicted to be H_2-dependent autotrophs, using carbon dioxide (CO_2) as electron acceptor in the energy metabolism.[18, 19] Syntrophy involves the mutually beneficial exchange of nutrients or metabolic by-products between different organisms. The syntrophic exchange of H_2 between archaea and bacteria is believed to have largely influenced an important evolutionary milestone, eukaryogenesis—the transition from single-cellular prokaryotes to multicellular eukaryotes.[20] However, the syntrophy hypothesis remains a subject of debate, as alternative models suggest that bacterial endosymbiosis and environmental changes may have been more influential in this transition.[21] Additionally, the origins and characteristics of the bacterial ancestors of eukaryotic components remain enigmatic.[22] Nevertheless, investigations to better differentiate between or refine current models are on-going.

Hydrogen exhibits physical characteristics that are desirable for biological systems. Its negative redox potential, $E^{\circ\prime} = -0.42$ V vs Standard Hydrogen Electrode (SHE) at pH 7.0, is crucial in many biological processes, such as cellular respiration. Moreover, its ability to efficiently permeate through biological tissues and cells (diffusion coefficient 4×10^{-9} m^2 s^{-1}) is important for gas exchange and diffusion across the cell membrane. Indeed, H_2 as a microbial fuel is of vital importance for the growth and survival of H_2-processing microorganisms.

Microorganisms consume and produce H_2 using ancient metalloenzymes known as hydrogenases (**Fig. 1.1**).[23-25] These enzymes convert protons (H^+) and electrons (e^-) into H_2, and vice-versa, while leveraging abundant earth metals such as nickel and iron. The capacity to uphold high rates, stability, efficiency, and specificity while using abundant metals has garnered them attention for their use in renewable and carbon-neutral energy technologies.

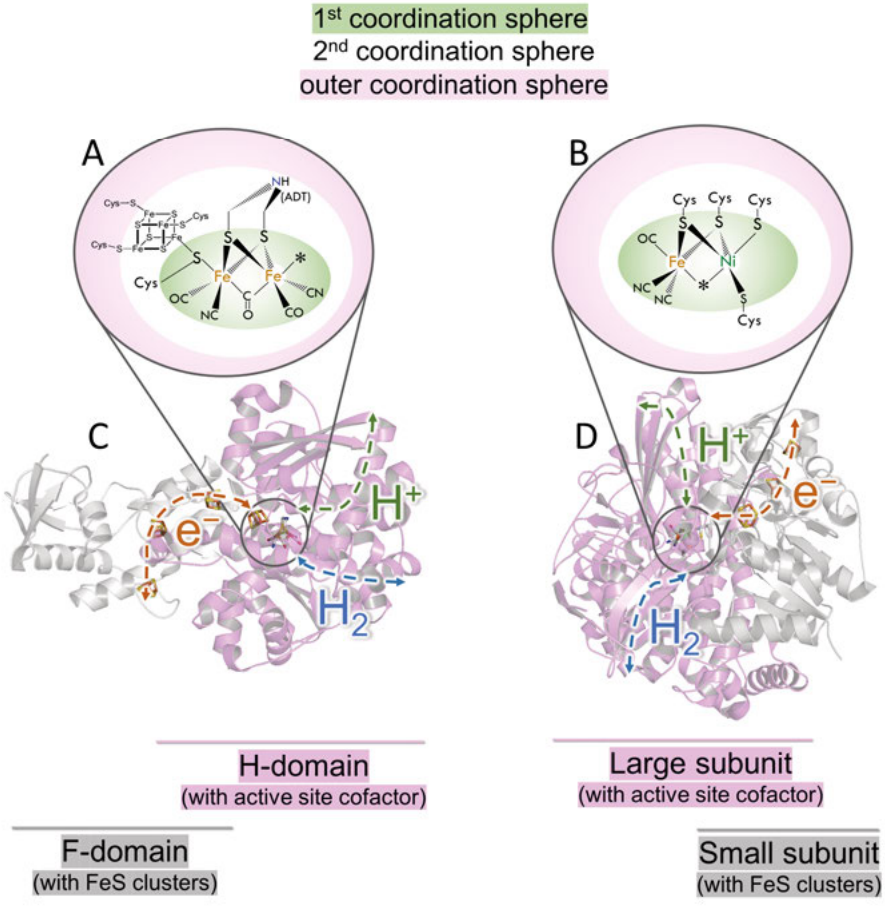

Figure 1.1. The active sites of **(A)** [FeFe] hydrogenases (H-cluster) and **(B)** [NiFe] hydrogenases. From the perspective of the catalytic cofactor metal ions (Fe or Ni), the first coordination sphere (green) includes the π-accepting, strong-field ligands CO and CN^- and the thiols (S). The asterisk (*) indicates the open coordination site (OCS) for substrate binding. In (A), the $[4Fe\text{-}4S]_H$ of the H-cluster, connected to the $[2Fe]_H$ site via a bridging cysteinyl thiolate, acts as a "non-innocent", redox-active ligand. The second coordination sphere (white) includes the hydrophobic and electrostatic (*e.g.*, hydrogen-bonding) contacts of the cofactor with the protein structure and for (A), the amine bridgehead of the azadithiolate (ADT) ligand. **(C-D)** The outer coordination sphere encompasses the remaining scaffold of the protein and includes electron transfer (e^-), proton transfer (H^+), and hydrophobic gas channels. In (C), the H-cluster is in the H-domain (magenta cartoon) and the additional FeS clusters (F-cluster) are in the F-domain (grey cartoon). The PDB ID for this structure is 4XDC. In (D), the NiFe cofactor is in the large subunit (magenta cartoon) and the FeS clusters are in the small subunit (grey cartoon). The PDB ID for this structure is 3UQY. Genetic, structural, and biophysical studies consistently show that the core H-cluster structure in [FeFe] hydrogenases and the NiFe active site in [NiFe] hydrogenases are highly conserved across phylogenetic groups, despite variations in the second and outer coordination spheres.

Prior to the work presented in this thesis, hydrogenases were summarized as follows (for review, see refs.[25, 26]). Three distinct families have independently evolved:

Main classification according to the metal content (Fig. 1.1):

- Homobinuclear [FeFe] hydrogenase, with a diiron subsite and iron-sulfur cluster(s).[27] This was previously denoted as iron-only hydrogenases before it was discovered that mononuclear [Fe] hydrogenase also contains iron.
- Heterobinuclear [NiFe] hydrogenase, with an iron-nickel subsite and iron-sulfur clusters.[28]
- Mononuclear [Fe] hydrogenase, with an iron site but without iron-sulfur clusters. This was previously denoted as iron–sulfur-cluster free hydrogenase or H_2-forming methylenetetrahydromethanopterin dehydrogenase (Hmd)[29]

General proposed physiological roles (see also Appendix I and II):

- [FeFe] hydrogenase: fermentative H_2 disposal, respiratory electron release, electron bifurcation, H_2-dependent CO_2 reduction, or H_2-sensing.[15, 30, 31]
- [NiFe] hydrogenase: fermentative H_2 disposal, respiratory electron release, electron bifurcation, or H_2-sensing.[15, 32]
- [Fe] hydrogenase: adopt a single function, coupling H_2-oxidation to reduction of a second substrate (5,10-methenyltetrahydromethanopterin)[15, 33]

Historical record and taxonomic distributions:

- [FeFe] hydrogenases are believed to have evolved in fermentative bacteria (< 4 billion y. a.). They are encoded by anaerobic bacteria and eukaryotes.[15, 30, 34, 35]
- [NiFe] hydrogenases date back to the last universal common ancestor (LUCA) (≈ 4 billion y. a.). They are encoded by bacteria and archaea across all ecosystems.[15, 32, 36]
- [Fe] hydrogenases evolved in methanogenic archaeal species (< 4 billion years ago), aiding the reduction of CO_2 to methane under anaerobic conditions.[15, 33]

General biochemical properties (notable exceptions described in the subsequent sections):

- [FeFe] hydrogenases are typically O_2-sensitive (irreversibly inhibited by O_2) yet fast-acting and catalyzes both H_2 oxidation and proton reduction (bidirectional).[30, 37, 38]
- [NiFe] hydrogenases are typically O_2-tolerant (functions in the presence of low levels of O_2; often reversibly inhibited) or O_2-insensitive (unaffected by fluctuating O_2 levels) and has a notable preference towards H_2 oxidation.

- [Fe] hydrogenases are typically oxygen-sensitive and slow-acting and can only activate H_2 in the presence of a hydride-accepting substrate (methenyl-H_4MPT^+).[39]

This thesis primarily explores the structural and functional diversity of hydrogenases, with a specific focus on binuclear [FeFe] and [NiFe] hydrogenase families. Their shared uniqueness lies within the active site cofactor (**Fig. 1.1A-B**). The presence of both π-accepting, strong-field ligands such as carbon monoxide (CO) and cyanide (CN^-) as intrinsic components is highly unusual for biological systems. Because they are strong field, the ligands play a crucial role in enabling the metal ion(s) to exist in low-spin states. Low-spin configuration in this context is beneficial for forming a vacant coordination site or easily accessible orbitals, making the metal center more receptive to H_2 binding and activation, and for allowing the reaction to proceed without a large energy barrier.

However, [FeFe] and [NiFe] hydrogenases are considered to be unrelated, *i.e.,* they did not evolve from the same evolutionary origin or ancestor. This makes them a striking example of convergent evolution, which is described as when unrelated species independently evolve similar structures and functions.

The findings presented in this thesis may prompt a re-evaluation of certain long standing assumptions and beliefs concerning the general characteristics of these binuclear enzymes, as will be covered in the following chapters.

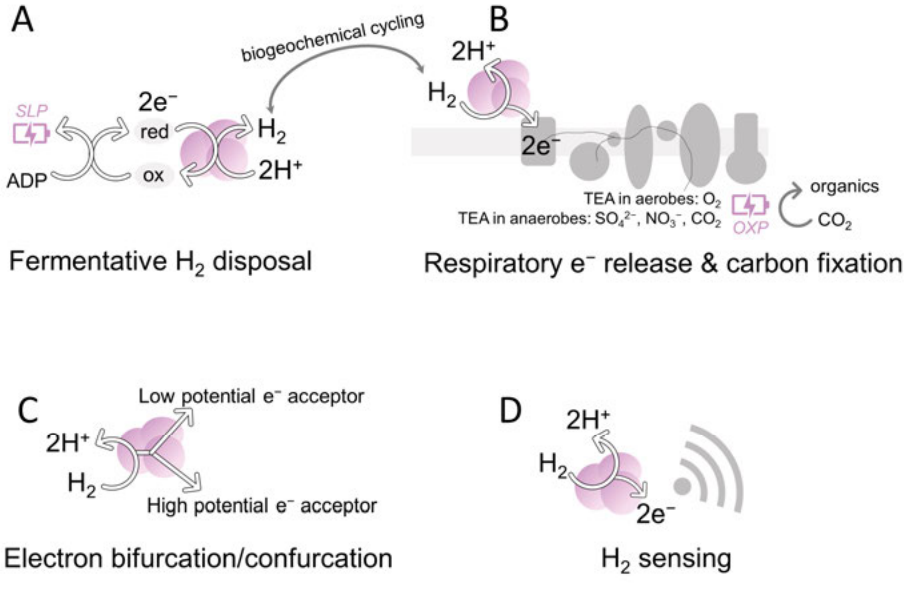

Figure 1.2 Simplified schematic diagram illustrating the common roles of hydrogenases in microbial physiology. Reduced and oxidized cofactors (*e.g.*, Fd and/or NADH/NAD$^+$) are indicated as "red" and "ox", respectively. *SLP*-substrate level phosphorylation; *OXP*-oxidative phosphorylation; *TEA*-terminal electron acceptor.

The extensive diversification of the two families into (sub)groups—with unique catalytic properties, level of O_2-tolerance/sensitivity, and substrate affinities—has been pivotal for the long-term survival and adaptation of microorganisms across various ecosystems: ranging from low-O_2 environments rich in H_2 (*e.g.,* anaerobic waters, peat soils, sediments, and animal gastrointestinal tracts), aerated soils and waters with minimal H_2 content, to ice-free desert ecosystems.[15, 36] It has also been observed that certain microbial species exhibit diversity in H_2-related enzymes, not just across, but also within them, suggesting metabolic adaptability to environmental changes. This diversification has allowed hydrogenases to carry out various functions linked to H_2 metabolism (**Fig. 1.2**).[15, 25, 30, 32, 36]

Dissipating excess reductant via fermentation: Excess reducing power (electrons) is converted to H_2 gas, which can easily diffuse out of the cell. In anaerobic environments, where alternative electron acceptors can be scarce, microbial fermentation comes into play, converting carbon sources into alcohols, gases, or organic acids without O_2.[24, 40, 41] Similarly, photobiological fermentation involves sunlight-driven microorganisms like green algae and cyanobacteria, which convert water and sometimes organic matter into H_2. Fermentation serves to re-oxidize electron carriers (*e.g.,* NADH, Fd) that are crucial for the continuation of glycolysis and other metabolic pathways in the absence of O_2, as well as the production of ATP via substrate-level phosphorylation (SLP in **Fig. 1.2A**). In parallel, buildup of excess electrons, which

could otherwise lead to harmful redox stress within the cell, is prevented. The diffusible H_2 can be oxidized by other organisms in the environment, contributing to the ecological cycling of H_2.

Respiratory electron release and carbon fixation: Oxidation of H_2 releases low-potential electrons, which are subsequently transduced through respiratory chains to generate energy through oxidative phosphorylation (OXP in **Fig. 1.2B**).[38, 42] Energy harnessed from this process can drive carbon fixation processes. Hydrogenase-containing respiratory chains have been found to efficiently generate energy in oligotrophic (low-level nutrients) environments.[43, 44]

Energy conservation via bifurcating electrons: Electron bifurcation in hydrogenases couples exergonic and endergonic redox reactions (**Fig. 1.2C**). This process enables the simultaneous transfer of electrons to high and low potential acceptors, effectively splitting energy from a single source into two separate pathways and propelling thermodynamically unfavourable reactions forward.[45-47] This unique mechanism is essential for anaerobic microbes, aiding them in efficiently utilizing H_2 for metabolic processes, including cellulolytic fermentation, acetogenesis (making CH_3COOH from H_2 and CO_2), and methanogenesis (making CH_4 from H_2 and CO_2).[48-51]

Sensing external H_2: Some sensory hydrogenases encoded by anaerobes can detect high partial pressures of H_2 (pH_2) and trigger regulatory cascades that govern the expression of respiratory hydrogenases (**Fig. 1.2D**).[52-55] These sensory hydrogenases are encoded by an operon (*i.e.*, functionally related genes controlled by a shared operator, allowing for coordinated gene expression) that include the Per-Arnt-Sim (PAS) domain, which act as sensors and are widespread across all kingdoms of life. Some sensory hydrogenases may regulate broader cellular functions, such as motility, in response to changes in pH_2 in anaerobic environments.

Other (proposed) functions: Other specialized physiological functions will be described briefly in the overview of [FeFe] and [NiFe] phylogenetic groups in subsequent sections (see also **Appendix I and II**).

[FeFe] hydrogenases

The [FeFe] hydrogenases exhibit exceptional activity, catalyzing H_2 evolution and oxidation rates at 10^4−10^5 s^{-1}, which exceeds activities displayed by synthetic catalysts.[25, 56] Across all phylogenetic groups, the active site cofactor denoted as "H-cluster", embedded within the H-domain, is proposed to be the unifying feature based on genetic, structural, and biophysical studies of known enzymes (**Fig 1.1A**).[32] This biologically unique cofactor consists of a canonical iron-sulfur cluster ($[4Fe\text{-}4S]_H$) linked via a bridging cysteinyl thiolate to a diiron subsite ($[2Fe]_H$) with CO and CN^- ligands that stabilize the iron ions in a low-spin state.[27, 57-60] The two iron ions of the $[2Fe]_H$ subsite are further ligated by the sulfur atoms of the azadithiolate ligand ($^-\mathbf{S}CH_2NHCH_2\mathbf{S}^-$, ADT).[61-64] The distal (Fe_d) and proximal (Fe_p) iron in $[2Fe]_H$ are designated based on their proximity to the $[4Fe\text{-}4S]_H$. The direct ligation to the metal ion encompasses the first coordination sphere.

A fully catalytically active $[2Fe]_H$ subsite transpires when it is linked to its redox-active ligand $[4Fe\text{-}4S]_H$ and is incorporated into its protein framework—the minimum being the "H-domain"—enabling critical interactions within the second and outer coordination spheres (**Fig 1.1C**).[63, 65-67] Similar to other metalloenzymes, the spheres beyond the first coordination enhance catalytic rate, stability, thermodynamic efficiency, and selectivity. The influence and significance of secondary and outer coordination sphere effects are increasingly recognized in the design of mimics for H_2 catalysis.[68-70]

The second coordination sphere encompasses hydrophobic and electrostatic contacts between the H-cluster and the protein fold. The geometric positioning of the CO, CN^-, and ADT ligands is maintained by specific, fairly to highly conserved amino acid residues within each phylogenetic group.[71-73] The amine bridgehead of the ADT ($-S\mathbf{C}H_2\mathbf{NHC}H_2S-$) ligand provides a second coordination sphere interaction and is involved in proton transfer from the bulk solution to the $[2Fe]_H$ subsite, and vice-versa. The frustrated Lewis pair (FLP) interaction between the basic ADT-amine and acidic Fe_d of the H-cluster plays a vital role in both the formation and cleavage of the H_2 bond.[74] In a FLP, the Lewis acid and base sites remain in close proximity but are "frustrated" from forming the typical adduct due to steric hindrance. Insights into the control of ligand spatial arrangement and H-cluster reactivity by the second coordination sphere have been gathered from structural, functional studies, and site-directed mutagenesis studies.[72, 75-77]

The outer coordination sphere comprises of accessory electron-transferring FeS clusters (F-clusters)[30, 78-80], proton transfer pathway consisting of protonatable amino acid residues or structured water molecules[81-85], gas channels[86-89], and interactive amino acid residues beyond the second coordination sphere.[30, 71, 72] The ferredoxin-type F-clusters (additional [4Fe-4S] clusters) act as molecular conduits, enabling long-distance electron transfer between the H-cluster and external redox partners. Additionally, a selective delivery system for

substrates and products (H^+ or H_2) is provided. Transport systems in the outer-coordination sphere can have long-range electronic (electron density or distribution), thermodynamic (energetic landscape of reactions or relative stabilities of reactants, intermediates, and products), and kinetic (rates of key steps, such as H_2 diffusion/binding, proton/electron transfer) on the H-cluster.[30, 71, 72, 78-80, 84, 85, 90-92]

Collectively, the first, second, and outer coordination spheres streamline the interconversion of protons, electrons, and molecular H_2. The deficiency of a single sphere can undermine overall catalytic performance.

Given its structural complexity, it is to no surprise that H-cluster synthesis requires a dedicated machinery. [FeFe] hydrogenases can be "activated" into "*holo*" enzymes either naturally by using multiple maturation enzymes (HydE, HydF, and HydG) and iron-cluster assembly enyzmes or synthetically by adding mimics of the $[2Fe]_H$ subsite into immature "*apo*" enzymes.[63, 67, 93] The experimental section briefly outlines the "natural" biosynthesis process and the artificial maturation method for activating heterologously-expressed enzymes.

Although there is on-going debate about mechanistic models, all proposed catalytic cycles include oxidized, singly reduced, and doubly reduced H-cluster states, with the site of H_2 catalysis happening at the OCS of the distal iron ion (Fe_d) (**Fig. 1.3A**).[94-96] This thesis adopts the nomenclature proposed by Haumann, Stripp, and colleagues[97], without making any value judgements or claims about the molecular structures.

The oxidized "resting" state, H_{ox} and its protonated equivalent form, $H_{ox}H$, comprise a $[4Fe\text{-}4S]_H^{2+}$ cluster and a $Fe^I\text{-}Fe^{II}$ site, with the iron ions bridged with a CO ligand (μCO) (**Fig. 1.3A**).[98, 99] Singly reduced states involve an electron residing in the $[4Fe\text{-}4S]_H^+$ cluster forming the H_{red}' state ($[4Fe\text{-}4S]_H^+ \cdot Fe^I\text{-}Fe^{II}$).[98, 100, 101] An "inactive", slow pathway occurs when H_{red}' transitions to H_{red}, resulting from deprotonation of $[4Fe\text{-}4S]_H^+$ and the formation of a bridging hydride (μH), with the μCO moved to an apical position. Involvement of a second electron forms the doubly reduced or "super-reduced" states called H_{sred}, having a configuration of $[4Fe\text{-}4S]_H^+ \cdot Fe^I\text{-}Fe^I$. Tautomerization of H_{sred} results in a terminal hydride (H^-) at the OCS to form the H_{hyd} state ($[4Fe\text{-}4S]_H^+ \cdot Fe^{II}\text{-}Fe^{II}$).[64, 102, 103] Proton-coupled electron transfer (PCET) from H_{red}' bypasses the slow pathway involving μH to directly form H_{hyd} with a protonated $[4Fe\text{-}4S]_H$. Protonation of H_{hyd} at the ADT-amine is proposed to yield $H_{hyd}H^+$.[104, 105] The ADT-amine positions a proton close to the Fe_d hydride to facilitate H_2 bond formation.[74] An elusive $H_{ox}\text{-}H_2$ state is hypothesized to form and upon H_2 release, the H-cluster reverts to H_{ox}. The cycle is reversed for H_2 oxidation, with the FLP enabling H_2 bond cleavage.

Inhibited states of the oxidized and singly reduced forms can occur upon binding of cysteine thiol or exposure to inhibitors such as sulfide, leading to H_{inact} or H_{trans}, and carbon monoxide, resulting in $H_{ox}\text{-}CO$ or $H_{red}\text{-}CO$ (**Fig.1.3B**).

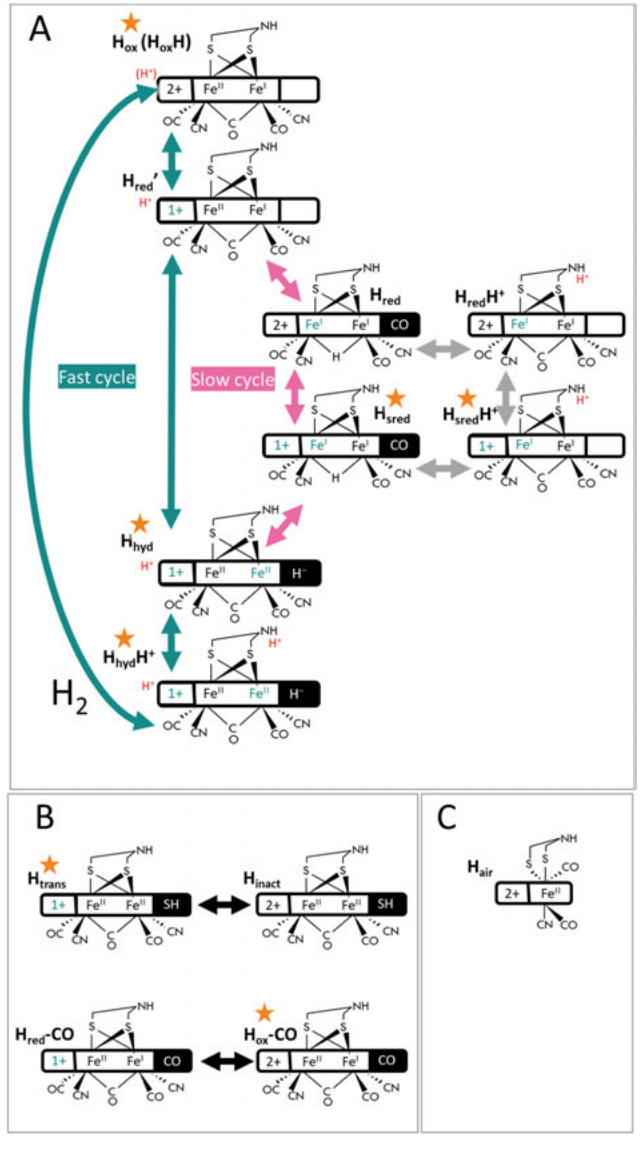

Figure 1.3 (A) The proposed mechanistic model for H_2 turnover by Haumann, Stripp *et al.*[97] The fast cycle is shown in dark cyan arrows, and the slow cycle is shown in magenta arrows involving ligand rotation between μCO and μH. Black-filled squares indicate a terminal CO or H^- occupying the OCS. The grey arrows indicate the proposed equivalent molecular structures of H_{red} ($H_{red}H^+$) and H_{sred} ($H_{sred}H^+$) by Lubitz, Birrell *et al.*[95] The structure and catalytic significance of these states remain an active area of debate, with the divergence of these models extensively discussed in recent literature.[26, 30, 95, 97, 106] **(B)** Reported inhibited states of the oxidized and singly reduced forms of the H-cluster. **(C)** Proposed structure of the mononuclear H-cluster species (H_{air}) of O_2-exposed Group D *Tam*HydS.[71] Orange star indicates that the state has been observed in electron paramagnetic resonance spectroscopy (**Tab. 4.1**).

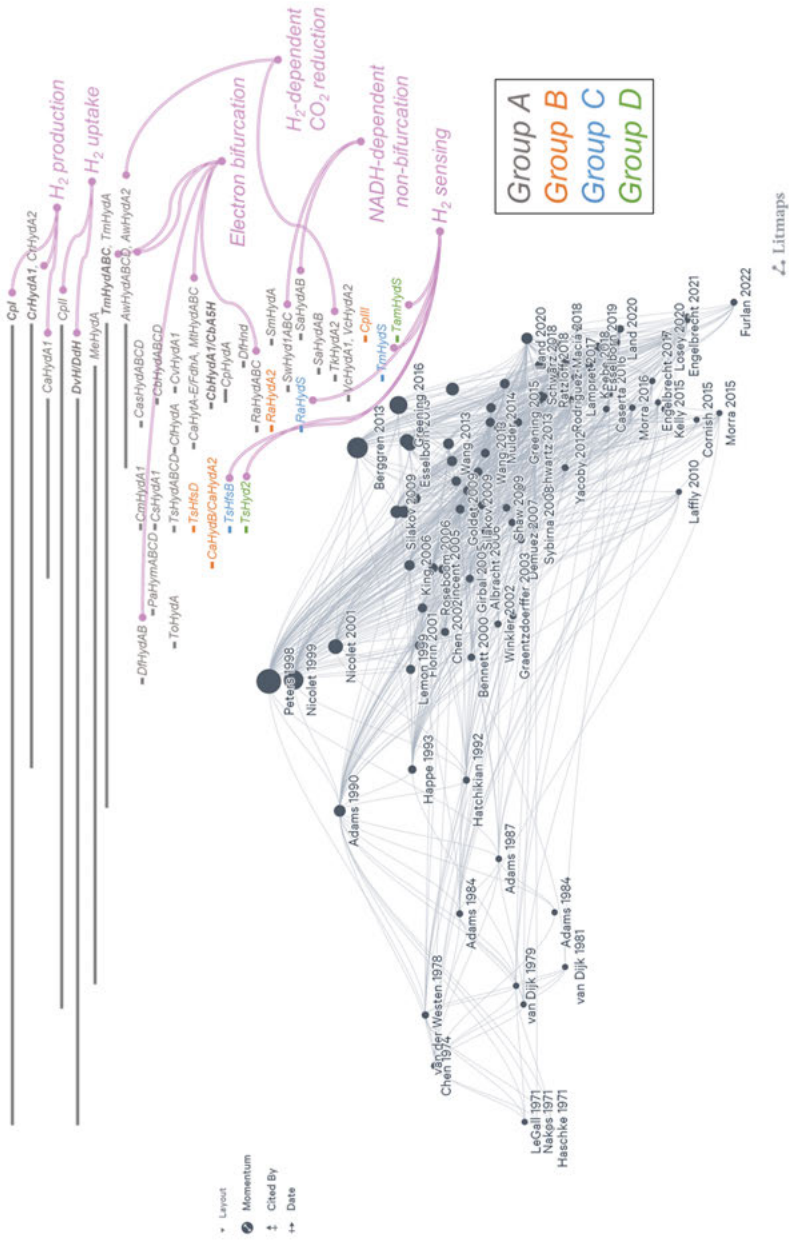

Figure 1.4 This timeline illustrates the progression of [FeFe] hydrogenase literature, with specific enzymes characterized at various points in time (bars corresponding to each enzyme indicate duration). Each reference (first author, year) is represented as a grey circle, with the size of each circle indicating the relative level of influence of that reference ("momentum" that was calculated by *Litmaps*® based on cite count and weighed by recency). The interconnecting lines between the circles illustrate the citations and cross-references. Enzyme names are color-coded according to their phylogenetic groups. Proposed physiological functions are indicated in magenta.

At the start of my PhD studies, [FeFe] hydrogenases were classified into Group A−D (**Fig. 1.4**).[15, 30, 31, 56, 107] However, some of the findings from this work may prompt a reassessment of this prevailing classification framework.

Group A: The most extensively studied [FeFe] hydrogenases are from Group A, which can be further divided into Group A1−A4 (based on proposed functions)[15] or subclasses M1−M5 (based on domain architecture)[30]. Examples include hydrogenases from green algae *Chlamydomonas reinhardtii* (*Cr*HydA1), soil bacterium *Clostridium pasteurianum* (*Cp*I and *Cp*II), dimeric hydrogenase from sulfate-reducing *Desulfovibrio vulgaris* (DvH)/ *Desulfovibrio desulfuricans* (*Dd*H/*Dd*HydAB), ruminal *Megasphaera elsdenii* (*Me*HydA), and the electron-bifurcating enzymes from hyperthermophilic *Thermotoga maritima* (*Tm*HydABC) and acetogenic bacterium *Acetobacterium woodii* (*Aw*HydABCD).

Most members of Group A1 such as *Cp*I, *Cr*HydA1, and the hydrogenase from butanol-producing *Clostridium acetobutylicum* (*Ca*HydA1), are proposed to facilitate the oxidation of ferredoxin (Fd) during anaerobic fermentative or photobiological H_2 production. Exceptions include cytoplasmic *Cp*II[108] and periplasmic *Dd*H[109, 110], which prefer H_2 oxidation and are proposed as electron liberators for respiration and growth. Group A2 is uncharacterized and, thus, their function is unknown. Group A3 members have been proposed to reversibly bifurcate electrons between H_2 and the enzyme's redox partners, ferredoxin and NAD(P)H (*e.g., Tm*HydABC). Other members of Group A include formate-dehydrogenase linked Group A4 from *Clostridium autoethanogenum* (*Ca*HytA-E/FdhA)[111], H_2-dependent CO_2 reducing enzyme from *A. woodii* (*Aw*HydA2)[112] and thermophilic *Thermoanaerobacter kivui* (*Tk*HydA2)[113], as well as NADH-dependent non-bifurcating enzymes from *Syntrophomonas wolfei* (*Sw*Hyd1ABC)[114], and *Syntrophus aciditrophicus* (*Sa*HydAB).[115]

Although the highest turnover frequency rates were recorded from Group A (TOF up to 10^5 s^{-1}), most of these enzymes exhibit complete H-cluster degradation upon exposure to even minimal levels of O_2.[86, 116, 117] Only a few characterized members in this group show O_2-tolerance such as *Me*HydA, *Dd*H, and the hydrogenase from soil or fecal bacterium *Clostridium beijerinckii* (*Cb*A5H).[79, 86, 118, 119]

With regards to electrochemical properties, Group A enzymes are deemed as "reversible" catalysts capable of sustaining high rates of proton reduction and H_2 oxidation exceptionally close to the thermodynamic potential of the reaction (**Fig. 2.5D**).[120]

Group B: Despite their phylogenetic divergence from Group A, Group B enzymes share fairly conserved amino acid motifs around the H-cluster (**Fig. 3.4D**). Limited data exists on the in-depth characterization of Group B [FeFe] hydrogenases. However, based on genomic data, they are suggested to play a role in coupling the oxidation of Fd to fermentative evolution of H_2.[15] Some

examples are from *C. pasteurianum* (*Cp*III), *C. acetobutylicum* (*Ca*HydB/*Ca*-HydA2), hydrogenase from cellulolytic bacterium *Ruminococcus albus* (*Ra*HydA2), and from hemicellulolytic bacterium *Thermoanaerobacterium saccharolyticum* (*Ts*HfsD).

Recent electrochemical studies indicate that Group B *C. pasteurianum* III (*Cp*III) *and M. elsdenii* II (*Me*II) show bidirectionality, without any inherent bias, and exhibit high susceptibility towards oxidative inactivation at high redox potentials.[121]

Group C: Group C [FeFe] hydrogenases are predicted to sense H_2 and induce cascades through co-transcribed regulatory elements (*e.g.,* kinases and phosphatases), thus acquiring the designation of a "sensory" group. All known members of this group feature the signalling PAS domain.

A characterized enzyme from hyperthermophilic *Thermotoga maritima* (*Tm*HydS) demonstrated low catalytic rates.[91] Moreover, *Tm*HydS has been documented to exhibit higher tolerance to inhibitor CO compared to those in Group A. However, like most Group A enzymes, its affinity for H_2 appears to be quite low (K_m >400 μM) and O_2 can infiltrate and impair its active site.

Transcriptional evidence suggests that the putative phosphatase-linked sensory hydrogenases of *R. albus* (*Ra*HydS) and *T. saccharolyticum* (*Ts*HfsB) may regulate the transcription of Group A enzymes.[15, 52, 122] However, this has not been biochemically verified.

Group D: Group D [FeFe] hydrogenases are proposed to be putatively sensory as they are closely related to Group C, sharing similar genomic localizations and domain structures. However, Group D lacks the PAS domain. In comparison to Group A, Group D representative from thermophilic *Thermoanaerobacter mathranii* (*Tam*HydS) shows lower catalytic activity rates, an increased tolerance against CO inhibition, and require a significant amount of overpotential for both proton reduction and H_2 oxidation, which makes it an "irreversible" catalyst (**Fig. 2.5D**).[71, 120] Interestingly, *Tam*HydS has a unique reactivity towards to O_2, forming a mononuclear version of the H-cluster, with limited catalytic ability and peculiar O_2-stability (**Fig. 1.3C**).

A higher "apparent" affinity or substrate binding for H_2 was reported (K_m 90–100 μM) for *Tam*HydS[71], athough contradictory findings of a higher Michaelis' constant (600 μM) have also been published.[123] Although K_m provides insights into the affinity between an enzyme and its substrate, the value does not directly quantify this affinity. Instead, K_m reflects the combined rates of substrate binding and catalysis. Additionally, the K_m's value can be affected by experimental variables that complicate direct comparisons between studies unless the conditions are consistent. Different enzyme-substrate pairs may exhibit the same K_m value if either a high binding affinity is paired with slow catalytic turnover, or a low binding affinity is accompanied by rapid catalysis.

The protein scaffold surrounding the H-cluster, also denoted as the "active site pocket", is conserved within each group, but exhibits notable differences

between groups.[30, 90] Additionally, comparative genetic and structural analyses suggest differences in proton transfer pathways among various hydrogenase groups, though this requires experimental validation (**Chapter 4**).[84, 85, 91, 124] Even within a group, the F-cluster domain exhibits structural diversity.[30]

While the H-cluster is the proposed common denominator in all phylogenetic groups, any discrepancies in reactivity are likely attributed to differences in second and/or outer coordination sphere effects–such as the active site environment encompassing the H-cluster or the pathways for substrate transfer (**Chapter 4−5**). Hence, comparative analyses of various [FeFe] hydrogenase groups are anticipated to generate a wealth of novel insights into the impact of the protein framework on modulating hydrogenase activity.

[NiFe] hydrogenases

[NiFe] hydrogenases are recognized for their superior O_2-tolerance/insensitivity. These enzymes are composed of a catalytic (large, ≈60 kDa) subunit and an electron-relaying Fe-S (small, ≈30 kDa) subunit (**Fig. 1.1D**).[28] The large subunit accommodates the Ni-Fe cofactor, which is anchored by four cysteine thiolate units: two terminal ligands to the nickel and two bridging ligands between the nickel and iron ions (**Fig. 1.1B**).[125]

During the catalytic cycle, the Ni–Fe cofactor exhibits several redox states, with the nickel ion transitioning through multiple oxidation states (Ni^{3+}, Ni^{2+}, and Ni^{+}) (**Fig. 6.4F**). Conversely, the low-spin iron ion maintains a constant Fe^{2+} state (S = 0), and is coordinated by one CO and two CN^{-} ligands, along with an additional ligand that may occupy the Ni–Fe bridging position (μOH, or μH).[25, 126] Further details on the proposed catalytic cycle for [NiFe] hydrogenases are outlined in **Chapter 6**.

Analogous to [FeFe] hydrogenase, some well-conserved amino acid residues in proximity to the Ni–Fe cofactor (second coordination sphere) are proposed to play important roles in catalysis.[28, 125, 127] The outer coordination sphere includes accessory electron-transferring FeS clusters ([4Fe-4S], [3Fe-4S], or [4Fe-3S] clusters) in the small subunit, proton transfer pathway(s) and gas channels (reported to be susceptible to blockage when pH_2 is high).[128]

Depending on the subgroup, the large and small subunits of the [NiFe] hydrogenase associate with other subunits.[15] The resulting complexes can mediate a variety of processes, including respiration, fermentation, energy conversion, electron bifurcation, carbon fixation, and H_2 sensing. Comprehensive reviews on the classification of [NiFe] hydrogenases, considering phylogeny, genetic structure, and physiological roles, are available.[15, 32, 36] A brief overview of the four main groups is provided here:

Group 1: Group 1 [NiFe] hydrogenases are membrane-bound and are further divided into subgroups (Group 1a−1h) based on their proposed physiological functions, including liberating electrons for the respiration of sulfate, nitrate, and fumarate (**Fig. 1.2B**; **Appendix II**). The two Group 1 [NiFe] hydrogenases from *E. coli*, *Hyd*1 (Group 1d) and *Hyd*2 (Group 1c), exhibit different biases: *Hyd*1 is unidirectional and strongly biased towards H_2 oxidation, while *Hyd*2 is bidirectional. This group also includes O_2-tolerant and O_2-insensitive enzymes such as Group 1d low-H_2 affinity hydrogenases from *Ralstonia eutropha* / *Cupriavidus necator*, *E. coli*, and *Aquifex aeolicus* and Group 1h high-H_2 affinity hydrogenases from *R. eutropha* / *C. necator*, *Mycobacterium smegmatis*, and *Streptomyces avermitilis*.

Group 2: Group 2 [NiFe] hydrogenases are primarily located in the cytosol, with most members serving sensory functions. The well-characterized sensory hydrogenases are the Group 2b [NiFe] hydrogenases (*e.g.*, *R. eutropha* / *C. necator* and *Rhodobacter capsulatus*). These enzymes have adapted the [NiFe] active site to sense high partial pressures of H_2 (pH_2) and

subsequently activate two-component regulatory cascades that control the expression of respiratory hydrogenases. The operons encoding these hydrogenases contain predicted PAS domains (similar to Group C [FeFe] hydrogenases) that likely transduce the signal of hydrogenase activity to downstream components, such as heme. A noteworthy member of this group is the Group 2a high-H_2 affinity, O_2-insensitive hydrogenase from *M. smegmatis*, which can oxidize atmospheric pH_2 under atmospheric pO_2 levels (**Chapter 6**).

Group 3: Group 3 [NiFe] hydrogenases are typically bidirectional, catalyzing both H_2 oxidation and proton reduction. These enzymes are known to couple H_2 oxidation with the reduction of cofactors, and also enable the bifurcation of electrons from H_2 to cofactors. Several examples include enzymes from *Methanothermobacter marburgensis*, *Methanosarcina barkeri*, and *Pyrococcus furiosus*. Some Group 3 enzymes can behave as sulfhydrogenases *in vitro*, reducing elemental sulfur (S^0) to hydrogen sulfide (H_2S).[129]

Group 4: Group 4 [NiFe] hydrogenases, like Group 1, are membrane-bound but are distinguished by their general role as fermentative H_2 evolvers. The evolution of H_2 are coupled with the oxidation of cofactors and translocation of protons. Some Group 4 enzymes form complexes with CO dehydrogenase (CODH) to anaerobically respire CO using protons as terminal electron acceptors. Examples from this group include formate hydrogenlyase (disproportionation of CHO_2^- to CO_2 and H_2) from *E. coli* and *Salmonella enterica*, and the CODH-linked hydrogenases from *Carboxydothermus hydrogenoformans*, and *Rhodospirillum rubrum*.

(Bio-)technological applications of hydrogenases

Biotic, biological H_2 production: Since its initial description in the 19th century, biological H_2 production has made substantial progress, with some techniques evolving into nearly mature technology levels.[130, 131] These processes leverage (non-)photosynthetic microorganisms like green algae, anoxygenic photosynthetic bacteria, and some heterotrophic bacteria encoding hydrogenases for H_2 production. Both photo- and dark fermentation, which convert organic substrates into H_2 in the presence and absence of light, respectively, have demonstrated promising potential.

While these biological methods can be technically feasible for attaining carbon-free H_2 production and can operate well under ambient conditions, they face several limitations.[130, 131] These include a lower-than-expected biohydrogen yield, and suboptimal solar-to-hydrogen (STH) efficiency. High costs linked to materials, production, and storage also pose challenges. System instability in large volumes and the rapid inhibition of reactions, due to O_2 production from water splitting, further complicate the process.

Cyanobacteria, as photoautotrophs, offer a distinct route to H_2 production through photosynthesis-related mechanisms. Using cyanobacteria and [FeFe] hydrogenase in tandem for photobiological H_2 production, the main challenges are: achieving *in vivo* maturation in cyanobacteria, efficiently redirecting electrons from native metabolic pathways to the enzyme, and engineering O_2-tolerant variants.[132]

Despite existing challenges, biological H_2 production is still a promising avenue for renewable energy, given its potential for minimal to zero carbon emissions. Ongoing research aims to improve efficiency and commercial feasibility.

Abiotic, bio-mimetic catalysts: Although Nature has enabled hydrogenases to possess top-tier turnover rates (particularly for [FeFe] hydrogenases), their susceptibility to O_2 and costs for large-scale production limit their economic viability. Mimicking the active site cofactor is an attractive alternative. The relatively more simple and adaptable property of mimics not only pique interest in catalyst design efforts, but also provide insights into the fundamental aspects of hydrogenase structure, maturation, and its catalytic mechanism.[63, 67, 133-136]

Despite the extensive array of [FeFe] hydrogenase cofactor mimics reported in literature, they often grapple with instability in aqueous or aerobic conditions, reduced catalytic efficiencies, unidirectionality, and high overpotential requirements.[137-139]

While research on the influence of the protein framework on rates, bias, thermodynamic efficiency, electronic distribution, and geometry of the active site cofactor is limited, a consistent insight from these outer sphere coordination effect studies is evident: the protein scaffold is crucial for fine-tuning the active site cofactors[72, 75-77] and for the delivery of substrates and products.[84, 85]

This is most elegantly demonstrated by "artificially maturing" a [FeFe] hydrogenase with the insertion of the closest mimic of the $[2Fe]_H$ subsite: $[2Fe]^{ADT}$ $[Fe_2(\mu\text{-ADT})(CO)_4(CN)_2]^{2-}$ (**Fig. 2.1C**). Artificial maturation with $[2Fe]^{ADT}$ results in a *holo* [FeFe] hydrogenase that can catalyze rates comparable with the native enzyme.[63, 67]

To develop base-metal H_2-processing catalysts for practical applications, mimics should provide second and/or outer coordination spheres that can minimize solvation shifts, reorganization energies, synchronize electron and proton transfers, manage the formation and stability of intermediates, and protect catalytically relevant states from participating in side reactions.[139, 140]

Researchers have endeavored to replicate the protein environment of hydrogenase enzymes to overcome some of the limitations inherent in synthetic cofactor mimics.[141-145] A notable example of a functional cofactor mimic is the H_2-oxidizing Dubois catalyst[146-148] featuring a Ni center ligated by two bidentate phosphines and at least one pendant amine group in the second coordination sphere that emulate the natural enzyme's architecture. This highlights the catalytic significance of the amine group, later verified as the bridgehead atom of the "native" H-cluster.

Further advancements in bio-mimicry have been achieved through fine-tuning electron density. For instance, capping dicyanide ligands with Lewis acids mimics the H-bonding interactions between the cyanide ligands of the natural H-cluster and the protein backbone. This strategy enabled proton reduction at biologically relevant oxidation states, which was previously hampered by proton-induced decomposition.[135] Similar reactivity trends have been observed with alternative ligands, such as phosphines, which do not exhibit H-bonding in the same manner as the Lewis acid-capped cyanides. This observation highlights that while mimicking the H-bonding environment of the natural system can be a viable strategy, other factors inherent to ligand design, such as ligand field strength and metal center electrophilicity, are key determinants of catalytic activity.

Despite this progress with catalysts that operate in aqueous environments and incorporate proton transfer pathways, obtaining a deeper understanding of catalyst-H_2 interactions, H_2 cleavage mechanisms, and catalyst deactivation causes remains crucial for future developments.[66]

Although the top-performing mimics exhibit promising catalytic features, their practical implementation is hindered by limited stability and electrode surface immobilization challenges. Recent strides have been made in addressing these issues by integrating bio-mimetic catalysts into modified macromolecular scaffolds, like organic polymers or carbon nanotubes. These modifications have led to improvements in immobilization techniques, catalytic efficiency, and overall stability.[149]

Biotic and abiotic: semi-artificial photosynthesis: Semi-artificial photosynthesis is an emerging field that seeks to circumvent the limitations and

complexity of natural photosynthesis by combining the light-harvesting capacity of photosensitizers (abiotic) with hydrogenase catalysis (biotic).

In a typical biohybrid setup, photosensitizers capture light energy and transfer electrons to a redox mediator, often a viologen-based molecule. This mediator enables efficient electron transfer from the photosensitizer to the hydrogenase, preventing energy loss through charge recombination. These systems often require (sacrificial) electron donors, which provide a source of electrons to regenerate the photosensitizer and maintain the catalytic cycle.

One approach utilizes non-photosynthetic microorganisms, such as *E. coli* to produce H_2 upon illumination.[150-152]Another technique involves water-splitting photoelectrochemical cells (PECs). Notable STH efficiency was achieved by combining a photoanode with a cathode having a hydrogenase immobilized in a viologen-based polymer.[153]

The field of artificial photosynthesis is advancing towards sustainable energy solutions; however, challenges persist, including limited efficiency, along with scale and cost that remain significant obstacles in constructing a device at high technology readiness levels.

Rationale for investigating hydrogenase biodiversity

The post-genomic era (2000−present), characterized by an exponential increase in available sequences, presents a vast, untapped reservoir of hydrogenases, exhibiting remarkable diversity in their genetic makeup, structural domains, and proposed physiological roles in H_2 metabolism.[15, 30] This wide-ranging structural and functional diversity is enabled by a modular architecture and extensive genetic variation, that remain under-explored and not fully understood. Only a select few branches of the phylogenetic trees have been physiologically, biochemically, and biophysically characterized, with well-studied model microorganisms coming from only five phyla (*Proteobacteria*, *Firmicutes*, *Cyanobacteria*, *Euryarchaeota*, and *Chlorophyta*).[24, 25] Moreover, high resolution structures are only available for a restricted number of subgroups (see **Appendix I** and **II** for list of PDB codes). Generalizing mechanistic principles based on a limited 'species pool' is unjustifiable since it essentially restricts the expansion of model systems that could further elucidate the intricate details that owe hydrogenases their remarkable catalytic prowess for H_2-turnover.

Investigating hydrogenase diversity is, thus, not just an endeavor for fundamental studies, but can be a strategic move towards the development of green H_2-based technologies for several reasons:

Evolutionary principles: The evolutionary principles of hydrogenases serve as a narrative of Nature's ingenuity. Understanding their evolutionary principles not only provides insights into microbial energy metabolism and the tracing of evolutionary origins, but also reveals how they optimize rates, stability, energy efficiency, and selectivity, all of which have been honed for billions of years.

Molecular blueprints: Hydrogenases serve as structural and functional models for designing and optimizing mimics, incorporating low-valent transition metals, hydride chemistry, and proton-coupled electron transfer, due to "fine-tuning" effects by the protein framework.

Discovery of novel enzymes: The surge in genomic databases offers prospects to discover enzymes with improved properties (*e.g.,* compactness, O_2-tolerance, H_2-affinity, or stability). These newly-discovered enzymes can be further optimized for desired properties through directed evolution or rational design, and assessed in sustainable (a)biotic technological applications (*e.g.,* integration into photosynthetic microbes or biohybrid photosynthetic systems).

By leveraging abundant metals like iron and nickel, the use of rare and costly noble metals like platinum is avoided, thereby, positioning H_2 as a viable green energy fuel for the future. While this is indeed a long-term goal, I hope that my thesis will contribute small yet deep insights towards this vision.

Summary and Aims

With the rationale discussed above, the main goal of my Ph.D. research is to discover and characterize hydrogenases, as well as show that an improved understanding of their diversity will allow us to optimize them for (bio-)technological applications. This is done through the following key steps:

Gene mining and biochemical validation: Potential hydrogenase-encoding genes are identified and screened through genome and metagenome searches (performed in collaboration with Prof. Chris Greening). These genes are then heterologously expressed in *E. coli*, and their ability to produce H_2 is biochemically verified, following artificial maturation techniques.[63, 67]

Spectroscopic validation: The capacity of the *E. coli*-expressed hydrogenase genes to bind the active site cofactor is verified spectroscopically.

Purification and artificial maturation: The expressed enzymes are purified, the iron-sulfur clusters reconstituted, and artificially matured.

Biochemical and biophysical characterization: The matured enzymes (and in one case, the enzyme is purified and matured in the native host) are systematically characterized using biochemical assays, electrochemistry, FTIR, and EPR spectroscopy.

Optimization and mutagenesis: Enzyme engineering and site-directed mutagenesis studies are conducted to elucidate the effects of the second and outer coordination spheres. Variants targeting the active site environment and proton transfer pathway are included in the catalog of characterized isolates.

In line with the main goal, the following manuscripts have been published, submitted, or prepared:

Chapter 3, Paper I and Appendix III validate the existence of active archaeal [FeFe] hydrogenases, which have been conventionally assumed to be confined to the other two domains of life.[154]

Chapter 4, Paper II elucidates the roles of the second and outer coordination spheres in altering the catalytic rates, electronic distribution, apparent bias, and geometry of the active site cofactor. This chapter also highlights that the proton transfer pathway is not universal across phylogenetic groups of [FeFe] hydrogenase.[124]

Chapter 5, Paper III presents a novel approach to improve the H_2-production rate and O_2-tolerance of a [FeFe] hydrogenase by rationally designing variants based on a genetic and structural comparison of representatives from different phylogenetic groups.

Chapter 6, Paper IV provides structural, electrochemical, and spectroscopic insights into how an O_2-tolerant, high-affinity [NiFe] hydrogenase can oxidize atmospheric levels of H_2.[155]

Chapter 2, Experimental Methods

In this chapter, I will outline the main tools used in my work to investigate the catalytic and spectroscopic properties of hydrogenases, both *in vivo* and *in vitro*. Attenuated total reflection − Fourier-transformed infrared spectroscopy (ATR−FTIR) and Electron Paramagnetic Resonance spectroscopy (EPR) are used to examine the electronic configuration of the active site cofactor and/or iron sulfur clusters. I employed biochemical assays and protein film electrochemistry to assess activity rates, bias, and/or thermodynamic efficiencies. The protein purification pipeline and the "artificial maturation" technique, which enabled these investigations, is also discussed briefly in this chapter.

Hydrogenase purification and activation pipeline

Heterologous Expression and Purification (Fig. 2.1A): The hydrogenase genes (and site-directed mutagenesis variants) were equipped with Strep tags for affinity-based purification and were heterologously expressed in *E. coli* chosen for its simplicity, reliability, and well-documented ability to often produce recombinant proteins with properties comparable to their native counterparts (**Appendix I**). While *E. coli* expression systems are commonly effective, differences in post-translational processing or protein folding can sometimes lead to variations between the properties of the expressed proteins and the native form.[156] One approach to overcome this challenge was the use of codon-optimized genes, which can help address issues related to codon bias and translation efficiency.[157]

In some cases, small-scale expression tests were conducted in different *E. coli* cells to determine which yielded the best expression and solubility levels. The cells were aerobically cultured at 37ºC and 150 rpm in minimal media until an optical density (OD_{600}) of approximately 0.4 to 0.6 was reached under these specific conditions. Within this range, the cells are in the mid-exponential growth phase, which is optimal for protein expression. Subsequently, 0.1 mM $FeSO_4$ was added, and the cells were induced with 1 mM IPTG, followed by overnight incubation at lower temperatures (20°C, 150 rpm, 16 hours). Afterward, the cells were harvested by centrifugation (4,424 × *g*, 10 min). To maintain an anaerobic environment during protein extraction, the harvested cell pellets were lysed in an MBRAUN glovebox ($[O_2] < 5$ ppm).

Lysis was performed either by three cycles of freezing/thawing in liquid N_2 or sonication, and the lysate was clarified via ultracentrifugation (222,592 × *g*, 60 mins). The hydrogenase was purified from the clarified lysate using Strep-Trap™ affinity chromatography, followed by size exclusion chromatography (Superdex™) when necessary to enhance purity. The concentrated samples (using 30 kDa centrifugal filters), were stored anaerobically at −80 °C until further use. Coomassie-stained SDS-PAGE was used to assess purity.

Iron-Sulfur Cluster Reconstitution (Fig. 2.1B): To ensure the presence of fully assembled FeS clusters, a crucial component of hydrogenase activity, an established *in vitro* reconstitution protocol was employed.[158] This procedure was conducted under strictly anaerobic conditions to mimic the enzyme's native environment. Briefly, purified hydrogenase was incubated with iron (Mohr's salt: ferrous ammonium sulfate), and sulfur (L-cysteine) sources both added in 1.5-fold molar excess to the desired number of Fe-atoms to be added. Cysteine desulfurase from *E. coli* was added to facilitate cluster assembly by releasing sulfide *in situ* from L-cysteine. UV-Vis spectroscopy was used to monitor the increase of absorbance at 405 nm. The reconstitution process ended by running the reaction mixture through a desalting column (PD-10).

EPR spectroscopy allowed checking for the integrity of the FeS clusters, which are typically bound through cysteine (C) residues in a specific sequence motif. For the canonical [4Fe-4S] clusters, the motif is commonly represented as $CX_nCX_nCX_nC$, where "X" represents any amino acid residue and "n" is the number of amino acid residues between the C residues. A cuboidal structure is generated with four iron atoms connected by four sulfide ions. Protein and iron content were determined using standard protocols[159, 160] to further confirm successful reconstitution.

H-cluster Maturation (Fig. 2.1C): *E. coli* lacks the native machinery for the H-cluster maturation involving three maturase enzymes (HydG, HydE, HydF).[161] Therefore, the purified hydrogenase was in its *apo* form, lacking the complete H-cluster. To obtain the *holo* form, the *apo* hydrogenase was artificially matured by incubation with the synthetic mimic of the $[2Fe]_H$ subsite, $[2Fe]^{ADT}$ ($[Fe_2(\mu\text{-ADT})(CO)_4(CN)_2]^{2-}$).[63, 67] In certain cases, the $[2Fe]_H$ subsite was purposefully locked in a mixed valent state, which was achieved by activating the *apo* hydrogenase with another $[2Fe]_H$ subsite mimic ($[2Fe]^{PDT}$, $[Fe_2(\mu\text{-PDT})(CO)_4(CN)_2]^{2-}$) that replaces the amine bridgehead of the $[2Fe]^{ADT}$ ligand with a methylene ($-CH_2-$) group. This approach can yield the EPR-active H_{ox} state, but the $[2Fe]^{PDT}$ -activated enzymes may also exhibit EPR silence by yielding the H_{red}' state (**Fig. 1.3A**).

After *apo* enzyme incubation with the mimic for at least an hour, the samples were desalted through a PD-10 column equilibrated with the desired buffer (typically 10 mM Tris-HCl, 2 mM sodium dithionite, pH 8.0). The eluted proteins were concentrated, aliquoted into PCR tubes, and transferred into airtight serum vials (3-5 µL each) before they were flash-frozen in liquid N_2 and stored at -80°C until further use.

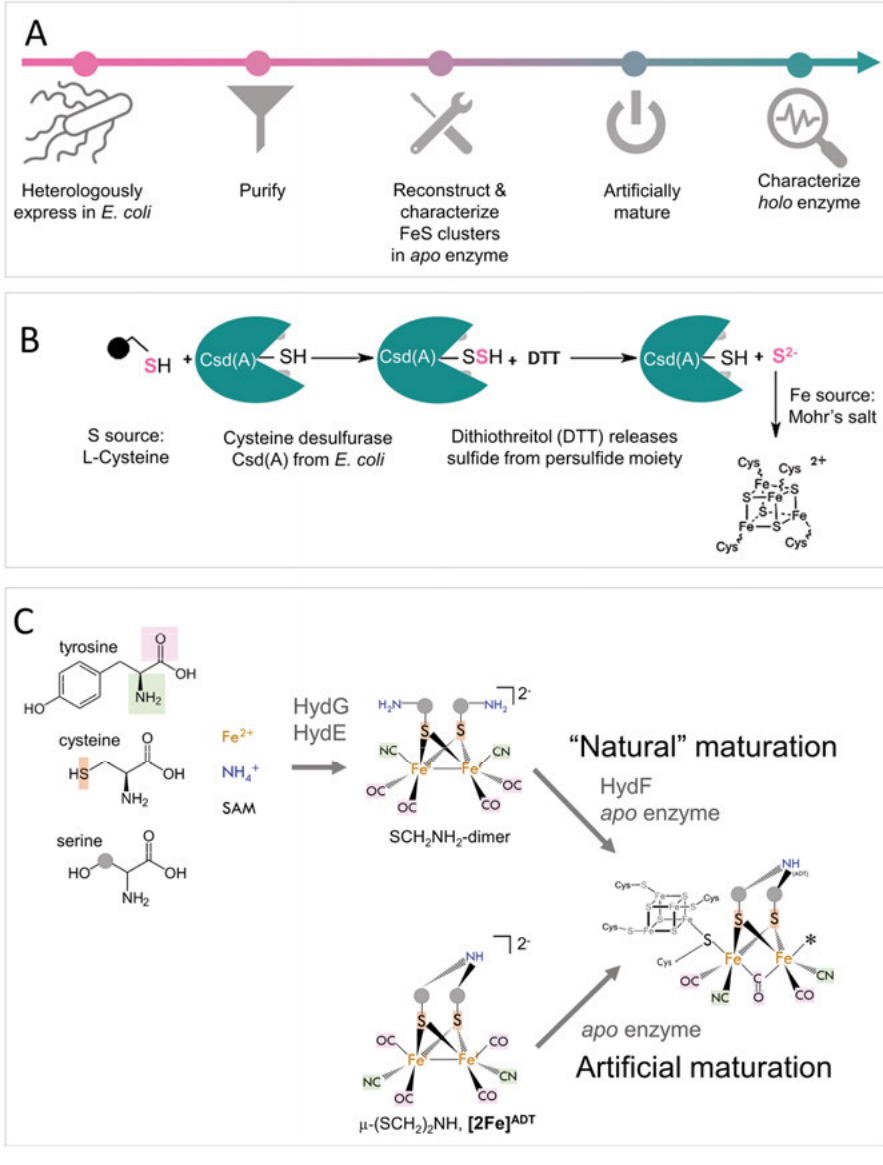

Figure 2.1 (A) Schematic representation of protein expression, isolation, reconstitution of FeS clusters, artificial maturation, and characterization. **(B)** Semi-enzymatic assembly of [4Fe-4S] clusters, inspired by the mitochondrial iron-sulfur cluster assembly (ISC) machinery, is depicted. In this process, L-cysteine and Mohr's salt serve as the sulfur and iron sources, respectively. Cysteine desulfurase, Csd(A), catalyzes the reaction, releasing readily available sulfide. **(C)** Illustrates the natural maturation of [FeFe] hydrogenase, involving maturation enzymes (HydG, HydE, HydF) to form the H-cluster.[161] The $[2Fe]_H$ subsite is color-coded based on the proposed molecular origin of its elements (CN: green, CO: magenta, S: orange, Fe: gold, NH: blue). SAM: S-adenosyl-l-methionine. Alternatively, the artificial maturation technique bypasses the need for the complete maturation machinery by introducing the $[2Fe]_H$ subsite mimic ($[2Fe]^{ADT}$) to the *apo* enzyme, resulting in H-cluster formation.[63, 67]

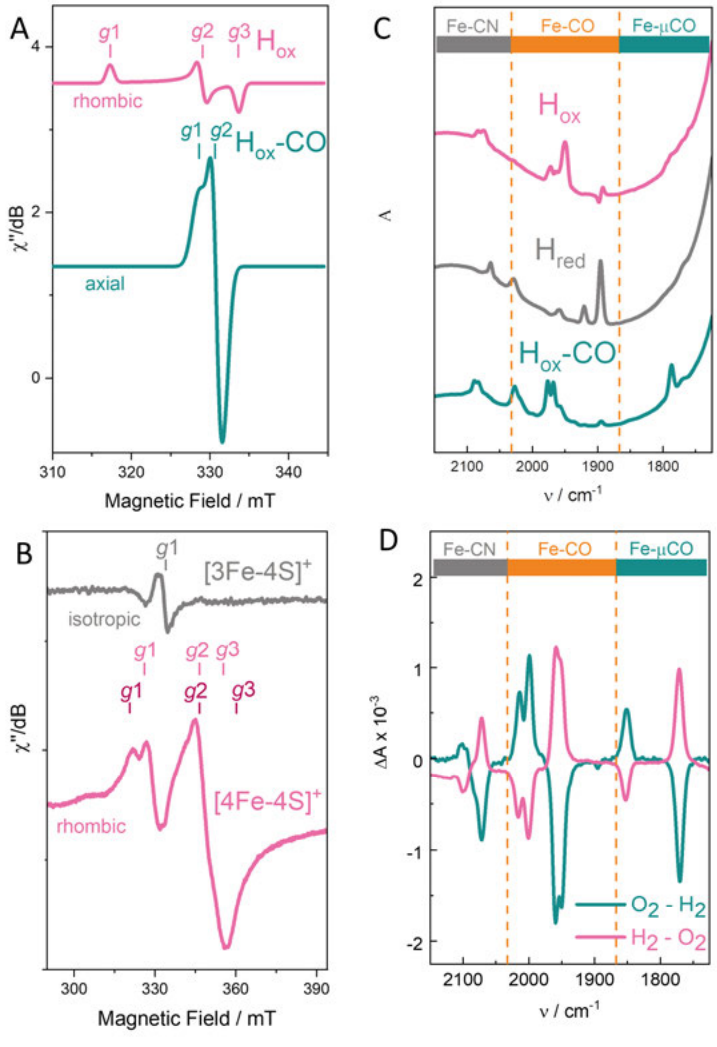

Figure 2.2 Example spectra illustrating information obtained from EPR spectroscopy (A-B) and FTIR spectroscopy (C-D). **(A)** Higher temperature (20 K) spectra probe the H-cluster, with indicated g-factors of the rhombic signal typically observed for the H_{ox} state (magenta) and of the axial signal typically observed for the H_{ox}-CO state (dark cyan). The spectra shown are from simulated data. Reduced H_{red} is EPR silent and undetectable. **(B)** Lower temperature (10 K) spectra probing FeS clusters. The oxidized $[3Fe\text{-}4S]^+$ state is EPR active (grey), while the reduced form of $[4Fe\text{-}4S]^+$ is EPR active (magenta). The spectra shown are from experimental data. **(C)** Absolute FTIR experimental spectra, revealing infrared absorbance bands corresponding to different H-cluster states: H_{ox} (magenta), H_{red} (grey), H_{ox}-CO (dark cyan). Top bars indicate regions that are expected to show terminal CN (grey) or terminal CO (orange), and bridging CO (μCO, dark cyan) vibrations. **(D)** Difference FTIR experimental spectra, highlighting negative bands that disappear and positive bands that form during reactions with specific atmospheric conditions.

Attenuated total reflection Fourier-transformed infrared (ATR FTIR) and Electron Paramagnetic Resonance (EPR) spectroscopy were employed to characterize the H-cluster of the artificially matured hydrogenase (**Fig. 2.2**). This combined approach provided a detailed analysis of the H-cluster's redox behavior and electronic properties, essential for understanding the catalytic mechanism and the integrity of the cofactors. These spectroscopic techniques can be applied to investigate the redox centers both in the native cellular environment (*in vivo*) and in the isolated enzyme (*in vitro*).[30]

ATR-FTIR spectroscopy

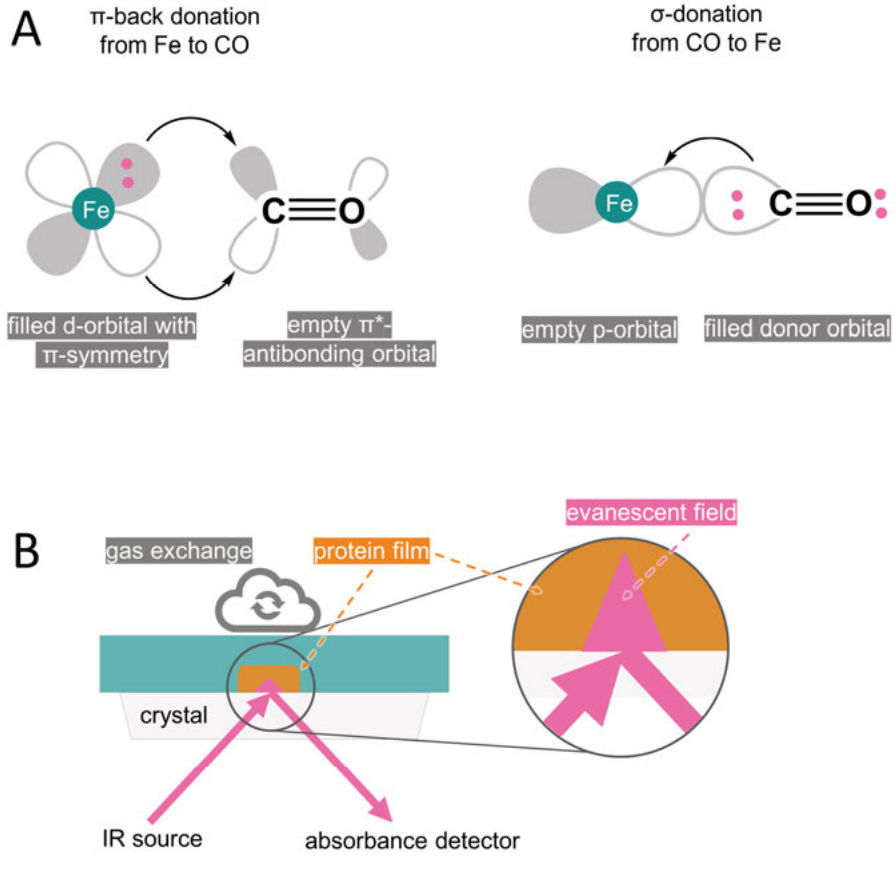

Figure 2.3 (A) Schematic diagrams illustrating the bonding and antibonding interactions for a ligand (CO) bound to (Fe) **(B)** The ATR FTIR setup involves a protein film (orange) placed atop a refracting crystal (light grey). The incident IR beam interacts with the sample as an evanescent wave or field (magenta). The intensity of this field rapidly decays, allowing selective probing of the first few microns of the sample. A custom-made titration cell facilitates gas exchange for a controlled atmosphere (dark grey).

Molecules selectively absorb infrared light at specific frequencies corresponding to the vibrations of their chemical bonds. For a vibration to be infrared active, it must lead to a change in the molecule's dipole moment. When CO/CN^- undergoes a stretching vibration, the distance between the partially negative O/N and partially positive C changes, altering the dipole moment of the CO/CN^- bond.

In the context of this study, FTIR exploited the unique vibrational frequencies of the strong-field, π-accepting ligands, CO and CN^-, present within the H-cluster (**Fig. 2.3A**).[162] These vibrations occur in a characteristic region of the infrared spectrum (1700–2100 cm^{-1}) that is largely free from interference by protein vibrations (amide I: 1600–1800 cm^{-1}; amide II :1470–1570 cm^{-1}).

In the attenuated total reflection (ATR) configuration, the IR beam does not directly contact the sample (**Fig. 2.3B**). Instead, it generates an evanescent wave (as light waves tend to diminutively spread in space) at the surface of an IR-transparent, high-refractive index crystal. The IR beam is directed into the crystal from below, while the sample is deposited on top. The higher refractive index of the crystal compared to the sample allows the IR wave to undergo total internal reflection, creating an evanescent wave that penetrates the sample. After interacting with the sample, the IR wave travels back through the crystal, and the absorbance is detected.

The ATR setup enables the use of relatively low-concentration protein solutions. During sample preparation, the protein concentration and hydration level are monitored in real-time. Initially, the ATR crystal is recorded as a background before a small volume of protein solution is added to the surface. The diluted protein solution initially resembles the IR absorbance spectrum of liquid water, but exposure to a dry carrier gas causes characteristic protein bands to appear over time. The protein solution becomes more concentrated until a relatively dry "protein cake" is formed. The formation of salt or buffer crystals can reduce the absorbance of the protein cake, so low-salt buffers are used in preparing the activated enzyme sample.

Here are the key insights from FTIR analysis in the context of studying the H-cluster[25, 162]:

Dependence of vibrational shifts on the electron density and protonation changes: The vibrational frequencies of CO/CN^- stretching modes are highly sensitive to changes in the electron density of the $[2Fe]_H$ subsite, providing insights into changes in the redox state and protonation state of the H-cluster. When the $[2Fe]_H$ subsite experiences high electron density, it can donate electrons to the vacant antibonding π*-orbital of the CO/CN^- ligands (**Fig. 2.3A**). This electron transfer weakens the CO/CN bond, resulting in a red-shift (lower vibrational frequency), which is generally interpreted as an indicator of a reduction at the H-cluster. Conversely, protonation in the vicinity of the H-cluster decreases the electron density of the $[2Fe]_H$ subsite, which in turn reduces the capability of Fe ions to donate electrons to the CO or CN^- ligands. This results in a blue-shift (higher vibrational frequency) in the

ligands' stretching modes. An illustrative example is the $H_{ox} \rightarrow H_{ox}H$ conversion, which exhibits this characteristic blue-shift.

Dependence of vibrational frequency on the coordination geometry of the $[2Fe]_H$ subsite and bonding mode of CO/CN^-: The vibrational behaviour also depends on the coordination geometry of the metal center and the bonding mode of the π-accepting ligands (CO/CN^-). In hydrogenases, CO ligands can assume terminal, bridging, or semi-bridging configurations (**Fig. 2.2C-D**). The bridging CO ligand has a lower vibrational frequency compared to the terminal CO ligands, primarily attributed to stronger bonding interaction or greater electron density overlap of the bridging CO with the iron ions. Conversely, CN ligands tend to be blue-shifted compared to CO ligand bands due to the higher force constant (greater stiffness) of the carbon-nitrogen triple bond (C≡N) relative to the carbon-oxygen double bond (C=O).

Difference spectra over time can reveal specific changes induced by environmental conditions: The thin film thickness allows the IR wave to minimally interact with the gas phase above the sample, a key requirement for gas-induced difference spectra. The setup also allows for controlled exchange of the gas phase, enabling difference spectra to extract cofactor signals when specific changes are induced. Calculating the "before-after" difference spectrum can make subtle changes visible in frequency regimes obscured by the protein and water absorbance bands.

EPR spectroscopy

Unpaired electrons possess a magnetic moment and will align themselves in the presence of an external magnetic field (B_0). EPR spectroscopy exploits the Zeeman effect (**Eq. 1**, **Fig. 2.4A**), where B_0 lifts the degeneracy of electron spin states levels (m_s, magnetic moments). The greater the strength of B_0, the larger the energy difference (ΔE).

$$\Delta E = g\mu_B B_0 = h\nu \qquad \text{Equation 1}$$

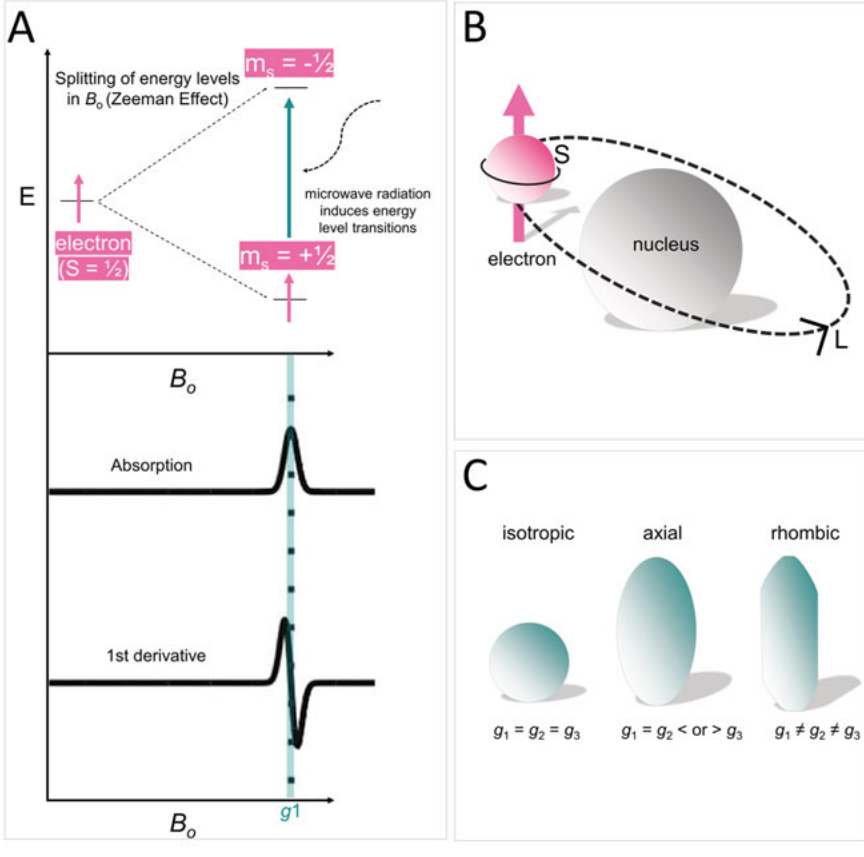

Figure 2.4 (A) Schematic diagram illustrating the change in energy between electron magnetic moments as an external magnetic field (B_0) is applied. As B_0 increases, the energy levels diverge due to the Zeeman effect. The energy difference between the electron spin states (m_s) corresponds to the microwave energy absorbed by the sample giving rise to an EPR signal. For enhanced sensitivity and resolution, the signal is typically presented as the first derivative of the absorption spectrum. The spectrum shown here represents an isotropic signal. **(B)** Simplified illustration of a spin-orbit interaction between the electron (magenta) and nearby nucleus (grey). S: electron's intrinsic spin angular momentum; L: orbital angular momentum **(C)** Depiction of the spatial distribution of g-tensor strength (examples of first derivative absorption EPR spectra for each type are given in **Fig. 2.2A-B**).

When the energy difference between these two electron magnetic moments or states (ΔE) matches the energy of incident microwave radiation ($h\nu$), absorption occurs, generating an EPR spectrum. The Planck's Constant (h) is a fundamental constant in quantum mechanics (6.626×10^{-34} J·s), relating the energy of a quantum (photon) to its frequency (ν), while the Bohr magneton (μ_B) quantifies the magnetic moment linked to an electron's orbital motion (9.274×10^{-24} J·T^{-1}).

EPR spectra are typically presented as the first derivative of the absorption spectrum for enhanced sensitivity and resolution (**Fig. 2.4A**, **Fig. 2.2A-B**). Several factors influence the observed EPR spectra, providing structural and electronic information of the enzyme's metallocofactors:

Spin-orbit coupling significantly influences g-value: The g-value (akin to chemical shift of NMR) is a dimensionless conversion factor that reflects the effective magnetic moment of the unpaired electron. The electron in its "free" state, which is not associated with an orbital, has a g_e value ≈ 2.0023. Deviation from the g_e results from coupling between an electron's intrinsic spin angular momentum (S) and orbital angular momentum (L; orbit around the nucleus) (**Fig. 2.4B**). When an electron moves in the electric field created by the nucleus, its orbital motion affects its spin. The energy levels are influenced by this total angular momentum (S + L). The deviation from g_e induced by this spin-orbit coupling reveal details about the electronic states and coordination environment within the metal center.

Anisotropy of the g-value depends on the directional nature of the molecular orbitals: The anisotropy ("not having the same properties in all direction") of the g-factor refers to its dependence on orientation or alignment relative to B_0. In anisotropic systems, the g-factor can be described by three values along the Cartesian coordinate axes (g_x, g_y and g_z or g_1, g_2, and g_3). These values characterize how the g-factor changes when the magnetic field is applied in different directions. In flash-frozen enzyme samples with random molecular orientations, the observed spectrum represents a sum of all possible orientations (**Fig. 2.4C**). (An)isotropic systems can exhibit:

- $g_1 = g_2 = g_3$, isotropic (spherical symmetry)
- $g_1 = g_2 <$ or $> g_3$, axial (elongated or axially symmetric)
- $g_1 \neq g_2 \neq g_3$, rhombic (no symmetry)

Hyperfine coupling provides insights about interacting paramagnetic centers: Hyperfine coupling arises from the interaction between the spin of an unpaired electron and the spin of a nearby atomic nucleus, provided the nucleus possesses a non-zero nuclear spin. This interaction provides information about the identity and number of nuclei interacting with the paramagnetic center. The specific number of hyperfine lines observed in a spectrum arises from differences in nuclear spin values. In straightforward situations,

the EPR spectrum exhibits isotropic hyperfine splitting, displaying multiple lines that correspond to different nuclear spin states.

EPR also probes FeS clusters within hydrogenases. The information obtained from EPR can complement the FTIR data, offering a more comprehensive understanding of the electronic structure of the H-cluster and how it changes during reduction or oxidation. A key advantage of EPR is its ability to detect different types of FeS clusters (*e.g.*, [3Fe-4S] or [4Fe-4S]) due to their distinct EPR signatures (**Fig. 2.2B**), which depend on the oxidation state and geometric configuration of the clusters. This gives insights into the redox behavior of these FeS clusters, contributing to an understanding of the electron transfer processes within the enzymes. As observed in hydrogenases, the cubane-like [4Fe-4S] clusters in its reduced state ($[4Fe\text{-}4S]^{+}$) typically exhibit a rhombic EPR shape due to an anisotropic environment created by the electronic interactions between the Fe and S atoms. In contrast, the more symmetric electronic environment in [3Fe-4S] clusters often show an isotropic EPR shape in its oxidized state ($[3Fe\text{-}4S]^{+}$). This symmetry leads to an isotropic EPR signal, where the g-values are nearly identical.

Catalytic properties

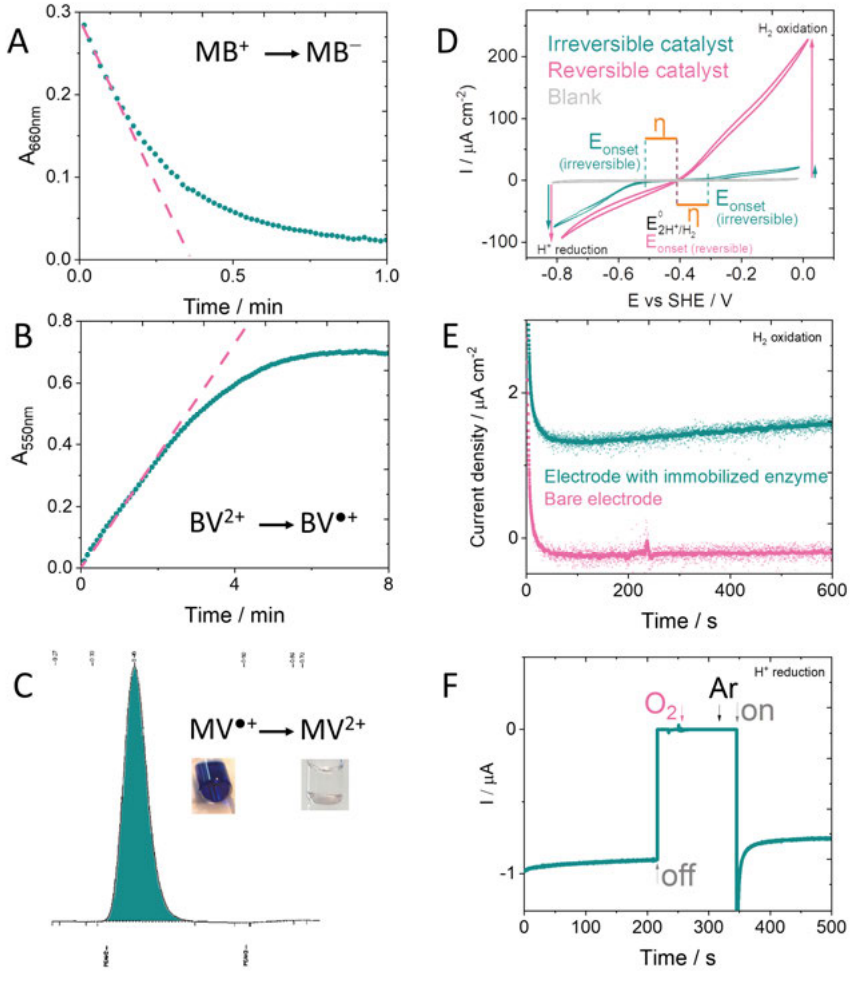

Figure 2.5: Example graphs illustrating information obtained from classical biochemical assays (A-C) and from protein film electrochemistry (PFE) experiments (D-F). **(A)** A decrease in absorbance of the redox mediator methylene blue is observed when H_2 is oxidized by the enzyme. **(B)** Conversely, an increase in absorbance for the redox mediator benzyl viologen is observed during H_2 oxidation. **(C)** Typical gas chromatogram showing the peak area of H_2 from the headspace of a mixture containing the enzyme incubated with redox mediator methyl viologen and sodium dithionite as a sacrificial electron donor. **(D)** Cyclic voltammetry (CV) traces showing currents that are proportional to the rate for H_2 oxidation at higher redox potentials and proton reduction (H_2 evolution) at lower redox potentials. Reversible catalysts (magenta) require minimal overpotential (η). Irreversible catalysts (dark cyan) demand a significant η. The bias indicates the preferred direction of the catalyst, particularly evident when comparing currents at higher driving forces. **(E)** Chronoamperometric traces at a specific applied potential, monitoring currents over time. **(F)** Inhibition experiments using chronoamperometry to track current changes before and after injecting an inhibitor (*e.g.*, O_2) into the buffer.

Classical biochemical assays

H_2 oxidation activity was determined spectrophotometrically using standard biochemical assays with redox mediators (**Fig. 2.5A-B**). The rate of change in absorbance of the redox mediator, either methylene blue ($E^{0'}$ = −90 mV vs Ag/AgCl at pH 5.45[163]) or benzyl viologen ($E^{0'}$ = −359 mV vs SHE at pH 7.0[164]), was monitored over time after mixing with the enzyme and H_2-saturated buffer (≈ 1 mM H_2 in solution).

A steeper slope indicates higher enzymatic activity. The use of two redox mediators with different reduction potentials allowed for the assessment of enzyme performance under different driving force conditions.

Specific activity (U/mg) was measured by the initial rate of absorbance change at 550 nm (BV) or 660 nm (MB) where one unit (U) of activity catalyzes 2 μmol of BV reduced per min or 1 μmol of MB reduced per min[165] (1 μmol of H_2 oxidized per min).

H_2 evolution activity was measured by incubating the enzyme with methyl viologen (MV, $E^{0'}$ = −449 mV vs SHE at pH 7.0[164]) as the redox mediator and sodium dithionite as the sacrificial electron donor (**Fig. 2.5C**).[166, 167]

The amount of H_2 gas produced was then quantified (typically after 15 minutes of incubation at pH 6.8). To determine the amount of H_2 associated with the peak area at around 0.4 min in the chromatogram, a calibration curve made up of standard points from 0 to 60% H_2 at 1 atm in the headspace was generated.

This assay provided a direct measurement of the enzyme's ability to catalyze H_2 production under specific conditions of incubation time, pH, and temperature, where specific activity (U/mg) catalyzes 1 μmol of H_2 evolved per min per amount of enzyme.

The insights gained from biochemical assays were further complemented by the information obtained from protein film electrochemistry (PFE; discussed in the next section), providing a better understanding of the hydrogenase's catalytic properties and behavior. Their strengths and limitations are compared in the subsequent section.

Protein film electrochemistry

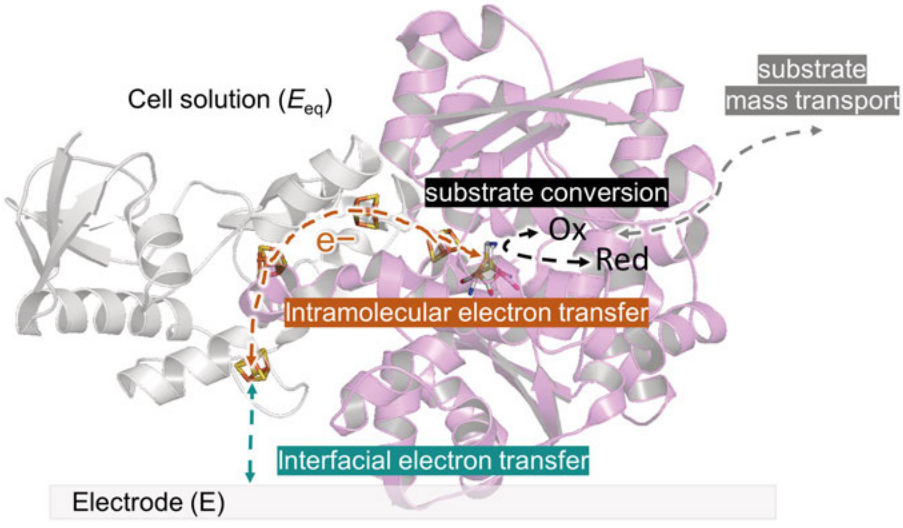

Figure 2.6 This schematic depicts the adsorbed [FeFe] hydrogenase, functioning as a molecular electrocatalyst. Key features include: Interfacial Electron Transfer (dark cyan arrow) between the electrode and the FeS cluster (depicted as sticks with Fe: orange and S: yellow) near the enzyme's surface (distal FeS). Intramolecular Electron Transfer (orange arrow) between the FeS clusters and the H-cluster (depicted as sticks with Fe: orange, S: yellow, N: blue, C: grey, and O: red). Substrate Conversion (black arrow): The enzyme's catalytic turnover rate, converting substrates to products. Substrate mass transport, primarily by convection (grey arrow): The rate at which substrate diffuses into the active site. Equilibrium Potential (E_{eq}): Reflects the activities or concentrations of oxidized (Ox) and reduced (Red) redox-active species.

A three-electrode system was used for protein film electrochemistry (PFE) experiments with: (1) Ag/AgCl (4 M KCl) as a reference electrode, (2) rotating disk 5 mm OD pyrolytic graphite edge (PGE) plane (epoxy encapsulated) as a working electrode, and (3) graphite rod as a counter electrode. The enzyme was immobilized on the working electrode surface. Prior to immobilization, the working electrode were polished either with an aqueous slurry of 0.3 μm Al_2O_3 on an alumina pad or with P1200 sandpaper and rinsed with purified water before they were brought into the glovebox. To remove residual O_2 in the PGE electrode, cyclic voltammograms (CV) were run at 100 mV/s from -100 to -600 mV (vs. SHE) for 40 scans, reducing O_2 to H_2O.

The CV of the blank electrode (no enzyme immobilized) was recorded with the working electrode rotated at 3,000 rotations per minute (rpm). Polycationic polymyxin B sulfate (10 μL of 0.2 mg/mL) was added onto the deaerated PGE surface before adding 10 uL of 5 μM *holo* enzyme. The mixture was left for 10 min for maximal adsorption before the excess solution was removed by pipet.

This setup enabled the direct measurement of the current generated by the enzyme at various applied potentials (CV; **Fig. 2.5D**) or at fixed applied potential (chronoamperometry, **Fig. 2.5E-F**) with the desired scan rate and chosen conditions (pH$_2$, temperature, and pH).

The Nernst equation (**Eq. 2**) relates the (solution) potential (E, potential in the given non-standard condition) to the standard reduction potential (E^0) of the analyte and the equilibrium concentrations of its oxidized ([Ox]) and reduced ([Red]) forms.[168] The ν and μ are the stoichiometric coefficients of [Red] and [Ox], respectively. The Faraday's constant reflects the charge on one mole of electrons (F = 96,485 C mol^{-1}), n is the number of moles of electrons transferred, while R is the universal gas constant (R = 8.314 J K^{-1} mol^{-1}), and the temperature is measured in kelvin (T).

$$E = E^0 - \frac{RT}{nF}\ln\left(\frac{[Red]^{\nu}}{[Ox]^{\mu}}\right) \qquad \text{Equation 2}$$

The E^0 value of the half-reaction involving H$_2$ gas and protons (2H$^+$/H$_2$) at standard conditions (1 atm H$_2$, 1 M [H$^+$], and 298.15 K) is determined with respect to the SHE, which is arbitrarily assigned a potential of 0 V.

The "open circuit potential" (OCP) is the potential where no net current flows. The Nernst equation also demonstrates how changes in substrate, particularly the concentration of protons ([H$^+$] = 10^{-pH}) or the partial pressure of hydrogen (pH$_2$), can shift the OCP. The reduction potential of 2H$^+$/H$_2$ couple under non-standard conditions ($E^0_{2H^+/H_2}$) can be calculated given the desired T, pH$_2$ in atm, and pH of the solution. (**Eq. 3**):

$$E^0_{2H^+/H_2} = -\frac{RT}{2F}\ln\left(\frac{\left[10^{-pH}\right]^2}{[pH_2]}\right) \qquad \text{Equation 3}$$

However, the real power of PFE lies in its ability to drive the enzyme away from the OCP by applying a potential (additional driving force) and measuring the resulting catalytic current. Catalytic currents in PFE are determined by the interplay of the following processes (**Fig. 2.6**):

Enzyme kinetics: The rate constants for each step in the enzyme's catalytic cycle.

Mass transport in solution: The rate at which substrate and product are transported to and from the solution.

Interfacial electron transfer rates: The efficiency of electron transfer between the enzyme's electron donor (or acceptor) and the electrode.

Intramolecular electron transfer rates: The efficiency of electron transfer between the metal cofactors within the enzyme.

In essence, the Nernst equation sets the stage by describing the thermodynamic landscape, while PFE and analysis of the catalytic currents allow us to probe the kinetic and mechanistic details of how the enzyme navigates that

landscape.[120, 140, 169] To summarize, the following key catalytic parameters were determined through PFE (**Fig. 2.5D-F**):

Catalytic rate: The observed current serves as a measure of the catalytic rate within the controlled environment of the PFE setup.

Catalytic bias: The ratio of the catalytic currents for H_2 oxidation and production can reveal whether the enzyme is biased towards one reaction over the other, providing clues about its physiological role.

Efficiency: The enzyme's effectiveness near equilibrium or in the absence of a driving force. While a larger overpotential, defined as the difference between the applied and the thermodynamic potential of the reaction ($|E_{app} - E^0_{2H^+/H_2}| = \eta$), is often associated with energy losses, it does not necessarily translate to lower catalytic efficiency. Catalyst efficiency is best described by the relationship of turnover frequency and overpotential (TOF-η).[170] Irreversible enzymatic systems with high overpotentials show little response to changes in potential near the equilibrium, whereas more reversible systems exhibit a stronger sensitivity to potential changes.

Substrate affinity: The enzyme's binding and interaction with its substrate (protons or H_2) can be probed. The gas-tight glass cell permits control of atmospheric composition, enabling the manipulation of H_2 partial pressure (pH_2). The solution buffer's pH can be varied between measurements while using the same enzyme film.

Temperature dependence: The glass cell also featured a water jacket for temperature control. Temperature-dependent studies could provide insights into enthalpic and entropic parameters.

Operational stability or tolerance towards inhibitors: The enzyme's resilience and ability to maintain activity (current) can be monitored in the presence of inhibitors (*e.g.*, O_2 or CO).

Potential-dependent (in)activation: The activation or inactivation properties of the enzyme can be observed under varying applied potentials. By analyzing changes in the catalytic current or the appearance of new redox features, insights into the enzyme's (in)activation pathways can be gained.

Classical biochemical assays vs protein film electrochemistry

The benefits and limits of both methods are outlined here:

Advantages and limitations of classical *in vitro* assays: These methods have been instrumental in traditional enzymatic studies as well as in initial screening methods to identify novel enzymes (**Chapter 3**) and in comparing wild-type enzyme to its variants (**Chapter 4-5**). However, they present limitations:

- Unless performed over a range of different experiments with varied conditions, one crucial shortfall is the inability of conventional assays (and PFE) to fully delineate the precise nature of rate-limiting steps that govern the overall catalytic rates. This lack of resolution may mask key aspects of enzyme turnover.
- The determination of specific activities utilizing MV in H_2 evolution assays may not accurately reflect the enzyme's maximum turnover rates. The inadequacy mainly stems from the suboptimal driving force provided by the reduced form of MV. Quantifying H_2 in the headspace typically involves incubation periods (*e.g.*, 15 minutes), deviating from initial rate measurements commonly employed for determining maximum turnover frequency.
- Factors such as potential inhibition by sacrificial electron donors (*e.g.,* sodium dithionite) or the enzyme's affinity for redox mediators may also introduce uncontrolled variables that can influence the measured rates.

Advantages and limitations of PFE: PFE offers a more direct examination of enzyme kinetics by enabling precise control over the electrode potential, allowing for targeted investigations of enzymatic reactions and inhibition. However, this method is not without drawbacks.

- The interpretation of currents is often muddled by various rate-limiting factors, obscuring a clear comprehension of intrinsic catalytic rates. Constraints by electron transfer kinetics, along with the inherent complexities of PFE in interpreting absolute currents (dependent on the amount of immobilized active enzyme or mass transport limitations), making conclusions based only on absolute current densities potentially misleading.
- Additionally, while the inclusion of a redox partner like MV in the reaction mixture has been shown to enhance reaction rates through mediated electron transfer (MET) (**Chapter 5**)—suggestive of overcoming some electron transfer limitations— these limitations may not be entirely eliminated. An increase in current due to MET highlight that direct electron transfer (DET) currents (without mediator) can be limited by processes other than catalytic turnover, even at high driving forces.

- The nature of the electrode-enzyme interaction itself can considerably affect observed catalytic properties. The enzyme's orientation on the electrode surface, the distance between the enzyme's electron accepting cofactor and the electrode, and potential denaturation or conformational changes upon immobilization can influence electron transfer kinetics and overall catalytic efficiency. These factors can be relevant to any *in vitro* experiments as well.

In conclusion, while both classical *in vitro* assays and PFE offer valuable insights into enzyme kinetics, neither method is perfect nor provides a complete picture in isolation. The selection between these methodologies depends on the specific needs of the study, including the enzyme under scrutiny, the depth of kinetic data desired, and the resources at hand. However, to gain a more comprehensive understanding of enzyme catalysis, a combined approach leveraging the strengths of both methods is often necessary to overcome their respective limitations. This is particularly important when discrepancies arise between the two methods, as reconciling these differences can often reveal deeper mechanistic insights.

Chapter 3, Paper I and Appendix III:
Discovery of active [FeFe] hydrogenases from anaerobic archaea

This chapter describes our efforts to validate the presence of active [FeFe] hydrogenases from archaea. I received several putative [FeFe] hydrogenase encoding genes from Prof. Chris Greening and assessed the H_2 production (biochemical validation) and H-cluster binding capacity (spectroscopic validation) of the *E. coli*-expressed enzymes, which were activated through artificial maturation. The subsequent sections in this chapter delve into the spectroscopic and electrochemical characterization of select isolates. The chapter culminates with notes on how these findings necessitate updates to existing hydrogenase literature.

Introduction

Long-held assumptions about [FeFe] and [NiFe] hydrogenases prior to this study include the following:

- While [NiFe] hydrogenases are found in bacteria and archaea across all types of ecosystems, [FeFe] hydrogenases are assumed to be restricted to anaerobic bacteria and eukarya.
- The smallest size for a functioning [FeFe] hydrogenase is believed to be 45 kDa, encoded by green algae *C. reinhardtii* (*Cr*HydA1).
- Despite sharing certain structural and functional similarities, [FeFe] and [NiFe] hydrogenases do not structurally associate and are known to be phylogenetically unrelated.

While these assumptions have informed our understanding of known organisms, they also underline the limitations of extrapolating this knowledge to the vast majority of microbial life that remains uncharacterized (representing ≈99% of the estimated 1 trillion species of microbes on Earth).

Phyla composed solely of uncultured representatives are termed Candidate Phyla (CP), or what microbiologists define as 'microbial dark matter'.[171] Despite likely constituting a significant portion of the Earth's biomass and biodiversity, they remain enigmatic due to our lack of knowledge about their basic metabolic and ecological properties. It might be that our perception of

the microbial world remains profoundly skewed by what has been known or cultivated in the laboratory. Thus, the notion of 'microbial dark matter' challenges us to reconsider such long-held beliefs about [FeFe] hydrogenases.

Genome-resolved metagenomics offers a lens into this enigmatic world. This method involves environmental sampling, DNA sequencing, DNA fragment assembly, and functional prediction of each assembled DNA via sequence alignment with existing DNA databases. Metagenomics has profoundly expanded our knowledge of microbial diversity, especially within the archaea domain. Recognized as a third domain of life four decades ago, archaea has expanded to include new key lineages such as DPANN and Asgard superphyla.[172] DPANN, introduced in 2013, encompasses nanoarchaea or ultra-small archaea, notable for nanometric size.[173] The known smallest organism comes from DPANN with its size nearly touching the theoretical lower limit for life, a mere 9 nm^3. On the other hand, Asgard or *Asgardarchaeota*, proposed in 2015, comprise a group of archaea that harbour eukaryotic signature proteins (ESPs), previously known to distinguish eukaryotes from archaea and bacteria.[20, 174] This suggests that Eukarya is a sister group to archaea, or that eukaryotes descended from archaea, positioning Asgard as the closest prokaryotic kin of eukaryotes.

Genomic analysis of Asgard superphylum suggest the presence of [FeFe] hydrogenases in lineages such as that of *Candidatus Prometheoarchaeum syntrophicum* and *Candidatus Lokiarchaeum ossiferum*.[20, 175] Despite breakthroughs in genomic identification, these archaea represent a tremendous challenge for researchers due to their exceedingly slow growth rates and high specificity of culture requirements, which hinders their culturability. For instance, the successful enrichment of *Ca. P. syntrophicum* took nearly a decade of perseverant culturing efforts, and its growth yields are generally so low that the cell density is on par with the clarity of tap water. The arduous task of culturing and the lack of genetic tools for these archaea make *in vivo* studies of their potential [FeFe] hydrogenases nearly impossible. As such, verifying the nature and functionality of [FeFe] hydrogenases mined from genomic sequences cannot rely on traditional culturing methods. Instead, we must turn to culture-independent approaches to confirm whether these sequences are *bona fide* [FeFe] hydrogenases and to gather enough biological material for subsequent in-depth study.

Beyond the Asgard superphylum, genomic research preliminarily indicates that uncultivated DPANN archaea might also encode [FeFe] hydrogenases.[176, 177] However, this hypothesis remains contentious due to the apparent absence of the three maturation enzymes (*Hyd*EFG), which are essential for synthesizing the unique catalytic H-cluster, a hallmark of [FeFe] hydrogenase functionality. Moreover, there is no empirical evidence supporting the activity of these enzymes from archaea.

In this study, circumventing the need of native culture-dependent approaches, data from representative genomes and metagenome-assembled

genomes (MAGs) were evaluated to identify genes potentially encoding [FeFe] hydrogenases of archaeal origin. To validate, heterologous enzyme production coupled with artificial maturation was utilized to assess their catalytic activity through biochemical assays and their H-cluster binding capacity through spectroscopy. This was supplemented with AlphaFold2-based structural modelling to ascertain if conserved gene clusters encode novel hydrogenase complexes, and was further validated with transcriptomic, proteomic, and metabolic analyses of the archaeal genomes.

This chapter will hone in on the biochemical, spectroscopic, and electrochemical characterization of the (ultra-)minimal Group A and E hydrogenases from DPANN, the Group B hydrogenase encoded by Asgard archaeon *Ca. P. syntrophicum*, and the so-called [FeFe]-[NiFe] hybrids from *Thermoplasmata* (**Fig. 3.1**).

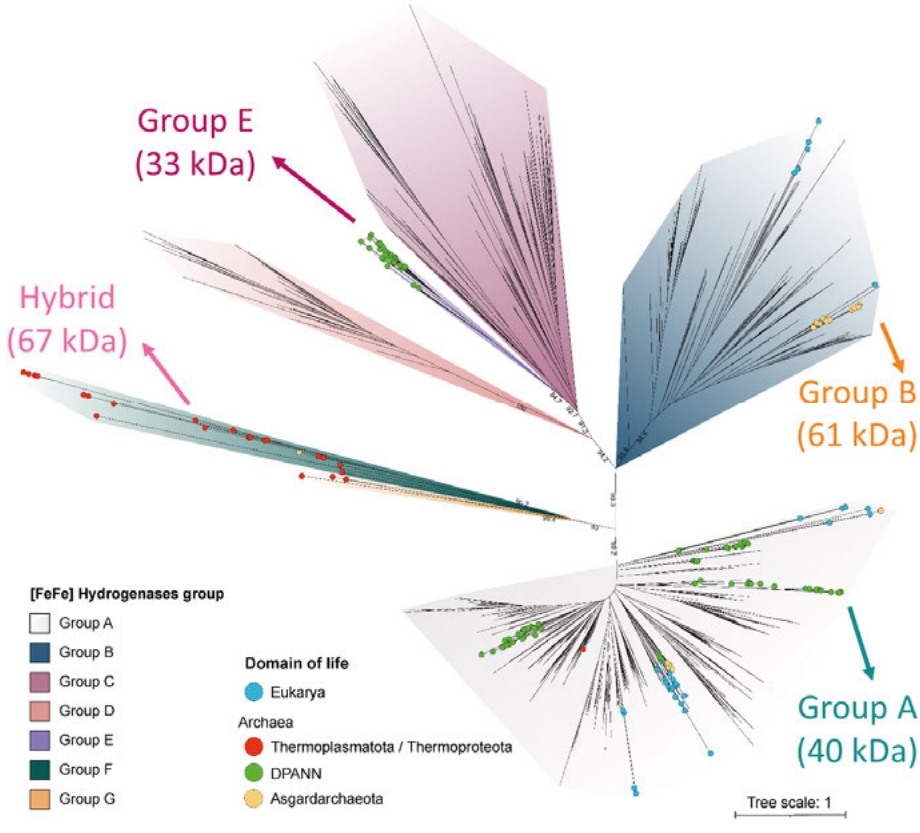

Figure 3.1 Phylogenetic tree of the catalytic subunit (*Hyd*A) of [FeFe] hydrogenases and the hybrid hydrogenases based on 3,677 amino acid sequences across all domains of life. Branch tips indicate sequences from eukaryotes (blue circles), major archaeal groups (red circles: Thermoplasmatota / Thermoproteota; green circles: DPANN; yellow circles: Asgardarchaeota), and bacteria (not highlighted). The different Groups A, B, E, and F (Hybrid) are marked in arrows to facilitate visualization and the representative enzyme kDa sizes for each group are indicated in parenthesis. *Adapted figure with permission from* **Paper I**.[154]

Activated lysates demonstrate H_2 production activities

To better understand the prevalence and diversity of [FeFe] hydrogenases in archaea, a comprehensive search was conducted for *Hyd*A—the catalytic subunit of [FeFe] hydrogenases—within the 2,339 archaeal species in the Genome Taxonomy Database, as well as within our collaborator's collection of novel archaeal MAGs. The analysis revealed that 130 archaeal genomes, including 90 previously identified and 40 novel genomes, encode [FeFe]

hydrogenases. These genes span across nine different phyla and 17 classes, highlighting the widespread distribution of [FeFe] hydrogenases across the archaeal domain. To further refine the inquiry, these genes were classified based on the domain structures, presence of maturases for H-cluster assembly, gene organization, and phylogenetic relationships, enabling their distribution into five distinct groups—designated as the canonical Groups A (subgroups A1, A3), B, and the newly identified Groups E, F, and G (**Fig. 3.1**).

Building on the foundational principles of protein biochemistry as articulated in the central dogma—wherein DNA and RNA sequences ultimately determine the amino acid sequence, and consequently, the structure and function of proteins—recombinant heterologous expression in *E. coli* was used. Taking the well-studied *Cr*HydA1, for instance, the enzyme's specific H_2 production activities (700-800 U/mg) align closely whether produced within its native host or expressed recombinantly, a finding supported by nearly three decades of consistent data on *Cr*HydA1 (**Fig 1.3**; **Appendix I**). Drawing on this precedent, presumed archaeal [FeFe] hydrogenase genes, after codon optimization for *E. coli*, were expressed to determine whether the encoded proteins exhibit the expected hydrogenase activity.

Representatives from Groups A1, B, E, and F [FeFe] hydrogenases were tested to verify their capacity to produce H_2. The enzymes were recombinantly expressed in *E. coli* BL21(DE3) and cultivated in M9 minimal media enriched with an iron source. IPTG was added to induce protein expression. Without concurrent expression of the maturation machinery genes, the expressed enzymes solely carried the $[4Fe\text{-}4S]_H$ cluster ("*apo"* enzymes). The *apo* enzymes lacking the $[2Fe]_H$ subsite were then liberated into the mixture via cell lysis, and anaerobically matured to "*holo*" enzymes using $[2Fe]^{ADT}$ (**Fig. 2.1C**). Hydrogen production of the lysates was measured using gas chromatography, with methyl viologen as a redox mediator and sodium dithionite as a sacrificial electron donor.

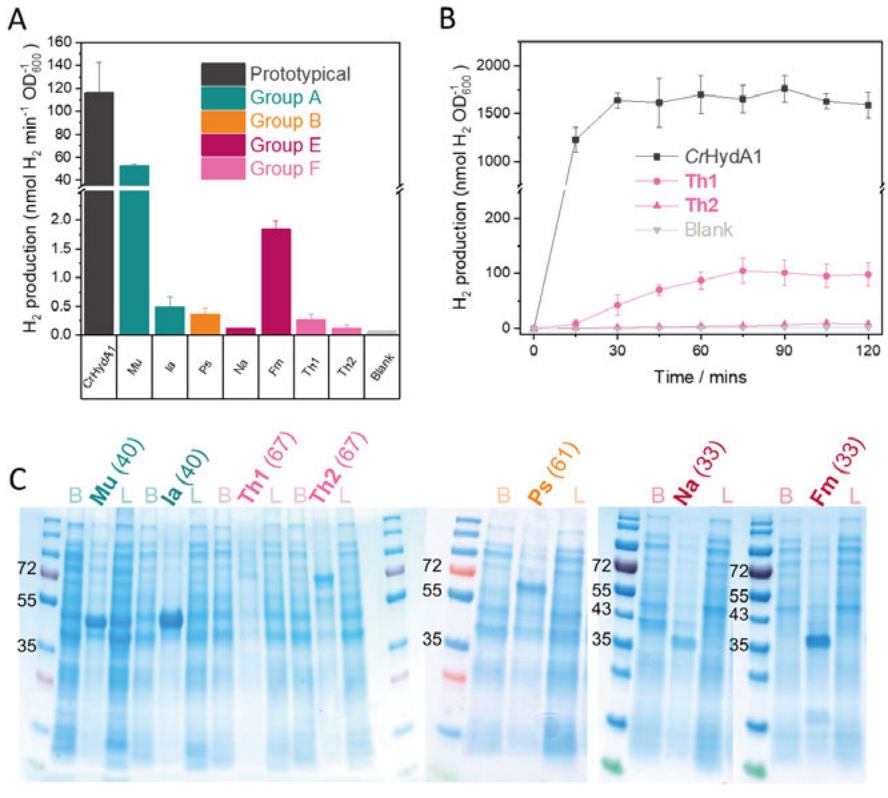

Figure 3.2 (A) H_2 production monitored from cell lysates in *E. coli* BL21(DE3) cells expressing group A1, B, E, and F [FeFe] hydrogenases from archaea. All cell lysates including the blank were activated by addition of $[2Fe]^{ADT}$. H_2 was measured by GC after addition of methyl viologen and sodium dithionite to activated cell lysates, set to pH 6.8 with 100 mM potassium phosphate buffer. Activities are normalized for number of cells used (nmol H_2 min^{-1} OD_{600}^{-1}) and error bars reflect standard deviation from biological triplicates. The strain expressing prototypical *Cr*HydA1 was used as a positive control while "Blank" represents the same strain but containing an empty vector. **(B)** Time-dependent H_2 gas production of Group F **Th1** and **Th2**. H_2 levels were measured every 15 mins for 2 hours. Activities are normalized for number of cells used (nmol H_2 OD_{600}^{-1}) and error bars reflect standard deviations from two biological triplicates. "Blank" represents the same strain but containing an empty vector. **(C)** SDS-PAGE visualising the molecular weights of the heterologously expressed archaeal [FeFe] hydrogenases. Expression constructs with verified sequences were transformed in chemically competent *E. coli* BL21(DE3). Protein bands are shown from before induction with IPTG "B", after induction (Name and with the expected kDa size in parenthesis), and lysate after cell lysis and centrifugation "L". The bands in each after-induction lane corresponded well with the expected molecular weights in kDa. Both Group A1 (**Mu** and **Ia**) had the highest expression and solubility levels. In contrast, the Group B (**Ps**) and Group F (**Th1**, **Th2**) enzymes exhibited moderate expression levels but poor solubilities in aqueous solutions. The Group E (**Na** and **Fm**) enzymes exhibited high expression levels but poor solubility. *Adapted figures with permission from* **Paper I**.[154]

To establish a benchmark, the well-characterized prototypical *Cr*HydA1 served as a positive control. Conversely, the lysate from the same *E. coli* BL21(DE3) strain without a hydrogenase encoding gene, but treated with $[2Fe]^{ADT}$, served as the negative control. Relative to the negative control, H_2 production was clearly discernible in enzymes matured from all groups (**Fig. 3.2A-B and Tab. 3.1**).

The standout performers emerged from DPANN with minimal Group A1 and ultraminimal Group E as representatives. The highest activity was observed from a *Micrarchaeota* Group A1 enzyme (**Mu**), evolving H_2 at half the rate of *Cr*HydA1. The homologous enzyme from '*Ca. Iainarchaeum andersonii'* (**Ia**) also produced H_2, though at a hundredfold lower rate. Group E enzyme from '*Ca. Forterrea multitransposorum*' (**Fm**) also showed substantial activity. Both Groups A1 and E possess lower molecular weights (40 kDa and 33 kDa, respectively) than the prototypical *Cr*HydA1 (45 kDa). This challenges the existing assumption that functional [FeFe] hydrogenases cannot be smaller than 45 kDa, presenting them as the smallest known H_2 biocatalysts.

Additionally, the Group B hydrogenase (**Ps**) from Asgard archaon *Ca. P. syntrophicum* has been found to produce significant amounts of H_2, in line with previous findings that this organism can generate H_2 via fermentation. Initially, this activity was assumed to be linked to its Group 3c [NiFe] hydrogenase, while its [FeFe] hydrogenase was misannotated as an $F_{420}H_2$-dependent dehydrogenase subunit.[20]

Lastly, the most intriguing set of genes examined comprised the so-called "hybrids" from Group F, which merge the C-terminal catalytic domain of [FeFe] hydrogenase (*Hyd*A) and the N-terminal domain homologous to a [NiFe] hydrogenase small subunit (*Hyh*S). Two such *Hyd*A-*Hyh*S fusion proteins, originating from *Thermoplasmata*, were examined, namely **Th1** and **Th2**. While **Th1** rapidly produced H_2, with relative activities of 5.1% compared to *Cr*HydA1, **Th2** demonstrated only minimal activity, aligning closely with the negative control (**Fig. 3.2B**). Although **Th2** is inactive in the assay, such result in isolation is not conclusive to rule it out as a non-hydrogenase.

The measured activities are contingent on expression levels, solubility, and abundance of expressed and activated enzymes in the cells (**Fig. 3.2C**), thus, the measured values may underestimate specific activities. Incubation time with $[2Fe]^{ADT}$ can be ruled out as a variable, as there was consistent H_2 production across varied incubation periods (1 to 4 hours), implying that the differences in H-cluster formation rates are not a major determinant in the measured enzyme activity. The extent to which each enzyme achieves proper folding could also influence their performance. This becomes particularly relevant when explaining the contrasting activities between highly homologous enzymes. Despite these limitations, the data set clearly demonstrates the biochemical activity of the [FeFe] hydrogenases encoded by different archaeal groups—DPANN (Group A1 and E), Asgard (Group B), and *Thermoplasmata* (Group F)—attesting to their genuine capability to produce H_2.

Group	Subclass	Code	Species	F-Domain Architecture	Size (kDa)	Relative Activity (%)*
A	M1a	**Mu**	UBA95 sp002499405 (Micrarchaeota)	no F-clusters	40	45 ± 8
A	M1a	**Ia**	*Iainarchaeum andersonii* (Iainarchaeota)	no F-clusters	40	0.42 ± 0.07
B	M3a'	**Ps**	*Prometheoarchaeum syntrophicum* (Asgardarchaeota)	†[6 × C], 2 × [4Fe4S]	61	0.31 ± 0.05
E	M1a	**Na**	CABMGN01 sp902385635 (Nanoarchaeota)	no F-clusters	33	0.10 ± 0.02
E	M1a	**Fm**	*Forterrea multitransposorum* (Iainarchaeota)	no F-clusters	33	1.6 ± 0.3
F	M3d	**Th1**	UBA147 sp002496385 (Thermoplasmatota)	††$[NiFe]_{ss}$, 2 × [4Fe4S]	67	5.1 ± 0.2
F	M3d	**Th2**	UBA147 sp013791785 (Thermoplasmatota)	††$[NiFe]_{ss}$, 2 × [4Fe4S]	67	0.36 ± 0.04

*with respect to *Cr*HydA1's H_2-evolution rates obtained from the screening studies determined after 15 minutes (Groups A, B, and E) or 60 minutes (Group F)
†cysteine consensus gene sequence motif indicating FeS cluster binding
††ss – contains the small subunit of [NiFe]-hydrogenases

Table 3.1 H_2 production activities from archaeal [FeFe] hydrogenases. *Adapted with permission from* **Paper I**.[154]

Activated whole cells display partial H-cluster signals

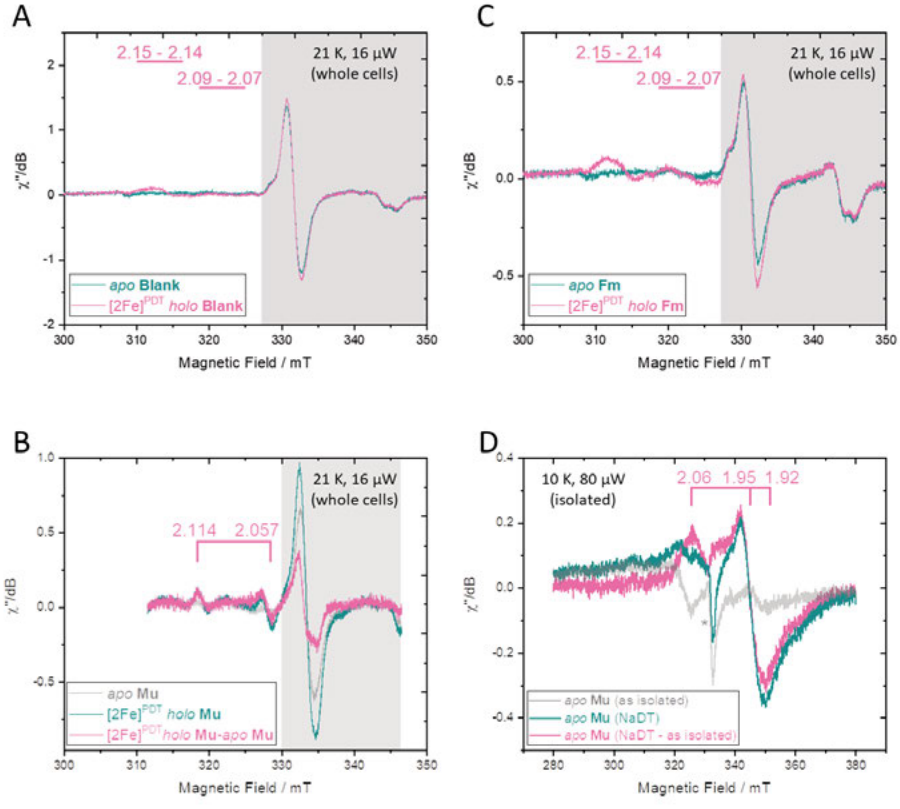

Figure 3.3. X-band EPR spectra recorded of whole cells following anaerobic incubation with $[2Fe]^{PDT}$ containing the **(A)** Empty vector *E. coli* or blank **(B) Mu**, and **(C) Fm**. In panel B, a distinct partial rhombic EPR signal attributable to the H_{ox} state with two discernible g-values ($g_1 = 2.114$, $g_2 = 2.057$; indicated in magenta) while the third g-value is not clear due to signal overlap with the cell background (shaded in grey). Settings: T=21 K; microwave frequency 9.4 GHz, power 16 µW. **(D)** Spectra of isolated and reconstituted *apo* **Mu**. Grey: as-isolated; green: reconstituted and reduced with sodium dithionite (NaDT); magenta: difference between the dark cyan and grey spectra. The g-values in magenta correspond to components typical for a $[4Fe–4S]^{+}$ cluster. The weak signal marked with * appearing at g = 2.02 is linked to a trace amount of $[3Fe–4S]^{+}$ and cavity signal. Settings: T=10 K; microwave frequency 9.4 GHz, power 80 µW. *The experimental procedures for obtaining these unpublished spectroscopic data are provided in the supplementary* **Appendix III**.

To monitor H-cluster assembly, X-band EPR spectroscopy was employed—a technique utilized successfully on *E. coli* whole cells expressing *Cr*HydA1.[104, 178] Incremental addition of $[2Fe]^{ADT}$ to *apo Cr*HydA1 under whole cell conditions enhanced the H-cluster signal, suggesting a correlation between mimic concentration and the level of H-cluster incorporation. This approach also extended our capabilities to identify new hydrogenases from unconventional

groups, such as *Tam*HydS from Group D.[179] Hence, EPR spectroscopy can allow qualitative detection of the H-cluster in whole cell preparations.

As a reference, *E. coli* BL21(DE3) harbouring the empty vector served as the "Blank" control. Additionally, the binding effects of two distinct $[2Fe]_H$ subsite mimics was assessed: $[2Fe]^{ADT}$ and $[2Fe]^{PDT}$. The $[2Fe]^{PDT}$ mimic lacks the proton-relay amine bridgehead of $[2Fe]^{ADT}$ and can aid in accumulating a $[2Fe]_H$ subsite in a mixed valence state H_{ox} (**Fig. 1.3A**), which is an EPR-active state. However, the addition of $[2Fe]^{PDT}$ can also yield an EPR-silent state H_{red}'.

For the whole cell samples, the dense cell suspension was centrifuged following addition of the H-cluster mimic. The resulting pellet was washed, resuspended in buffer, and transferred into EPR tubes, which were immediately frozen in liquid nitrogen. The samples were categorized into three distinct experimental groups: (1) *apo*, (2) $[2Fe]^{ADT}$ *holo*, and (3) $[2Fe]^{PDT}$ *holo*.

The "Blank", devoid of H-cluster mimic, is expected to exhibit broad signals around $g = 2.0$, consistent with the presence of *apo* enzymes and other iron-containing proteins present in the *E. coli* BL21(DE3) strain (**Fig. 3.3A-C**, shaded in grey). The *apo* spectra served as a baseline for interpreting the enzyme-linked signals in the ensuing experimental groups.

When analyzing the $[2Fe]^{PDT}$-treated whole cells expressing the top-performer **Mu**, spectral features akin to the H_{ox} state was observed, exhibiting a partial rhombic signal (**Fig. 3.3B**). The first two g-values ($g_1 = 2.114$, $g_2 = 2.057$) align well with those previously reported [FeFe] hydrogenases, typically with values above $g = 2.0$ (**Tab. 3.2**). The third g-value, theoretically positioned around 2.010−2.009, remains unresolved due to substantial interference from *E. coli* background signals, complicating the identification of the full rhombic signal. The $[2Fe]^{ADT}$-treated whole cells expressing **Mu**, however, did not yield detectable signals linked to the H-cluster. Nonetheless, the discernible g_1 and g_2 from $[2Fe]^{PDT}$-**Mu** are consistent with the formation of H_{ox}, providing partial spectroscopic evidence for the capacity of an archaeal [FeFe] hydrogenase to bind the H-cluster.

Spectra of whole cells expressing **Ps**, **Fm**, **Th1**, and **Th2** with either $[2Fe]^{ADT}$ and $[2Fe]^{PDT}$ did not reveal any discernible EPR signal attributable to the H-cluster (**Fig. 3.3C**). Although changes in signals were observed after H-cluster mimic addition ($g_1 = 2.15−2.14$ and $g_2 = 2.09−2.07$), these changes closely resembled those found in the "Blank", thus precluding them from being conclusively linked to the H-cluster. The signals at $g_1 = 2.15−2.14$ are broader than the typical $g_1 = 2.1$ observed in $[2Fe]^{PDT}$-treated whole cell samples of *Cr*HydA1, *Tam*HydS, and **Mu**. The signals around $g_2 = 2.09−2.07$, which intersect the baseline, can potentially represent the g_2 signal of H_{ox}. Although such crossover is absent in $[2Fe]^{PDT}$-blank, the g-value range (2.09−2.07) is too high-field to correspond to the g_2 of a conventional rhombic signal from H_{ox}.

Group-Subclass	Species	H_{ox}-[2Fe]^{PDT}		
		g_1	g_2	g_3
A-M1	*Cr*HydA1[180]	2.094	2.039	1.998
A1-M1	**Mu**†	2.114	2.057	n.d.*
A-M3	*Cp*I[92]	2.092	2.039	2.000
A-M2	*Sm*HydA[179]	2.100	2.040	2.010
A-M2(D)	*Dd*H[80]	2.095	2.041	1.998
C-M2f	*Tm*HydS[91]	2.108	2.043	2.000
D-M2e	*Tam*HydS[179]	2.106	2.051	2.010

*n.d. = not detected
†obtained from whole cells

Table 3.2 Previously reported g-values for [FeFe] hydrogenases matured with [2Fe]^{PDT}.

Given these ambiguous results from the whole cell experiments, activated lysates were analysed in an attempt to gain a clearer spectroscopic recognition of the H-cluster. However, the analysis of lysates proved to be problematic mainly due to background interference potentially caused by interactions between the mimic and various cellular components. Additional complications stemmed from low enzyme expression and solubility, meaning few enzymes were present at detectable levels. The subsequent logical step required the isolation of the enzymes from large scale cultures, and removing them from the cellular mixture.

Group A & E: Smallest H_2 biocatalysts from (ultra-) minimal DPANN

Monomeric *apo* **Mu** and *apo* **Fm** bind a single [4Fe-4S] cluster

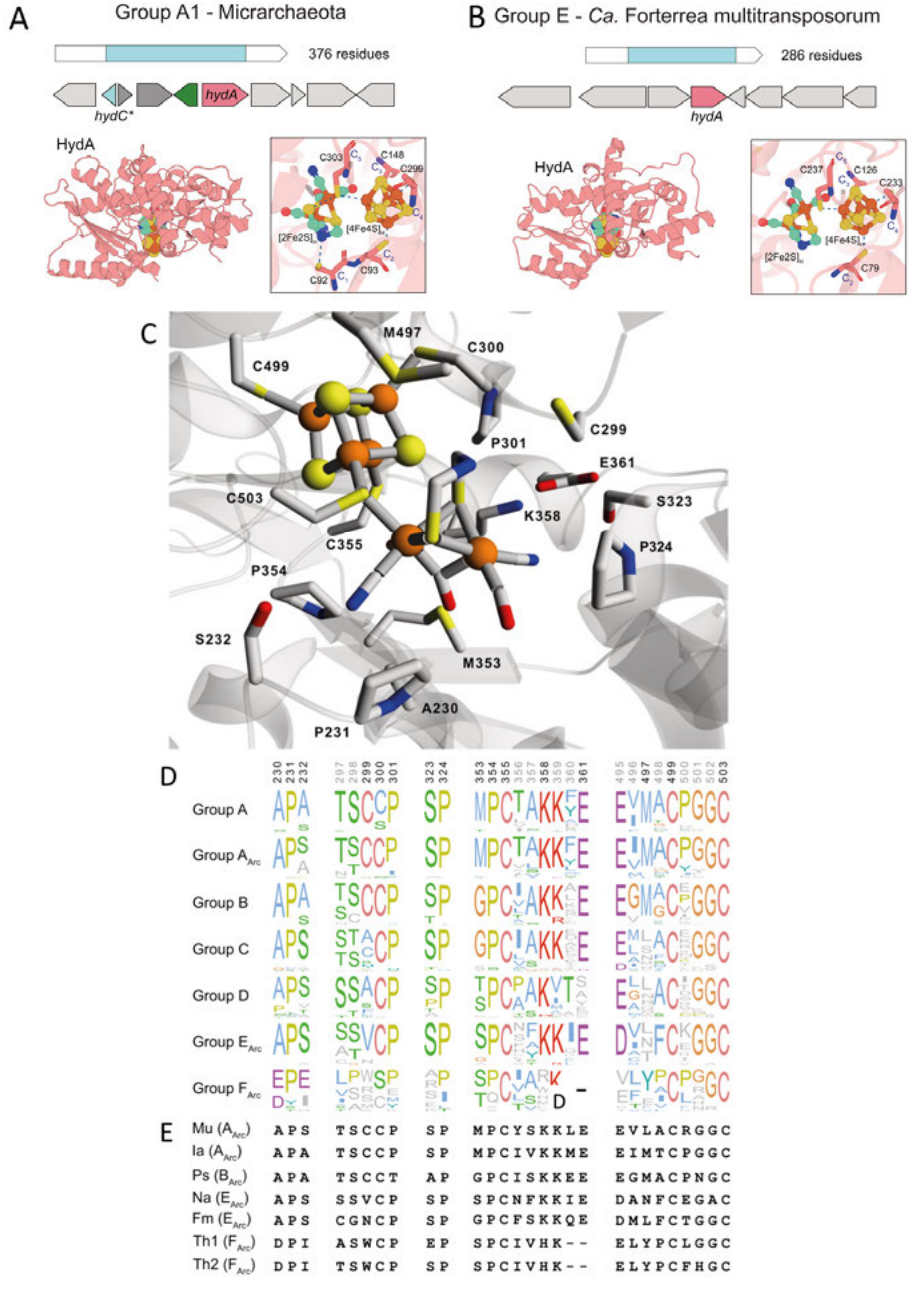

Figure 3.4 Catalytic domain structure, genetic organisation, and AlphaFold2-based structural modelling of **(A) Mu (B) Fm**. The subunits in their genetic context are shown, labelled and coloured consistent with the corresponding subunit in the structural models. Predicted cofactors are positioned based on the structures of homologous proteins. A zoomed view of the H-cluster and conserved coordinating cysteine residues (C_1 to C_5) is provided. **(C)** Structural view of the active site of *Cp*I (PDB ID: 4XDC) showing the H-cluster and interacting amino acid residues. **(D)** Normalized consensus logos of Groups A−F generated in Jalview using a ClustalΩ sequence alignment of sequences retrieved from Greening *et al.* 2016[15] and this work. Numbering is based on *Cp*I and black numbers are illustrated in the top panel. **(E)** Amino acid sequences of the archaeal [FeFe] hydrogenases heterologously expressed in this work. *Reprinted with permission from* **Paper I**.[154]

In the biochemical screening assay, Group A1 **Mu** and Group E **Fm** emerged as top performers and remarkably display the lowest molecular weights for a hydrogenase, prompting their isolation for further study.

Mu exhibited the highest expression and solubility levels with *E. coli* BL21(DE3) (**Fig. 3.2C**). Optimal growth conditions incorporated iron-supplemented M9 media and induction with IPTG. The protein was purified under strictly anaerobic conditions, using StrepTactin XT to achieve a single SDS-PAGE band around 40 kDa (**Fig. 3.5A**). The initial choice of 100 mM Tris buffer with 150 mM NaCl at pH 8.0 led to unexpected challenges, as the concentrated protein solution exhibited precipitation—a phenomenon explainable by the salting-out effect which occurs when high salt concentrations cause proteins to precipitate. To mitigate this, a buffer of lower ionic strength was used. Subsequent use of a more dilute 10 mM Tris buffer at the same pH avoided the precipitation issue.

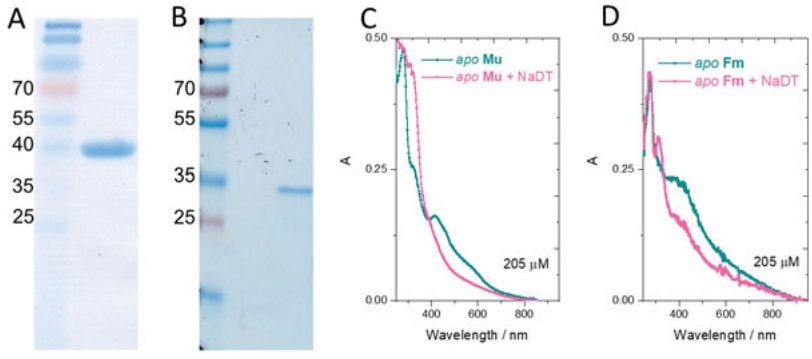

Figure 3.5 SDS-PAGE gels visualizing purified **(A)** *apo* **Mu** and **(B)** *apo* **Fm**. UV-visible spectra of **(C) Mu** (205 µM) and **(D) Fm** (205 µM) after reconstitution of [4Fe-4S]$^{2+}$ cluster (dark cyan spectrum), indicated by the absorbance at 405 nm. Upon addition of 20× excess sodium dithionite (NaDT, magenta spectrum), a decrease in absorbance at 405 nm is observable, indicating the reduction of [4Fe-4S]$^{2+}$ cluster to [4Fe-4S]$^{+}$. Spectra were recorded using a 1 mm path length cuvette, with distinct spectrophotometers employed for each set of spectra (Panel C: Infinite 200 Pro – Infinite M Nano; Panel D: AvaSpec-ULS2048-USB2-UA-50: Avantes Fiber Optic). *Adapted figures with permission from* **Paper I**.[154] *The experimental procedures for obtaining the unpublished data on* ***Mu*** *are provided in the supplementary* **Appendix III**.

Following semi-enzymatic reconstitution of the iron-sulfur clusters (**Fig. 3.5C**), the iron content of the enzyme was determined to be 3.7 ± 0.5 per protein, in agreement with the structural modelling that suggests this enzyme contains a single [4Fe-4S] cluster. This is further supported by EPR spectroscopy (**Fig. 3.3D**). The EPR spectra recorded on "as-prepared" *apo* **Mu** showed a signal marked appearing at g = 2.02, and is attributed to the combined contributions from the instrument cavity and trace amounts of [3Fe–4S]$^{+}$. Upon reduction with sodium dithionite (NaDT), the reduced *apo* enzyme exhibited a single rhombic EPR signal attributable to [4Fe-4S]$^{+}$ (S = ½), with g-values: $g_{1,2,3}$ = 2.06, 1.95, 1.92. These values closely align with those reported for other [FeFe] hydrogenases, such as monomeric *Cr*HydA1, which exhibited a single rhombic signal for its [4Fe-4S]$_{H}$ having $g_{1,2,3}$ = 2.08, 1.94, 1.88. **Mu** exhibits a "narrower" rhombic character for its [4Fe-4S]$_{H}$ compared to *Cr*HydA1.

Hydrogenases with F-clusters, such as Group A *Cp*I (4 x [4Fe-4S], 1 x [2Fe-2S]), Group C *Tm*HydS (4 x [4Fe-4S]), and Group D *Tam*HydS (4 x [4Fe-4S]), are known to display multiple sets of rhombic signals for [4Fe-4S]$^{+}$ spread within the g~2 region.[71, 91, 92] EPR analysis of the F-clusters of *Tm*HydS and *Tam*HydS revealed two distinct rhombic signals, suggesting the reduction of two unique [4Fe-4S] clusters upon NaDT treatment (**Fig. 5.4A**). This observation was further corroborated by spin quantification, which yielded approximately two spin centers per protein. These findings indicate that, out of the four anticipated [4Fe-4S] clusters, two exhibit susceptibility to reduction

by NaDT. The contrasting spectral simplicity of *apo* **Mu**, featuring a single rhombic signal, supports the findings from gene analysis, Alphafold modelling, and biochemical data, indicating that it can only bind one [4Fe-4S] cluster (**Fig. 3.4A**). The [4Fe-4S] cluster is crucial for the proper assembly of the H-cluster (**Fig. 2.1C**).

On the other hand, **Fm** showed high expression levels but poor solubility with *E. coli* BL21(DE3) as host strain (**Fig. 3.2C**). Given the suboptimal amount of soluble **Fm** for further isolation, other *E. coli* strains were tested, aimed at enhancing protein expression and solubility:

***E. coli* BL21 (DE3) ΔiscR (ΔiscR)**: The deletion of the transcriptional negative regulator, IscR, had been shown to enhance recombinant [FeFe] hydrogenase activity.[181]

***E. coli* (DE3) Origami (Ori)**: Thioredoxin reductase (trxB) and glutathione reductase (gor) gene mutations can increase cytoplasmic disulfide bond formation. Additional lac permease (lacY) mutation can enhance IPTG uptake, ensuring uniform cellular entry of IPTG and homogeneous induction.

***E. coli* B (DE3) Arctic Express (AX)**: Engineered to address protein insolubility, this strain expresses cold-adapted chaperonins Cpn10 and Cpn60 (optimum temperature 4-12°C), providing an alternative protein folding environment.

The Ori strain was promising for **Fm**, with improvements in expression levels, though solubility remained suboptimal. In contrast, the ΔiscR and AX strains resulted in poor expression and solubility levels. This led to the decision to proceed with **Fm** isolation in the Ori strain. Co-expression of the maturation machinery could potentially enhance both expression and solubility. However, it appears that **Fm** lacks the three maturation enzymes (HydEFG) necessary for synthesizing the H-cluster, suggesting that **Fm** uses an alternative, native maturation pathway and/or has an atypical $[2Fe]_H$ subsite.

The growth conditions were similar to those used for **Mu**; however, after purification with StrepTactin XT, two bands were observed: one around 30 kDa and another at around 60 kDa. Subsequently, size exclusion chromatography was employed to eliminate the high-molecular weight impurity (**Fig. 3.5B**). Following purification under strictly anaerobic conditions and semi-enzymatic reconstitution of the iron-sulfur clusters (**Fig. 3.5D**), the iron content of the *apo* **Fm** was determined to be 4.2 ± 0.4 per protein. This aligns with the structural modelling that predicts the presence of a single [4Fe-4S] cluster (**Fig. 3.4B**). While EPR spectroscopy could ideally reinforce these results, it was bypassed due to the reliable structural modelling and biochemical methods (as affirmed in examining *apo* **Mu**), the extremely low yield of the purified enzyme, and the high sample requirement for EPR.

holo **Fm** displays unique H-cluster signals

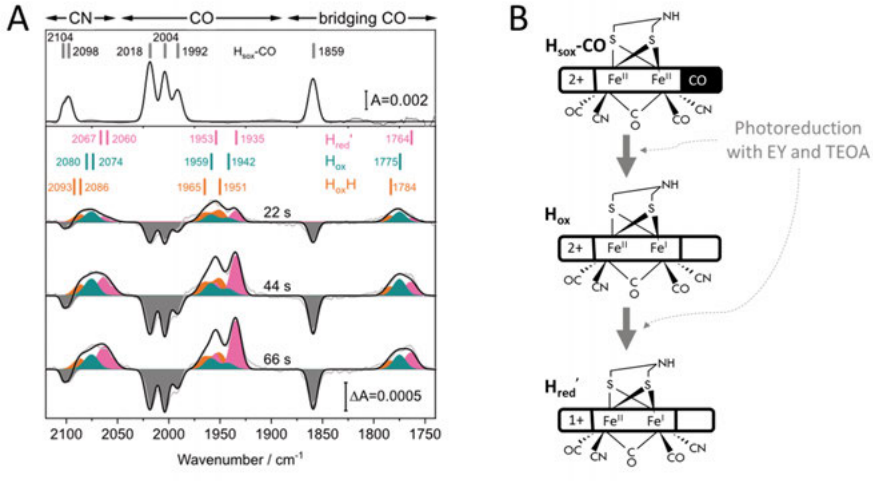

Figure 3.6. (A) FTIR spectra of **Fm** after activation with $[2Fe]^{ADT}$ and photoreduction. **(B)** the proposed H-cluster intermediates after photoreduction with photosensitizer Eosin Y (EY) and sacrificial electron donor triethanolamine (TEOA). The absorbance spectrum (top) in panel A indicates a CO inhibited H-cluster state (H_{sox}-CO). The difference spectrum (bottom) depicts the transitions of **Fm** into catalytically active states via photoreduction. During illumination bands linked to H_{sox}-CO decreased (grey bands), while new bands reflecting reduced and catalytically active H-cluster states emerge (orange: $H_{ox}H$; dark cyan: H_{ox}; magenta: H_{red}'). The spectra are arranged chronologically from top (22 s) to bottom (66 s). *Adapted figure with permission from* **Paper I**.[154]

The reconstituted *apo* **Fm** was incubated with $[2Fe]^{ADT}$, and purified using desalting columns to generate the corresponding *holo* enzyme. Successful H-cluster assembly was verified through FTIR spectroscopy, as evidenced by sharp cofactor bands in the expected CO/CN ligand band region (**Fig. 3.6A**).

"As-prepared" *holo* **Fm** displayed signals with peak positions reminiscent of those from bacterial [FeFe] hydrogenases, suggesting a di-ferrous (Fe^{II}-Fe^{II}) oxidation state of the $[2Fe]_H$ subsite (H_{inact} and H_{trans}, **Fig. 1.3B**).[99, 118] The lack of detectable reactivity when exposed to H_2 further supports the notion that the enzyme is isolated in an "over-oxidized" inhibited state. The presence of two CN (2105, 2097 cm^{-1}) and four CO (2018, 2001, 1992, 1860 cm^{-1}) cofactor ligand bands suggests an H-cluster inhibited by a sixth ligand, CO. This is consistent with previous findings that H_{ox}-CO formation can occur during the artificial activation process.[182] Hence, the as-isolated **Fm** is proposed to be a super-oxidised CO inhibited (H_{sox}-CO) species (**Fig. 3.6B**).

Upon photoreduction with photosensitizer Eosin Y (EY) and sacrificial electron donor triethanolamine (TEOA), H_{sox}-CO transitions into catalytically active states $H_{ox}H$ and H_{ox}.[98] The bands for $H_{ox}H$ are 2093, 2086, 1965, 1951, 1784 cm^{-1}, while for H_{ox} they are 2081, 2068, 1965, 1953, 1776 cm^{-1},

respectively. These patterns are indicative of H-cluster species with a mixed valent Fe^{I}-Fe^{II} oxidation state of the $[2Fe]_H$ subsite (**Fig. 3.6**). With prolonged photoreduction, the redox state population at lower wavenumbers accumulates, likely arising from the formation of H_{red}'.[94, 101] This state exhibits a band pattern with red-shifts of 7-13 cm^{-1} (2075, 2061, 1944, 1933, 1764 cm^{-1}), reflecting a reduction of the $[4Fe\text{-}4S]_H$ cluster (**Fig. 3.6**).[94, 101] After transitioning to more reduced states, there was no observable reactivity with CO or H_2. Finally, preliminary data suggests that **Fm** remains stable when exposed to O_2 (air), indicating potential O_2-insensitivity that merits further investigation.

holo **Mu** displays H-cluster signals when activated in lysates

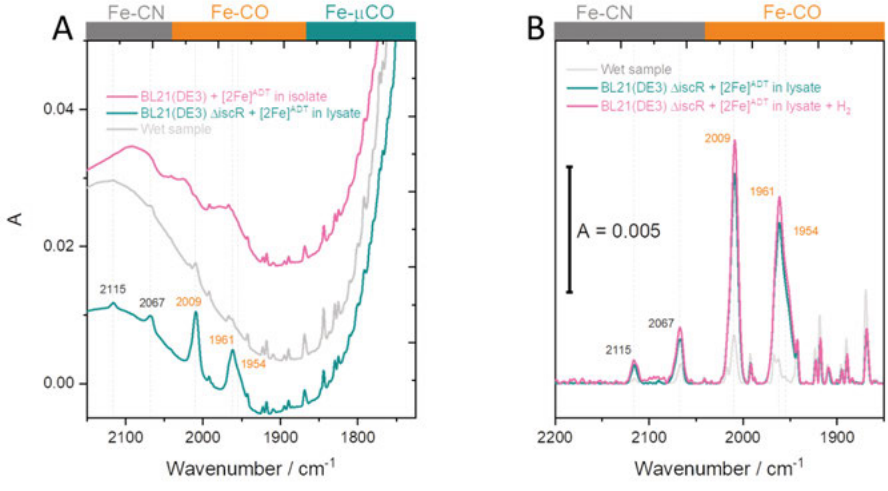

Figure 3.7. (A) FTIR spectra of "as-prepared" **Mu**. Comparison of spectra for isolated **Mu** expressed in BL21(DE3) with the $[4Fe\text{-}4S]^{+}$ clusters reconstituted prior to activation using $[2Fe]^{ADT}$ (magenta) and **Mu** expressed in BL21(DE3) ΔiscR, activated with $[2Fe]^{ADT}$ in the lysate (dark cyan). The grey spectrum corresponds to the latter sample in wet droplet form, highlighting water bands. **(B)** Baseline-corrected spectra of the dark cyan spectrum from (A) and the same sample after 1-hour flushing with H_2. *The experimental procedures for obtaining these unpublished spectroscopic data are provided in the supplementary* **Appendix III**.

In the activation of reconstituted *apo* **Mu**, a similar approach was taken as with *apo* **Fm**. However, contrary to observations from whole cell EPR spectroscopy, H-cluster signals were absent in purified *holo* **Mu**, as evidenced by both FTIR (**Fig. 3.7**) and EPR spectroscopy.

The standard procedure for activation involves the addition of mimics, either $[2Fe]^{ADT}$ or $[2Fe]^{PDT}$, to a diluted *apo* enzyme in a 100 mM sodium phosphate buffer (pH 6.8), followed by an incubation period of at least one hour. The mixture is then passed through desalting columns with 10 mM Tris buffer, pH 8.0 to purify the *holo* enzymes. Shifting to a lower buffer concentration

post-activation eases FTIR analysis, as higher salt concentrations can increase noise background levels in the CO/CN region. This is also beneficial particularly when concentrating **Mu**, as the enzyme tends to precipitate in higher buffer concentrations.

FTIR analysis on $[2Fe]^{ADT}$-activated **Mu** was dominated by broad peaks, contrasting with the sharp H-cluster bands observed in previously reported [FeFe] hydrogenases and $[2Fe]^{ADT}$-activated **Fm** (**Fig. 3.6A, Fig. 3.7A**). Broad signals resembled those of free $[2Fe]^{ADT}$ in solution but did not match reported bands.[183] These bands remained stable under short-term H_2 or O_2 exposure (minute timescale) but decreased in intensity after prolonged exposure, indicating slow reactivity. Reduction with Europium (II)-EGTA yielded no observable changes as well. Further activation attempts with $[2Fe]^{ADT}$, using 10% acetonitrile to remove unspecifically bound $[2Fe]^{ADT}$, resulted in persistent broad signals. Photoreduction did not alter band intensity, suggesting the absence of interactive H-cluster states.

Activation of **Mu** with $[2Fe]^{PDT}$ only led to broad FTIR bands similar to the free $[2Fe]^{PDT}$ complex in solution. Again, these bands do not correspond to the broad bands of the free complex[183], and also exhibited no reactivity towards O_2 on a minute timescale. Despite testing various conditions, including different incubation times for each mimic (2 hours vs 6 hours), buffers with varying pH levels (pH 6.0 vs pH 8.0) and concentrations (10 mM vs 100 mM Tris), the sharp H-cluster bands remained undetectable.

Due to the lack of success using FTIR, EPR was subsequently used due to its higher sensitivity. EPR analysis of the $[2Fe]^{ADT}$-**Mu** revealed a spectrum nearly identical to *apo* **Mu**. This suggests the as-isolated **Mu** either only stabilized EPR silent states or lacked a detectable bound H-cluster.

In the context of second coordination sphere effects, methionine residues $M497_{CpI}$ and $M353_{CpI}$ (*Cp*I numbering) are proposed to modulate the H-cluster reactivity and fine-tune H_2 affinity in Group A enzymes. This hypothesis is further supported by gain-of-function studies on the less-active Group D *Tam*-HydS, underscoring the significance of a sulfur-rich H-cluster canopy for catalysis (see **Chapter 5**). Examining the protein sequence and structural models of **Mu** revealed an intriguing substitution: one of these methionines ($M497_{CpI}$) is replaced by a leucine in **Mu** ($L297_{\mathbf{Mu}}$) (**Fig. 3.4C-E, Appendix III**). Earlier research on a $M415L_{CrHydA1}$ variant reduced H_2-processing rates and was linked to a substantial loss of an intact H-cluster.[75] Due to its high conformational flexibility and low rotational energy requirement, the methionine likely mitigates interactions between the H-cluster and the protein framework.

The rationale behind Nature's choice for this specific substitution in **Mu**, which is not common in most Group A1 archaeal sequences (**Fig. 3.4D-E**), raises intriguing questions. Even the homologous Group A1 enzyme, **Ia**, retains this methionine ($M497_{CpI}$). Generally, evolutionary changes are driven by mutations (beneficial or neutral changes in the protein's function or structure), selection (Nature "choosing" the best proteins), and drift (random

changes over time). Several plausible explanations for this substitution exist: (a) diversification to perform a slightly different role or function more efficiently under certain conditions[184], (b) structural stability at the expense of a particular function or catalytic property[185], (c) selective evolutionary pressures that can improve host microbe survival[186], or (d) a product of neutral evolution (*i.e.,* changes in DNA that do not confer any significant advantage or disadvantage), but occur randomly and persist in the microbial population.[187]

These hypotheses provide a preliminary framework for further investigation into the evolutionary mechanisms that drive the M to L substitution. Both residues, characterized by hydrophobic side chains, exhibit differences in bulkiness or backbone angles that can influence the H-cluster's flexibility, function, and stability. An interesting line of inquiry would be to assess the effectiveness of the artificial maturation process *in vitro* upon substituting leucine ($L297_{Mu}$) with methionine, specifically examining the potential "restoration" of **Mu**'s full functionality.

Artificial maturation of **Mu** proceeded successfully when conducted in lysates but fails when working with purified **Mu** (**Fig. 3.7A**). Preliminary spectroscopic analyses reveal sharp signals characteristic of the H-cluster in **Mu** that was expressed in BL21 ΔiscR cells and subsequently activated in the cell lysates before purification. Photoreduction experiments on this sample are underway to identify and assign the spectral bands to specific H-cluster state/s. These experiments will enable the observation of band changes occurring during the photoreduction process.

The discrepancy between the two activation methods may be attributed to the optimal and protective environment provided by lysates, encompassing suitable pH and/or concentrations of essential *E. coli* proteins, cofactors or substrates. These conditions may not be accurately replicated in purified enzyme systems.

The precise reasons for the successful maturation in lysates but not *in vitro* and the absence of a maturation machinery like *Hyd*EFG in the **Mu** genome warrant further investigation. Although the lack of *Hyd*EFG does not preclude efficient *in vitro* maturation, as observed with **Fm**, it may still influence the process. Future research should explore the specific factors governing **Mu** maturation, including the potential role of alternative maturation pathways and the influence of the cellular environment present in lysates.

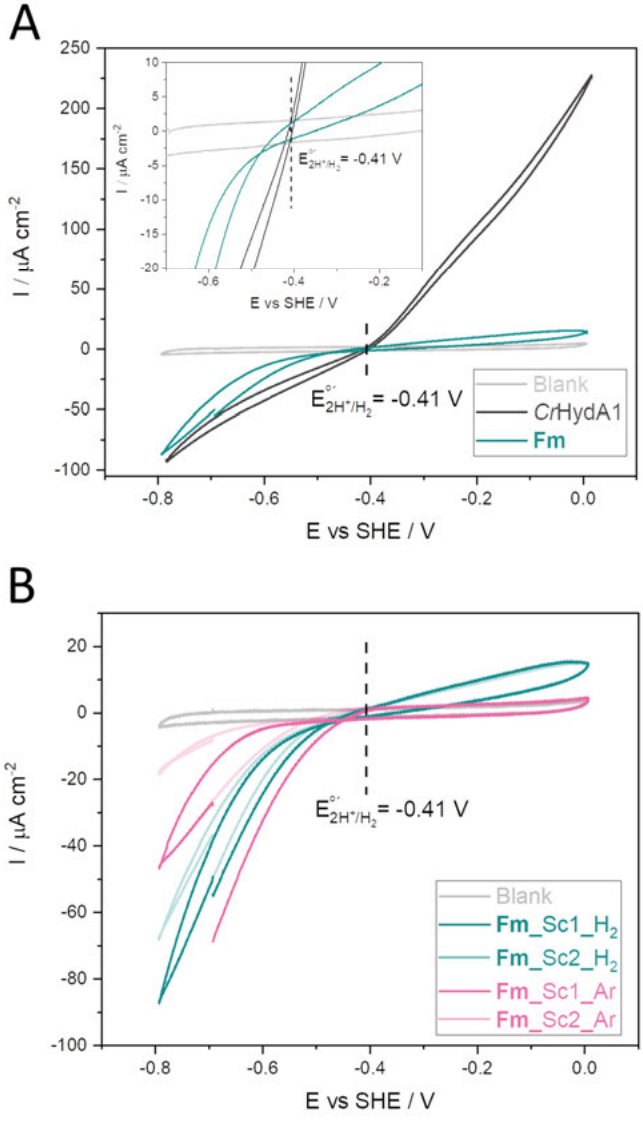

Figure 3.8 (A) CV traces of immobilized *Cr*HydA1 (black), **Fm** (dark cyan) with H_2 oxidation current densities at high potentials and proton reduction currents at low potentials. The thermodynamic potential of the $2H^+/H_2$ redox couple is labelled with a dashed line. The "Blank" trace (grey) represents the electrode without an immobilized enzyme film. Inset panel shows zoom in of the regions close to the thermodynamic potential. The experiments were performed on at least two independent films for each enzyme at pH 7.0 (5 mM MES, 5 mM CHES, 5 mM HEPES, 5 mM TAPS, 5 mM NaOAc, 0.1 M Na_2SO_4) and under 1 atm H_2. **(B)** First (Sc1), second (Sc2, more transparent) CV traces of **Fm** under 1 atm argon (magenta: Ar) or 1 atm H_2 (dark cyan). The working electrode was rotated at 3,000 rpm and the scan rate was 10 mV/s.

PFE confirmed **Fm** as being electrocatalytically active. Under a H_2 atmosphere, the CV traces of immobilized **Fm** exhibited the bidirectional catalytic behaviour typical of [FeFe] hydrogenases (**Fig. 3.8A-B**).

Although **Fm** operates with slight indications of an overpotential from the thermodynamic potential for both proton reduction and H_2 oxidation ($E^{0\prime}_{2H^+/H_2}$), this observation warrants careful interpretation. The observed overpotential might largely stem from the lower current densities achieved with **Fm** compared to *Cr*HydA1. **Fm** also exhibits pronounced bias towards proton reduction, particularly at high driving forces, in contrast to *Cr*HydA1, which favors H_2 oxidation. The observation that the oxidation currents of **Fm** approach a plateau, particularly at very high potentials, suggests that the catalytic turnover, rather than the interfacial electron transfer, is the rate-limiting step under these conditions (**Fig. 2.6**).[188] However, mass transport limitations, potentially arising from slow diffusion of H_2, cannot be definitively ruled out and require further investigation.

Immobilized **Fm** seems to deactivate at high oxidation potentials (**Fig. 3.8A-B**). The CVs begin at a reducing potential (−700 mV vs SHE), sweep to higher redox potentials (up to 0 mV vs SHE), and then revert to the initial potential (−700 mV vs SHE). A sign of inactivation is a signal crossover near −500 mV vs SHE. After sweeping to higher oxidative potentials, there is a decrease in reductive currents compared to the initial sweep, indicating oxidative inactivation.

While loss of enzyme film during the experiment adds complexity to the interpretation, FTIR results can partly explain the nature of the observed inactivation. FTIR data demonstrates that **Fm** can adopt a super-oxidized, inhibited state (H_{sox}-CO), as indicated by the wavenumber positions (**Fig. 3.6A**). The detection of four distinct CO bands is a peculiar observation, implying the incorporation of an additional CO ligand. The source of this CO can be speculated to be from the degradation of a fraction of the H-cluster, leading to the release of CO and its subsequent binding to a subpopulation of enzyme active sites.

The CVs showed a decrease in the strength of oxidative inhibition when H_2 is present, as opposed to when the reducing gas is replaced with argon (Ar) (**Fig. 3.8B**). This suggests that H_2 binding may have a protective role against oxidative inactivation, potentially by hindering the formation of the H_{sox}-CO state and help maintain the enzyme in a catalytically active state. Another possibility is that H_2 promotes a rapid transition from the H_{sox}-CO state to the catalytically active $H_{ox}H/H_{ox}$ state. While the presence of H_2 appears to mitigate oxidative inactivation, a sustained current loss in the reverse sweep persists. This could be attributed to several factors, including slow H_2 binding kinetics, sluggish re-reduction of the inhibited H_{sox}-CO population back to the active state, gradual enzyme loss from the electrode surface, or a combination of these factors.

Reversible, anaerobic inactivation at high potentials has been extensively studied for [NiFe] hydrogenases (*Av*[NiFe]-MBH).[189] Notably, oxidative inactivation is more pronounced at lower H_2 levels, highlighting the protective role of H_2.[59, 189] While initial oxidative inactivation involves μOH binding to the Ni-Fe cofactor, the subsequent reactivation process is more complex than a direct ligand exchange with H_2, involving intermolecular electron transfer events, potentially mediated by other [NiFe] hydrogenases.

Similarly, some [FeFe] hydrogenases are susceptible to reversible, anaerobic, oxidative inactivation, resulting in sulfide-bound H_{trans} or H_{inact} (Fe^{II}-Fe^{II}) states (**Fig. 1.3B**).[190-192] Reactivation from these inactive states can be achieved through either chemical reduction, typically using NaDT, or by applying reducing potentials. However, the observed inactivation of **Fm** is unlikely to stem from mechanisms involving cysteine binding. This assertion is supported by the observed resilience of *Cr*HydA1, which does not seem to oxidatively inactivate, despite a previous report of H_{trans}-like or H_{inact}-like state formations.[178] Moreover, endogenous cysteine binding to the H-cluster can be ruled out because the $C299_{CpI}$ is replaced with an asparagine in **Fm** (**Fig. 3.4C-E**). Previous studies have linked *Cr*HydA1 inactivation to inhibition by halide salts in the buffer mixture[193]; however, the CVs for **Fm** (and *Cr*HydA1 in this study) were recorded in the absence of halides, indicating that inactivation is not due to halide inhibition but rather an inherent and unique mechanism. Recent research reveals that Group B *Cp*III and *Me*II can inactivate under oxidative conditions, albeit through a distinct mechanism not observed in Group A enzymes.[121]

To elucidate the physiological functions and interactions within complex microbial communities, studies involving native host cells and with other organisms are necessary. However, preliminary insights into the roles of DPANN enzymes can be derived from the CV data of **Fm**. Genomic analysis reveals that most DPANN lack genes linked to a complete electron transport chain and the necessary pathways for respiratory reductases or carbon fixation. Due to their nanometric size and absence of many key metabolic pathways, DPANN archaea are thought to be obligate fermenters reliant on host-derived organic compounds. As a result, they typically harbour genes for carbohydrate degradation and fermentation. The CVs of **Fm** reflects the anticipated fermentative functions.

Collection of PFE data on the lysate-activated **Mu**, demonstrating sharp H-cluster bands in FTIR (**Fig. 3.7**) is underway.

Perceivable benefits of the (ultra-)minimal structures

Many DPANN archaea solely encode the minimal Group A1 (**Mu**) and ultra-minimal Group E (**Fm**) [FeFe] hydrogenases. These microorganisms have optimized the genetic and cellular costs associated with H_2 metabolism, likely further eased by the relatively less complex maturation pathways of [FeFe] hydrogenases compared to [NiFe] hydrogenase.

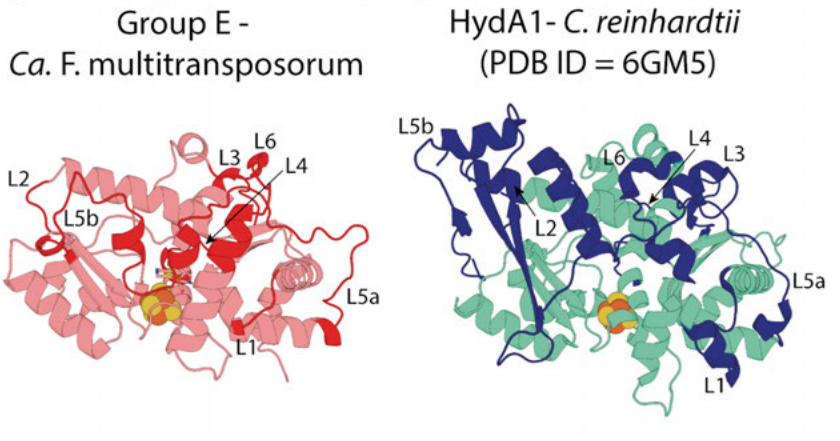

Figure 3.9 A comparison of **Fm** with *Cr*HydA1 with the location of structural elements with reduced size in **Fm** labelled L1 to L6. Predicted cofactors are positioned based on the structures of homologous proteins. *Reprinted with permission from* **Paper I**.[154]

The Group A1 enzymes (including **Mu**) represents a 30−40% reduction (324−386 amino acid residues long) compared to its bacterial and eukaryotic counterparts, which on average consist of 564 residues. The **Fm** from Group E, takes this size reduction even further. Consisting of only 286 amino acids, it stands as the smallest known [FeFe] hydrogenase to date, exhibiting a nearly 40% decrease in residue count compared to *Cr*HydA1 (457 residues). Both **Fm** and *Cr*HydA1 share a scaffold cutback partly attributed to the absence of the N-terminal F-cluster domain (**Fig. 1.1C**). However, **Fm** distinguishes itself from *Cr*HydA1 by having a more compact loop structure (**Fig. 3.9**), further minimizing its overall size. This remarkably compact structure, with its significantly reduced amino acid count, suggests that **Fm** might be approaching the lower limit for the protein scaffold required to support the essential structural and functional elements of an active [FeFe] hydrogenase.

The diminutive size of hydrogenases in DPANN archaea offers potential advantages for the survival of the host microorganisms:

Resource Efficiency: Synthesis of smaller enzymes require fewer resources, a useful trait for resource-scarce environments.

Genomic Compactness: The reduced size allows for efficient encoding within the condensed genome, thereby optimizing the use of genetic coding space.

Evolutionary considerations: Smaller enzymes can evolve more rapidly, which can allow microorganisms to adapt more quickly to fluctuating environmental conditions. However, the size may not be the primary determinant of its evolutionary trajectory. While smaller proteins, in general, may experience higher mutation rates due to their shorter sequence lengths, simple correlations between evolutionary rate and adaptability should be treated with caution. Rather, factors such as protein structure, stability, functional constraints, and environmental selective pressures can exert a more significant influence in shaping its evolutionary path.

The specific benefits conferred by smaller enzymes can vary depending on the microorganism and its environmental context. In parallel, larger enzymes also have unique benefits, such as the ability to catalyze more complex reactions, possibly due to their modularity and functional flexibility (see Group F section). Evolution appears to delicately calibrate these various factors, emphasizing the adaptability and resilience of life not only at the microscopic but even at the nanoscopic level.

Potential (bio-)technological advantages

The compact size of (ultra-)minimal hydrogenases holds potential for future biotechnological applications:

Flexible scaffolds for genetic engineering: The reduced size simplifies genetic manipulation, whether through directed evolution or (semi-)rational design. However, this is a generalized statement and the actual time can vary significantly based on factors such as the efficiency of the high-throughput assay used, the specific changes desired, or level of randomness defined.

Understanding parameters for bio-mimic design: The small size of these enzymes, combined with the ease of genetic manipulation, aids in pinpointing determinants of rate, directionality, substrate affinity, substrate transport, efficiency, overpotential-dependence, and tolerance towards gaseous inhibitors. By understanding these parameters, we can, for example, design artificial enzyme-like scaffolds that mimic the enzyme's active site architecture and electron/proton transfer pathways, or engineer such scaffolds to optimize substrate channeling and/or reaction kinetics.

Resource efficiency: The need for fewer resources for synthesis is especially relevant in the context of biohydrogen production, abiotic electrolytic or fuel cells, or semisynthetic photosynthetic systems. The ease of genetic manipulation, resulting in improved stability under cost-effective environmental conditions, can further reduce process costs.

These points highlight the potential of (ultra-)minimal hydrogenases in advancing sustainable H_2-based technologies. Yet, realizing this potential will require further research and development.

Group B: Hydrogenase from an Asgard archaeon at the prokaryote–eukaryote interface

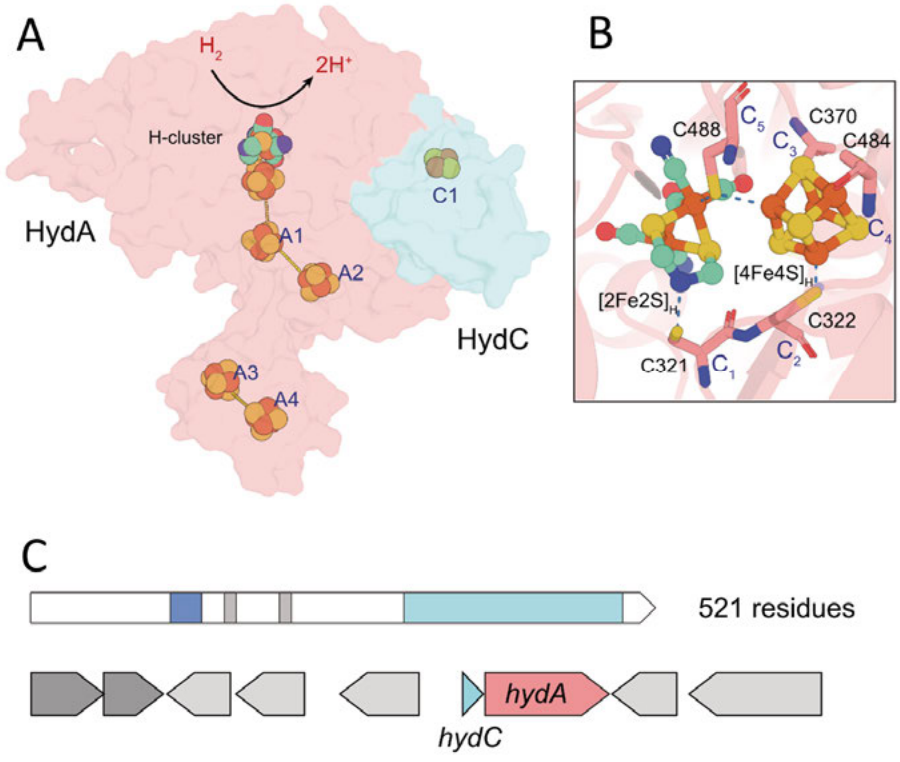

Figure 3.10. Catalytic domain structure, genetic organisation, and AlphaFold2-based structural modelling of **Ps**. **(A)** Predicted cofactors are positioned based on the structures of homologous proteins. **(B)** A zoomed view of the H-cluster and conserved coordinating cysteine residues (C_1 to C_5) is provided. **(C)** Predicted operon is shown on the right with genes encoding structural subunits shown in their genetic context, labelled and coloured consistent with the corresponding subunit in the structural model in (A). *Reprinted with permission from* **Paper I**.[154]

Among archaea, the Group B [FeFe] hydrogenases were exclusively found in *Asgardarchaeota* and were detected in the genomes of cultured strains, *Ca. P. syntrophicum* and *Ca. L. ossiferum*. These *Hyd*A subunit possess two [4Fe-4S] cluster binding domains at the N-terminal region acting as an electron relay (A1 and A2) and a conserved putative FeS cluster binding motif with six cysteine residues (A3 and A4; $CX_2CX_{10}CX_2CX_4CX_3C$). The gene for the disulfide-reducing thioredoxin (*Hyd*C) is located immediately upstream of *Hyd*A. The Group B enzyme from *Ca. P. syntrophicum* (**Ps**), which has been biochemically verified, is predicted as a heterodimer of *Hyd*A-*Hyd*C subunits (**Fig. 3.10**). *Hyd*C could aid in cysteine reduction, electron shuttling, and

regulation of hydrogenase activity. Despite the potential for *Hyd*A-*Hyd*C interaction, the predicted [2Fe-2S] cluster (C1) of *Hyd*C subunit is not within electron transfer distance (> 15 Å) from the main body. This implies unidentified interacting subunits or significant conformational changes during catalytic activity, which could contribute to efficient electron transfer for this enzyme.

The observed H_2 evolving activities in this study and the reported hydrogenogenic lifestyle of *Ca. P. syntrophicum*[20], suggest that Group B enzymes in Asgard archaea are unlikely to be involved in oxidizing H_2 to support anaerobic respiration or carbon fixation. However, PFE and biochemical analyses on isolated representatives are required to validate this hypothesis, as the enzymes may exhibit bidirectional activity. *Ca. P. syntrophicum* metabolizes amino acids and peptides, producing H_2 as by-product, which is then utilized by methanogenic archaea *Methanogenium* to produce methane. This symbiotic relationship affirms the hypothesis that Asgard archaea engage in "syntrophic" partnerships, which are believed to have been important in the evolutionary process that led to the rise of eukaryotes.[20]

Group F: Hybrids reveal potential structural association between [FeFe]-[NiFe] hydrogenase families

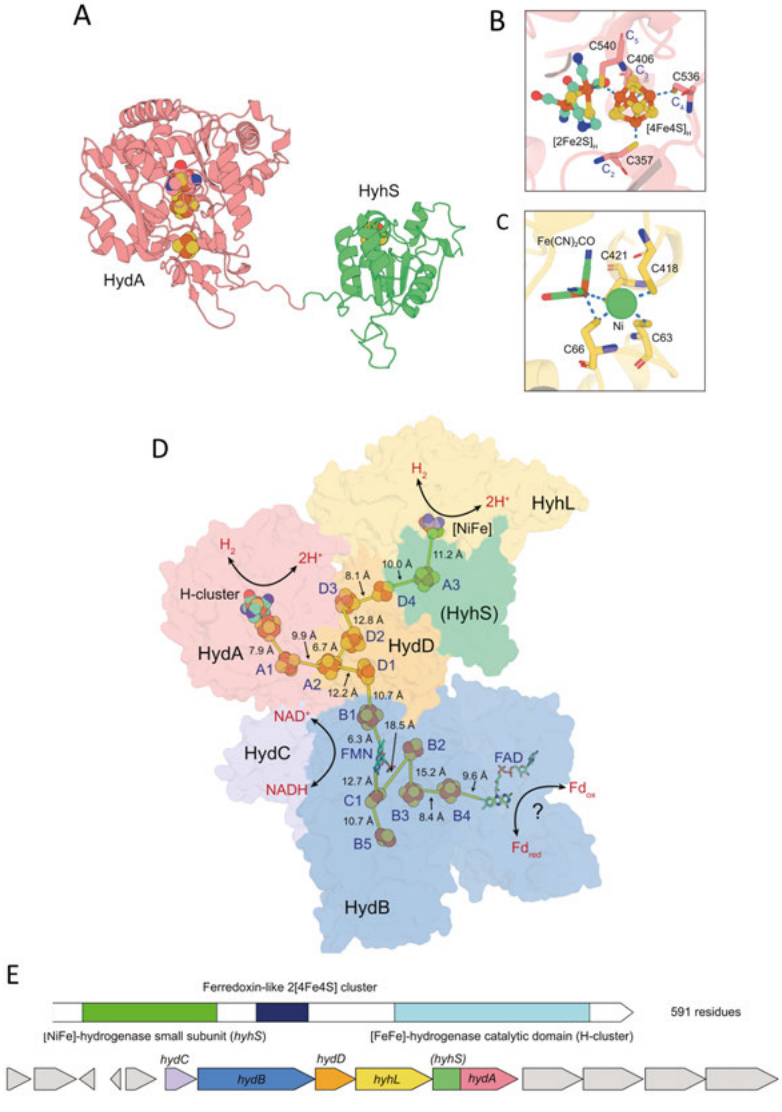

Figure 3.11. (A) *Hyd*A-*Hyh*S fusion structural model of a Group F [FeFe] hydrogenase and Group 3 [NiFe] hydrogenase in *Thermoplasmatota* (hybrid). Predicted cofactors are positioned based on the structures of homologous proteins. **(B)** Zoomed view of the H-cluster and **(C)** NiFe cofactor, emphasizing the conserved coordinating cysteine residues. **(D)** Predicted structure, cofactor composition, and electron flow through four arms in the full hybrid hydrogenase complex. FeS clusters are numbered and labelled according to their subunit of origin (*e.g.*, A1, A2, A3 originate from the *Hyd*A subunit). **(E)** Genes encoding hydrogenase structural subunits are shown in their genetic context, labelled and coloured consistent with the corresponding subunit in structural models shown in (A) and (D). *Reprinted with permission from* **Paper I**.[154]

The hybrids feature a C-terminal *Hyd*A of [FeFe] hydrogenase linked via a flexible linker to an N-terminal domain sharing homology with the small subunit of Group 3 [NiFe] hydrogenase (*Hyh*S*)* (**Fig. 3.11A-E**).

The genes contiguous with *Hyd*A-*Hyh*S include:

***Hyh*L:** The large subunit of Group 3 enzymes with the NiFe cofactor. ***Hyd*B (diaphorase) and *Hyd*C (thioredoxin):** Two subunits of the electron-bifurcating (reduction of two different acceptors by one donor) or electron-confurcating (reduction of one acceptor by two donors) Group A3 [FeFe] hydrogenase. ***Hyd*D:** Conduit subunit with four iron-sulfur clusters.

Structural modelling suggests that subunits (*Hyd*A-*Hyh*S, *Hyd*BCD, *Hyh*L) form an electron-bifurcating/confurcating complex, which is stabilized via non-covalent interactions. This complex is predicted to receive electrons from the [FeFe] or [NiFe] hydrogenase through iron-sulfur clusters to an electron-converging [4Fe-4S] cluster on the hybrid subunit, or vice versa. Electrons are then transferred simultaneously to the high-potential NAD^+ at the *Hyd*C subunit and a low-potential acceptor (*e.g.*, Fd) at the *Hyd*B subunit (**Fig. 3.11C**). The archaeal complex is distinct from the electron-bifurcating [NiFe] hydrogenase from *Acetomicrobium mobile*[194] such that the former contains the catalytic H-domain.

A single hybrid contains two seemingly redundant hydrogenase modules. While both modules possess features characteristic of hydrogenases, particularly having the conserved coordinating cysteine residues, further investigation is necessary to definitively confirm the catalytic activity of each module. The observation that the *Hyd*A-*Hyh*S fusion produces H_2 indicates the presence of at least one functional hydrogenase module. This apparent redundancy might be explained by several factors, including:

Differential regulation: Distinct regulatory mechanisms allow for metabolic control under varying environmental conditions. For instance, the two modules might possess different affinities for H_2 or exhibit varying sensitivities to O_2.

Substrate specificity: While both modules might act as hydrogenases, they could potentially utilize or react with alternative substrates in addition to H_2.[129]

Redox balancing: The complex could function as a dynamic redox valve, mediating electron flow between different electron carriers. For example, it could facilitate electron transfer from reduced NADH and Fd to an H_2-producing [FeFe] hydrogenase when reductant levels are high. Conversely, it could channel electrons from an H_2-oxidizing [NiFe] hydrogenase to oxidized NAD^+ and Fd when reductant levels are low. During bacterial growth, an electron-bifurcating [FeFe] hydrogenase (HydABC*)* functions as a redox valve, generating H_2 in response to changes in substrate availability and redox state of cellular carriers (*e.g.,* NADH and Fd).[195]

Two representatives from Group F, **Th1** and **Th2**, posed challenges for purification, hindering in-depth *in vitro* characterization. Despite substantially lower *in vitro* activities compared to *Cr*HydA1 (**Fig. 3.2B**), these enzymes

could exhibit higher activity when complexed with their respective subunits. However, achieving this would be challenging as the archaea encoding them are uncultivated and [NiFe] hydrogenases are notoriously difficult to produce heterologously. Nonetheless, the measurements from the screening assay confirm that at least one of them is biochemically capable of producing H_2.

The striking conservation in the genetic organization of Group F enzymes provides a unique model for examining the functional interaction between [FeFe] and [NiFe] hydrogenase families. Our findings diverge from the traditionally held view that these two binuclear enzymes are not structurally associated, suggesting a potential modularity within the [NiFe] hydrogenase domain that could have evolved to enable interaction with [FeFe] hydrogenases.

Enhancing our knowledge of electron transfer mechanisms and substrate range of these modules will be critical. While heterologous expression utilizing a bacterial host like *Ralstonia*, which natively expresses [NiFe] hydrogenases, presents a promising strategy for producing these hybrids, several factors favor a eukaryotic host like a protease-deficient yeast strain optimized for high-level expression. Eukaryotic systems often exhibit superior capabilities for the proper folding and assembly of complex, multi-subunit enzymes. This approach could leverage codon-optimized gene constructs to align with the yeast host's codon usage, co-expression of chaperones for large enzymes like the hybrids, and incorporate secretion signals.

Techniques like cryo-electron microscopy, coupled with site-directed mutagenesis studies, could offer deeper insights into the structural and functional dynamics of these complexes. The predicted modularity could potentially guide the design of hybrid enzymes with customizable functionalities.

Determinants of *faux* [FeFe] hydrogenases

A gene encoding a putative [FeFe] hydrogenase may not function as intended if it lacks a complete set of maturases or H-cluster binding cysteines.

Absence of maturases: The known natural maturation of [FeFe] hydrogenase requires a set of maturases (HydEFG). They are all essential for the full functionality of the H-cluster. However, a previous study has shown that Group A *Cp*I can exhibit trace levels of activity even without HydE or HydF present,[196] suggesting that partial maturation can occur with only HydG.

Out of the 130 archaeal genomes examined in this study, only five presented the entire maturase repertoire necessary for H-cluster synthesis, while a few others have an incomplete set. Despite this, the archaeal [FeFe] enzymes studied do display hydrogenase activity following heterologous production and artificial maturation. The absence of maturases cannot be attributed solely to genome incompleteness, indicating a potential deviation from the established maturase dependency in hydrogenase functionality.

The occurrence of maturase-independent activation pathways for H-cluster assembly is supported by observations of active enzymes from eukaryotic organisms lacking maturases.[197, 198] Phylogenetic analyses have implied notable phylogenetic proximity between archaeal and eukaryotic maturases[199], suggesting a possible shared mechanism or common ancestral trait between these domains of life. These new perspectives invite further exploration into how organisms can assemble functional H-clusters independent from "traditional" maturases.

Absence of a complete H-cluster binding motif: Ordinarily, for [FeFe] hydrogenases to function, they require a complete set of cysteines (C_2-C_5) for the ligation of the $[4Fe\text{-}4S]_H$ cluster. The H-domain embedding the H-cluster via four cysteines (**C**) is characterized by three highly-conserved polypeptide sequence/signature motifs (P1-TS**C**CPXW, P2-MP**C**X_2KX_2E, and P3-ExMA**C**X_2G**C**X_2G).[32]

Within archaeal groups, all four conserved H-cluster coordinating cysteines (C_2-C_5) are encoded in all tested genes (**Fig. 3.4C-E**). However, more than half of the gene sequences in Group F replaces a cysteine ($C300_{CpI}$ or $C115_{CrHydA1}$, RS-) to a structurally homologous serine residue (RO-). While a C-to-S switch has been linked to loss or rearrangement of [4Fe-4S] clusters in many instances, a few cases show retention of H-cluster integrity and activity[200], suggesting structural adaptability that preserves stability and function. Intriguingly, serine is present in the equivalent position for a minor percentage (roughly 20%) of analysed non-archaeal Group A sequences. This is despite reports showing impaired integration of the $[2Fe]_H$ subsite mimic and undetectable catalytic activities in $C115_{CrHydA1}$ loss-of-function variants (including C-to-S variations).[200] The reason behind the prevalence of serine in this position for archaeal Group F enzymes is unknown.

The capacity of archaeal genomes to encode functional hydrogenases despite the absence of complete maturases hints at yet to uncover alternative pathways in maturation. Future research efforts could also include elucidating the structural determinants that allow archaeal Group F hydrogenases, and potentially other prototypical enzymes, to maintain structural integrity and activity despite substitutions in the coordinating cysteines. This includes in-depth computational modelling, site-directed mutagenesis, kinetic and spectroscopic studies to map the adaptive capacity of these enzymes.

Conclusions and outlook

The assumptions drawn from previous literature (see introduction of this chapter) can be updated based on this study's findings, with each corresponding point being revisited:

- [FeFe] hydrogenases are active across all three domains of life, challenging the prior assumption that these enzymes were restricted in domain distribution.
- The smallest [FeFe] hydrogenases originate from (ultra-)minimalistic symbionts, providing a new size threshold for a hydrogen-handling biocatalyst.
- [FeFe] and [NiFe] hydrogenases can structurally associate, suggesting a more interconnected evolutionary history.

Collectively, these findings reshape our knowledge of microbial hydrogen metabolism and hydrogenase biochemistry. However, one key limitation is the known difficulty in culturing archaea, which has significantly restricted our capacity to carry out *in vivo* studies and verify the functional roles of hydrogenases within native hosts. These *in vivo* studies could shed light on native activity rates, especially for the slow-acting Group F hybrids.

While genome-wide metabolic analysis, modelling, biochemical and electrochemical data have helped infer potential functions, extensive in-host experiments can further validate their physiological roles and cellular interactions. Potential biases may also arise from the chosen methodologies, such as over-reliance on predictive structural modelling and extrapolation from heterologous systems. I hope that the exciting discoveries presented in this work will inspire research to develop specialized genetic and biochemical systems tailored for in-depth examination in native hosts.

Despite the absence of native *in vivo* characterization, this study provides compelling evidence that novel (ultra-)minimalistic and hybrid [FeFe] hydrogenases from archaea can bind the conserved H-cluster and demonstrate biochemical and electrochemical activities, and are therefore *bona fide* enzymes. This claim is backed by our multifaceted approach that combines genomics, phylogenetic analysis, in-depth heterologous biochemistry with semi-synthetic hydrogenase maturation, electrochemistry, spectroscopy, metabolic reconstructions, and structural modelling. This approach uncovered new enzymes and functions in uncultured microorganisms, bypassing the arduous, time-consuming, and costly process of archaeal culturing. As a result, we have gained unprecedented insights into the existence, diversity, history, structure, and role of [FeFe] hydrogenases from anaerobic archaea, laying a solid foundation for further exploration in this field.

This work also provides a foundational understanding that may inform both current and future studies into hydrogenase functionality in terms of bioengineering disciplines. The detection of smaller [FeFe] hydrogenases in (ultra-)

minimalistic symbionts may offer pathways for the production of more efficient and compact biocatalysts in the field of energy conversion and storage.

Chapter 4, Paper II: Probing the universality in substrate transport in [FeFe] hydrogenases

This chapter illustrates the nature of the substrate (proton) transfer pathway in [FeFe] hydrogenases from different phylogenetic groups. Biochemical, electrochemical, and spectroscopic studies of loss-of-function variants, targeting the putative proton transfer pathway in Group D *Tam*HydS, are outlined. The ensuing discourse will address how these variations have affected the rates, apparent bias, and stabilization of previously uncharacterized H-cluster states.

Introduction

To-date, research on substrate transport effects in [FeFe] hydrogenases has primarily focused on Group A enzymes (**Fig. 1.4**). However, recent studies have shown that the Group A enzymes hardly represent the entirety of [FeFe] hydrogenases.[71, 91, 120] While data on "sensory" Group C and D [FeFe] hydrogenases remain limited, representative examples display divergent properties from Group A.[71, 91] Firstly, Group D representative *Thermoanaerobacter mathranii* (*Tam*HydS), has sluggish H_2 evolution rates.[71] The enzyme's affinity for H_2 remains ambiguous, as prior investigations have reported inconsistent findings regarding its Michaelis' constant (K_m). [71, 123] Nonetheless, K_m is a complex parameter that combines the rates of substrate binding and catalysis, and does not directly reflect the enzyme's inherent affinity for its substrate. Secondly, *Tam*HydS despite being bidirectionally capable of catalysis, is an irreversible catalyst since it requires a significant amount of overpotential for both H_2 oxidation and proton reduction.[120] Thirdly, it exhibits enhanced tolerance towards CO inhibition. Lastly, an unusual O_2-stable and H_2-unreactive mononuclear species forms upon O_2 exposure, denoted as H_{air} (**Fig. 1.3C**).[71]

Genetic, structural, and biophysical investigations of known [FeFe] hydrogenases suggest that these enzymes share a common H-cluster motif. (**Fig. 1.1A**, **Fig 4.1A**). Hence, the varied reactivity of the enzymes must be due to changes in the surrounding protein environment (*e.g.,* active site pocket, electron and substrate transport pathways).[30, 90]

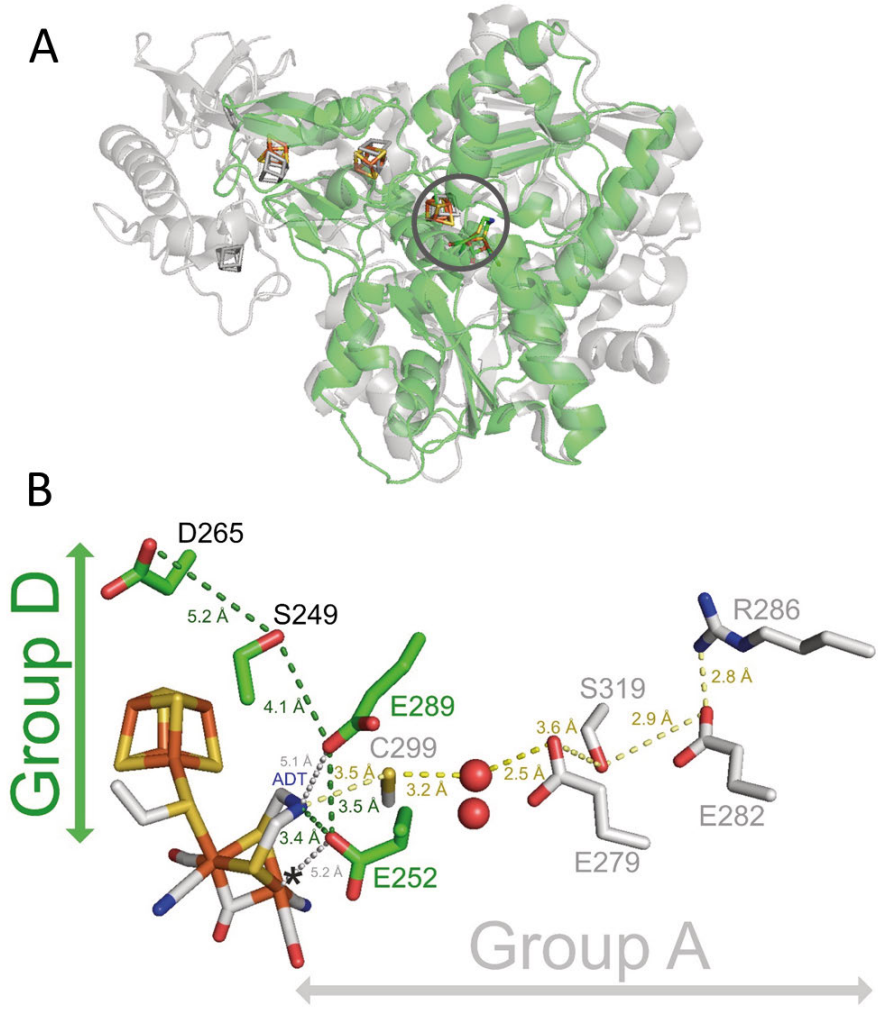

Figure 4.1 (A) Alignment of the X-ray crystal structure of Group A *Cp*I in grey (PDB ID: 4XDC)[201] versus the YASARA homology model of Group D *Tam*HydS[71] in green (RMSD = 1.541 Å). The H-cluster is encircled for emphasis. **(B)** Overview of the proposed proton transfer pathway (PTP) in *Tam*HydS (green sticks) versus the PTP of *Cp*I (grey sticks). The iron in the H-cluster is coloured in orange and the ADT-amine bridgehead in blue. The apical open coordination site at the distal iron (Fe_d) is indicated by an *. For *Cp*I, water molecules (red spheres) are present between C299 and E279. In this study, E252 and E289 are exchanged conservatively (E252D, E289D) and non-conservatively (E252V, E289A). Distance between ADT-amine and E252 as well as between the side chains that are part of the proposed PTP of *Tam*HydS are numbered (dark green). The distances between Fe_d to E252 and ADT to E289 are indicated in grey dashed lines and labels. The yellow dashed lines and numbers indicate the distances between neighbouring positions of the PTP of *Cp*I.[84] The *Tam*HydS model does not account for potential intraprotein water molecules, which if present, could help bridge the long distances between E289, S249, and D265. *Reprinted with permission from* **Paper II**.[124]

The electron-relaying accessory [4Fe-4S] clusters (F-clusters) do not appear to dictate group-specific reactivity, given the variability of FeS cluster content and location across and within phylogenetic groups. In addition to rapid electron transfer, the activity of the enzymes is dependent on efficient proton transfer via proton transfer pathways (PTPs). Alterations of the proton transfer kinetics have been shown to change the catalytic properties in Group A enzymes[77, 83, 84] and could potentially account for activity variations across groups. This chapter focuses on the influence of the PTPs, while the effects of the active site pocket will be covered in **Chapter 5**.

Extensive studies on Group A reveal that the PTP is composed of conserved amino acids and water molecules, forming a H-bond network from the enzyme surface to the ADT-amine (**Fig. 4.1B**).[77, 81, 82, 84, 85, 202-204] The first amino acid of this proposed PTP, C299 (*Cp*I numbering), is situated very close to the amine bridgehead of the ADT ligand (3.5 Å), potentially allowing for H-bonding interactions. In addition to proton transfer, $C299_{CpI}$ arguably influences the positioning of the amine base for efficient heterolytic H_2 cleavage. However, $C299_{CpI}$ is replaced into a hydrophobic alanine in "sensory" Groups C and D (Group C $A131_{TmHydS}$, Group D $A137_{TamHydS}$). Other key residues for proton transfer in Group A are also replaced mostly with non-protonatable hydrophobic side chains in these atypical groups. Since the buried H-cluster requires protons to be delivered to and from the bulk solvent to be active, this raises questions about alternative pathways and their possible influence on the overall enzyme properties, particularly in sensory enzymes.

This chapter presents the identification of a Group D PTP, marking the first alternative to the established PTP in well-characterized Group A enzymes. Two of the proposed residues are examined via site-directed mutagenesis, with mutation effects analysed through activity assays, electrochemistry, FTIR and EPR spectroscopy.

Unique and highly conserved protonatable residues in Group D

The potential PTP residues in the *Tam*HydS were identified by aligning the YASARA-generated homology model of *Tam*HydS with the crystallographic structure of the Group A representative *Cp*I[71], yielding a root mean square deviation (RMSD) of 1.541 Å. Initially, all residues within a 5 Å distance of the ADT-amine were inspected. This led to the identification of E252 as the sole candidate for proton transfer to/from the H-cluster, with a distance of 3.4 Å to the ADT-amine. Using the same screening method, the closest protonatable residue to E252 was identified as E289, followed by S249 and D265, forming a proposed PTP of E252 → E289 → S249 → D265 for *Tam*HydS (**Fig. 4.1**).

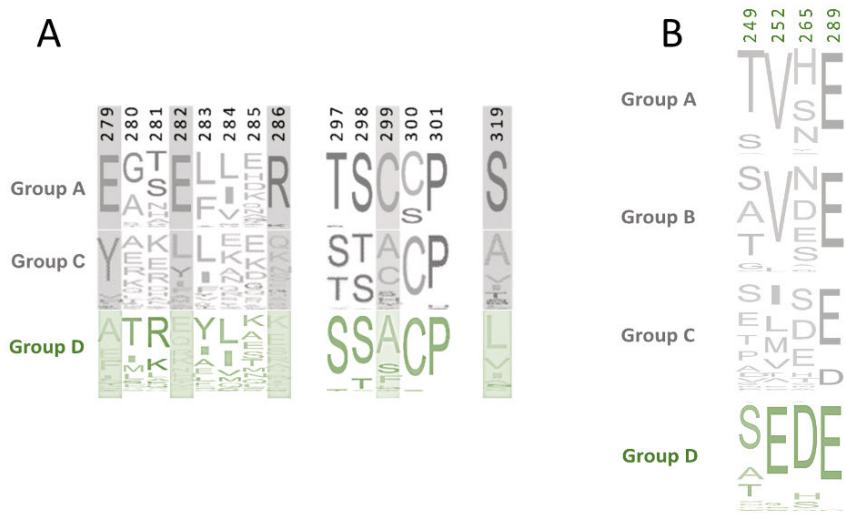

Figure 4.2. Normalized consensus logos of Groups A−D [FeFe] hydrogenase generated in Jalview using ClustalΩ sequence alignment[205] of sequences retrieved from Greening *et al.* 2016.[15] The larger the font of the amino acid, the more conserved it is in the specified sequence position. **(A)** The numbering system is based on *Cp*I, with the proposed PTP residues in Group A highlighted (C299 → E279 → S319 → E282 → R286). **(B)** The numbering system is based on Group D *Tam*HydS (proposed PTP: E252 → E289 → S249 → D265). Note that the glutamate positioned at 289 ($E289_{Tam\text{-}HydS}$) is highly conserved across all phylogenetic groups.

To support the structural analysis, the available sequences of enzymes from all groups were aligned to generate a consensus sequence, revealing varying conservation patterns between the proposed PTP residues in Group A and their corresponding residues in Group C and D (**Fig. 4.2A**). "Sensory" Group C and D exhibits a notable absence of the conserved PTP residues that are otherwise highly conserved in Group A. The alignment of multiple Group D sequences shows that the amino acids most proximal to the H-cluster, E252 and E289, are highly conserved (**Fig. 4.2B**). Similarly, the final residue of the proposed pathway (D265) is also well-conserved, while the intermediate residue (S249) is moderately conserved, showing a strong preference for residues with hydroxy groups (*i.e.*, serine and threonine). These amino acids are not conserved in Groups A, B, or C, with the exception of the glutamate at position 289 (E289). Thus, the sequence alignment analysis strongly indicates that the potential PTP identified here is exclusive for Group D [FeFe] hydrogenases.

To elucidate the role of two putative proton relay sites most proximal to the H-cluster (E252 and E289) in *Tam*HydS on H_2-processing activity rates, these residues were replaced conservatively to aspartic acid (E252D, E289D) and non-conservatively to valine or alanine (E252V, E289A) through site-directed mutagenesis. Valine was chosen for position 252 due to its presence in the same position in Group A, while alanine was selected for position 289 as a

typical loss-of-function variant. The variants were expressed in *E. coli*, purified, reconstituted, and activated with $[2Fe]^{ADT}$ to generate the *holo* variants.

Functional impairment in *holo* variants

The effects of *Tam*HydS variants E252V, E252D, E289A and E289D on the rates for reduction of proton (H_2 evolution) and oxidation of H_2 were studied in solution assays, each performed in pH 6.8 buffer and at 25°C ($E^{\circ}_{H^+/H_2}$ = −403 mV vs SHE). Methyl viologen (MV, $E^{0'}$ = −449 mV[164] vs SHE) and benzyl viologen (BV, $E^{0'}$ = −359 mV[164] vs SHE) were employed as electron donor and acceptor, respectively.

The results from the solution assays revealed that all variants negatively impacted H^+/H_2-interconversion activities relative to the wild-type *Tam*HydS (**WT**) (**Fig. 4.3**). H_2 oxidation was most severely affected, with E252V/D and E289A/D displaying less than 0.01% and up to 3% residual activities, respectively. In terms of H_2-evolution, the non-conservative (E252V) and conservative (E252D) substitutions of E252 were the least functional, with activities ranging from 10−20% relative to **WT**. The conservative exchange of E289 to a glutamate (E289D) had the least effect, retaining 70% residual activity, followed by the non-conservative exchange to an alanine (E289A) at 30% residual activity. Overall, the substitution of E252 had a greater impact in both catalytic directions, likely due to its closer proximity to the ADT-amine. Similar patterns of reduced activity have been observed in Group A hydrogenase variants with altered PTP amino acid residues.[84, 102]

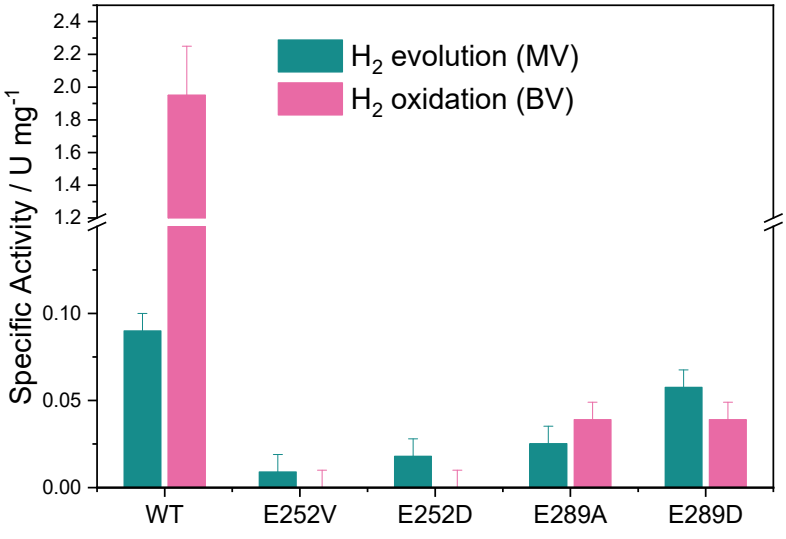

Figure 4.3 Comparison of the specific H_2 -oxidation and -evolution activities of *Tam*-HydS variants quantified using benzyl viologen (BV) and methyl viologen (MV) as external redox partners versus the wild-type *Tam*HydS enzyme (**WT**) (note the break of the Y-axis). All reactions were performed in 100 mM potassium phosphate buffer pH 6.8. H_2 oxidation (magenta bars) was measured by reducing 1 mM BV at 550 nm in H_2-saturated buffer. The amount of H_2 produced from 10 mM MV + 100 mM sodium dithionite was measured by gas chromatography (dark cyan bars).[166, 167] Specific activity (U/mg) is one unit (U) of activity that catalyze 1 µmol of H_2 oxidized/evolved per min under the indicated assay conditions over the amount of enzyme in the reaction mixture (mg). Error bars indicate standard error, with n = 6 (three technical repeats each for two biological samples). *Adapted figure with permission from* **Paper II**.[124]

Stabilization of unknown H-cluster states by *holo* variants

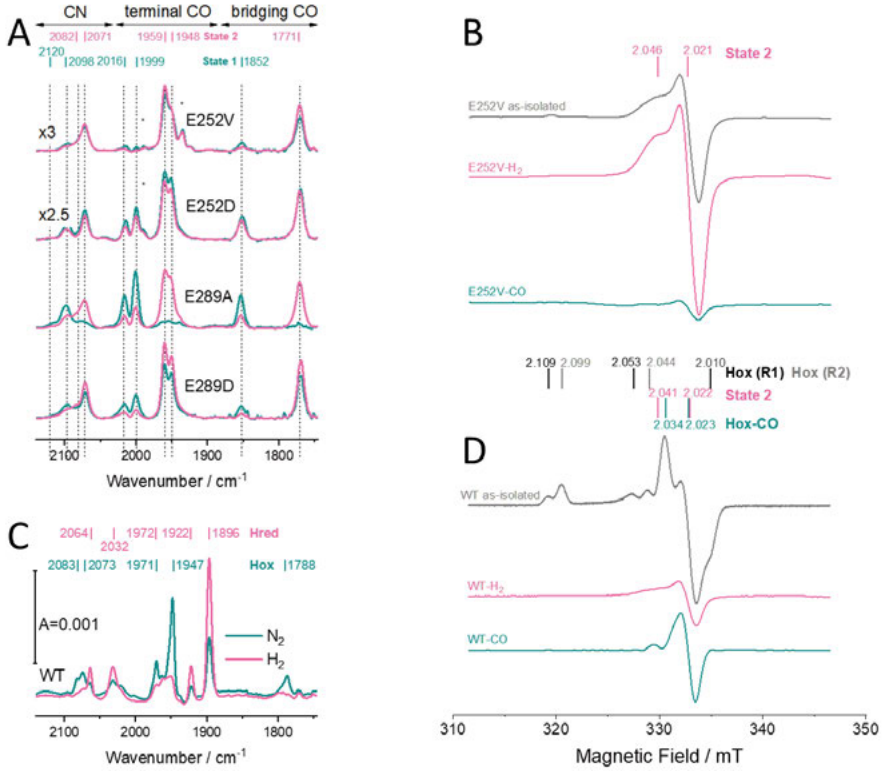

Figure 4.4 (A) FTIR spectra of *Tam*HydS variants exposed to N_2 (dark cyan) and H_2 (magenta). Two IR signatures indicative of different redox states are observed. **State 1** with bands at 2120, 2098, 2016, 1999 and 1852 cm^{-1} (indicated with dark cyan vertical bars) and **State 2** shifted to lower energies (red shifted) with bands at 2082, 2071, 1959, 1948 and 1771 cm^{-1} (indicated with magenta vertical bars). **(B)** EPR spectra of *Tam*HydS variant E252V prepared under neat argon atmosphere ("as-isolated", grey spectrum) revealed a dominant axial signal, assigned to **State 2** ($g_{\parallel}$ =2.046 and $g_{\perp}$ = 2.021), which increases after H_2-flushing (magenta spectrum) and disappears after flushing with CO (dark cyan spectrum). **(C)** FTIR spectra of *Tam*HydS **WT** exposed to N_2 (dark cyan) accumulating the oxidized state (H_{ox}) and to H_2 (magenta) accumulating the reduced state (H_{red}). **(D)** EPR spectra of *Tam*HydS **WT** (grey) reveal rhombic features of the H-cluster in the H_{ox} states (two components denoted as R1 and R2 with the corresponding g-values in black, grey respectively) and an axial feature corresponding to H_{ox}-CO (g-values in dark cyan). *Tam*HydS **WT** samples incubated under H_2 (magenta spectrum) and CO (dark cyan spectrum) shown for reference. Data adapted from Land *et al*. (2020)[71], revising the g-values assigned to H_{ox}-CO and assigning the previously unknown signal that appears when **WT** is flushed with H_2 to **State 2**. EPR spectra were recorded with the following settings: T = 21K; modulation frequency = 100 kHz; amplitude = 10 G; microwave frequency = 9.4 GHz; microwave power = 16 µW. *Adapted figures with permission from* **Paper II**.[124]

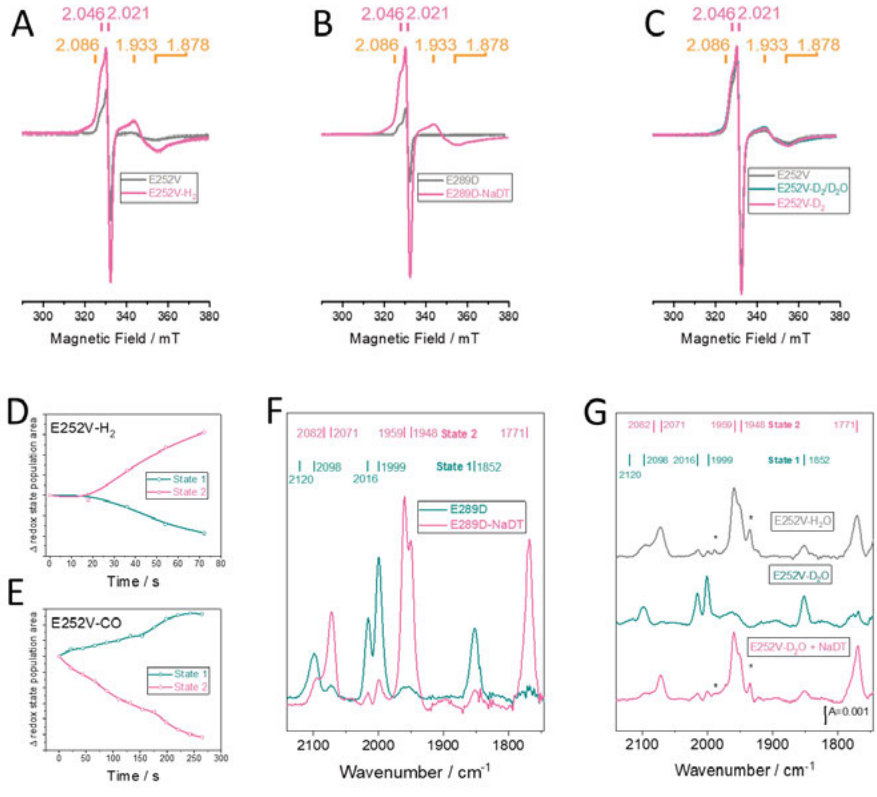

Figure 4.5 EPR spectra of variants E252V or E289D before (grey) and after **(A)** H_2-flushing (magenta), **(B)** addition of 20-fold excess of sodium dithionite (NaDT) (magenta), and **(C)** D_2-flushing with (dark cyan) and without (magenta) 95% D_2O. EPR spectra collected at 10 K, microwave power = 80 µW, modulation frequency = 100 kHz; modulation amplitude = 10 G; microwave frequency = 9.4 GHz. FTIR difference spectra and redox state kinetics of E252V exposed to **(D)** H_2 and **(E)** CO. **(F)** FTIR spectra of E289D mildly oxidised by exposure to air (dark cyan) and subsequent treatment with excess NaDT (10 mM; magenta). **(G)** FTIR spectra of E252V in H_2O (grey), in D_2O (dark cyan; **State 1** accumulated via limited exposure to air), and in D_2O in the presence of additional NaDT (magenta). Peaks of unassigned redox species are labelled with *. *Adapted figures with permission from* **Paper II**.[124]

In addition to lowering catalytic rates, altering the putative PTP impacts the accumulation of H-cluster states of *Tam*HydS. FTIR and low-temperature EPR measurements show that the variants do not accumulate any typical H-cluster states observed in [FeFe] hydrogenases (**Fig. 4.4**). *Tam*HydS **WT** stabilizes the oxidized state (H_{ox}) under a N_2 atmosphere, the reduced state (H_{red}) and unknown "State A2" under a H_2 atmosphere, and an inhibited state (H_{ox}-CO) with CO-flushing (**Fig. 4.4C-D**). These states were not discernible in the variants, except "State A2", referred to as **State 2** in this study. Another unidentified **State 1** is also stabilized. A summary of the spectroscopic features

of **States 1** and **2** under various treatments—isolation under N_2, reduction by H_2 or NaDT, exposure to CO, and D_2/D_2O—is presented here:

Nonconservative versus conservative exchanges: "As-isolated" nonconservative variants, E252V and E289A, appeared to stabilize one state over the other (**Fig 4.4A**). E252V predominantly yielded **State 2**, while E289A was largely in **State 1**. However, conservative exchanges, E252D and E289D, showed a mixture of **State 1** and **State 2**. As-isolated *Tam*HydS **WT**, on the other hand, typically favours formation of H_{red} and H_{ox} (**Fig 4.4C**).

Reducing State 1 to State 2 by H_2 and NaDT: Reduction by H_2 atmosphere led to a clear shift towards **State 2** in in at least three of the variants (E289A/D and E252V), with the more pronounced conversion observed in the more active E289 variants (**Fig. 4.4A-B**). The E252 variants showed only minor (E252V) or no (E252D) shift of the redox state equilibrium towards **State 2**. This correlates with the observed H_2 oxidation activity rates, where the E289 variants displays partial activity, while the E252 variants led to even lower residual activity (**Fig. 4.3**). Reduction using NaDT also causes an accumulation of **State 2**, a change that was clearly discernible in NaDT-treated EPR samples of as-isolated E289D (**Fig. 4.5B, F-G**). This behaviour diverges from the reactivity of the H_{ox} state, which usually converts to H_{red} under H_2 (**Fig 4.4C**). Notably, EPR analysis indicates that **WT** transitions to **State 2** with H_2, but this transition is not obvious when **WT** is reduced with NaDT.[71]

Slow State 2 to State 1 conversion induced by CO: None of the variants bind external CO to form the inhibited H_{ox}-CO state (**Fig 4.4**). Instead, exposure to CO led to a slow conversion from **State 2** to **State 1** (**Fig 4.4B**, **Fig. 4.5E**). This behaviour differs from the reactivity of the H_{ox} state, which typically accumulates H_{ox}-CO (**Fig. 4.4D**). EPR data suggests that **State 1** is distinct from the H_{ox}-CO state, as H_{ox}-CO is typically observed as an EPR-active species with a typical axial spectroscopic signature, while **State 1** is EPR-silent.

Lack of isotopic shift induced by D_2/D_2O, ruling out hydride binding: In Group A, alterations in the PTP close to the H-cluster (*e.g.*, $C299_{CpI}$), enable the build-up of H_{hyd} under H_2 atmosphere.[102, 105] Subsequent studies have shown that H_{hyd}, accumulates also in wild-type Group A enzymes, strongly supporting its catalytic relevance.[102, 103, 106, 206] However, H/D exchange experiments in this study revealed no specific shifts of cofactor ligand bands for **State 1** nor **State 2** that potentially rule out (terminal) hydride binding (**Fig. 4.5C**). Fitting the FTIR band positions of the CO ligands for E252V samples in H_2O and in D_2O revealed that the bands of **State 1** and **State 2** exhibit only minor shifts (max. 1.5 cm^{-1}) upon exchange (**Fig. 4.5G**).

Lack of external sulfur inhibitor (exogenous) or nearby cysteine thiol (endogenous), ruling out sulfide binding: The *holo* variants were prepared without the use of external sulfide sources, which are known to exogenously bind to Fe_d and form the H_{inact} state.[118] Furthermore, the absence of cysteine

residues near the Fe_d negates the possibility of endogenous cysteine thiol binding.[190] Therefore, thiol coordination in **State 1** and **State 2** can be ruled out.

Proposed assignments of the unknown H-cluster states

Having established the observed reactivity of **State 1** and **State 2**, and that they are unlikely to be equivalent to H_{hyd} (hydride-bound) or H_{inact} (sulfide-bound), the following discussions look into their probable identities.

State 1: The EPR-silent nature of **State 1** implies it may represent the H_{red} state. However, the finding that **State 1** does not emerge under reducing conditions or is transformed into **State 2** under such conditions suggests it is unlikely to be the reduced H_{red} state. Instead, **State 1** is proposed to be another EPR-silent, "over-oxidized" di-ferrous species yielding an oxidation state analogous to the previously reported inhibited "over-oxidized" H_{inact} state (*i.e.* $[4Fe\text{-}4S]^{2+}$-$[Fe^{II}Fe^{II}]$).[74, 99, 118, 119, 191, 192, 207] However, the ligation of the $[2Fe]_H$ subsite likely differs, with **State 1** proposed to be ligated by an aqua (or hydroxide) ligand instead, similar to earlier H_{inact} state models[99, 208, 209] (**Fig. 4.6**).

Structural support for the notion of aqua ligation to the H-cluster has been reported. X-ray crystallographic studies of *Cp*I revealed that the distance between the oxygen atom of a water molecule (referred to as the "distal water") and the distal iron is 2.38 Å.[210] Despite the distal water oxygen-distal iron distance being slightly longer than the anticipated Fe^{II}-O distance (2.095 Å to 2.13 Å), the bond length of Fe-O can be influenced by secondary coordination sphere effects. A previous study has shown that the bond length in Fe^{III}-OH complexes can be elongated by the presence of intramolecular hydrogen bonds. [211, 212]

From the reasoning above, **State 1** could represent a (reversibly) inhibited H-cluster state with no catalytic relevance for H_2 turnover. To enter the catalytic cycle, the proposed bound aqua or hydroxide ligand must dissociate from Fe_d to leave an OCS.

State 2: The red-shift observed by FTIR spectroscopy indicates that **State 2** reflects a reduced state relative to **State 1**. Given the axial and relatively narrow nature of **State 2** signal in the EPR spectrum (**Fig. 4.4B**), the unpaired electron likely resides on $[2Fe]_H$ rather than $[4Fe\text{-}4S]_H$, as the latter usually displays broader rhombic signals in its reduced state (**Fig. 5.4A-C**).[30, 71]

Additionally, a striking similarity between the CO/CN bands of **State 2** and those of the H_{ox} state of **WT** is observed (**Fig. 4.4A,C**), implying they might be of the same oxidation state. Based on these observations, **State 2** is tentatively assigned to a formal oxidation state analogous to that of H_{ox} (*i.e.*, $[4Fe\text{-}4S]^{2+}$-$[Fe^{I}Fe^{II}]$), due to the red-shift observed in FTIR spectroscopy relative to

State 1 (shift of μCO ligand by 81 cm^{-1} in particular) and an overall similar FTIR band pattern with H_{ox}.

However, **State 2** being distinct from the "classical" H_{ox} is reinforced by the following observations:

- **State 2** exhibits an axial EPR shape while H_{ox} generally gives rise to a rhombic signal (**Tab. 4.1**), as also reported previously in the case of **WT**.[71]
- Combined FTIR and EPR spectroscopic data implies a variation in H-bonding strength of the CN ligands, cofactor geometry, and/or an altered electronic structure compared to the "classical" H_{ox}.[58]
- **WT** exhibits both "classical" H_{ox} and **State 2**. While both are proposed to possess the same oxidation state, their accumulation under distinct conditions suggests additional factors have influence on their relative stabilities. H_{ox} accumulates under inert atmosphere or oxidizing conditions, whereas **State 2**, despite its putative oxidized nature, accumulates under H_2 or reducing conditions.[71] The identity of the H_2-induced species in **WT** (denoted A2, $g_{\parallel}$ =2.041 and $g^{\perp}$ = 2.022)[71] is most likely analogous to **State 2**. This suggests that factors beyond the H-cluster oxidation state, such as redox state of the F-clusters, or conformational changes, might contribute to the preferential stabilization of **State 2** under reducing conditions.

Establishing them as separate H-cluster states, however, is not fully conclusive, as similar states can display distinct EPR spectra. Unique EPR properties of H_{ox} or H_{ox}-CO related states has been observed in Group A *C. beijerinkii* (*Cb*HydA1) (**Tab. 4.1**).[213] Two distinct EPR signals were detected for the H_{ox} states, contrasted by a single set of observable FTIR bands. This discrepancy might arise from the localized nature of EPR sensitivity, which primarily probes the immediate environment of the $[4Fe\text{-}4S]_H$ cluster. The observed spectral heterogeneity in the EPR data is believed to be due to the structural flexibility of the "SCCP" loop. This flexibility might allow for dynamic reorganization of $C367_{CbHydA1}$ (equivalent to $C299_{CpI}$), and consequently influence the electronic environment of the $[4Fe\text{-}4S]_H$. Another instance is from Group A enzyme from *M. elsdenii* (*Me*HydA) (**Tab. 4.1**).[79] The H_{ox}-CO of wild-type *Me*HydA is more isotropic than its truncated version, *Me*H-HydA, which lacks the N-terminal F-domain.

Despite divergent spectroscopic fingerprints and reactivities suggesting that **State 2** is distinct from H_{ox} and other known H-cluster states, pinpointing an exact assignment remains challenging. Nonetheless, given its reactivity with reductants (accumulating under H_2), **State 2** is proposed to be a state of catalytic relevance and could represent a form of the H-cluster residing in "non-classical" H_{ox} oxidation state, and potentially coupled to a reduced F-cluster.

Group & Subclass	[FeFe] hydrogenase	Species	g-values			Refer-ence
			g_1	g_2	g_3	
A-M1	*Cr*HydA1	H_{ox}	2.100-2.101	2.037-2.039	1.996-1.998	104, 214, 215
		H_{ox}-CO	2.052	2.007	2.007	215
		H_{sred}	2.145	1.860	1.860	216
		H_{hyd}	2.069-2.080	1.935-1.938	1.870-1.880	104, 105, 206, 216
		$H_{hyd}H^+$	2.073	1.935	1.881	217
A-M2c	*Cb*HydA1	H_{ox} (1)	2.098	2.037	1.997	213
		H_{ox} (2)	2.099	2.041	1.999	213
		H_{ox}-CO (1)	2.021	2.010	2.006	213
		H_{ox}-CO (2)	2.063	2.006	2.002	213
A-M2(D)	*Dd*H	H_{ox}	2.100	2.040	1.998	207
		H_{ox}-CO	2.065	2.007	2.001	207
		H_{trans}	2.060	1.960	1.890	207
A-M3	*Cp*I	H_{ox}	2.097	2.039	1.999	218
		H_{ox}-CO	2.072	2.006	2.006	218
A-M2	*Me*HydA	H_{ox}	2.093	2.041	1.999	79
		H_{ox}-CO	2.061	2.007	2.002	79
	*Me*H-HydA variant	H_{ox}	2.090	2.033	1.996	79
		H_{ox}-CO	2.020	2.009	2.008	79
C-M2f	*Tm*HydS	H_{ox}	2.113	2.045	2.001	91
		H_{ox}-CO	2.047	2.018	2.007	91
D-M2e	*Tam*HydS	H_{ox}-R1	2.109	2.053	2.010	71, 124
		H_{ox}-R2	2.099	2.044	2.010	71, 124
		H_{ox}-CO*	2.034	2.023	2.023	124
		State 2*	2.041	2.022	2.022	71, 124
	*Tam*HydS E252V / E289D variants	State 2	2.046	2.023	2.020	124
	*Tam*HydS AS variant	H_{ox}-R2	2.109	2.048	2.011	**Paper III**
		H_{ox}-CO	2.030	2.022	2.017	**Paper III**
	*Tam*HydS PTP variant	H_{ox}-R1	2.100	2.050	2.012	**Paper III**
		H_{ox}-R2	2.109	2.034	2.008	**Paper III**
		H_{ox}-CO	2.038	2.023	2.018	**Paper III**
	*Tam*HydS CM variant	H_{ox}-R1	2.101	2.051	2.005	**Paper III**
		H_{ox}-R2	2.109	2.035	2.009	**Paper III**
		H_{ox}-CO	2.038	2.023	2.017	**Paper III**
		State 2	2.050	2.022	2.019	**Paper III**

Table 4.1 Tabulated g-values of selected states reported for the H-cluster in Group A−D enzymes and variants. The g-values of the *Tam*HydS variants, E252V and E289A, studied in this work (**Chapter 4, Paper II**) as well as variants **AS**, **PTP**, and **CM**, presented in **Chapter 5, Paper III** are also included. The asterisk (*) indicates correction of assigned species to the previously reported g-values based on the results of this study. The State A2 (assigned as H_{ox}-CO) in Land et al., 2020[71] likely corresponds to **State 2** of E252V and E289D variants.

Structural changes that affect FLP interaction

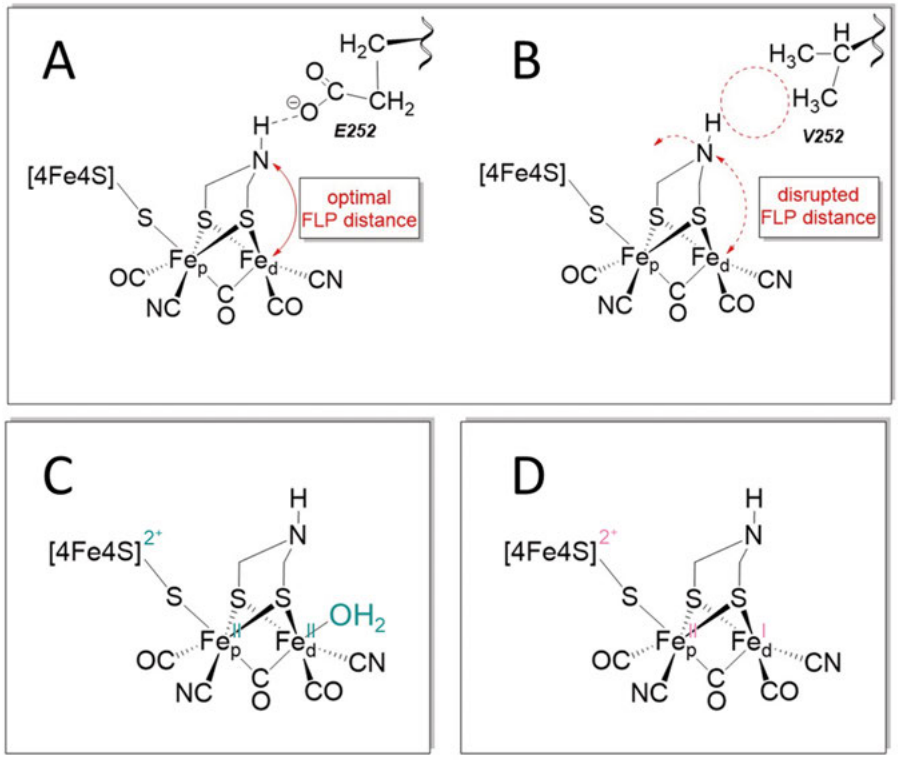

Figure 4.6 Proposed models illustrating the structural changes at the H-cluster by the PTP variants. **(A)** Schematic model illustrating an optimal Frustrated Lewis Pair (FLP) interaction between the ADT-amine and Fe_d of the H-cluster. The E252$_{TamHydS}$ likely fine-tunes the positioning of the ADT-amine, either through direct H-bonding or indirectly via intermediate water molecules, thus ensuring an optimal FLP distance from Fe_d for heterolytic H_2 cleavage. **(B)** The absence of H-bonding provided by the carboxylate side chain upon exchange of E252 to V252, shifts the ADT-amine towards a relatively farther distance from Fe_d, releasing cofactor strain and consequently elongates the FLP distance. **(C)** A reduced steric hindrance, due to a relaxed FLP geometry as illustrated in (B), could facilitate the binding of exogenous ligands to Fe_d, thereby easing the formation of inhibited states. The binding of an aqua (or hydroxide) ligand is proposed for **State 1**. **(D)** Upon dissociation of the proposed ligand, it leaves an OCS forming **State 2**, which is tentatively assigned with a formal oxidation state analogous to that of H_{ox}. *Adapted figure with permission from* **Paper II**.[124]

The reduced catalytic rates and altered electronic properties of the H-cluster in the variants support a substantial influence of the varied residues. Variations of the PTP studied here is also proposed to induce a structural change at the H-cluster, disrupting the frustrated Lewis pair (FLP) interaction between the ADT-amine and Fe_d (**Fig. 4.6A-B**). Particularly, the E252 (3.4 Å from ADT-amine, **Fig. 4.1B**) likely orients the ADT-amine for optimal distance from the Fe_d for efficient H_2 cleavage or formation. The distance observed in the

structural model slightly exceeds the typical range for a conventional H-bond, suggesting the presence of other electrostatic interactions that could help stabilize this contact. Removing this carboxylate (E252V), or shortening the residue (E252D), relieves the geometric strain or weakens the H-bond with ADT-amine, leading to a relaxed FLP in a less active conformation. Similarly, variations of the second target residue, E289, can affect the positioning of the ADT-amine, most likely through H-bond interactions with E252 (3.5 Å from E289, **Fig. 4.1B**).

In Group A, structural effects are observed in analysing crystallographic data on *Cp*I variants, with the C299A$_{CpI}$ and C299D$_{CpI}$ slightly reducing the Fe_d and ADT-amine distance by 0.3–0.4 Å (**Tab. 4.2**).

PDB ID	Resolution (Å)	*Cp*I	Fe_d-ADT Å (Chain A)	Fe_d-ADT Å (Chain B)
4XDC	1.63	WT	3.4	3.4
6GLY	2.09	C299A	3.1	3.0
6GLZ	2.02	C229D	3.1	3.1
5LA3	2.29	E279A	3.2	3.2
6YF4	1.77	E279D	3.3	3.3
6GM0	2.11	E279Q	3.3	3.1
6GM4	1.97	S319A	3.4	3.4
6GM1	2.05	E282A	3.3	3.3
6GM2	2.76	E282D	3.4	3.0
6GM8	1.96	E282Q	3.2	3.2
6GM3	2.22	R286A	3.3	3.3

Table 4.2 Distances (in Å) between the distal iron (Fe_d) and ADT-amine across wild-type *Cp*I and variant structures.

When the C178A$_{DdH}$ (corresponding to C299$_{CpI}$) was varied to an alanine, enhanced exogenous cyanide ligand binding to the OCS was observed.[219] Initially, the increased ligand binding was linked to a reduced electron density at $[2Fe]_H$, but a lowered steric hindrance could also be applicable. A less obstructed OCS by the *Tam*HydS variants provides a more accessible binding site, potentially easing **State 1** formation. In the absence of potential inhibitors, the primary candidate for the incoming ligand is H_2O. A relaxed FLP could simplify the binding of a H_2O molecule to the OCS, resulting in the "over-oxidized" **State 1** (**Fig. 4.6C**), while the removal of the bound aqua ligand results in **State 2** (**Fig. 4.6D**). The confirmation of this hypothesis is dependent on future crystallographic studies.

Apparent bias changes

While the quantification of catalytic bias is not uniform in literature, the solution assays reveal a shift in apparent bias towards H_2 evolution in all the variants. Interestingly, the finding that the E289D, located over 5 Å from the H-cluster, exhibits this notable apparent bias shift, suggests the presence of a "remote controller" that can modulate the bias through distal mutations.

The observed shift seems to result from the disproportionate effect on the rates of H_2 oxidation and H_2 evolution. While both processes are impacted, the effect is more pronounced for H_2 oxidation, which is inherently faster in **WT**. This observation, however, contrasts with the **WT** CV data at nearly identical pH, which indicates a bias towards proton reduction especially at higher driving force (≥200 mV).[71] This discrepancy likely stems from the limitations of the solution assays, which is estimated to employ a weaker driving force. Accurately determining the solution potential in these assays, however, is challenging due to the difficulty in precisely measuring the ratio of oxidized/reduced MV. The solution assays may not fully represent the catalytic behavior observed at the higher driving forces achieved in CV experiments.

Various factors have been identified as influencing bias in [FeFe] hydrogenases. This summary outlines potential and non-potential contributors to the apparent bias shift exhibited by the variants in this study:

Changes in the redox potential of the H-cluster[200, 220], and the F-clusters regulating intramolecular ET rates[78, 79, 221, 222] have been implicated in bias shifts. For instance, substituting a cysteine ligand ($C499_{CpI}$ or $C362_{CrHydA1}$) of $[4Fe\text{-}4S]_H$ with histidine and aspartate favoured H_2 oxidation, owing to an increase in the H-cluster's reduction potential.[200, 220] Moreover, F-clusters with higher and lower potentials accelerate H_2 oxidation and proton reduction, respectively. While the study did not directly target F-clusters or the $[4Fe\text{-}4S]_H$, it is possible that the *Tam*HydS variants indirectly alter the reduction potential, contributing to the observed apparent bias shift.

Changes in relative acidity (*p*Ka) of the proton relay sidechain and ADT-amine.[84, 223] A shift in bias towards H_2 oxidation and proton reduction occurs when $C299_{CpI}$ was mutated to $C299S_{CpI}$ and more acidic $C299D_{CpI}$ residues, respectively.[84, 223] However, the comparison between the E252D and E252V variants suggests that the *p*Ka of the proton relay may not be the sole determinant of this bias shift. Despite the inability of E252V to deprotonate, both variants exhibit comparable bias shifts.

The given existing models exhibit limitations in fully elucidating these reactivity trends, indicating the potential influence of other factors on the observed shift in bias. It is conceivable that the disruption of the ADT-amine geometry, which impairs proton transport, may function as a "bias controller." The proposed elongation or more relaxed FLP interaction, due to weaker H-bonding (E252D) or reduced steric hindrance and loss of H-bonding partner (E252V), could ease H_2 binding but could impede proton transfer ensuing H_2

bond cleavage. However, this raises an intriguing question: if the ADT-amine and Fe_d are not optimally positioned, how does H_2 cleavage occur? One possibility is that some level of protein flexibility and conformational changes allow the ADT-amine and Fe_d to transiently adopt catalytically competent positions, even if their average positions appear suboptimal. Further studies investigating the dynamic behavior of these residues in the context of these variations are necessary to confirm this hypothesis and fully elucidate the impact of ADT-amine geometry on apparent bias changes.

Other metalloenzymes with non-conserved PTPs

Metalloenzymes such as O_2-processing heme–copper oxidases (HCuO) and [NiFe] hydrogenases display variations in proton transfer pathways across phylogenetic groups. The HCuO superfamily exemplifies this diversity, with observed variations correlating with differences in biochemical properties such as O_2-affinity and proton pumping stoichiometry.[224] While studies of the [FeFe] hydrogenase groups remain limited, a wider variety of [NiFe] hydrogenases have been studied. However, the PTPs for [NiFe] hydrogenases are not clearly defined, with four proposed models under consideration.[37, 225-227]

In characterized [NiFe] hydrogenases, the directionality of proton movement is governed by the reorganization of the H-bond network around the Ni-Fe cofactor, $C546_{DvMF}$, $E34_{DvMF}$, and a water molecule (numbering based on catalytic Group 1a *D. vulgaris miyazaki*). The cysteine ligand ($C546_{DvMF}$) of Ni is recognized as the primary site for proton uptake following H_2 bond cleavage. For most proposed models, protons are believed to transit to an adjacent, highly conserved glutamate ($E34_{DvMF}$)[65], as supported by impaired function in site-directed mutagenesis variants. This glutamate is also conserved in sensory Group 2b enzyme from *R. eutropha / C. necator*.[228] While this points to a possible shared PTP across [NiFe] hydrogenase phylogenetic groups, the pathway involving $E34_{DvMF}$ as a proton relay to $C546_{DvMF}$ is contentious.

Alternative models propose roles for other amino acids, such as an arginine ($R355_{PfSH-1}$, equivalent to $R479_{DvMF}$). Variations of this arginine altered the ligand binding environment at the Ni-Fe cofactor, destabilized a hydride-bound state, and resulted in a tautomeric equilibrium between the hydride-bound and singly protonated NiFe cofactor states.[229]

As there is currently no definitive consensus on a single PTP, the question remains as to whether the route of proton transfer is universal across [NiFe] hydrogenase groups.

Evolution's rationale for modulating enzyme reactivity

The (non-)conservation of certain enzymatic principles by evolution can be linked to multiple factors such as functional diversification or optimization[184, 185], environmental adaptation for microbial survival[186], or random genetic variability[187]. Differences in substrate transport systems across [FeFe] hydrogenase groups can be rationalized by the prioritization of enzyme functions beyond their primary roles as H_2 activators.

Catalytic enzymes are likely engineered to maximize catalytic rates, aided by faster substrate transport. Conversely, sensory enzymes could have evolved to prioritize precise environmental sensing, often at the expense of substrate transport speed and, subsequently, catalytic rates. An unresolved aspect, however, is the divergent PTP between Group D *Tam*HydS and its close relative, Group C *Tm*HydS, both considered "sensory" groups. Sequence analysis indicates the coexistence of these sensory groups in roughly 25% of analyzed organisms, including *T. mathranii*.[15] These enzymes might detect varying H_2 concentrations or elicit distinct cellular responses, conferring advantage in fluctuating conditions that require metabolic adaptation. The presence of multiple isozymes within certain organisms, either from Group C or D, supports the idea that a range of sensory [FeFe] hydrogenases enhances adaptability.

Conversely, evolution preserves certain principles of enzyme catalysis that underpin fundamental function or stability. The intrinsic reactivity of the shared H-cluster likely enables analogous or even identical catalytic cycles across [FeFe] hydrogenase groups. This allows the different enzymes to employ the same cofactor for the essential task of H_2 activation, yet adapt to various physiological contexts by modulating the H-cluster's distinct states.

The exact reasons behind evolution's (non-)conservation of certain principles over others can be complex and context-specific. Initial insights from these studies suggest that the success of microorganisms expressing [FeFe] hydrogenases can be associated with a seemingly dual strategy: varying outer coordination spheres (*e.g.,* PTPs) while upholding the integrity of the H-cluster. These microorganisms adeptly balance adaptive flexibility and conservation of fundamental function amidst evolutionary pressures.

Conclusion and outlook

This study provides insights on the relationship between substrate (proton) transfer pathway and catalysis in Group D [FeFe] hydrogenase, highlighting the significant influence of the second and outer coordination spheres in controlling overall enzyme performance.

A putative PTP within atypical Group D is proposed—the first alternative from the previously established PTP observed in prototypical Group A enzymes. (Non-)conservative variations to the proposed proton relay sites closest to the ADT-amine, targeting E252 and E289, significantly reduced catalytic rates, strongly suggesting that they are involved in substrate transfer. All variants shifted the apparent catalytic bias towards proton reduction. The more proximal E252 variants could have direct effects, while the more distal E289 variants, situated outside the immediate vicinity of the H-cluster, may employ a "remote control" mechanism to influence apparent bias shifts.

Spectroscopy studies revealed that all variants stabilized previously uncharacterized H-cluster states, at least one of which represents a possible intermediate with catalytic relevance. This demonstrates the tight coupling between structural perturbations in the proposed PTP and geometric/electronic changes within the H-cluster, indicating that the impact of the variations on structure and catalysis is not isolated.

The uniqueness of the proposed PTP for Group D enzymes suggests an evolutionary strategy for fine-tuning enzyme function, where each phylogenetic group evolves distinct PTPs. These insights not only deepen our understanding of hydrogenase biochemistry and evolution, but also offer principles for the design of bio-mimics. By revealing key structural and electronic prerequisites for optimizing catalytic rate and bias, these findings can guide the development of bio-mimics that effectively couple proton-transfer and redox chemistry.

Future studies are needed to examine the roles of additional amino acids (S249 and D265), clarify local structural and electronic changes, and insights from high-resolution structural analyses. Broadening the comparative analyses to include a wider range of groups could help determine whether PTP conservation or diversity dictates enzymatic function. Such efforts may help in overcoming current limitations in bio-mimetic design and in advancing our understanding of proton transfer in biological systems.

Chapter 5, Paper III: Optimization of a [FeFe] Hydrogenase through rational design

This chapter presents a rational enzyme engineering strategy aimed at enhancing the catalytic performance of slow-acting Group D *Tam*HydS, by leveraging the design principles of fast-acting Group A *Cp*I. It outlines the biochemical, electrochemical, and spectroscopic investigations of gain-of-function variants that mimic the active site pocket and proton transfer pathway of Group A enzymes. The discussion will cover proposed key determinants of catalytic performance from both a catalytic rate and inhibitor tolerance standpoint. The chapter culminates by underscoring the implications of these insights for the design of bio-inspired catalysts that incorporate second and outer coordination spheres.

Introduction

While **Chapter 4** hinted at the role of substrate transfer in the unique attributes of Group D representative *Tam*HydS, this chapter further examines the hypothesis that the divergence between Group A and D enzymes largely stems not just from variations in outer coordination sphere (substrate transport pathway) but also in the second coordination sphere (active site environment).

For Group A enzymes (*e.g.*, *Cr*HydA1 and *Cp*I), second coordination sphere methionine residues M497$_{CpI}$ and M353$_{CpI}$ are proposed to be crucial for modulating the reactivity and regulating the H_2 affinity of the H-cluster.[75, 96] In *Tam*HydS, these residues are replaced by leucine (L291$_{TamHydS}$) and serine (S191$_{TamHydS}$), respectively (**Fig. 5.1**). Moreover, a key relay point for the proton transfer pathway in Group A[85], C299$_{CpI}$, is substituted by alanine in *Tam*HydS (A137$_{TamHydS}$). This alteration is noteworthy, as the corresponding cysteine-to-alanine variants in Group A enzymes (C169A$_{CrHydA1}$[102, 230], C299A$_{CpI}$[84], and C298A$_{CaHydA1}$[89]) exhibit a drastic reduction in H_2 turnover, highlighting the cysteine's crucial role in catalysis.[81] As outlined in **Chapter 4**, all residues central to proton transfer in Group A[82, 83, 85], are replaced in *Tam*HydS, with the exception of a glutamate (E122$_{TamHydS}$, E282$_{CpI}$) (**Fig. 4.2**).

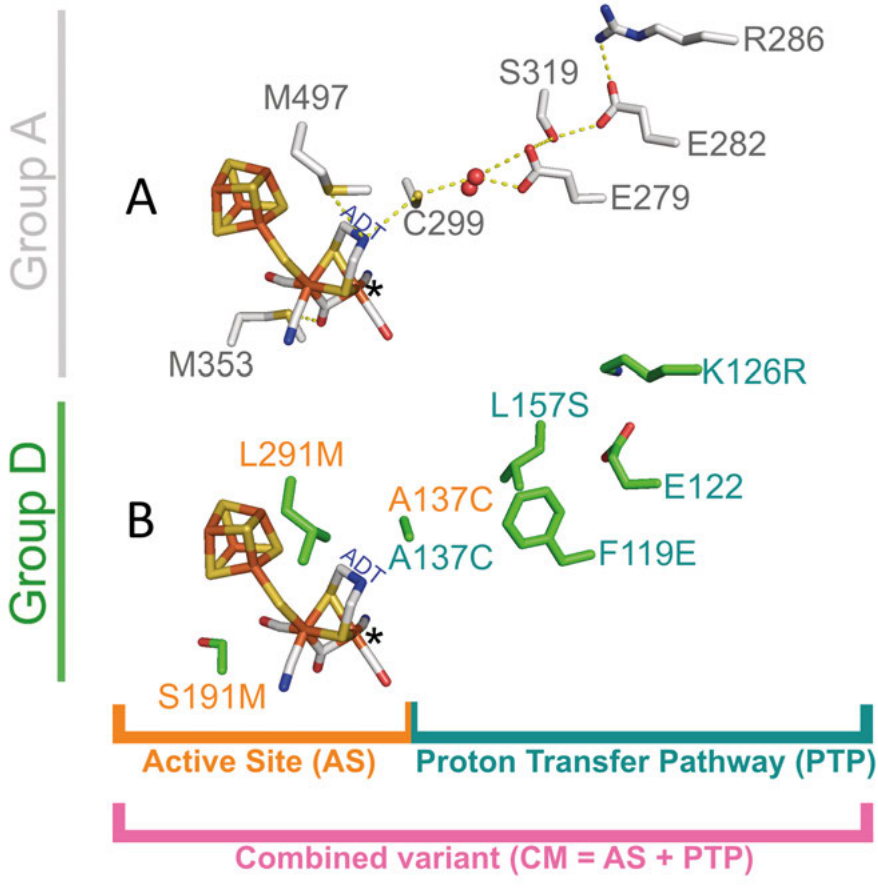

Figure 5.1 (A) Atoms are color-coded: C: grey, O: red, N: blue, Fe: orange, S: yellow. Group A's proton transfer pathway is proposed to include C299, E279, S319, E282, and R286. Sulfur-rich residues C299, M353, and M497 interact with the H-cluster through H-bonding and other electrostatic interactions. The Fe_d is indicated with an asterisk (*), while the ADT ligand is highlighted in blue text. **(B)** The corresponding residues in Group D *Tam*HydS (C: green). Four variants were investigated: "active site" (**AS**) with substitutions A137C, L291M, and S191M (orange labels); "proton-transfer pathway" (**PTP**) with substitutions A137C, F119E, L157S, and K126R (dark cyan labels); "combination" of **AS** and **PTP** variations (**CM**); and a sole-variant **A137C**. The $E122_{TamHydS}$ was not altered as the analogous glutamate is conserved in *Cp*I ($E282_{CpI}$).

This study aims to discern the impact of the active site environment and substrate transport pathway on H-cluster reactivity, both separately and collectively. While previous studies have provided insights through loss-of-function approaches, this study originally tackles the challenge through gain-of-function strategies. By borrowing from the design principles of the more catalytically active Group A hydrogenases and implementing them into the less active

Group D *Tam*HydS, a potential enhancement in the latter's catalytic performance is hypothesized.

To test this hypothesis, three *Tam*HydS variants were isolated, each constructed to mimic the expected central features of Group A hydrogenases, specifically pertaining to the active site (**AS**) or proton transfer pathway (**PTP**), as well as a combination of both (**CM** = **AS** + **PTP**) (**Fig. 5.1**). A fourth variant, **A137C** (equivalent to $C299_{CpI}$), was characterized as a reference, featuring a common mutation among all three aforesaid variants.

This chapter summarizes the examination of these engineered variants through spectroscopic, biochemical, and electrochemical studies, discerning factors from the second and outer coordination spheres that impact reaction rates, efficiency, and tolerance towards gaseous inhibitors (*i.e.,* O_2 and CO).

The **A137C**, **AS**, **PTP**, and **CM** variants were generated based on a structural and genetic sequence comparison between *Tam*HydS and *Cp*I (**Fig. 5.1**).[201] The **AS** triple variant introduces two methionine residues (S191M and L291M) along with the proton relay cysteine (A137C). The **PTP** quadruple variant combines the A137C with three additional changes: F119E, K126R, and L157S, to mimic Group A's proton transfer pathway. The **CM** sextuple variant encompasses all aforementioned mutations.

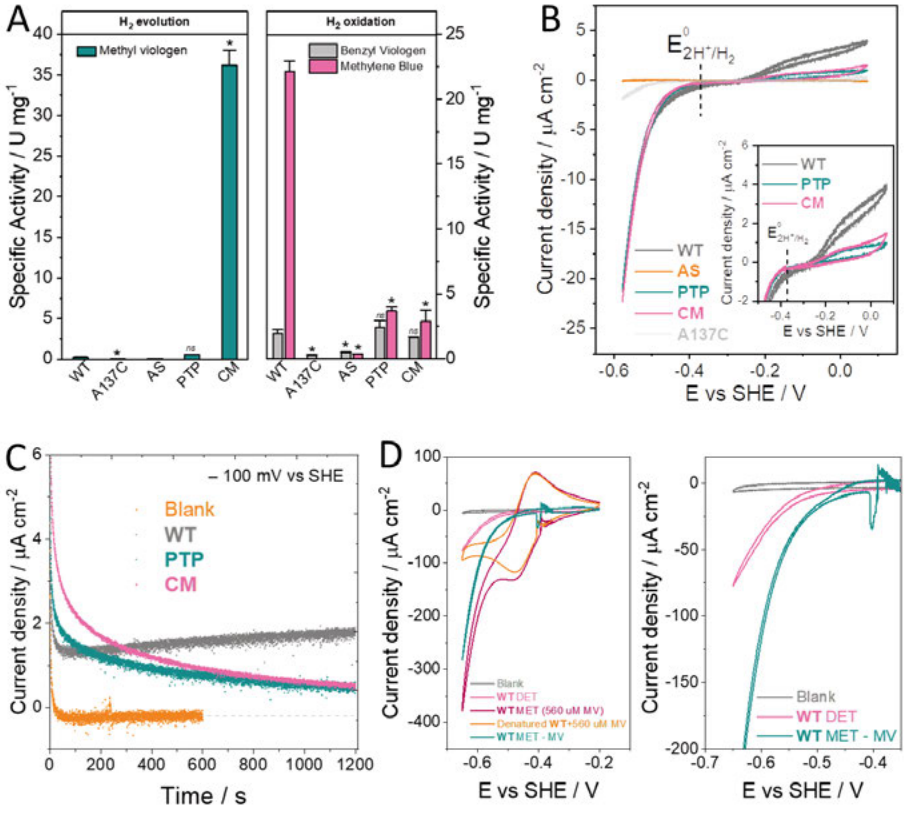

Figure 5.2 Catalytic properties (A) Comparison of the H_2 oxidation and evolution specific activities at pH 6.8 using methyl viologen (MV: 10 mM MV + 100 mM sodium dithionite, dark cyan), benzyl viologen (BV: 1 mM, grey bars), and methylene blue (MB: 30 µM, magenta bars). H_2 oxidation was measured in colorimetric assays at 25°C and H_2 evolution by gas chromatography at 28°C. Specific activity (U/mg) is one unit (U) of activity that catalyses 1 µmol of H_2 oxidized or evolved per min per mg of enzyme. One-way ANOVA (Tukey's Honestly Significant Difference Test) results are indicated above the bars: significantly different at the p = 0.05 level (*) and not significantly different (ns) based on mean exam scores between **WT** and variants. Data are presented as a mean of 2 biological replicates, each with 2-3 technical replicates with error bars showing standard error of the mean (SEM). Not detected – H_2 evolution rate in **AS**. Not determined – H_2 oxidation of **A137C** using MB. **(B)** CV traces (first scan) observed for **WT** (dark grey), **AS** (orange), **PTP** (dark cyan), and **CM** (magenta) subtracted with the blank electrode (no immobilized enzyme). Inset: Zoom in near the thermodynamic potential, emphasizing the apparent oxidative inactivation of **PTP** and **CM** at higher applied potentials. Conditions: pH 6.0, 40°C, 1 atm H_2, scan rate 2 mV/s, electrode rotation 3,000 rpm, following immobilization of the enzyme on a PGE electrode; all potentials given in V vs. SHE. **(C)** Chronoamperometry measurements of **WT** (dark grey), **CM** (magenta), and **PTP** (dark cyan) immobilized in deaerated PGE working electrodes recorded at – 100 mV vs SHE, pH 6.0,

40°C, 1 atm H_2, and rotation = 3 krpm. Sustained electrolysis at –100 mV vs SHE caused a slow but distinct decrease in oxidative current on a minute time-scale for both the **CM** and **PTP** variants, further confirming their oxidative inactivation at high potentials. **(D)** Direct electron transfer (DET) vs mediated electron transfer (MET) CV traces of PGE-immobilized *Tam*HydS **WT** under 1 atm of Ar, at pH 6.8, 40°C, scan rate 20 mV/s. The magenta line corresponds to the CV without MV, and reflects proton reduction currents by DET from the electrode to the enzyme. The dark magenta line corresponds to MET CVs with 560 μM MV.[231] The grey line represents the CV after denaturation of the immobilized enzyme for 30 minutes at 90ºC and buffer exchange ("Blank"). This Blank aligns closely with the CV of the bare electrode prior to enzyme immobilization, indicating minimal interference from the denaturation and buffer exchange processes on the electrochemical behavior of the electrode surface (data not shown). The orange line corresponds to the CV of denatured enzyme with the addition of 560 μM MV. The dark cyan line corresponds to the difference between the dark magenta (MET) and magenta (only MV) lines. Two independent enzyme films were tested, with approximately 10% error for current values between films and are therefore, considered reproducible. The right panel zooms in near the region of the thermodynamic potential.

The following discussion summarizes how the variants altered the catalytic properties of the **WT** (**Fig. 5.2A-C**), emphasizing key modifications in activity rates, bias, and tolerance towards O_2. PFE and *in vitro* assay methodologies are described in **Chapter 2**.

CM improved H_2 evolution rates and O_2-tolerance: CM exhibited a 170-fold increase in H_2 evolution activity (36.2 ± 1.8 U/mg) compared to **WT**. This contrasts with the similar proton reduction currents observed in PFE for **CM** and **WT**, likely due to distinct differences in reactivity between the immobilized and solubilized enzyme. Additionally, electron transfer (ET) limitations, evidenced by the increase in current with driving force, could also contribute to this observation.

It is also important to acknowledge that the observed direct electron transfer (DET) currents may not accurately reflect the intrinsic enzyme activities. As presented in **Fig. 5.2D**, the use of the redox mediator methyl viologen (MV, $E^{0'}$ = −449 mV vs SHE at pH 7.0[164]) in mediated electron transfer (MET) experiments resulted in higher current magnitudes compared to DET. This suggests that slow ET rates likely influence the measured currents. Therefore, a direct comparison of absolute current magnitudes between **WT** and variants may not be the best approach to assess catalytic changes. Instead, focusing on the shape and relative currents of the CV responses when comparing variants to **WT** can provide more informative insights.

The CV traces confirm that **CM** functions as a bidirectional, irreversible catalyst similar to **WT**. Although **CM** seems to exhibit a slight increase in the onset potential compared to **WT**, it is apparent that **CM** still preserve a significant potential window around the thermodynamic potential of the $2H^+/H_2$ couple, devoid of substantial currents. This irreversible behaviour starkly

contrasts with Group A [FeFe] hydrogenases, which, with few exceptions, operate with negligible overpotential in both directions ($\eta \approx 0$ mV).[71, 120]

A closer examination of the currents at high driving force ($\eta \approx 200$ mV) reveals that **CM** increased the apparent catalytic bias towards proton reduction, with currents relative to H_2 oxidation increasing up to threefold versus **WT**. This bias towards proton reduction is partially due to the oxidative inhibition of **CM** at high potentials (**Fig. 5.2B-C**). Unlike **WT**, **CM** showed minor current decrease despite a driving force increase, noticeable from approximately E > −120 mV vs SHE. This is supported by solution assays where the specific H_2 oxidation activities of **CM** (1.67 ± 0.03 U/mg) were comparable to **WT** (1.95 ± 0.27 U/mg) with BV as the electron acceptor, while its activity using MB (2.88 ± 0.89 U/mg) was notably lower than **WT** (22.1 ± 0.8 U/mg).

Finally, **CM** exhibited enhanced O_2-tolerance compared to **WT** (**Fig. 5.3**), as evidenced by a threefold increase in half-life ($t_{1/2}$ = 2.45 ± 0.07 min) during air exposure and higher residual proton reduction currents after O_2 injection as measured in PFE.

PTP retained H_2 evolution rates but improved O_2-tolerance: Similar to **CM**, **PTP** is also a bidirectional, irreversible catalyst with an increased bias towards proton reduction partially due to the oxidative inhibition at high potentials, as also corroborated by solution assays comparing BV and MB. Although **PTP** showed no significant difference in H_2 evolution activity (0.60 ± 0.01 U/mg) compared to **WT** (0.25 ± 0.03 U/mg), the variant displayed higher O_2-tolerance, with a half-life of 1.45 ± 0.20 min during air exposure (**Fig. 5.3**).

AS and A137C impaired overall catalytic performance: Both the **AS** and **A137C** variants exhibited significantly reduced catalytic activity. **AS** was essentially inactive in both H_2 evolution and oxidation assays, consistent with the negligible currents observed in PFE. **A137C** retained minimal H_2 evolution and limited H_2 oxidation activities (10% and 25% residual activities, respectively), indicating that as an individual variant, it does not entirely nullify catalytic activity, contrasting with the "catalytically dead" **AS** that incorporates additional methionine residues. Due to the severely diminished catalytic activities of these variants, their O_2-tolerance was not probed in detail.

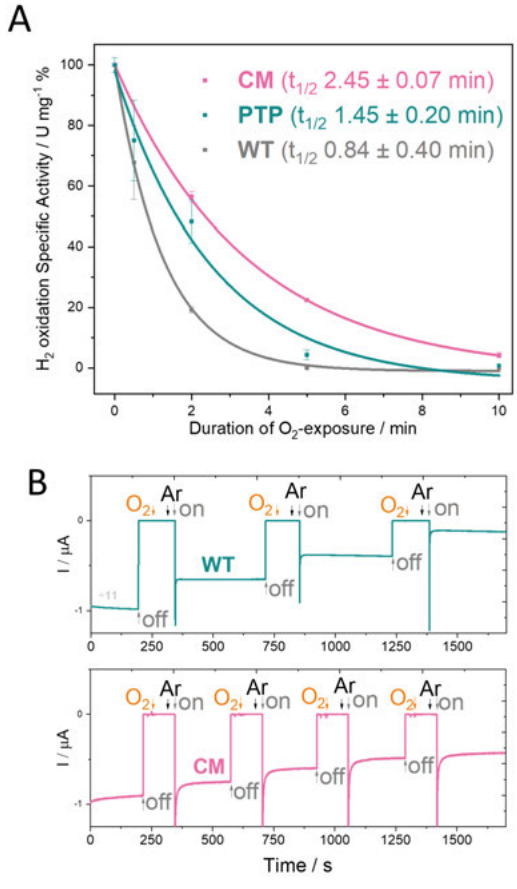

Figure 5.3 Probing O_2-tolerance (A) Stability towards air monitored via H_2 oxidation assays. Diluted aliquots of enzyme (50 µL, 2 µM) were incubated under air (20% O_2) for 0.5−10 min, sans any reductant in the buffer. After air treatment, the samples were flushed with Ar and returned to the glovebox. The relative specific activities of **WT** (grey), **PTP** (dark cyan), and **CM** (magenta) were measured following incubation under air. O_2-induced irreversible enzyme inactivation followed apparent first-order kinetics, with the half-life values ($t_{1/2}$) extracted from the single exponential decay curves (solid lines). Data are presented as a mean of 2-3 technical replicates, with error bars showing SEM. **(B)** Chronoamperometry measurements of **WT** (dark cyan) and **CM** (magenta), recorded at –600 mV vs SHE, pH 6.0, 40°C, and rotation = 3,000 rpm. Arrows indicate the moments when the potentiostat was turned off, followed by the injection of 0.67% O_2 (24 µM) into the mixture with Ar temporarily turned off; when Ar was restarted after 1 minute of equilibration with the added O_2; and when the potentiostat was turned on. Comparing the proton reduction currents before the potentiostat was turned off and after the potentiostat was turned on, a distinct decrease in current was observed for both **WT** and **CM**, but the effect is lower in **CM**. **WT** maintained 66 ± 5% residual activity, whereas **CM** preserved higher residual activity at 85 ± 3%. The reported percentage errors reflect the standard deviation across at least two independent films, each with a minimum of three technical replicates.

Retained spectroscopic attributes in variants

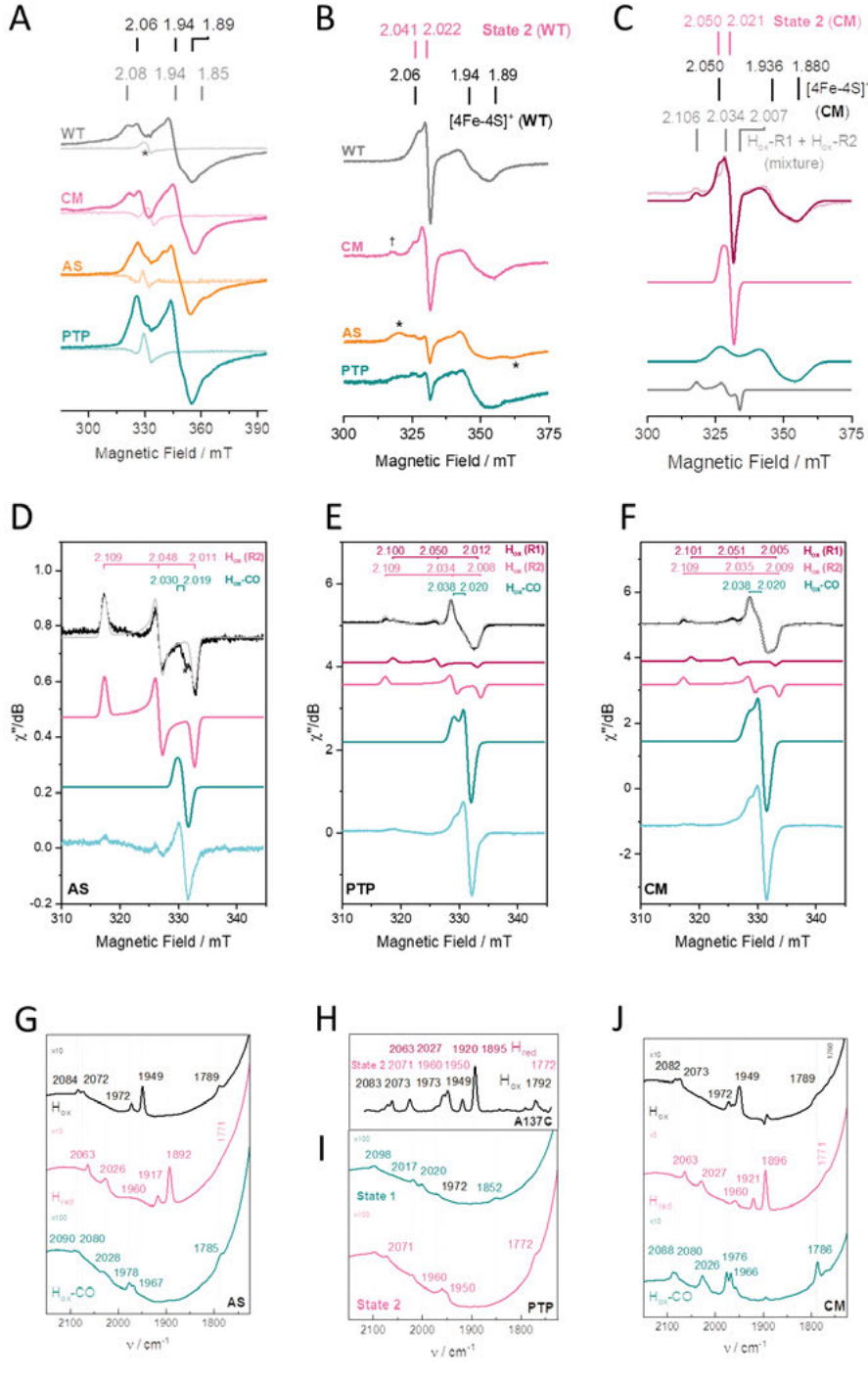

Figure 5.4 Spectroscopic characterization **(A)** Reconstituted *apo* **WT**[71] and variants highlighting the two contributing components typical for $[4Fe–4S]^+$ clusters. Lighter colors depict as-isolated samples while darker colors depict the corresponding sodium dithionite (NaDT) reduced samples. The weak signal marked with * appearing at g = 2.02 is attributed to a trace amount of $[3Fe–4S]^+$. Settings for **WT**: T=17 K; modulation frequency=100 kHz; amplitude=15 G; microwave frequency=9.4 GHz; power=8 mW. Settings for the variants: T=10 K; modulation frequency=100 kHz; amplitude=15 G; microwave frequency=9.4 GHz; power=80 μW. **(B)** H_2-reduced *holo* **WT**[71] and variants resulting in the formation of **State 2** (pseudo-axial signal) with parallel accumulation of reduced $[4Fe–4S]^+$ (rhombic signal). Settings: T=10 K; Modulation frequency=100 kHz; amplitude=10 G; Microwave frequency=9.4 GHz; power=80 μW. The dagger (†) in **CM** (magenta) indicates small contributions from a mixture of H_{ox}-R1 and H_{ox}-R2. The asterisks (*) in **AS** (orange) corresponds to the trace signal from the "wide" rhombic component of $[4Fe-4S]^+$ as seen in (A) which is presumed to arise from a population of *ap*o **AS**. This assignment is based on our previous data from ref.[71] **(C)** The experimental spectrum of **CM** (light magenta) as seen in (B) overlaid with its simulated spectra (dark magenta). The three individual components contributing to the overall simulated spectrum are shown for **State 2** (magenta), "narrow" component of the $[4Fe–4S]^+$ (dark grey), and minor contributions from a mixture of H_{ox}-R1 and H_{ox}-R2 that was treated as a single component (light grey). **(D-F)** EPR spectra of as-isolated (black) and CO-flushed (light cyan) *holo* **AS**, **PTP**, and **CM**. Settings: T=21 K; modulation frequency=100 kHz; amplitude=10 G; microwave frequency=9.4 GHz; power=16 μW; except CO-flushed **PTP**, which was recorded at 253 μW. Simulations are provided for the as-isolated spectra (grey), H_{ox} (dark and light magenta), and H_{ox}-CO (dark cyan spectra). The H_{ox}-CO simulations were based on the light cyan spectra except **PTP** for which the H_{ox}-CO simulation was derived from the spectrum of CO-flushed **PTP** recorded at 64 μW. **(G-J)** FTIR spectra of **AS** (G), **A137C** (H), and **PTP** (I), **CM** (J). Spectra in panels G, H, and J were calculated by subtraction of absorbance spectra at different time points from H_2/N_2 (magenta/black) and CO/N_2 (dark cyan/black) titrations. The H-cluster states observed under N_2 (black labels, H_{ox}), H_2 (magenta labels, H_{red}), and CO (dark cyan labels, H_{ox}-CO) are annotated, except for **PTP**, showing **State 1** (dark cyan) and **State 2** (magenta). Panel H shows the as-isolated spectrum of **A137C** with black labels for H_{ox}; dark magenta labels for H_{red}; and magenta labels for **State 2**. In the oxidized form, **WT** and **CM** adopt a mixture of H_{ox} and $H_{ox}H$, with a low-frequency band at 1760 cm^{-1} assigned to an unknown H-cluster state.

This section demonstrates that despite exhibiting altered catalytic features, the variants retained most of the spectroscopic characteristics of **WT**, suggesting that the variations do not significantly disrupt the fundamental structure and assembly of its metalloclusters.

Unaltered F-cluster assembly: After purification to yield the respective *apo* variants, no alterations in the F-cluster binding domains were observed. All variants and **WT** shared a consistent final Fe:protein ratio of 15.9 ± 0.2 after semi-enzymatic reconstitution, in agreement with the expected four F-clusters. UV/Vis and EPR spectroscopy further confirmed the proper formation of the expected [4Fe-4S] clusters (**Fig. 5.4A**). Two out of [4Fe-4S] clusters are amenable to sodium dithionite (NaDT) reduction, displaying two rhombic signals with g-values for the wide ($g_{1,2,3}$ = 2.08, 1.94, 1.85) and for

the narrow ($g_{1,2,3}$ = 2.06, 1.94, 1.89) components of the $[4Fe–4S]^+$ clusters. These results reflect the $[4Fe\text{-}4S]^+$ fingerprint signatures of **WT**, indicating that the variants are expected to retain electron transfer mechanisms via these relays. The highly similar $g_{average}$ and $g_{anisotropy}$ for the narrow $[4Fe\text{-}4S]^+$ component between **WT** and **CM** (1.959 ± 0.004 and 0.170, respectively) suggests that the electron-transfer relays remain unaltered (**Fig. 5.4B-C**).

Uncompromised H-cluster assembly: A consistent Fe:protein ratio of approximately 17.9 ± 0.4 was established across $[2Fe]^{ADT}$-activated *holo* **WT** and variants, indicative of successful artificial maturation.[71] The data also demonstrates the robust nature of the H-cluster assembly, accommodating the incorporation of $[2Fe]^{ADT}$ even with extensive substitutions within the protein scaffold.

Preservation of H_{ox}, H_{red}, H_{ox}-CO, and State 2 fingerprint signals: EPR and FTIR spectroscopy corroborate the proper formation of the H-cluster across all examined *holo* variants (**Fig. 5.4D-J**). Freshly activated "as-isolated" variants exhibit typical rhombic H_{ox} signals, with **CM** and **PTP** variants also showing an axial signal arising from H_{ox}-CO. Albeit undetectable in the as-isolated sample, the H_{ox}-CO signal in **AS** was more discernible following CO-flushing. Overall, the observed g-values exhibit a high degree of similarity and reside within the g~2 region, as determined through spectral simulations. This aligns with prior studies on **WT**, wherein the g-values invariably exceed those reported for prototypical [FeFe] hydrogenases (**Tab. 4.1**). Moreover, the FTIR signatures of H_{ox}, H_{red}, and H_{ox}-CO have been confirmed in **AS** and **CM**, differing marginally from **WT**, thereby reinforcing the EPR data. Analysis of H_2-reduced spectra (**Fig. 5.4B-C**) revealed that the variants also formed **State 2**. Similar to the H_{ox} signals, a comparison of the simulated spectra of H_2-reduced **CM** and **WT** revealed a high degree of similarity in the **State 2** signals, indicating only minor perturbations in its electronic structure (**Fig. 5.4C**). The highly similar $g_{average}$ and $g_{anisotropy}$ for **State 2** (2.031 ± 0.001 and 0.025 ± 0.006, respectively) suggests minor changes in the g-tensor rhombicity of the H-cluster, indicating minimal shifts in its electronic structure.

Spectroscopic deviations and potential implications for catalysis

While the variants retain the majority of the **WT**'s spectroscopic features, some notable deviations offer insights into their altered catalytic properties related to catalytic H_2 turnover:

Single set of H_{ox} signal in inactive AS: Contrary to the two distinct rhombic H_{ox} signals discerned for **WT**, **CM**, and **PTP**, variant **AS** produced a singular rhombic H_{ox} signal in its as-isolated spectrum (**Fig. 5.4D**). This suggests that **AS** might lock the H_{ox} state into a single conformation. The presence of two H_{ox} conformations in the active variants could be functionally significant, potentially representing two catalytically relevant conformations. By restricting the H_{ox} state to a single conformation, **AS** might hinder efficient progression through the catalytic cycle, explaining its diminished activity. Further investigation using techniques capable of probing protein dynamics in solution would be necessary to resolve this ambiguity.

Additionally, the introduced mutations in **AS** could disrupt the native proton transfer pathway, potentially contributing to its reduced activity. This aspect will be explored more in the subsequent section.

Dominance of State 1 and State 2 in active PTP: The FTIR spectrum of "as-isolated" **PTP**, showed a minor fraction of the H-cluster residing in the H_{ox} and H_{red} states, and instead is predominantly characterized by a signature strikingly similar to **State 1** (**Fig. 5.4I**). The respective "as-isolated" EPR spectrum exhibits distinct H_{ox} and H_{ox}-CO signatures. This discrepancy could be attributed to a rapid loss of the more oxidized states upon the exposure to the H_2-rich atmosphere encasing the FTIR instrument, or the inherent differences between the spectroscopic techniques. For instance, **State 1** and H_{red} evade detection by EPR due to their silent nature (S = 0). FTIR may fail to detect certain low-concentration species, while EPR can provide complementary information and potentially identify these species due to its sensitivity to electronic structures and paramagnetic centers. Conversion of **State 1** to **State 2** with H_2 was also observed (see **Fig. 3** of **Paper III**). **PTP** remaining catalytically active supports the catalytic relevance of **State 2** proposed in **Chapter 4, Paper II**.

Proposed determinants of catalytic performance improvement

Catalytic activity rates

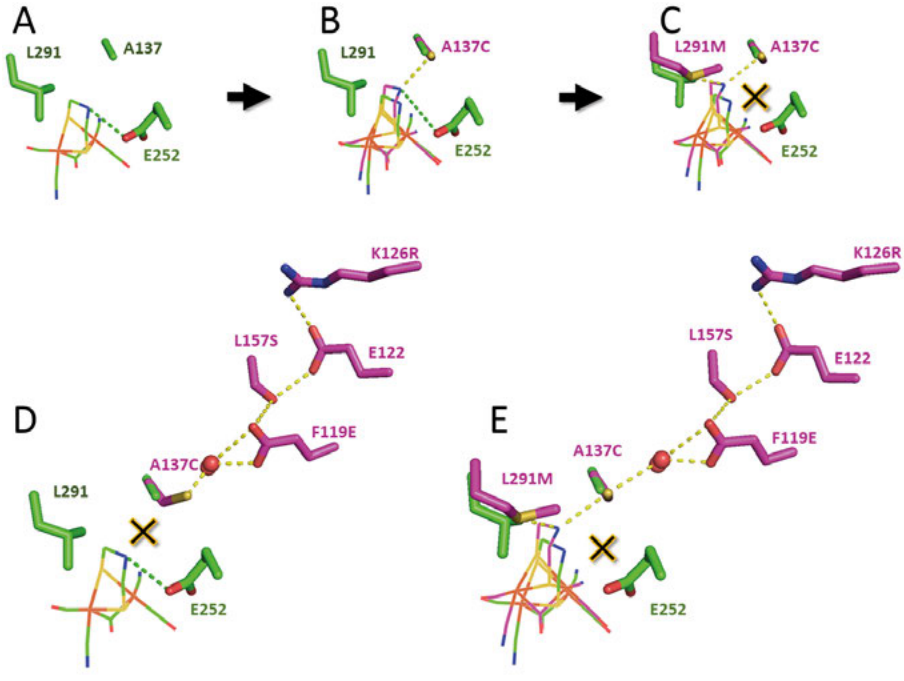

Figure 5.5 Proposed effect of single-point variant, **A137C**, in isolation and combined with other variations. **(A)** Homology model of *Tam*HydS highlighting residues L291 and A137 (green sticks), targeted for variation, and the proposed native proton relay residue of *Tam*HydS E252 (green stick), which is located ≈3.4 Å from the ADT-amine (green dashed lines).[124] The H-cluster ($[2Fe]_H$ subsite is only shown for clarity) is depicted as a wire with C: green, O: red, N: blue, S: yellow, and Fe: orange. **(B)** The crystal structure of *Cp*I (PDB ID: 4XDC[201]) serves as the reference model, where variant A137C (pink stick) corresponds to $C299_{CpI}$. The proposed modified positions of the H-cluster in each variant **A137C (B)**, **AS (C)**, **PTP (D)**, and **CM (E)** are depicted as a wire with C: pink, O: red, N: blue, S: yellow, and Fe: orange. Refer to the accompanying text for further details.

Neither optimizing the active site environment (**AS**) nor the proton transfer pathway (**PTP**) in isolation leads to significant improvement in overall catalytic performance. It is the combination of alterations to these two structural features that produces a synergistic effect, markedly enhancing H_2 evolution activity rates in **CM**, without negatively impacting inhibitor stability.

This study initially hypothesized that emulating the sulfur-rich conditions of the faster-acting prototypical [FeFe] hydrogenases could improve the catalytic efficiency of *Tam*HydS **WT**. However, as evidenced by **AS**, modifying

the active site alone does not suffice to augment catalysis in **WT**. This finding aligns with other recent studies, such as the observed ineffectiveness of active site pocket modifications in the slow-acting Group C enzyme *Tm*HydS in improving catalytic rates.[232] The absence of an electrochemical current in CV and undetectable solution activity substantiate the **AS** variant's loss of function. Yet, spectroscopic analysis via EPR and FTIR shows that H-cluster reactivity concerning H_2 activation remains. The steric displacements and modifications in electrostatic interactions by the introduced variations in **AS** are likely disrupting the native proton transfer pathway of *Tam*HydS, severing the H-cluster's contact with the bulk solution.

The characterization of the single-point variant, **A137C**, offers insights into how the triple variant **AS** completely abolished catalytic activity. The alanine at the $A137_{TamHydS}$ site corresponds to Group A $C299_{CpI}$ ($C169_{CrHydA1}$, $C298_{CaHydA1}$), which is known to be essential for effectively coupling the H-cluster to the long-range proton-transfer network, and likely fine-tunes the spatial positioning of the amine bridgehead of the ADT through H-bonding.[75, 89]

Exploring the potential role of the **A137C** involves considering two distinct scenarios, as illustrated in **Fig. 5.5**. The first scenario examines the independent influence of **A137C**, drawing parallels to its cysteine counterpart in Group A enzymes. The second scenario delves into the potential synergistic effects arising from the interaction between **A137C** and the other variations.

A137C only (Fig. 5.5B): As a lone variant, **A137C** potentially interacts with the amine through electrostatic interactions such as H-bonding (3.5 Å).[75, 201] This standalone interaction may elongate the distance between the amine and the proposed native proton transfer pathway of *Tam*HydS ($E252_{TamHydS}$)[124], but not enough to completely sever the connection, and abolish catalytic activity.

A137C in AS (Fig. 5.5C): In the triple variant **AS**, **A137C** is combined with L291M (and S191M, not shown). The L291M can allow the ADT-amine to optimize its position relative to Fe_d and the cysteine introduced in **A137C** via H-bonding (3.6−3.7 Å) and increase flexibility of the active site environment due to decrease of steric hindrance.[75, 201] However, the combined interaction of L291M and A137C on ADT-amine is proposed to be detrimental, as seen in the abolished catalytic activity in **AS**, likely due to the complete disconnection of the ADT-amine from *Tam*HydS' native proton transfer pathway. The impact of S191M is unknown, warranting further investigation.

A137C in PTP (Fig. 5.5D): In the quadruple variant **PTP, A137C** is combined with other residues, diverting **A137C** away from the amine bridgehead. This shift, potentially due to indirect or direct electrostatic interactions with the other **PTP** residues or water molecule(s), reduces the interaction of **A137C** with the ADT-amine. This allows continuous operation of the native proton transfer pathway via $E252_{TamHydS}$, and thus, preservation of the catalytic activity of **WT**. However, we speculate that the H-cluster does not benefit from the

engineered proton trajectory of the **PTP** as long as the active-site methionines interacting with the H-cluster are absent.

A137C in CM (**Fig. 5.5E**)**:** In the sextuple variant **CM**, reintroducing the methionines (L291M and S191M) enables **A137C** to reconnect with the amine bridgehead, and now also connecting the ADT amine to the improved proton trajectory that likely speeds up proton transfer, compared to the slower native proton transfer pathway of **WT**, where E252$_{Tam\text{HydS}}$ is connected to the amine bridgehead.

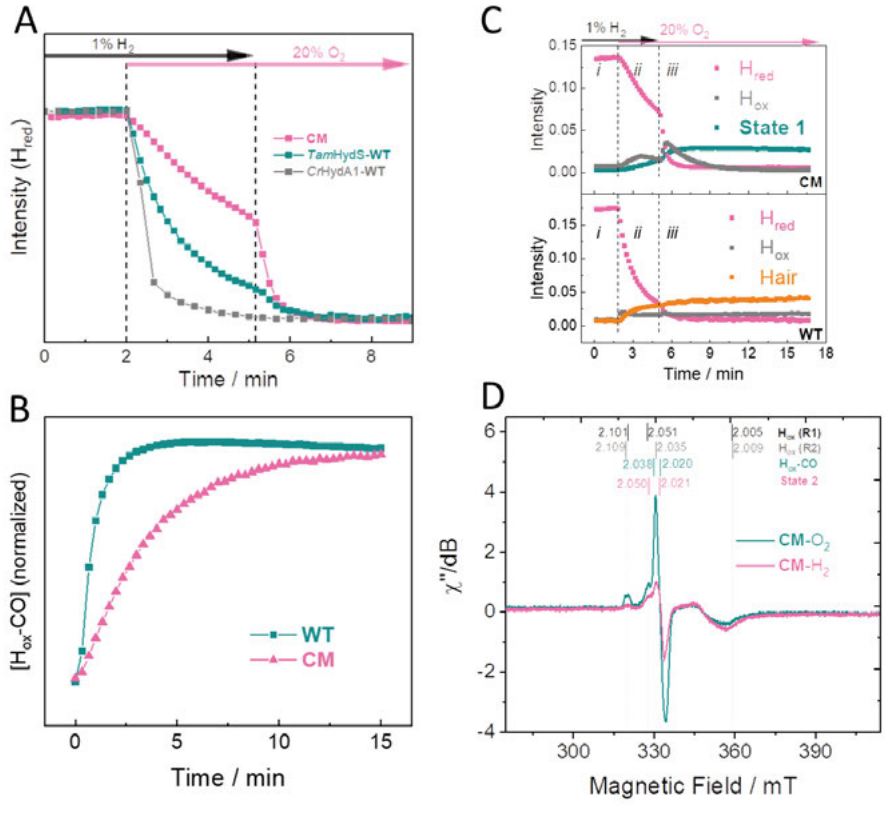

Figure 5.6 Probing inhibitor tolerance by spectroscopy (A) The prolonged O_2-tolerance in **CM** compared to **WT** and *Cr*HydA1 is reproduced by *in situ* ATR FTIR spectroscopy followed the decay of the H_{red} state over time. The presence of 1% H_2 in the gas phase stabilizes H_{red} and prolongs the deactivation of *Tam*HydS, most clearly observed with **CM**. **(B)** In the presence of 99% CO and 1 % N_2, H_{ox}-CO accumulates. Formation of H_{ox}-CO under CO was observed to be five-fold slower in **CM** than **WT**. No H_{ox}-CO formation was detected when 1% H_2 was present in the headspace. **(C)** Reaction of **CM** (top) and **WT** (bottom) with 20% O_2. The traces show the reaction as a function of time and gas composition, starting with (*i*) 1% H_2 + 99% N_2, (*ii*) 1% H_2 + 79% N_2 + 20% O_2, and (*iii*) 80% N_2 + 20% O_2. Condition (*i*): H_{red} (magenta) accumulates. Condition (*ii*): At the expense of H_{red}, **WT** accumulates H_{air}, indicating a partially degraded H-cluster[71], while **CM** accumulates **State 1**. Condition (*iii*): **CM** accumulates much less H_{ox}, shows only minor protection against O_2 under H_2, and forms **State 1** (dark cyan). **WT** experiences lesser protection against O_2 under H_2, shows only traces of H_{ox} and forms significant amounts of H_{air} (orange). **(D)** EPR spectra of H_2-reduced **CM** (magenta) resulting in the formation of **State 2** and reduced $[4Fe–4S]^+$. After H_2-flushing for an hour, **CM** was exposed to air for 5 minutes. The air-exposed **CM** (dark cyan) displayed H_{ox}, H_{ox}-CO, and traces of **State 2** related signals. These findings were consistent with FTIR traces, which pinpointed H_{ox} as the initial result of O_2-induced oxidation. Settings: T=10 K; Modulation frequency=100 kHz; amplitude=10 G; Microwave frequency=9.4 GHz; power=80 µW.

Biochemical assays and electrochemistry demonstrate improved O_2-tolerance in **CM** compared to **WT**, as evidenced by greater residual activities after exposure to O_2 across various time points (**Fig. 5.3**). This enhancement is further supported by spectroscopic data (**Fig. 5.6**) with FTIR monitoring H-cluster states during O_2 exposure, and EPR spectroscopy confirming the formation of fully assembled H-cluster states in **CM** after 5 minutes of exposure to O_2.

This discussion delves into the primary hypotheses concerning the mechanisms of O_2-tolerance in hydrogenases, focusing on the contribution of said mechanisms to the enhanced O_2-tolerance observed in **CM**.

Mechanism I, complete reduction of O_2 to H_2O: This process, observed in [NiFe] hydrogenases, reduces O_2 to benign H_2O, bypassing the generation of damaging reactive oxygen species (ROS).[86, 233, 234] While the enhanced catalytic activity rates observed in **CM** might hint at a capacity for rapid O_2 reduction, it is crucial to acknowledge that this observation alone does not confirm a causal relationship. O_2-tolerance is more likely governed by other factors (as outlined further below).

Mechanism II, restricting access to inhibitors: Another theory posits that O_2-tolerance is increased by physically impeding access to the active site via proteinaceous structures acting as gas filters (**Fig. 6.5**).[155, 235] The slower reaction with CO observed for **CM** relative to **WT** could support this hypothesis (**Fig. 5.6B**).

Mechanism III, external ligand binding: Data in this study suggests that external ligand binding serves as a protective mechanism against O_2 stress. Instances of such binding, like the hydroxide-inhibited states of [NiFe] hydrogenase, have been reported (**Fig. 6.4**).[236] Observations of **CM** (and **PTP**) reveal FTIR spectra similar to the thiol-inhibited state H_{inact}[74, 118, 192], forming **State 1** upon O_2 exposure (**Fig. 5.6C** and **Fig. S22** of **Paper III**). Notably, **PTP** demonstrated reversibility without significant loss of H-cluster cofactor bands from **State 2** to **State 1** during O_2 exposure. This suggests that the H-cluster in **PTP** retains a greater degree of structural integrity after O_2 exposure compared to **WT**. The proposed bound aqua or hydroxide ligand at the Fe_d could block O_2 binding and suppress outer sphere electron transfer, thus, preventing irreversible H-cluster degradation. However, solution assays reveal a faster loss of H_2 oxidation residual activity in **PTP** compared to **CM**. This discrepancy might stem from differences in sample states between FTIR and solution assays or variations in the kinetic rates of reactivation from the inhibited state. It is hypothesized that **PTP** has a slower reactivation rate from **State 1** to an active state compared to **CM**.

While these mechanisms have been observed in other hydrogenases, their relative contributions in the current work remain to be fully understood. Particularly the O_2-protective role of **State 1** as introduced in **Chapter 4, Paper II**, highlight the complexity of this process.

A comprehensive understanding of the intermolecular forces and steric limitations that facilitate protective conformations and ligand interactions requires a broader approach. In-depth kinetic analyses can quantify the rates of O_2 reduction, reactivation from inhibited states, and potential competition between these processes; molecular simulations can model O_2 diffusion pathways, assess conformational changes upon O_2 binding, and identify potential steric barriers; high-resolution structural studies can visualize ligand interactions at the active site in the inhibited state and potentially capture transient intermediates during O_2 exposure.

Deciphering the O_2-tolerance mechanisms could pave the way for engineering robust catalytic systems, particularly in environments where O_2 exposure is inevitable.

Balancing rigidity and flexibility within the active site

Comparative sequence analysis of the "sensory" characterized representatives from Group C and D [FeFe] hydrogenases and the catalytic Group A enzymes indicates potential variations in the flexibility of their active site regions. This offers insights into the evolutionary adaptations between enzymes with divergent proposed physiological functions.

Putatively sensory Group D *Tam*HydS has relatively less flexible active site environment than catalytic Group A enzymes. Methionine at the $M497_{CpI}$ site potentially serves a dual purpose: it mitigates movements between the H-cluster and the surrounding protein scaffold[75], and enhances active site flexibility. The methionine with its flexible C_{methyl}–S bond[237] is replaced with a relatively more rigid leucine in *Tam*HydS. The second methionine at the $M353_{CpI}$ site can interact electrostatically with the bridging CO. This methionine is replaced with a serine ($S191_{TamHydS}$). Serine can form H-bonds, but it is generally considered to have less conformational flexibility than methionine. Prior studies on Group A have shown that replacing this methionine to leucine led to reduced activities compared to wild-type enzymes, though not as severely as variations in the two residues interacting with the amine bridgehead (*i.e.,* $C299_{CpI}$ and $M497_{CpI}$).[96]

Sensory Group C *Tm*HydS also has relatively less flexible active site environment than Group A enzymes. $M497_{CpI}$ is replaced with a serine ($S267_{TmHydS}$)[232] (**Fig. 3.4D**) while $M353_{CpI}$ is replaced with a glycine ($G177_{TmHydS}$). While a glycine residue could increase rigidity within the immediate active site environment, it can permit greater overall protein flexibility.

The substitution of the methionine residues in Group A into relatively less flexible residues in “sensory” group representatives, *Tm*HydS and *Tam*HydS, prompts us to consider whether introducing rigidity in the active site

environment translate to a more precise detection of environmental cues such as pH_2, thereby maintaining more reliable signaling transduction.

The two methionine residues show distinct conservation patterns across the two groups. Substitutions for $M353_{CpI}$ are relatively more conserved, with glycine predominantly found in Group C and threonine or serine in Group D (**Fig. 5.7**). This conservation in each group suggests a potentially significant functional role for this position. In contrast, residues equivalent to $M497_{CpI}$ are less conserved and generally feature less flexible, non-methionine residues (asparagine, arginine, glutamine). The functional relevance of this position in these groups remains unclear.

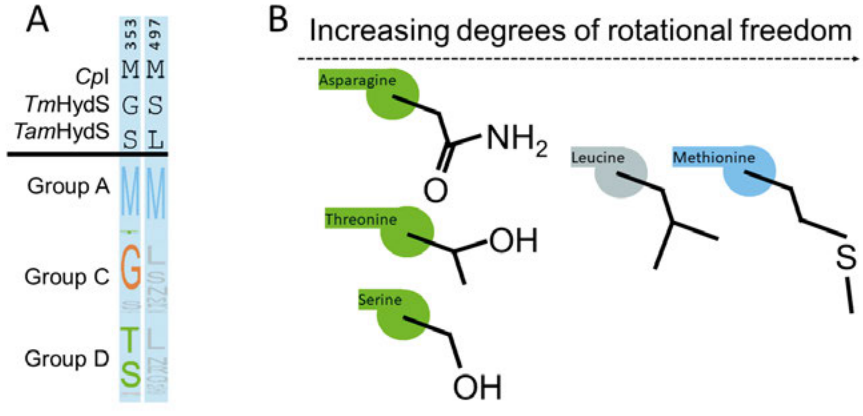

Figure 5.7 (A) Comparative sequence analysis was performed on *Cp*I, *Tm*HydS, and *Tam*HydS using a ClustalΩ sequence alignment[205] of sequences retrieved from Greening *et al.* 2016.[15] The numbering on top is based on the *Cp*I sequence. Normalized consensus sequence logos were generated for Groups A, C, and D using the Jalview software with the Clustal X color scheme. **(B)** The degree of rotational freedom of amino acid side chains is determined by the number and nature of their rotatable bonds. Methionine, with its four-carbon, thioether-containing structure, exhibits the greatest rotational freedom owing to its multiple rotatable single bonds. Leucine's branched hydrocarbon side chain also allows for substantial rotation, although the branching introduces some steric limitations compared to methionine. Asparagine's side chain, with two rotatable bonds, experiences somewhat restricted rotation due to the planar amide group. Threonine and serine each possess a single rotatable bond, with serine's smaller side chain resulting in less overall rotational freedom compared to threonine. In contrast, glycine's single hydrogen atom side chain lacks any rotatable bonds (not shown), but the absence of a bulky side chain provides flexibility to the protein backbone. It is important to note that this order reflects general trends, and the actual flexibility of a bond in a protein can be influenced by the local environment, including neighboring amino acids and intermolecular interactions.

The catalytic Group A enzymes might depend on an adaptable active site capable of efficiently accommodating substrates and expediting conformational state transitions.[238] These findings warrant a closer look into the methionine-

rich active site environment, considering that methionine's capacity to oscillate between different conformational states could modulate the enzyme's affinity for H_2 and its overall reactivity.

The proposed structural effects within the active site of [FeFe] hydrogenases potentially reflect a subtle balance between structural rigidity and flexibility, an evolutionary design that appears to be important for the function of both sensory and catalytic [FeFe] hydrogenases.

Conclusion and outlook

This study highlights the merit of integrating a broad range of phylogenetic insights into the design of macromolecular catalysts and presents a compelling case for further exploration of representatives from other groups beyond those commonly studied.

The **PTP** quadruple variant increased O_2-tolerance while retaining H_2 production activities, and the **CM** sextuple variant exemplified concurrent improvement in both aspects. These enhancements were enabled by the strategic incorporation of cross-group phylogenetic analysis to identify structural elements, such as the sulfur-rich active-site canopy and proton transfer pathway of catalytically proficient Group A enzymes. While the underlying rationale for this engineering approach suggested the potential for improved H_2 production, the substantial gains in O_2-tolerance was surprising. This outcome highlights the potential of this approach for optimizing these enzymes for practical applications, even if the magnitude of the improvement was unexpected.

The elucidation of key structural attributes reveals the potential for independent modulation of activity rates, gas inhibitor resistance, and overpotential. Derived insights that can be used for bio-mimic design are as follows:

- An essential consideration for molecular mimics, especially when immobilized in larger electrocatalytic structures, is a strategic placement of the catalyst in relation to the proton delivery pathway.
- For faster turnover rates, the active site's structure might require some degree of flexibility to enable rapid conformational changes between catalytic states.
- To enhance resilience against O_2, mimics can adapt a combination of mechanisms such as reversible external ligand binding, employing gas tunnels to slow down inhibitors and speed up substrates, or faster reduction of O_2 to benign H_2O.
- The underlying cause of the persistent irreversibility observed in *Tam*HydS remains to be fully elucidated. Nevertheless, insights can be derived from the direct and mediated ET studies: optimizing the interaction between the electrode or electron donor and the catalyst, as well as the selection of suitable redox mediators for effective electron shuttling, are critical considerations.

Chapter 6, Paper IV: Extracting trace atmospheric H_2 by a [NiFe] hydrogenase

This chapter outlines the structural properties that enable a [NiFe] hydrogenase ("**Huc**") to extract atmospheric levels of H_2, and elucidate how this is reflected in the enzyme's electrochemical and spectroscopic properties. The primary focus is on the electrochemical and spectroscopic analyses of the natively purified enzyme, supplemented by insights from Cryo-EM structural data, biochemical assays, and MD simulations. The chapter highlights the role of the outer coordination sphere, which equips **Huc** to execute H_2 oxidation under atmospheric O_2 levels, thereby, informing development of (a)biotic catalysts that operate under ambient conditions.

Introduction

Before the "Great Oxidation Event," (2.4–2.1 billion y. a.), Earth's atmosphere was essentially devoid of the oxygen that is so essential to most life today.[239] Instead, it was markedly more reducing, likely composed of gases like nitrogen, carbon dioxide, water vapor, methane, ammonia, and carbon monoxide. Although still escaping to space[240], H_2 is estimated to have been several hundred times more abundant in the early atmosphere, likely fueling the metabolism of primordial microbes. Despite its miniscule atmospheric concentration today (0.00006%), H_2 remains to sustain a diverse array of microorganisms, maintaining the equilibrium of the biogeochemical H_2 cycle.

Contrary to earlier long-held beliefs that H_2 consumption was the exclusive area of expertise for anaerobic life in O_2-deprived habitats (hypoxic soil, deep-sea hydrothermal vents, or hot spring sediments), recent findings have illuminated the role of aerobic soil bacteria as the primary consumers of atmospheric H_2.[241] Surprisingly, these microbes are responsible for approximately 80% of the annual H_2 uptake. This process is not only pivotal for atmospheric regulation, but also enhances soil resilience, enriches biodiversity, and shapes ecosystems—factors increasingly influential under the impact of climate change. Even in the light-deprived soils of Antarctica, these resilient aerobic microbes exhibit sufficient energy generation by scavenging H_2.[241]

Aerobic respiration of H_2 is energetically favorable ($H_2 + ½\ O_2 \rightarrow H_2O$; $\Delta H° = –276$ kJ mol$^{–1}$), and the reduction of various electron acceptors with

H_2-derived electrons is central to energy production and carbon fixation (**Fig. 1.2B**). This process is often facilitated by [NiFe] hydrogenases. Yet, these enzymes typically lack the capacity to oxidize atmospheric H_2 due to their low affinity for the gas and their reversible or irreversible inhibition by O_2.

Within this diverse enzyme family, certain [NiFe] hydrogenases stand out. Several have adapted to efficiently oxidize atmospheric H_2 under air (20% O_2). Among them, the Group 2a **Huc**, from *Mycobacterium smegmatis*, has gained notable attention. *M. smegmatis,* which utilizes **Huc** especially under carbon starvation, displays an impressive capacity to selectively oxidize even picomolar levels of H_2 in the presence of O_2.[242, 243]

Though whole-cell studies have confirmed **Huc** to function in H_2-scant, O_2-abundant environments, this trait is not well understood. Moreover, the mechanisms by which **Huc** relay H_2-derived electrons to the respiratory chain is uncertain, although a quinone derivative is hypothesized to be the direct electron acceptor (**Fig. 6.1**).

This chapter will delve into the investigation of natively purified **Huc**, aiming to clarify whether its high affinity for H_2 is an inherent characteristic or a result of its interaction with the respiratory electron transport chain.[244] Techniques such as biochemical analysis, electrochemistry, spectroscopy, mass spectrometry, molecular dynamics simulations, and high-resolution cryogenic electron microscopy (cryo-EM) were employed.

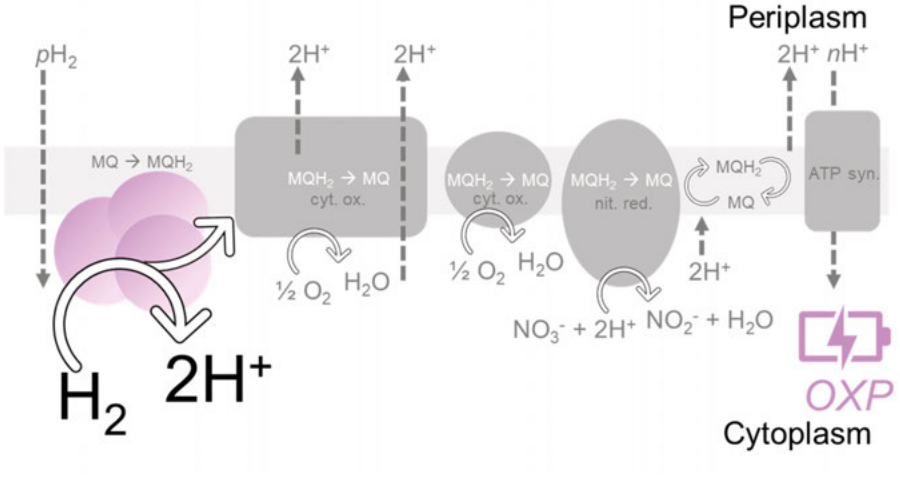

Figure 6.1 A simplified schematic representation of the respiratory electron transfer chain in *Mycobacterium smegmatis.* [NiFe] hydrogenase Group 2a **Huc** is represented as magenta, catalysing H_2 oxidation and releasing protons and electrons. Electrons derived from H_2 are used to reduce terminal electron acceptors (O_2 and NO_3^-) while the protons help drive ATP production through oxidative phosphorylation (OXP). $MQ(H_2)$ – menaquinone; Cyt. ox. – cytochrome oxidase; Nit. red. – nitrate reductase; ATP syn. – ATP synthase. *Adapted figure with permission from ref.*[242]

Structural properties of **Huc**

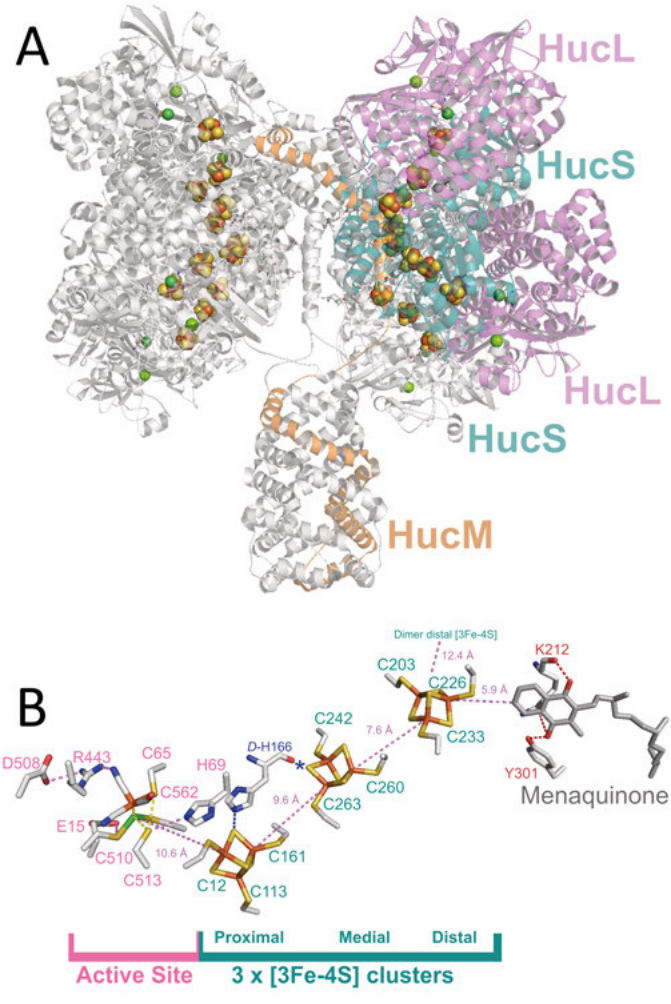

Figure 6.2 Structure of purified Huc (A) A cartoon representation of the complete **Huc** complex, reconstructed from the 1.52 Å cryo-EM structure and the AlphaFold model of the HucM C-terminal, which is fitted to the cryo-EM density map of the stalk region (PDB ID: 7UUS). The complex is composed of the small subunit (HucS, dark cyan), large subunit (HucL, magenta), and the HucM central stalk (orange). **(B)** A magnified view of the [NiFe] active site cofactor, with Ni and Fe represented in green and orange sticks, respectively. The coordinating cysteine sulfur atoms are in yellow. Key amino acid residues (H69, E15, R443, and D508), conserved in [NiFe] hydrogenases, are emphasized. The [3Fe-4S] clusters are shown as sticks with their coordinating cysteine ligands. Distances (in Å) between the [NiFe] cofactor, [3Fe-4S] clusters, as well as the electron carrier menaquinone, are indicated in purple. Residues capable of forming H-bonds with menaquinone are shown with distances in red dashed lines. The close proximity of HucL *D*-His166 to the proximal and medial [3Fe–4S] clusters, and the position of an unidentified ligand (denoted by a blue asterisk *) is also shown.

The analysis of the 1.52 Å Cryo-EM structure of **Huc** revealed a distinctive quaternary structure reminiscent of a four-leaf clover (**Fig. 6.2A**). This complex comprises an octameric assembly, with each 'leaf' formed by a pair of HucS and HucL subunits. The integrity and spatial arrangement of the oligomer are apparently maintained by four HucM subunits, which also mediate its attachment to the membrane through a tube-like extension derived from their C-terminal regions. This complex exhibits a considerable molecular mass of 833 kDa, structured around stalk with a peripheral membrane association.

Conserved secondary coordination sphere: Residues within the immediate environment of the NiFe active site cofactor of **Huc** (*e.g.*, H69, E15, and R443) are conserved among [NiFe] hydrogenases (**Fig. 6.2B**).

Non-conserved outer coordination sphere: Although the spatial configuration of the FeS clusters in the $HucS_2L_2$ dimer allows electron transfer at distances below 15 Å, similar to other [NiFe] hydrogenases, a notable distinction within **Huc** is its exclusive coordination of three [3Fe-4S] clusters. This diverges from the typical binding of at least one [4Fe-4S] clusters found in other known O_2-tolerant and O_2-insensitive [NiFe] hydrogenases (**Fig. 6.4**).

Internal reduction of menaquinone. Density maps suggest menaquinone (MQ) as the immediate electron acceptor near the distal [3Fe-4S], with its head group stabilized via H-bonding by specific residues (K212 and Y301). This was supported by biochemical assays and mass spectrometry. Enzyme kinetics studies reveal a significantly higher maximum velocity with menadione (MQ analogue) compared to NBT or benzyl viologen (BV) (**Fig. 6.3A-B**). Mass spectrometry confirms the association of another MQ analogue, β-dihydromenaquinone-9, with purified **Huc**, implying a direct interaction between the enzyme and the electron acceptor. The entry and exit conduit for MQ to the hydrophobic chamber is likely provided by the membrane-associated HucM stalk. This contrasts with Group 1 [NiFe] hydrogenases, where small subunits act as ET relays without catalytic roles and need additional subunits like cytochrome b for electron transfer from H_2 to the electron acceptor.

Unusual *D*-isomer His166: Unlike other [NiFe] hydrogenases that conserve an *L*-isomeric histidine with its imidazole head group interacting with the proximal FeS cluster, **Huc**'s equivalent histidine (H166) deviates to a *D*-isomeric configuration. This alteration allows H166 to interact with an unidentified ligand near the medial cluster (marked blue * in **Fig. 6.2B**). The ligand indicates a non-water entity due to its apparent elongated density map. However, the precise mechanism of how this isomeric shift can affect the redox potential of the [3Fe–4S] clusters remains to be investigated.

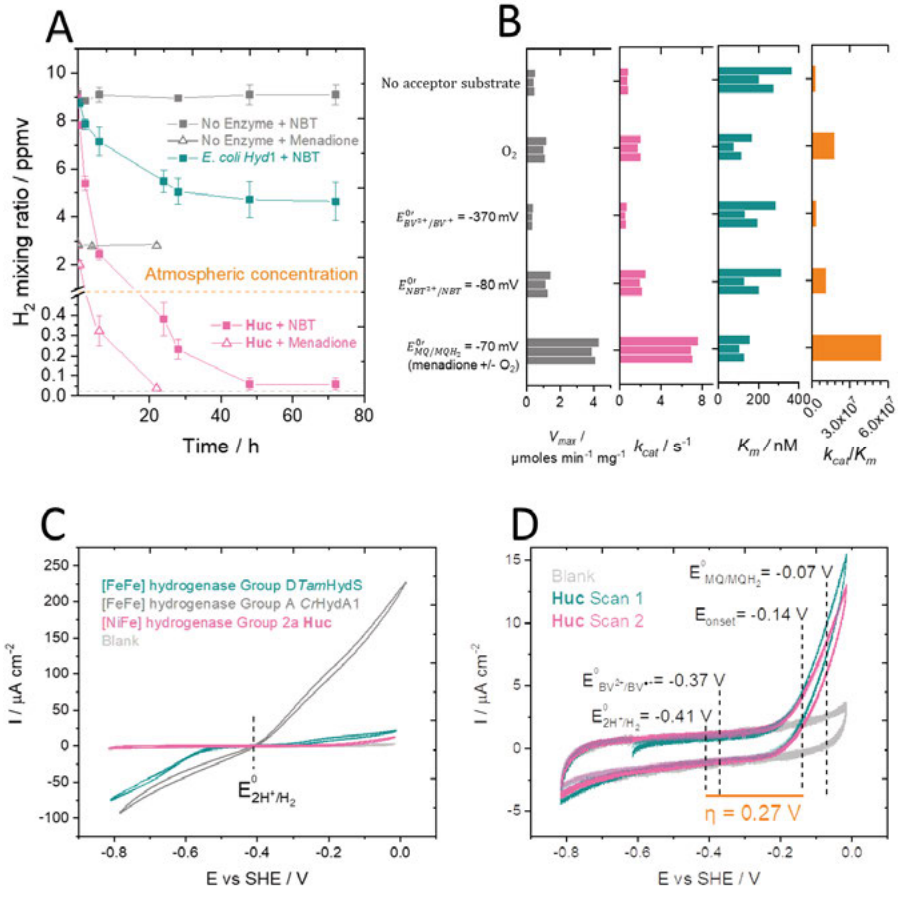

Figure 6.3 Catalytic properties of purified Huc (A) Gas chromatography analysis of vials containing purified **Huc**, *E. coli Hyd*1, or no enzyme, with 200 µM menadione or nitro blue tetrazolium (NBT) as the electron acceptor. **Huc**—but not *Hyd*1—can oxidize H_2 below atmospheric levels (orange dashed line) to the limit of detection (light grey dashed line). **(B)** Michaelis–Menten kinetic parameters of H_2 oxidation by **Huc** in buffer with different electron acceptors. Without any alternative electron acceptor, O_2 stimulates H_2 oxidation by **Huc**, indicating the enzyme can transfer electrons directly to O_2. There was no significant difference in rate or affinity of H_2 oxidation with varying O_2 concentrations with menadione as electron acceptor (see also **Fig. 1C** in **Paper IV**).[155] V_{max}, maximum velocity; K_m, Michaelis' constant; k_{cat}, catalytic constant; k_{cat}/K_m, specificity constant. **(C)** CV traces of immobilized **Huc** (magenta), and [FeFe] hydrogenases *Cr*HydA1 (dark grey) and *Tam*HydS (dark cyan) pH 7.0, 20°C, 1 atm H_2, scan rate 10 mV/s, electrode rotation 3,000 rpm, following immobilization of the enzyme on a PGE electrode; all potentials given in V vs. SHE. The CV for the blank electrode (no immobilized enzyme) is in light grey. **(D)** Zoom in for the **Huc** CVs, emphasizing the onset potential of **Huc**, denoted as E_{onset}, which is de-

termined from the average of four separate experiments, with two scans per film displayed (darker and lighter colors for the first and second films, respectively). Between scans, a decrease in oxidative currents was observed, a trend also observed in chronoamperometry showing a gradual decrease of currents over time at 0 V (data not shown) likely due to film loss. The overpotential of **Huc**, represented by η, is estimated in comparison to the thermodynamic potential of the $2H^+/H_2$ redox couple. The figure also indicates the midpoint potentials of benzyl viologen ($BV^{2+}/BV^{\cdot+}$) and menaquinone (MQ/MQH_2). *Adapted with permission from* **Paper IV**.[155]

Here are the key catalytic properties of **Huc**, as elucidated through biochemical assays and PFE experiments (**Fig. 6.3**):

Oxidation of (sub-)atmospheric levels of H_2: Purified **Huc** exhibits the capacity to oxidize H_2 present at concentrations ranging from 3 to 100 parts per million (ppm) under air (**Fig. 6.3A-B**). **Huc** rapidly consumed H_2 at subatmospheric concentrations to levels below the detection limit when employing either nitro blue tetrazolium (NBT) or menadione (MQ analogue) as electron acceptors. In contrast, the O_2-tolerant Group 1d [NiFe] hydrogenase *Hyd*1 from *E. coli* displayed a slower rate and was unable to oxidize H_2 to concentrations below 4 ppm.

High catalytic efficiency largely due to high affinity for H_2: With menadione as electron acceptor, **Huc** seemingly demonstrates high affinity for H_2 (K_m = 129 nM) and functions even at low H_2 concentrations (threshold of >31 pM) as measured in the biochemical assays. While exhibiting a slow turnover rate (k_{cat} = 7.05 s^{-1}), the enzyme achieves a near "kinetic perfection" (10^8–10^9 $M^{-1}s^{-1}$) with a specificity constant (k_{cat}/K_m) of 5.4×10^7 M^{-1} s^{-1}. This indicates that **Huc** functions with high catalytic efficiency at extremely low H_2 concentrations, compensating for its slower reaction rate.

Kinetic stability in the presence of O_2: The ability of **Huc** to oxidize H_2 at low concentrations in ambient air indicates high tolerance to O_2 inhibition, as confirmed by amperometric measurements showing no significant differences in the H_2 oxidation rate or affinity even up to 100% O_2 saturation (see **Fig. 1C** in **Paper IV**).[155]

Highest overpotential recorded for a hydrogenase: To probe the potential dependence of **Huc** activity, **Huc** was immobilized on a PGE-electrode and the currents were measured using CV (**Fig. 6.3C-D**). The CV traces confirmed that **Huc** can only oxidize H_2 since there was no significant current attributable to proton reduction. Moreover, overpotential approximately 270 mV, relative to the thermodynamic potential of the $2H^+/H_2$ redox couple ($E^{0\prime}_{2H^+/H_2}$ = −410 mV vs SHE) at the given experimental conditions (pH 7.0, 20°C, 1 atm H_2). Notably, this exceeds the overpotentials recorded for other known [NiFe] hydrogenases, including O_2-tolerant *Hyd*1 and the membrane bound hydrogenase (MBH) from *R. eutropha / C. necator*[245], as well as the irreversible [FeFe] hydrogenase *Tam*HydS (**Fig. 6.3C**).

Onset potential rationalizes high selectivity for MQ: The CV traces demonstrates **Huc**'s significant overpotential requirement. The onset potential of **Huc** (E_{onset} = −140 mV vs SHE) is more negative than the potential required for MQ reduction ($E^{0\prime}_{MQ/MQH_2}$ = −70 mV vs SHE), rationalizing **Huc**'s activity with the MQ analogue in the biochemical assays and its inactivity with benzyl viologen (BV), with a more negative or lower reduction potential ($E^{0\prime}_{BV^{2+}/BV^{\cdot+}}$ = −370 mV vs SHE) (**Fig. 6.3D**). Although NBT can act as electron acceptor given the similar midpoint potential with MQ ($E^{0\prime}_{NBT^{2+}/NBT}$ = −80 mV vs SHE), **Huc** showed a significantly higher V_{max} with the MQ analogue, in line with MQ's role as the direct physiological electron acceptor and the primary respiratory quinone in mycobacteria.[246] Structural data (**Fig. 6.2B**) further support this preference, revealing that the MQ head group is stabilized through H-bonding with specific residues. Moreover, MQ's long hydrophobic side chain facilitates its embedding within the membrane. These structural features likely contribute to the observed preference for MQ over other electron acceptors.

Onset potential likely tuned to oxidize (sub-)atmospheric levels of H_2: Given the estimated higher end of atmospheric pH_2 (≈ 3.9×10^{-10} M)[241] and the lowest detectable H_2 threshold of **Huc** (3.0×10^{-11} M), the potentials for H_2 conversion under these conditions (E_{atm}) at pH 7.0 range from −136 mV to −103 mV vs SHE, depending on the prevailing pH_2 (**Eq. 3, Chapter 2)**. This range contrasts with the −410 mV vs. SHE calculated for 1 atm H_2 at the same pH. The close alignment between the **Huc**'s onset potential (−140 mV vs SHE) and the E_{atm} for (sub-)atmospheric H_2 concentrations suggests that this enzyme is evolutionarily optimized to function under the relatively high potentials encountered when utilizing the scarce H_2 in the atmosphere. This finding implies that the overpotential, which is defined relative to the thermodynamic potential at specific conditions, might be minimal for **Huc** at these very low H_2 concentrations. Furthermore, the high potential [3Fe-4S] clusters in **Huc**, while likely contributing to its high overpotential observed at 1 atm pH_2, could also play a role in conferring resistance to oxidative inactivation. This robustness in the presence of O_2 is a crucial advantage for an enzyme operating under atmospheric conditions, a concept explored further in the subsequent section.

While **Huc** appears to operate with slow turnover and high overpotential, this could be justified as a trade-off for its remarkable affinity for H_2 and high selectivity for electron acceptors. The limited availability of H_2 has arguably driven the evolution of **Huc**'s ability to effectively scavenge this scarce resource. Additionally, the slow turnover rate and selectivity for certain electron acceptors may help mitigate the risk of **Huc** interacting with O_2 and producing harmful ROS. Collectively, these specialized catalytic features reflect an adaptive strategy that optimizes **Huc**'s physiological function in environments where H_2 is scarce and O_2 is abundant.

Spectroscopic properties of **Huc**

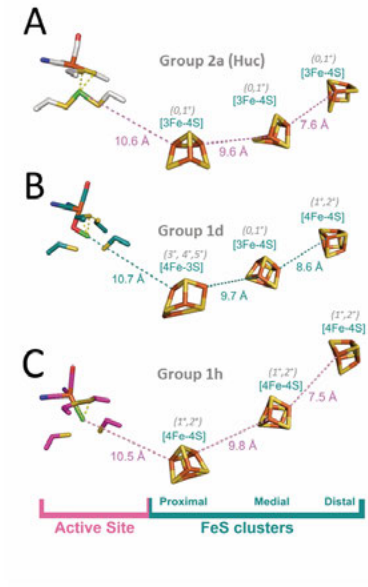

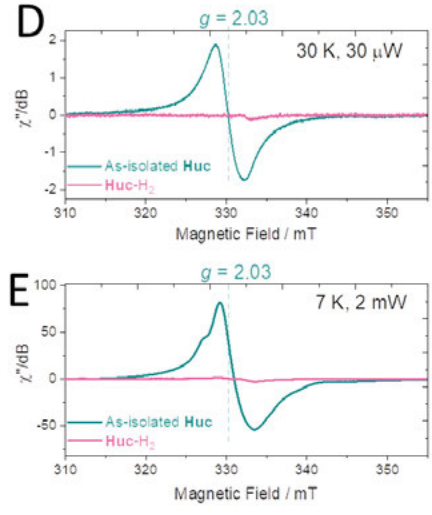

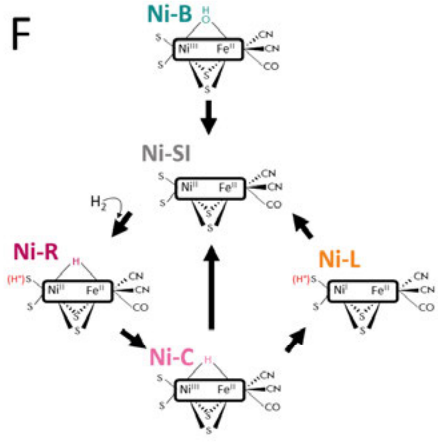

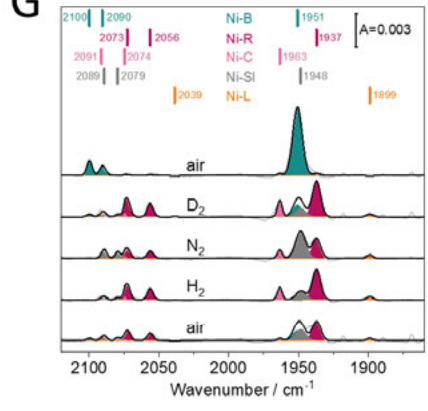

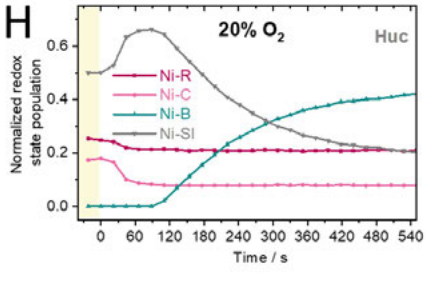

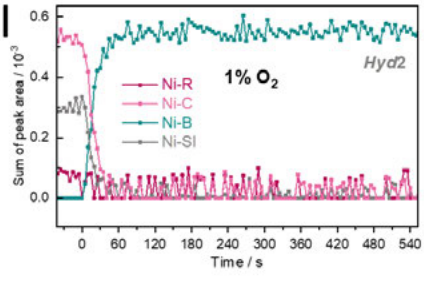

Figure 6.4 Spectroscopic properties of purified Huc (A-C) Comparison of the FeS clusters in (A) **Huc**, (B) Low-affinity, O_2-tolerant Group 1d [NiFe] hydrogenase from *R. eutropha / C. necator* in its as-isolated state (PDB ID: 7ODH),[247] and (C) high-affinity, O_2-insensitive Group 1h [NiFe] hydrogenase from *C. necator* H16 (PDB ID: 5AA5).[235] **(D-E)** EPR spectra of **Huc** in the as-isolated oxidized state (as-isolated **Huc**) and the H_2-reduced state (**Huc**-H_2) at high-temperature (30K, D) and low-temperature (7 K, E). The isotropic signal at $g = 2.03$ is associated with the oxidized [3Fe–4S]$^+$ clusters, which disappears in **Huc**-H_2 due to the reduction of the clusters to the [3Fe-4S]^0 state. No signal attributable to reduced clusters [4Fe–4S]$^+$ could be detected in the **Huc**-H_2. **(F)** Schematic representation of the proposed catalytic cycle of [NiFe] hydrogenases. **(G)** [NiFe] cluster state analysis of the **Huc** cluster by aerosol-controlled ATR-FTIR spectroscopy. **Huc** spectra were recorded under different atmospheric conditions, including air, deuterium (D_2), N_2, and H_2, revealing changes in the population of the various active site cofactor states. **(H-I)** Time-resolved FTIR data showing the kinetics of redox state transitions upon exposure to O_2 for **Huc** and the [NiFe] hydrogenase *Hyd*2 from *E. coli*. *Adapted with permission from* **Paper IV**.[155]

Selected spectroscopic insights into **Huc** derived from the analyses of its EPR and FTIR spectra include:

Exclusive binding of high-potential [3Fe-4S] clusters: The small subunit, HucS, distinguishes itself from other characterized [NiFe] hydrogenases, including low-affinity, O_2-tolerant (Group 1d) and high affinity, O_2-insensitive (Group 1h) enzymes from *R.* eutropha / *C. necator* (**Fig. 6.4A-C**), by exclusively coordinating three [3Fe-4S] clusters. This is further supported by the EPR analysis of **Huc**. The EPR spectrum of "as-isolated" **Huc** at 30 K exhibited an isotropic signal ($g = 2.03$), lacking the characteristic sharp, low-field features and anisotropic line shape of an oxidized [4Fe-4S]$^{2+}$ cluster (**Fig. 6.4D**). The isotropic signal is, instead, attributed to spin-spin interactions between the closely spaced [3Fe-4S]$^+$ clusters in **Huc**, which resulted in broadened spectral features.

Reduction of [3Fe-4S] clusters with H_2: Flushing **Huc** with H_2 led to an essentially EPR-silent sample both at 7 K and 30 K (**Fig. 6.4D-E**), consistent with the reduction of the [3Fe-4S]$^+$ clusters to their EPR-inactive form ([3Fe-4S]^0), demonstrating their redox capacity. Importantly, no broad rhombic signals characteristic of [4Fe-4S]$^+$ clusters were observed in the H_2-reduced **Huc**. This observation aligns with the Cryo-EM structural data (**Fig. 6.4A**), further supporting the conclusion that **Huc** exclusively binds high-potential clusters rather than low-potential clusters (**Fig. 6.4B-C**). This distinction is significant because [3Fe-4S] clusters generally undergo $1^+/0$ redox transitions at potentials approximately 250 mV higher than their [4Fe-4S] counterparts, transitioning between $2^+/1^+$ states.[25, 235, 248, 249]

Temperature-dependence of NiFe center: During the catalytic turnover, the Fe center of the active site cofactor maintains a divalent low-spin oxidation state (Fe^{2+}, S = 0), while the Ni center undergoes changes in oxidation and spin states (**Fig. 6.4F**). The commonly observed Ni states, such as Ni-A, Ni-B, Ni-C, and Ni-L, are more readily detected at lower temperatures (typically

up to 20 K). Under these conditions, the spectra may exhibit multiple peaks due to "splitting" of the signals, a result of strong interactions between the Ni center and the associated iron-sulfur cluster in the active site (see **Extended Data Fig. 5** in **Paper IV**).[25, 155] In contrast, at higher temperatures, the Ni states can still be detected, but with a lower intensity of split signals, and the signals may appear broader and less distinct. This can partially explain why a slightly rhombic signal emerged in the g~2 region at lower temperatures (7 K), potentially indicating interactions between the $[3Fe\text{-}4S]^{+}$ clusters and a nearby paramagnetic center, most likely the [NiFe] active site cluster (**Fig. 6.4E**).

FTIR provides spectroscopic support for the conservation of catalytic mechanism: The FTIR analysis of the **Huc**'s [NiFe] cluster revealed its redox state transitions in response to different atmospheric conditions (air, D_2, N_2, and H_2), providing spectroscopic evidence for the conservation of catalytic mechanism for H_2 oxidation (**Fig. 6.4F-H**). Under air, the cluster was in the oxidized Ni-B state (**Fig. 6.4F**), with a μOH ligand. Exposure to D_2 or H_2 replaced Ni-B with the catalytic Ni-SI, Ni-R, and Ni-C states, indicating that the inhibited Ni-B state can rapidly enter the catalytic cycle. Under N_2, the Ni-SI state is populated and re-exposure to H_2 reversed Ni-SI to the Ni-R and Ni-C states. The Ni-B state reacts more slowly with H_2 compared to the reduced Ni-SI state, as the μOH ligand must be displaced for catalysis to proceed. Re-introduction of air led to re-population of Ni-B (**Fig. 6.4G**), suggesting the **Huc** cluster can oxidize to Ni-B in O_2, like O_2-tolerant [NiFe] hydrogenases. Exposure of the mixed Ni-SI/Ni-R/Ni-C states to O_2 initially increased Ni-SI before forming Ni-B, contrasting the rapid Ni-B oxidation in O_2-sensitive [NiFe] hydrogenases such as the *Hyd*2 from *E. coli* (**Fig. 6.4H-I**), suggesting that **Huc**'s [NiFe] cluster is much more slowly oxidized by O_2. This property likely arises from the restricted access to the active site and altered redox chain properties as further discussed in the next section.

Outer coordination sphere enables ambient H_2 catalysis

A key question arises from the observation that **Huc** conserves the first and second coordination spheres and the catalytic mechanism for H_2 oxidation, yet efficiently extracts trace levels of H_2 under ambient, oxic conditions.

O_2-tolerant [NiFe] hydrogenases are proposed to employ a rapid four-electron reduction of O_2 to water at the active site. This detoxification requires delivery of four electrons by the electron relay of the small subunit, which includes a high-potential redox transition from an atypical [4Fe-3S] proximal cluster (**Fig. 6.4B**).[234] Contrastingly, O_2-sensitive types, lacking this high-potential proximal cluster, rely on slower long-range electron transfer, allowing competing degradative pathways to dominate upon O_2 exposure.

The exclusively binding of [3Fe-4S] clusters in **Huc** make it unlikely for the enzyme to perform the rapid four-electron reduction of O_2. While it is

conceivable that O_2 occasionally accessing the active site might undergo partial reduction—leveraging three electrons from the FeS clusters and one from the Ni center to yield water and a hydroxide-bound Ni-B-like state—atmospheric H_2 oxidation alone is unlikely to maintain sufficient reduction of the [3Fe-4S] clusters for this process to be sustainable.

Huc is proposed to employ a two-pronged approach for O_2-tolerance: a selective gas channel architecture that acts as a "filter", and an additional layer of protection provided by the susceptibility of the [3Fe-4S] clusters to oxidation:

Selective gas channels that filter out O_2 (Fig. 6.5): MD simulations revealed that **Huc** possesses a network of hydrophobic gas channels leading to the active site. The simulations suggest that a critical bottleneck located after the convergence of three gas tunnels immediately preceding the active site entrance plays a key role in selectively allowing the passage of H_2 while sterically excluding O_2. These specialized gas channels appear to provide a primary defense mechanism against O_2 inactivation. Furthermore, simulations of **Huc** variants designed to alleviate these bottlenecks showed increased access of O_2 to the active site, supporting the role of these selective proteinaceous filters in excluding O_2. Experimental validation of these computationally predicted effects in the **Huc** variants could provide further evidence for this mechanism. However, it should be noted that this filtering bottleneck is not unique to **Huc**, as it is also observed in the high-affinity, O_2-insensitive Group 1h [NiFe] hydrogenase from *C. necator*.[235]

Oxidation of [3Fe-4S] clusters by O_2: Even with the gas channel barrier, occasional O_2 molecules may reach the active site. Upon exposure of **Huc** to O_2, time-resolved FTIR spectroscopy reveals a sequential one-electron oxidation process (**Fig. 6.4H**). Initially, the Ni-SI state increases at the expense of the Ni-C and Ni-R states, followed by the appearance of the Ni-B state. Such a reactivity pattern suggests that O_2 primarily initiates outer-sphere oxidation of the [NiFe] active site. This electron transfer would result in O_2 reduction, potentially leading to the formation of ROS such as superoxide or peroxide. The exact fate of these reduced O_2 species and the mechanisms by which the enzyme might mitigate their potential damage is unknown. The now electron-deficient Ni in the active site coordinates a water molecule, which is subsequently deprotonated to form the hydroxide ligand of the Ni-B state. This contrasts with the O_2-sensitive *Hyd*2 from *E. coli*, where O_2 exposure leads to immediate loss of catalytically relevant states and concurrent formation of inactive Ni-B, supporting a more direct inactivation pathway in that enzyme (**Fig. 6.4I**).

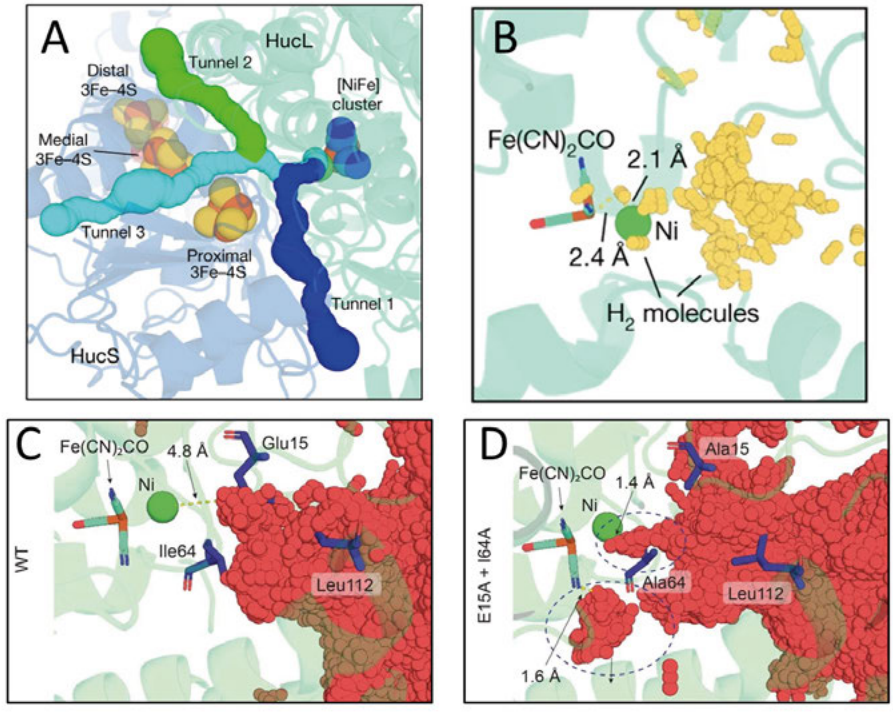

Figure 6.5 (A) MD simulations of the the HucSL dimer, illustrating the location and width of the hydrophobic gas channels (Tunnels 1-3) that enable substrate access to the active site. **(B)** The location of H_2 molecules (yellow spheres) when they are closest to the active site. **(C-D)** Depiction of the catalytic cluster from the wild-type **Huc** and gas channel mutant **Huc** variants in the MD simulations, showing the position of O_2 molecules (red spheres) in this region across the simulation frames. The residues targeted for mutagenesis are shown as sticks, and the regions with enhanced O_2 access in the E15A + I64A variant are indicated. Variant with mutations E15A + I64A + L112A can be found in **Extended Data Fig. 7**. *Reprinted with permission from* **Paper IV**.[154]

Conclusion and outlook

The structural, electrochemical, and spectroscopic investigations of purified **Huc** from trace H_2 scavenging *M. smegmatis*, yielded crucial insights into its exceptional capacity to efficiently couple atmospheric H_2 oxidation to the reduction of respiratory electron carrier menaquinone (MQ), even in the presence of "poisonous" O_2. This ability of turning "thin air into electricity" can be primarily ascribed to its intrinsic, distinctive outer coordination sphere, rather than being a consequence of coupling to other processes within the bacterial cell. These findings clearly demonstrate that the discussed properties are specific to isolated **Huc**, rather than its behavior within the cellular context.

The high H_2 affinity of **Huc** represents an adaptation to its ecological niche where H_2 is scarce. This characteristic allows **Huc** to efficiently scavenge trace H_2 and potentially outcompete other organisms for this limited energy source, stressing the importance of enzymatic affinity in shaping microbial fitness and survival in "challenging" environments.

The exclusive presence of high-potential [3Fe–4S] clusters, a departure from the typical metal cofactor composition in other [NiFe] hydrogenases, appears to be a defining feature that contributes to its elevated overpotential and directs its unidirectionality towards H_2 oxidation. This aligns with the precedent of electron transfer chain potential dictating catalytic bias in hydrogenases.[222] The overpotential modulates the enzyme's capacity to directly transfer the generated electrons to MQ. While **Huc** exhibits a high overpotential at 1 atm of H_2, this likely becomes minimal under the vanishingly low H_2 concentrations found in the atmosphere (< 1 atm). This suggests that its onset potential is a carefully calibrated adaptation that ensures efficient H_2 oxidation in its naturally H_2-scarce environment.

The shift from *L*- to *D*-histidine coordination of the proximal cluster and an unidentified ligand near the medial cluster suggest an additional mechanism for redox potential tuning in **Huc**. Further investigation into the identity and role of this ligand could provide insights for engineering enzymes with tailored redox potentials. The inherent chirality of the amino acid poses a methodological challenge, but site-directed mutagenesis techniques could be a viable approach. Given that the *D*-coordination appears integral to the enzyme's function, there are likely other residues that have co-evolved to accommodate this atypical chirality, and these could be targeted for variation. Alternatively, targeting genes potentially involved in the unconventional biosynthetic pathway for this atypical *D*-insertion is an option.

The O_2 insensitivity of **Huc** appears to arise from a combination of factors: selective gas channels that restrict O_2 access and allow selective H_2 routing to the active site, and oxidation of metallocofactors that favors the formation of a protective active site state upon limited O_2 exposure. These adaptations position **Huc** as a promising candidate for biotechnological applications requiring efficient H_2 oxidation under ambient, O_2-containing conditions.

Additionally, insights into the enzyme's high affinity for H_2 could lead to novel approaches for capturing and utilizing trace atmospheric gases. It is important to recognize that while **Huc** exhibits a slow turnover rate, approaches such as directed evolution and rational enzyme design could potentially improve its catalytic rates while maintaining its O_2-tolerance. More detailed electrochemical analyses could also provide insights into the electron transfer kinetics of **Huc** and its variants, which could help identify rate-limiting steps and guide further optimization efforts. Such efforts will be crucial to fully harness its potential in (a)biotic applications.

The study of **Huc** holds broader implications for our understanding of atmospheric chemistry and the microbial ecology of extreme environments. While **Huc** itself specializes in scavenging trace H_2, its existence hints at a broader array of microbial metabolic strategies yet to be uncovered. Could there be other enzymes, perhaps with different cofactors or electron transfer mechanisms, enabling organisms to utilize H_2 as an energy source across a spectrum of concentrations? Further exploration of these adaptations could illuminate not only the evolution of metabolism on early Earth but also the potential for life in the diverse energy landscapes beyond our planet.

Chapter 7: Summary and Final Remarks

Reflecting on the initial aims outlined in the introduction, my PhD journey exceeded expectations. While the primary objectives of identifying novel hydrogenases, investigating some of their underlying principles, and applying this knowledge to engineer improved biocatalysts were achieved, the research also ventured into unexpected avenues.

Challenging established paradigms: We overturned the long-held belief that [FeFe] hydrogenases are absent in archaea, uncovering their presence in diverse archaeal lineages, including minimal symbionts, ancient hybrid lineages, and at the prokaryote-eukaryote interface. This discovery reshapes our understanding of hydrogenase evolution and expands their known diversity, opening new doors to previously unimagined enzymatic properties. Characterizing the smallest hydrogenase to date redefined the minimal size requirement in functional H_2-processing biocatalysts, offering a new blueprint for the most compact catalysts.

Supporting the importance of proton transfer: The comparative analysis of [FeFe] hydrogenase groups revealed distinct proton transfer pathways, highlighting their significant role in fine-tuning enzymatic function. By disrupting these pathways, we demonstrated their impact on active site geometry, electronic structure, and catalytic bias. Such findings could provide mechanistic insights for engineering improved synthetic catalysts that integrate proton transfer and redox chemistry.

Harnessing evolutionary insights for rational engineering: Guided by phylogenetic comparisons and structural insights, we rationally engineered a Group D [FeFe] hydrogenase, significantly enhancing its H_2 production rates and inhibitor tolerance. This success underscores the potential of integrating evolutionary information with protein engineering for developing robust and efficient biocatalysts.

Revealing novel mechanisms for H_2 extraction and utilization: We elucidated the mechanism of an O_2-tolerant [NiFe] hydrogenase (**Huc**) capable of oxidizing trace atmospheric H_2. The enzyme's high H_2 affinity most likely stems from its selective molecular "sieves". Such principle, applicable to catalyst design, involves engineering channels or pores that act as gatekeepers, granting access only to H_2 while barring potential inhibitors (*e.g.*, O_2). The atypical composition of electron transfer cofactors in **Huc** can also inform the design of catalysts to control reaction pathways. Incorporating specific metal

clusters into catalysts can adjust the redox potentials. This can enhance the catalyst's selectivity towards the desired reactions, such as the unidirectional oxidation of H_2 observed in **Huc**.

While the initial roadmap yielded notable findings, the PhD journey also encountered bottlenecks. Future endeavors would benefit from:

Developing robust heterologous expression platforms: Engineering expression hosts capable of efficiently producing archaeal hydrogenases would accelerate their biochemical and biotechnological characterization. This could involve exploring alternative expression systems, such as engineered microbial hosts with optimized codon usage, chaperone machinery, and enhanced metal cofactor trafficking pathways for complex metalloenzyme production.

Investigating "non-traditional" maturation pathways: Understanding the machinery responsible for assembling hydrogenases particularly in diverse archaeal hosts could include identifying and characterizing the specific chaperones, scaffold proteins, and metal cofactor insertion mechanisms. Such knowledge could guide the development of co-expression systems or *in vitro* maturation protocols to overcome bottlenecks in heterologous production.

Expanding the repertoire of biophysical techniques for in-depth structure-function analysis: This work, while employing a range of techniques, was limited by the lack of experimentally determined structures for the studied hydrogenases, with the exception of **Huc**. Future work could benefit from integrating other biophysical approaches to gain a comprehensive understanding of structure-function relationships. For instance, efforts to obtain high-resolution crystal or cryo-EM structures of the novel hydrogenases identified in this study could provide a foundation for (re)interpreting biochemical data and guiding rational enzyme engineering efforts. Incorporating spectroelectrochemistry techniques could help determine reduction potentials, identify transient intermediates, and monitor (de)protonation events. Advanced imaging techniques like super-resolution microscopy and single-molecule tracking offer the potential to visualize interactions within cells. While directly observing real-time assembly of complex enzymes remains challenging, these *in vivo* approaches could provide insights into the factors governing enzyme function within their native cellular environment.

Implementing high-throughput screening platforms for accelerated biocatalyst discovery: We've only explored a tiny fraction (0.1-1%) of the vast diversity of these enzymes. Developing sensitive, scalable assays compatible with high-throughput methods will be crucial for rapidly characterizing their properties and identifying promising candidates for specific biotechnological applications. This could involve screening enzyme libraries for enhanced activity, stability, or tolerance to specific inhibitors or environmental conditions. The key challenge lies in developing highly sensitive, specific, and gas-tight detection methods to closely monitor catalytic activities and O_2-tolerance, as well as advancing miniaturization and automation technologies. One can

imagine high-throughput screening approaches using microfluidic devices and sensors that change their fluorescence intensity or wavelength upon binding to or reacting with H_2. Alternatively, microelectrode-based systems could detect the electrochemical currents generated during H_2 oxidation or production. Microfluidic systems that offer precise control over fluid flow and gas concentrations could facilitate the assessment of enzyme performance under varying O_2 levels. Additionally, colorimetric assays detecting ROS could help identify enzymes with notable O_2-tolerance, as those exhibiting lower ROS production would suggest improved tolerance to such conditions.

Directed evolution for tailored functionality: Directed evolution strategies, coupled with high-throughput screening, could be leveraged to evolve hydrogenases with tailored properties. This approach can generate enzymes with enhanced activity, altered substrate specificity, or increased tolerance to challenging industrial conditions, ultimately accelerating their development into robust and efficient biocatalysts.

Hydrogenases have profoundly shaped our planet's past and present. By studying how they are able to perfect H_2-handling while leveraging earth-abundant metals, we gain invaluable insights for substituting rare and expensive noble metals in electrolytic and fuel cells. Their extraordinary diversity offers a rich trove of natural solutions for optimizing catalytic activity, efficiency, gas specificity, and stability.

Building a H_2 society akin to the microbes might require exploring and tapping the undiscovered 99%. I hope that my thesis serves as a humble yet compelling invitation to delve deeper into this exciting field, where the keys to a “greener” future may very well be found in the vast microbial world.

Popular Science Summary

Some texts were adapted from the 2024 Coimbra Group 3-Minute Thesis (3MT) Live Finals presentation. Timestamp 10:30 at: youtube.com/watch?v=ZrNxcT8Fw1E

Imagine a world powered by the most abundant element in the universe, hydrogen. In the face of the climate crisis, this isn't merely a dream—it's a necessity. Hydrogen (H_2) as a fuel is so mighty it packs a punch three times stronger than gasoline. And when it burns? It doesn't pollute the air. But why isn't it powering our world yet?

Because getting energy from H_2 is like playing a game where it costs us more points to play than we can win. We use more energy than we get back. To make H_2, we're still using fossil fuels—the very culprits we're trying to replace. We also need expensive and hard-to-find metals like platinum to drive these H_2-related processes.

But perhaps we can take cues from Nature. For billions of years, tiny living things or microbes have been using H_2 as their source of energy. They achieve this using simple and cheap metals like nickel and iron. How? By using natural tiny machines or enzymes called hydrogenases.

In my thesis, I delve into these hydrogenases—catalysts that can efficiently handle H_2 even when using inexpensive metals. Among them are [FeFe] hydrogenases, consisting of iron atoms, and [NiFe] hydrogenases, combining both nickel and iron. By studying these enzymes, we could learn how to make or use H_2 in a better way.

For a long time, scientists thought they knew where to find [FeFe] hydrogenases: in bacteria and eukarya (*e.g.*, plants and animals). However, we challenged such long-held belief by uncovering their presence in archaea, a distinct prokaryotic domain of life often found in extreme environments. This discovery expands the known diversity of these enzymes and demonstrates their role in enabling some archaea to thrive in challenging habitats where most other life forms cannot.

Delving deeper into the intricacies of [FeFe] hydrogenases, we revealed that each group within this family possesses a distinct "proton transfer pathway"—the route taken by "positive particles" called protons to reach the enzyme's "action zone". This finding helps us understand how these enzymes have evolved to work efficiently in different organisms and environments.

Inspired by Nature's ingenuity, I leveraged structural knowledge and evolutionary insights to engineer a hybrid [FeFe] hydrogenase. By combining

elements from different groups, I created an enzyme that's faster and more resilient than its slower, natural counterpart. Evolutionary insights guided the way, showing that sometimes, a little genetic matchmaking can breathe new life into the slowest of enzymes.

Nature's prowess in H_2 utilization extends beyond [FeFe] hydrogenases. Imagine a device that could pull clean energy right out of thin air. Nature has already invented it – like a [NiFe] hydrogenase, nicknamed **Huc**. This enzyme is able to pull H_2 from the air, even though it's only a tiny fraction of what we breathe (a mere 0.00006%), while effectively filtering out its nemesis, oxygen, in the process. By incorporating **Huc** into an electrical circuit, we found that it can directly create electricity from the captured atmospheric H_2.

This thesis highlights Nature’s adaptability (even in the most challenging environments) and opens up exciting possibilities for using these enzymes in biotechnology and renewable energy. We can bypass fossil fuels and costly metals by turning to these ancient enzymes. By deciphering their secrets, we may unlock efficient and greener ways to store clean fuel or converting it into electricity. These seasoned architects could also provide the design specs for synthetic mimics.

Microbes have already cracked the code of a sustainable H_2 economy, but I’ve barely scratched the surface of their vast diversity. To build a H_2 society like theirs, we need to mine more of what’s out there.

Svensk Sammanfattning

Föreställ dig en värld som drivs av det mest förekommande ämnet i universum, väte. I ljuset av klimatkrisen är detta inte bara en dröm—det är en nödvändighet. Vätgas (H_2) som bränsle är så kraftfullt att det har tre gånger mer energi än bensin. Och när det brinner, förorenar det inte luften. Men varför driver det inte vår värld ännu?

Att få energi från H_2 är i nuläget ungefär som att spela ett spel där det kostar oss fler poäng att spela än vi kan vinna. Vi använder mer energi än vi får tillbaka. För att framställa H_2 använder vi fortfarande fossila bränslen—det problem vi försöker ersätta. Vi behöver också dyra och ovanliga metaller som platinum för att driva dessa H_2-processer.

Men kanske kan vi få inspiration från naturen. I miljarder år har små organismer eller mikrober använt H_2 som sin energikälla. De klarar detta genom att använda vanliga (och billiga) metaller som nickel och järn. Hur? Genom att använda naturliga små maskiner eller enzymer kallade hydrogenaser (som kan översättas till väteasaser).

I min avhandling dyker jag ner bland dessa hydrogenaser—katalysatorer som kan processa H_2 effektivt utan något behov av platina. Bland dem finns [FeFe] hydrogenaser, som använder järnatomer, och [NiFe] hydrogenaser, som kombinerar både nickel och järn. Genom att studera dessa enzymer kan vi lära oss hur vi kan tillverka eller använda H_2 på ett bättre sätt.

Under en lång tid trodde forskare att de visste var man skulle hitta [FeFe] hydrogenaser: i bakterier och eukaryoter (t.ex. växter och djur). Men vi omkullkastade detta genom att bevisa deras existens även i arkéer. Denna upptäckt utvidgar den kända mångfalden av dessa enzymer och påvisar deras roll i att möjliggöra för vissa arkéer att trivas i extrema miljöer där de flesta andra livsformer inte kan överleva.

Genom att dyka djupare i detaljerna kring [FeFe] hydrogenaser, avslöjade vi att varje grupp inom denna familj har en distinkt "protonöverföringsväg"—den väg som de "positiva partiklarna" kallade protoner tar för att nå enzymets "aktiva säte". Denna upptäckte hjälper oss att förstå hur dessa enzymer har utvecklats för att fungera effektivt i olika organismer och miljöer.

Inspirerad av naturens uppfinningsrikedom använde jag strukturell kunskap och evolutionära insikter för att konstruera ett hybrid [FeFe] hydrogenas. Genom att kombinera komponenter från olika grupper skapade jag ett enzym som är snabbare och mer motståndskraftigt än sin långsammare, naturliga

motsvarighet. Evolutionära insikter visade vägen och arbetet visade att ibland kan lite genetisk par-matchning ge nytt liv till de långsammaste av enzymer.

Naturens förmåga att utnyttja H_2 sträcker sig bortom [FeFe] hydrogenaser. Föreställ dig en maskin som extraherar ren energi direkt ur luften. Naturen har redan uppfunnit den – i form av ett [NiFe] hydrogenas, kallat **Huc**. Detta enzym klarar av att dra H_2 från luften, även om det bara är en liten bråkdel av det vi andas (enbart 0,00006%), samtidigt som det effektivt filtrerar bort sin nemesis, syrgas, i processen. Genom att inkorporera **Huc** i en elektrisk krets, har vi visat att det kan driva ström med den infångade atmosfäriska vätgasen.

Denna avhandling belyser naturens anpassningsförmåga (även i de mest utmanande miljöerna) och öppnar upp spännande möjligheter för att använda dessa enzymer inom bioteknik och förnybar energi. Vi kan kringgå fossila bränslen och kostsamma metaller genom att vända oss till dessa uråldriga enzymer. Genom att avkoda deras hemligheter kan vi kanske låsa upp effektiva och grönare sätt att lagra ren energi i form av H_2 eller omvandla det till elektricitet. Dessa erfarna arkitekter kan också ge designspecifikationer för syntetiska kopior.

Mikrober har redan knäckt koden för en hållbar H_2-ekonomi, men jag har knappt skrapat på ytan av deras stora mångfald. För att bygga ett H_2-samhälle som deras, behöver vi utforska mer av det som finns där ute.

Buod ng agham

Isipin mo ang isang mundong pinapapatakbo ng pinakamaraming elemento sa kalawakan—hydrogen. Sa harap ng krisis sa klima, hindi lang ito isang hangarin—isang pangangailangan ito. Ang hydrogen (H_2) bilang isang fuel ay napakalakas, tatlong beses na mas malakas kaysa gasolina. At kapag ito'y nasunog? Hindi nito pinapadumi ang hangin. Pero bakit hindi pa ito nagpapagana ng ating mundo?

Dahil ang pagkuha ng enerhiya mula sa H_2 ay parang pakikilahok sa isang laro kung saan mas malaki ang ginagastos kaysa sa nakukuhang puntos. Mas marami tayong enerhiyang ginagamit kaysa sa nakukuha. Para gumawa ng H_2, gumagamit pa rin tayo ng fossil fuels—ang mismong mga salarin na gusto nating palitan. Kailangan din natin ng mga mamahalin at bihirang metal tulad ng platinum para patakbuhin ang mga proseso na may kinalaman sa H_2.

Sakali ay may matututunan tayo mula sa Kalikasan. Sa bilyun-bilyong taon, ang maliliit na nilalang o microbes ay gumagamit ng H_2 bilang kanilang pinagmumulan ng enerhiya. Nagagawa nila ito gamit ang simple at murang mga metal tulad ng nickel at iron. Paano? Sa pamamagitan ng natural na maliliit na makina o enzymes na tinatawag na hydrogenases.

Natuklasan at nasuri ko ang mga hydrogenases—mga katalista na kayang mahusay na humawak ng H_2 gamit ang murang mga metal. Kabilang dito ang [FeFe] hydrogenases, na binubuo ng mga iron atoms, at [NiFe] hydrogenases, na pinagsasama ang nickel at iron. Sa pag-aaral ng mga enzyme na ito, maaari tayong matuto ng mas magandang paraan ng paggawa o paggamit ng H_2.

Sa mahabang panahon, inakala ng mga siyentipiko na alam na nila kung saan matatagpuan ang [FeFe] hydrogenases: sa bacteria at eukarya (halimbawa, halaman at hayop). Ngunit hinamon namin ang matagal nang paniniwalang ito sa pamamagitan ng pagtuklas ng kanilang presensya sa archaea, isang natatanging prokaryotic domain ng buhay na kadalasang matatagpuan sa mga ekstremong kapaligiran. Pinalawak ng tuklas na ito ang kilalang pagkakaiba-iba ng mga enzyme na ito at ipinakita ang kanilang papel sa pagpapahintulot sa ilang archaea na mabuhay sa mga hamong kapaligiran kung saan hindi kayang mabuhay ng karamihan ng iba pang mga anyo ng buhay.

Sa masusing pagsusuri sa mga detalye ng [FeFe] hydrogenases, natuklasan namin na ang bawat grupo sa loob ng pamilyang ito ay may natatanging "proton transfer pathway"—ang ruta na tinatahak ng mga "positibong partikulo"

na tinatawag na protons upang makarating sa "action zone" ng enzyme. Ang tuklas na ito ay tumutulong sa atin na maunawaan kung paano nag-evolve ang mga enzyme na ito upang gumana nang mahusay sa iba't ibang organismo at kapaligiran.

Sa inspirasyon ng kagalingan ng Kalikasan, ginamit ko ang kaalaman sa estruktura at mga natuklasan sa ebolusyon upang magdisenyo ng isang hybrid na [FeFe] hydrogenase. Sa pamamagitan ng pagsasama ng mga elemento mula sa iba't ibang grupo, nakalikha ako ng isang enzyme na mas mabilis at mas matibay kaysa sa mabagal na likas na katumbas nito. Ang mga kaalaman mula sa ebolusyon ang naging gabay, ipinapakita na minsan, ang kaunting genetic na pagmamanipula ay maaaring magbigay ng bagong buhay sa pinakamabagal na enzyme.

Ang kagalingan ng Kalikasan sa paggamit ng H_2 ay hindi nagtatapos sa [FeFe] hydrogenases. Isipin mo ang isang aparato na kayang kumuha ng malinis na enerhiya mula sa manipis na hangin. Nagawa na ito ng Kalikasan—gaya ng isang [NiFe] hydrogenase, na tinawag na **Huc**. Ang enzyme na ito ay kayang kumuha ng H_2 mula sa hangin, kahit na ito'y napakaliit na bahagi lamang ng ating nalalanghap (0.00006% lamang), habang epektibong sinasala ang kanyang kaaway na oxygen. Sa pamamagitan ng pag-incorporate ng **Huc** sa isang electrical circuit, natuklasan namin na kaya nitong direktang lumikha ng kuryente mula sa nakuhang H_2 sa hangin.

Ang tesis na ito ay nagpapakita ng kakayahan ng Kalikasan na mag-adapt (kahit na sa pinakamahihirap na kapaligiran) at nagbubukas ng mga kapana-panabik na posibilidad para sa paggamit ng mga enzyme na ito sa biotechnology at renewable energy. Maaari nating lampasan ang fossil fuels at mamahaling metal sa pamamagitan ng pagtutok sa mga sinaunang enzyme na ito. Sa pag-decipher ng kanilang mga sikreto, maaaring mabuksan natin ang mas episyente na mga paraan ng pag-iimbak ng malinis na fuel o pagkoconvert nito sa kuryente. Ang mga bihasang arkitekto na ito ay maaari ring magbigay ng disenyo para sa mga synthetic mimics.

Na-crack na ng mga microbes ang code ng isang sustainable na H_2 economy, ngunit ngayon pa lamang ako nagsisimulang magsaliksik sa napakalawak nilang pagkakaiba-iba. Upang makabuo ng isang H_2 society tulad ng sa kanila, kailangan nating tuklasin pa ang mas marami pang nandiyan.

Siyensya sa sumada

Imagineha ang usa ka kalibutan nga gipadagan sa pinakadaghang elemento sa tibuok universe—ang hydrogen. Sa atubangan sa krisis sa klima, dili lang kini usa ka damgo—usa kini ka kinahanglanon. Ang hydrogen (H_2) isip usa ka gasolina kay kusgan kaayo, tulo ka beses nga mas kusgan kaysa gasolina. Ug kung kini mosilaob? Dili kini makadaot sa hangin. Apan ngano nga wala pa kini nagpadagan sa atong kalibutan?

Tungod kay ang pagkuha ug enerhiya gikan sa H_2 sama sa pagdula ug usa ka duwa nga mas daghan pa ang magasto kaysa makuha. Mas daghan kita ug enerhiya nga gigamit kaysa nakuha. Aron makahimo ug H_2, naggamit gihapon kita ug fossil fuels—ang mga salarin nga gusto natong ilisan. Kinahanglan usab nato ang mga mahal ug lisud pangitaon nga mga metal sama sa platinum aron padaganon ang mga proseso nga apil ang H_2.

Apan tingali makaamgo kita gikan sa Kinaiyahan. Sulod sa bilyon ka mga tuig, ang mga kagaw o microbes naggamit na ug H_2 isip ilang tinubdan sa enerhiya. Nagbuhat sila niini gamit ang yano ug barato nga mga metal sama sa nickel ug iron. Giunsa? Pinaagi sa paggamit ug natural nga gagmayng mga makina o enzymes nga gitawag ug hydrogenases.

Sa akong tesis, akong gitun-an kini nga mga hydrogenases—mga katalista nga makahimo ug epektibong pagdumala sa H_2 bisan pa sa paggamit ug barato nga mga metal. Lakip niini ang [FeFe] hydrogenases, nga naglangkob ug mga iron nga atomo, ug [NiFe] hydrogenases, nga nagkumbinar sa nickel ug iron. Pinaagi sa pagtuon niini nga mga enzymes, mahimo kitang makat-on sa mas maayong paagi sa paghimo o paggamit sa H_2.

Sulod sa dugay nga panahon, nagtuo ang mga syentipiko nga nahibal-an na nila kung asa makita ang [FeFe] hydrogenases: sa bakterya ug eukarya (pananglitan, mga tanom ug hayop). Apan among gi-hagit kini nga dugay nang gibarugan nga pagtuo pinaagi sa pagdiskobre sa ilang presensya sa archaea, usa ka lahi nga prokaryotic domain sa kinabuhi nga kasagaran makita sa mga ekstremen nga palibot. Kini nga nadiskobre nagpalapad sa nailhang kalainan sa kini nga mga enzymes ug nagpakita sa ilang papel sa pagtugot sa pipila ka archaea nga molahutay sa mga lisud nga mga palibot diin ang kadaghanan sa uban nga mga porma sa kinabuhi dili makabuhi.

Sa mas lawom nga pagsusi sa mga [FeFe] hydrogenases, among nadiskobre nga ang matag grupo sulod niini nga pamilya adunay usa ka talagsaon nga "proton transfer pathway"—ang ruta nga agian sa mga “positibong partikulo”

nga gitawag ug protons aron makaabot sa "action zone" sa enzyme. Kini nga pagdiskobre makatabang kanato nga masabtan kung giunsa pag-milambo kini nga mga enzymes aron magtrabaho nga episyente sa lain-laing mga organismo ug palibot.

Pinaagi sa inspirasyon gikan sa Kinaiyahan, gigamit nako ang kaalam sa estruktura ug mga panan-aw sa ebolusyon aron mag-engineer ug usa ka hybrid nga [FeFe] hydrogenase. Pinaagi sa pagkombinar sa mga elemento gikan sa lain-laing mga grupo, nakabuhat ko ug usa ka enzyme nga mas paspas ug mas lig-on kaysa sa hinay nga natural nga kapariha niini. Ang mga panan-aw gikan sa ebolusyon ang naggiyahan sa dalan, nagpakita nga usahay, usa ka gamay nga pagpares sa mga genes makapabaskog sa labing hinay nga mga enzyme.

Ang kinaadman sa Kinaiyahan sa paggamit sa H_2 nagpadayon labaw pa sa [FeFe] hydrogenases. Imagineha ang usa ka himan nga makahimo ug malimpyo nga enerhiya gikan sa manipis nga hangin. Naimbento na kini sa Kinaiyahan—sama sa usa ka [NiFe] hydrogenase, nga gitawag ug **Huc**. Kini nga enzyme makahimo ug kuhaon ang H_2 gikan sa hangin, bisan pa sa gamay ra nga bahin sa atong ginaginhawa (0.00006% ra), samtang epektibo nga gisala ang iyang kaaway nga oxygen. Pinaagi sa pag-ilakip ni **Huc** sa usa ka elektrikal nga sirkito, among nadiskobre nga mahimo kini nga direktang maghimo ug kuryente gikan sa nakuha nga H_2 sa hangin.

Kini nga tesis nagpakita sa kakayahan sa Kinaiyahan sa pag-adapt (bisan pa sa labing lisud nga mga palibot) ug nagbukas sa mga makapadasig nga mga posibilidad alang sa paggamit niini nga mga enzymes sa bioteknolohiya ug renewable na enerhiya. Mahimo natong lampasan ang fossil fuels ug mahal nga mga metal pinaagi sa pag-atubang niini nga mga karaang enzymes. Pinaagi sa pag-decipher sa ilang mga sekreto, mahimo natong maablihan ang episyente ug limpyo nga mga paagi sa pagtipig sa malimpyo nga gasolina o pag-convert niini ngadto sa kuryente. Kini nga mga bihasang arkitekto mahimo usab nga maghatag ug mga disenyo para sa mga sintetiko na mimic o mga magsundog sa aning mga enzymes.

Naka-crack na sa mga microbes ang kodigo sa usa ka malungtaron nga H_2 na ekonomiya, apan bag-o pa lang ako nagsugod sa pag-usisa sa ilang daghan nga kalainan. Aron matukod ang usa ka H_2 katilingban sama sa ila, kinahanglan natong masusi ang dugang pang mga posibilidad nga anaa.

Acknowledgements

"It takes a village to raise a child."

This proverb aptly reflects the journey to get to this point. I would like to thank the following "village" members for helping me reach this PhD milestone:

I would first like to acknowledge my supervisor, **Gustav**. Thank you for taking a chance on an applicant for the PhD position who came from a country with a relatively unknown record of scientific training. I am grateful for your guidance throughout the whole process, which is marked by your patience, kindness, wisdom, and unwavering enthusiasm for science. Thank you also for ensuring that I am connected to the right people and providing the necessary tools and, often, motivation to do the job with excellence.

I am deeply grateful to my co-supervisors, **Henrik** and **Alina**, for paving the way and providing a solid foundation for me to pursue and complete my research projects. Thank you for your patience, especially when I initially struggled to grasp certain concepts. I am also thankful for your helpful feedback and clear guidance throughout the development of this thesis.

Thank you so much, **Johannes**, for your inspiring leadership in the research group, fostering a very pleasant work environment. I am grateful for your sharp, constructive comments as you thoughtfully reviewed my thesis drafts, guiding me to produce high-quality work.

To the EPR wizard, **Ping**, I extend my deepest gratitude for your steadfast openness and enthusiasm in measuring I think more than 200 of my samples (I have lost count). Your remarkable patience in teaching me the ways of EPR, even when I barely grasped the concepts, has been helpful in my growth and in finishing my projects.

To the FTIR dynamic duo, **Moritz** and **Sven T. S.**, thank you for always being ready to read some of my samples… even if that means "killling" the enzymes, which I worked hard to isolate, with O_2 in the end. Your contributions through your expertise and insights have been really invaluable.

Extending my gratitude to **Chris** and **Rhys**, on the other side of the world, for entrusting me with your samples and involving me in your most impactful projects. Your trust and collaboration have been tremendously meaningful to me.

To the OG "PhDinis", **Holly**, **Marco**, and **Afridi**, it was a pleasure to share this journey together. I'm deeply appreciative of how you smoothed the path, like ensuring the gloveboxes were operating properly, and assisting me, a

petite individual, in carrying the heavy gas tanks. You were all so kind, understanding, and fun to hang out with inside and outside the lab.

To the new hydrogenase enthusiasts, **Conrad**, **Eda**, and **Ivan**, I hope I was a decent mentor in a sense, even though my stressors did not always bring out the best in me. I wish you all the best with your PhD journey.

To my wonderful cat-sitter(s), **Larissa** (and **Corentin**), thank you so much for taking care of Yuumi whenever I'm on long trips. You cared for her so well, and even had the patience to walk her everyday, just as she prefers.

Thank you, **Max B.**, for also sharing this journey with me from the beginning and for helping me significantly when I was still a very clumsy first-year student. I'm glad we had the opportunity to hang out a lot in Seattle and enjoy the most delicious coffee from that area - I really miss those times.

To the echem bois, **Nikos**, **Zhao**, **Sagar**, **Andrew B.**, and **Alex**, thank you for answering many of my questions about electrochemistry and for always being ready to help me when there were issues with the instruments.

Thank you also to **Orkun**, **Nicholas**, **Claudia**, and **Sofie** for the check-ins and for contributing so much to the welfare of the group/lab. I have no doubt you will all excel in your PhD journeys.

To my former students, **Prasenjit**, **Max K.**, **Kaija**, and **Astrid**, thank you for teaching me how to become a better teacher. I hope you learned a lot from me, as I have learned a great deal from you.

Thanks to all the **BBC** members, both past and present, who have been so consistently helpful, supportive, and fun to spend time with in the office and in the lab: **Fikret**, **Felix**, **Ann**, **Michael**, **Marcus**, **Nessima**, **Shipra, Livia**, **Mira**, **Sergii**, **Fatemeh**, **Petko**, **Luca**, **Catia**, **Ankita**, **Manuel**, **Andrew H.**, **Leonardo**, **Meiyuan**, and **Shaoqi**.

Thank you, **Amit**, for co-weathering the stresses of our parallel thesis writing journey together. We finally made it.

To the other side of the corridor, **Peter**, **Pia**, **Cissi**, **Karin**, **Kate**, **João**, **Matina**, **Hao**, **Jorge**, **Kim**, **Nikoleta**, **Guillaume**, **Samantha**, **Paul**, and other **cyanos**, thank you for generously allowing me to use your instruments and reagents, which were necessary for completing some of my projects.

To the **Fyskem** and **SMC** members downstairs, especially to **Leif**, **Starla**, **Haining**, **Victor**, **Leigh Anna**, **Samir**, **Salauat**, **Sree**, **Vitor**, **Beri**, **Nora**, **Monika**, **Andrea**, **Rima**, **Anđela**, **Mariia**, **Belinda**, **Martin**, **Thuan**, **Sigrid**, **Nina**, and **Sina**, thank you for letting me use emergency liquid nitrogen, reagents, and regeneration tanks whenever we ran out upstairs and for allowing me to hang out downstairs while waiting for spectroscopy measurements to finish. I'd like to specifically thank **Roman** for the huge help in bringing up the heavy regeneration tanks and for assisting me in fixing Jodie when she was seriously malfunctioning.

To the perovskiters, **Aneta** and **Fiona**, thank you for graciously allowing me to use your office space whenever I needed it. I really appreciated the peaceful solitude it provided.

To the Chinese (and "ex-basement") gang, **Yawen**, **Sicong**, **Minli**, **Fangwen**, **Hongwei**, **Chen**, **Qixiao**, **Qian**, and **Bin**, thank you for all the hangouts, especially for the times we ate at the best restaurant in Uppsala, none other than Golden China.

Thank you, **Shima,** for always lifting my spirits with your encouraging words and positive energy even whenever we chance upon each other in the corridor between Hus 6 & 7. You're already achieving amazing success, and I'm confident you will complete your PhD studies with great distinction.

To **Sven**, the pillar of the whole Hus 7, I extend my sincerest gratitude for all your help. It has been wonderful to have someone with whom I can engage in random conversations about life, sometimes even in Filipino, especially when I miss home dearly. I hope you are thoroughly enjoying your retirement. I look forward to our future Filipino food hangouts. Again, maraming salamat.

I'm extremely grateful to the community of Filipinx scholars in Uppsala, **kuya Max** (and **Seb**), **Mark Dennis**, **Ella**, **Eula**, **Mac**, **Carla**, **Michelle**, **Richelle**, **Therese**, **Danjo**, **Jux**, **Louie**, **Romerino**, **Shery Rose**, and everyone else. The sense of belonging and familiarity makes me feel as if I'm home away from home. Maraming salamat mga beks sa lahat ng tawa, laps, chika, and for bringing life and warmth especially kapag winter. Special mention kay kuya Max and Mark Dennis for promptly proofreading the translated popular science summaries.

Shoutout to the **GradMAP PH** community for entrusting me to be part of the leadership committee. The outreach efforts helped keep me sane.

To **Kuya Joel** and **Kuya Zaldy**, salamat sa pag-ensure that I received my passport on time, despite the numerous challenges due to the COVID-19 pandemic. I was extremely stressed during that period and uncertain about my ability to fly to Sweden, but your extraordinary efforts made it possible for me to obtain my passport on time. Thank you sincerely for going above and beyond to make this happen.

I want to thank my MS mentors, **Sir Pat** and **Ms. Queenie**, for believing in me and wholeheartedly providing very convincing letters of recommendation to support my grad school apps.

To my fellow prom queens (char), **Andie**, **Shine**, and life-is-here beshie **Amor**, salamat kaayo mga dzae for your unwavering support and love, even though we are separated by multiple time zones. Love us forev.

Thank you, **Hranush**, for always being so game to take super nice photos during our random trips. I'm also grateful for all your insights about life in general, and for comforting me in times of need.

To min bror, **Catherine**, I couldn't have asked for a better PhD buddy on this whole journey. Thank you for the constant support, hype, for making sure that I eat (my veggies) well and that I am warm, for proofreading my thesis, for being my best dance buddy, for flying all the way to Paris with me for a concert, and so much more. You truly are the best min bror. I'm also grateful for your and **Svante**'s care of Yuumi whenever needed.

Shoutout to familja G: **Sari**, **Krister**, **Paui**, **Micke**, **Daniel**, **Fanny**, and, **Erik** for the fun hangouts, memorable vacation trips, and moral support.

To my own little family, **Anton** and **Yuumi**, I am profoundly thankful. Anton, you have taught me that there is more to life than just work. Words cannot express how deeply grateful I am for you. Thank you for being so kind, patient, and understanding, for being my best friend, my best travel companion, the best 3MT speech proofreader, and the best co-pawrent for Yuumi. And Yuumi, even though you cannot read this, I want to thank you for meowtivating me and for giving me the inspurration to keep pushing forward.

Finally, to my parents who have sacrificed so much since day one. Daghang salamat, **papa Garry** and **mama Rosa**, for providing me with opportunities from a young age. I am truly privileged, and I owe you a great debt for devoting your resources to ensuring I receive the best education from the start. I am immensely grateful for your steadfast love and support, despite the great physical distance between us. This is all for you and I hope I have made you proud.

Special mention to the **Swedish Energy Agency** for funding my studies and to **C F Liljewalchs Resestipendier** for travel grants that enabled me to attend international conferences in the US and Japan.

I would like to end this acknowledgement section by quoting the words of a wise man named Snoop Dogg:

> "I want to thank me for believing in me, I want to thank me for doing all this hard work… I wanna thank me for never quitting."

References

(1) Devabhaktuni, V.; Alam, M.; Depuru, S. S. S. R.; Green, R. C.; Nims, D.; Near, C. Solar energy: Trends and enabling technologies. *Renewable & Sustainable Energy Reviews* **2013**, *19*, 555-564.

(2) Allendorf, M. D.; Stavila, V.; Snider, J. L.; Witman, M.; Bowden, M. E.; Brooks, K.; Tran, B. L.; Autrey, T. Challenges to developing materials for the transport and storage of hydrogen. *Nature Chemistry* **2022**, *14* (11), 1214-1223.

(3) IEA. *Global Hydrogen Review*. IEA, 2023.

(4) Rosen, M. A. The Prospects for Renewable Energy through Hydrogen Energy Systems. *Journal of Power and Energy Engineering* **2015**, *3*, 373-377.

(5) Barreto, L.; Makihira, A.; Riahi, K. The hydrogen economy in the 21st century: a sustainable development scenario. *International Journal of Hydrogen Energy* **2003**, *28* (3), 267-284.

(6) Nikolaidis, P.; Poullikkas, A. A comparative overview of hydrogen production processes. *Renewable & Sustainable Energy Reviews* **2017**, *67*, 597-611.

(7) Safari, F.; Dincer, I. A review and comparative evaluation of thermochemical water splitting cycles for hydrogen production. *Energy Conversion and Management* **2020**, *205*, 112182.

(8) Holladay, J. D.; Hu, J.; King, D. L.; Wang, Y. An overview of hydrogen production technologies. *Catalysis Today* **2009**, *139* (4), 244-260.

(9) Muradov, N. Z.; Veziroglu, T. N. "Green" path from fossil-based to hydrogen economy: An overview of carbon-neutral technologies. *International Journal of Hydrogen Energy* **2008**, *33* (23), 6804-6839.

(10) Turner, J.; Sverdrup, G.; Mann, M. K.; Maness, P.-C.; Kroposki, B.; Ghirardi, M.; Evans, R. J.; Blake, D. Renewable hydrogen production. *International Journal of Energy Research* **2008**, *32* (5), 379-407.

(11) Bullock, R. M.; Chen, J. G.; Gagliardi, L.; Chirik, P. J.; Farha, O. K.; Hendon, C. H.; Jones, C. W.; Keith, J. A.; Klosin, J.; Minteer, S. D.; Morris, R. H.; Radosevich, A. T.; Rauchfuss, T. B.; Strotman, N. A.; Vojvodic, A.; Ward, T. R.; Yang, J. Y.; Surendranath, Y. Using nature's blueprint to expand catalysis with Earth-abundant metals. LID - 10.1126/science.abc3183 [doi] LID - eabc3183. *Science* **2020**, (1095-9203 (Electronic)).

(12) Anwar, S.; Khan, F.; Zhang, Y. H.; Djire, A. Recent development in electrocatalysts for hydrogen production through water electrolysis. *International Journal of Hydrogen Energy* **2021**, *46* (63), 32284-32317.

(13) James, O. O.; Maity, S.; Mesubi, M. A.; Ogunniran, K. O.; Siyanbola, T. O.; Sahu, S.; Chaubey, R. Towards reforming technologies for production of hydrogen exclusively from renewable resources. *Green Chemistry* **2011**, *13* (9), 2272-2284.

(14) Weiss, M. C.; Sousa, F. L.; Mrnjavac, N.; Neukirchen, S.; Roettger, M.; Nelson-Sathi, S.; Martin, W. F. The physiology and habitat of the last universal common ancestor. *Nature Microbiology* **2016**, *1* (9), 16116.

(15) Greening, C.; Biswas, A.; Carere, C. R.; Jackson, C. J.; Taylor, M. C.; Stott, M. B.; Cook, G. M.; Morales, S. E. Genomic and metagenomic surveys of hydrogenase distribution indicate H_2 is a widely utilised energy source for microbial growth and survival. *International Society of Microbial Ecology Journal* **2016**, *10* (3), 761-777.
(16) Lane, N.; Allen Jf Fau - Martin, W.; Martin, W. How did LUCA make a living? Chemiosmosis in the origin of life. *BioEssays* **2010**, (1521-1878 (Electronic)).
(17) Moody, E. R. R.; Alvarez-Carretero, S.; Mahendrarajah, T. A.; Clark, J. W.; Betts, H. C.; Dombrowski, N.; Szantho, L. L.; Boyle, R. A.; Daines, S.; Chen, X.; Lane, N.; Yang, Z.; Shields, G. A.; Szollosi, G. J.; Spang, A.; Pisani, D.; Williams, T. A.; Lenton, T. M.; Donoghue, P. C. J. The nature of the last universal common ancestor and its impact on the early Earth system. *Nature Ecology and Evolution* **2024**.
(18) Martin, W.; Russell, M. J. On the origin of biochemistry at an alkaline hydrothermal vent. *Philosophical Transactions of the Royal Society B: Biological Sciences* **2007**, *362* (1486), 1887-1925.
(19) Lane, N.; Martin, W. F. The origin of membrane bioenergetics. *Cell* **2012**, *151* (7), 1406-1416.
(20) Imachi, H.; Nobu, M. K.; Nakahara, N.; Morono, Y.; Ogawara, M.; Takaki, Y.; Takano, Y.; Uematsu, K.; Ikuta, T.; Ito, M.; Matsui, Y.; Miyazaki, M.; Murata, K.; Saito, Y.; Sakai, S.; Song, C.; Tasumi, E.; Yamanaka, Y.; Yamaguchi, T.; Kamagata, Y.; Tamaki, H.; Takai, K. Isolation of an archaeon at the prokaryote-eukaryote interface. *Nature* **2020**, *577* (7791), 519-525.
(21) Lopez-Garcia, P.; Moreira, D. The Syntrophy hypothesis for the origin of eukaryotes revisited. *Nature Microbiology* **2020**, *5* (5), 655-667.
(22) Martijn, J.; Vosseberg, J.; Guy, L.; Offre, P.; Ettema, T. J. G. Deep mitochondrial origin outside the sampled alphaproteobacteria. *Nature* **2018**, *557* (7703), 101-105.
(23) Fontecilla-Camps, J. C.; Amara, P.; Cavazza, C.; Nicolet, Y.; Volbeda, A. Structure-function relationships of anaerobic gas-processing metalloenzymes. *Nature* **2009**, *460* (7257), 814-822.
(24) Schwartz, E.; Fritsch, J.; Friedrich, B. H_2-Metabolizing Prokaryotes. In *The Prokaryotes*, Rosenberg, E., DeLong, E. F., Lory, S., Stackebrandt, E., Thompson, F. Eds.; Springer Berlin Heidelberg, 2013; pp 119-199.
(25) Lubitz, W.; Ogata, H.; Rudiger, O.; Reijerse, E. Hydrogenases. *Chemical Reviews* **2014**, *114* (8), 4081-4148.
(26) Kleinhaus, J. T.; Wittkamp, F.; Yadav, S.; Siegmund, D.; Apfel, U. P. [FeFe]-Hydrogenases: maturation and reactivity of enzymatic systems and overview of biomimetic models. *Chemical Society Reviews* **2021**, *50* (3), 1668-1784.
(27) Peters, J. W.; Lanzilotta, W. N.; Lemon, B. J.; Seefeldt, L. C. X-ray crystal structure of the Fe-only hydrogenase (CpI) from Clostridium pasteurianum to 1.8 angstrom resolution. *Science* **1998**, *282* (5395), 1853-1858.
(28) Volbeda, A.; Charon, M. H.; Piras, C.; Hatchikian, E. C.; Frey, M.; Fontecilla-Camps, J. C. Crystal structure of the nickel-iron hydrogenase from Desulfovibrio gigas. *Nature* **1995**, *373* (6515), 580-587.
(29) Shima, S.; Pilak, O.; Vogt, S.; Schick, M.; Stagni, M. S.; Meyer-Klaucke, W.; Warkentin, E.; Thauer, R. K.; Ermler, U. The crystal structure of [Fe]-hydrogenase reveals the geometry of the active site. *Science* **2008**, *321* (5888), 572-575.
(30) Land, H.; Senger, M.; Berggren, G.; Stripp, S. T. Current State of [FeFe]-Hydrogenase Research: Biodiversity and Spectroscopic Investigations. *ACS Catalysis* **2020**, *10* (13), 7069-7086.

(31) Calusinska, M.; Happe, T.; Joris, B.; Wilmotte, A. The surprising diversity of clostridial hydrogenases: a comparative genomic perspective. *Microbiology (Reading)* **2010**, *156* (Pt 6), 1575-1588.
(32) Vignais, P. M.; Billoud, B. Occurrence, classification, and biological function of hydrogenases: an overview. *Chemical Reviews* **2007**, *107* (10), 4206-4272.
(33) Corr, M. J.; Murphy, J. A. Evolution in the understanding of [Fe]-hydrogenase. *Chemical Society Reviews* **2011**, *40* (5), 2279-2292.
(34) Peters, J. W.; Schut, G. J.; Boyd, E. S.; Mulder, D. W.; Shepard, E. M.; Broderick, J. B.; King, P. W.; Adams, M. W. [FeFe]- and [NiFe]-hydrogenase diversity, mechanism, and maturation. *Biochimica et Biophysica Acta (BBA) - Molecular Cell Research* **2015**, *1853* (6), 1350-1369.
(35) Morra, S. Fantastic [FeFe]-Hydrogenases and Where to Find Them. *Frontiers in Microbiology* **2022**, *13*.
(36) Ortiz, M.; Leung, P. M.; Shelley, G.; Jirapanjawat, T.; Nauer, P. A.; Van Goethem, M. W.; Bay, S. K.; Islam, Z. F.; Jordaan, K.; Vikram, S.; Chown, S. L.; Hogg, I. D.; Makhalanyane, T. P.; Grinter, R.; Cowan, D. A.; Greening, C. Multiple energy sources and metabolic strategies sustain microbial diversity in Antarctic desert soils. *Proceedings of the National Academy of Sciences* **2021**, *118* (45), e2025322118.
(37) Tai, H.; Hirota, S.; Stripp, S. T. Proton Transfer Mechanisms in Bimetallic Hydrogenases. *Accounts of Chemical Research* **2021**, *54* (1), 232-241.
(38) Schuchmann, K.; Chowdhury, N. P.; Muller, V. Complex Multimeric [FeFe] Hydrogenases: Biochemistry, Physiology and New Opportunities for the Hydrogen Economy. *Frontiers in Microbiology* **2018**, *9*, 2911.
(39) Vogt, S.; Lyon, E. J.; Shima, S.; Thauer, R. K. The exchange activities of [Fe] hydrogenase (iron-sulfur-cluster-free hydrogenase) from methanogenic archaea in comparison with the exchange activities of [FeFe] and [NiFe] hydrogenases. *Journal of Biological Inorganic Chemistry* **2008**, *13* (1), 97-106.
(40) Schoelmerich, M. C.; Muller, V. Energy-converting hydrogenases: the link between H_2 metabolism and energy conservation. *Cellular and Molecular Life Sciences* **2020**, *77* (8), 1461-1481.
(41) Berney, M.; Greening, C.; Conrad, R.; Jacobs, W. R., Jr.; Cook, G. M. An obligately aerobic soil bacterium activates fermentative hydrogen production to survive reductive stress during hypoxia. *Proceedings of the National Academy of Sciences* **2014**, *111* (31), 11479-11484.
(42) Shafaat, H. S.; Rudiger, O.; Ogata, H.; Lubitz, W. [NiFe] hydrogenases: a common active site for hydrogen metabolism under diverse conditions. *Biochimica et Biophysica Acta (BBA) - Bioenergetics* **2013**, *1827* (8-9), 986-1002.
(43) Kim, Y. J.; Lee, H. S.; Kim, E. S.; Bae, S. S.; Lim, J. K.; Matsumi, R.; Lebedinsky, A. V.; Sokolova, T. G.; Kozhevnikova, D. A.; Cha, S. S.; Kim, S. J.; Kwon, K. K.; Imanaka, T.; Atomi, H.; Bonch-Osmolovskaya, E. A.; Lee, J. H.; Kang, S. G. Formate-driven growth coupled with H_2 production. *Nature* **2010**, *467* (7313), 352-355.
(44) Lim, J. K.; Mayer, F.; Kang, S. G.; Muller, V. Energy conservation by oxidation of formate to carbon dioxide and hydrogen via a sodium ion current in a hyperthermophilic archaeon. *Proceedings of the National Academy of Sciences* **2014**, *111* (31), 11497-11502.
(45) Yan, Z.; Ferry, J. G. Electron Bifurcation and Confurcation in Methanogenesis and Reverse Methanogenesis. *Frontiers in Microbiology* **2018**, *9*, 1322.
(46) Katsyv, A.; Kumar, A.; Saura, P.; Poverlein, M. C.; Freibert, S. A.; S, T. S.; Jain, S.; Gamiz-Hernandez, A. P.; Kaila, V. R. I.; Muller, V.; Schuller, J. M. Molecular Basis of the Electron Bifurcation Mechanism in the [FeFe]-

Hydrogenase Complex HydABC. *Journal of the American Chemical Society* **2023**, *145* (10), 5696-5709.
(47) Yuly, J. L.; Lubner, C. E.; Zhang, P.; Beratan, D. N.; Peters, J. W. Electron bifurcation: progress and grand challenges. *Chemical Communications* **2019**, *55* (79), 11823-11832.
(48) Schut, G. J.; Adams, M. W. The iron-hydrogenase of Thermotoga maritima utilizes ferredoxin and NADH synergistically: a new perspective on anaerobic hydrogen production. *Journal of Bacteriology* **2009**, *191* (13), 4451-4457.
(49) Kaster, A. K.; Moll, J.; Parey, K.; Thauer, R. K. Coupling of ferredoxin and heterodisulfide reduction via electron bifurcation in hydrogenotrophic methanogenic archaea. *Proceedings of the National Academy of Sciences* **2011**, *108* (7), 2981-2986.
(50) Buckel, W.; Thauer, R. K. Energy conservation via electron bifurcating ferredoxin reduction and proton/Na^+ translocating ferredoxin oxidation. *Biochimica et Biophysica Acta (BBA) - Bioenergetics* **2013**, *1827* (2), 94-113.
(51) Schuchmann, K.; Muller, V. Autotrophy at the thermodynamic limit of life: a model for energy conservation in acetogenic bacteria. *Nature Reviews Microbiology* **2014**, *12* (12), 809-821.
(52) Zheng, Y.; Kahnt, J.; Kwon, I. H.; Mackie, R. I.; Thauer, R. K. Hydrogen formation and its regulation in Ruminococcus albus: involvement of an electron-bifurcating [FeFe]-hydrogenase, of a non-electron-bifurcating [FeFe]-hydrogenase, and of a putative hydrogen-sensing [FeFe]-hydrogenase. *Journal of Bacteriology* **2014**, *196* (22), 3840-3852.
(53) Lenz, O.; Friedrich, B. A novel multicomponent regulatory system mediates H_2 sensing in Alcaligenes eutrophus. *Proceedings of the National Academy of Sciences* **1998**, *95* (21), 12474-12479.
(54) Vignais, P. M.; Elsen, S.; Colbeau, A. Transcriptional regulation of the uptake [NiFe]hydrogenase genes in Rhodobacter capsulatus. *Biochemical Society Transactions* **2005**, *33* (Pt 1), 28-32.
(55) Greening, C.; Cook, G. M. Integration of hydrogenase expression and hydrogen sensing in bacterial cell physiology. *Current Opinion in Microbiology* **2014**, *18* (1), 30-38.
(56) Benoit, S. L.; Maier, R. J.; Sawers, R. G.; Greening, C. Molecular Hydrogen Metabolism: a Widespread Trait of Pathogenic Bacteria and Protists. *Microbiology and Molecular Biology Reviews* **2020**, *84* (1), e00092-00019.
(57) Nicolet, Y.; Piras, C.; Legrand, P.; Hatchikian, C. E.; Fontecilla-Camps, J. C. Desulfovibrio desulfuricans iron hydrogenase: the structure shows unusual coordination to an active site Fe binuclear center. *Structure* **1999**, *7* (1), 13-23.
(58) Silakov, A.; Reijerse, E. J.; Albracht, S. P.; Hatchikian, E. C.; Lubitz, W. The electronic structure of the H-cluster in the [FeFe]-hydrogenase from Desulfovibrio desulfuricans: a Q-band 57Fe-ENDOR and HYSCORE study. *Journal of the American Chemical Society* **2007**, *129* (37), 11447-11458.
(59) Vincent, K. A.; Parkin, A.; Armstrong, F. A. Investigating and exploiting the electrocatalytic properties of hydrogenases. *Chemical Reviews* **2007**, *107* (10), 4366-4413.
(60) Lorenzi, M.; Gellett, J.; Zamader, A.; Senger, M.; Duan, Z.; Rodriguez-Macia, P.; Berggren, G. Investigating the role of the strong field ligands in [FeFe] hydrogenase: spectroscopic and functional characterization of a semi-synthetic mono-cyanide active site. *Chemical Science* **2022**, *13* (37), 11058-11064.
(61) Adamska-Venkatesh, A.; Roy, S.; Siebel, J. F.; Simmons, T. R.; Fontecave, M.; Artero, V.; Reijerse, E.; Lubitz, W. Spectroscopic Characterization of the Bridging Amine in the Active Site of [FeFe] Hydrogenase Using Isotopologues

of the H-Cluster. *Journal of the American Chemical Society* **2015**, *137* (40), 12744-12747.
(62) Silakov, A.; Wenk, B.; Reijerse, E.; Lubitz, W. (14)N HYSCORE investigation of the H-cluster of [FeFe] hydrogenase: evidence for a nitrogen in the dithiol bridge. *Physical Chemistry Chemical Physics* **2009**, *11* (31), 6592-6599.
(63) Berggren, G.; Adamska, A.; Lambertz, C.; Simmons, T. R.; Esselborn, J.; Atta, M.; Gambarelli, S.; Mouesca, J. M.; Reijerse, E.; Lubitz, W.; Happe, T.; Artero, V.; Fontecave, M. Biomimetic assembly and activation of [FeFe]-hydrogenases. *Nature* **2013**, *499* (7456), 66-69.
(64) Silakov, A.; Kamp, C.; Reijerse, E.; Happe, T.; Lubitz, W. Spectroelectrochemical characterization of the active site of the [FeFe] hydrogenase HydA1 from Chlamydomonas reinhardtii. *Biochemistry* **2009**, *48* (33), 7780-7786.
(65) Stripp, S. T.; Duffus, B. R.; Fourmond, V.; Leger, C.; Leimkuhler, S.; Hirota, S.; Hu, Y.; Jasniewski, A.; Ogata, H.; Ribbe, M. W. Second and Outer Coordination Sphere Effects in Nitrogenase, Hydrogenase, Formate Dehydrogenase, and CO Dehydrogenase. *Chemical Reviews* **2022**, *122* (14), 11900-11973.
(66) Le, J. M.; Bren, K. L. Engineered Enzymes and Bioinspired Catalysts for Energy Conversion. *ACS Energy Letters* **2019**, *4* (9), 2168-2180.
(67) Esselborn, J.; Lambertz, C.; Adamska-Venkates, A.; Simmons, T.; Berggren, G.; Noth, J.; Siebel, J.; Hemschemeier, A.; Artero, V.; Reijerse, E.; Fontecave, M.; Lubitz, W.; Happe, T. Spontaneous activation of [FeFe]-hydrogenases by an inorganic [2Fe] active site mimic. *Nature Chemical Biology* **2013**, *9* (10), 607-609.
(68) Ginovska-Pangovska, B.; Dutta, A.; Reback, M. L.; Linehan, J. C.; Shaw, W. J. Beyond the active site: the impact of the outer coordination sphere on electrocatalysts for hydrogen production and oxidation. *Accounts of Chemical Research* **2014**, *47* (8), 2621-2630.
(69) Hardt, S.; Stapf, S.; Filmon, D. T.; Birrell, J. A.; Rudiger, O.; Fourmond, V.; Leger, C.; Plumere, N. Reversible H_2 Oxidation and Evolution by Hydrogenase Embedded in a Redox Polymer Film. *Nature Catalysis* **2021**, *4* (3), 251-258.
(70) Karayilan, M.; Brezinski, W. P.; Clary, K. E.; Lichtenberger, D. L.; Glass, R. S.; Pyun, J. Catalytic Metallopolymers from [2Fe-2S] Clusters: Artificial Metalloenzymes for Hydrogen Production. *Angewandte Chemie International Edition* **2019**, *58* (23), 7537-7550.
(71) Land, H.; Sekretareva, A.; Huang, P.; Redman, H. J.; Nemeth, B.; Polidori, N.; Meszaros, L. S.; Senger, M.; Stripp, S. T.; Berggren, G. Characterization of a putative sensory [FeFe]-hydrogenase provides new insight into the role of the active site architecture. *Chemical Science* **2020**, *11* (47), 12789-12801.
(72) Winkler, M.; Esselborn, J.; Happe, T. Molecular basis of [FeFe]-hydrogenase function: an insight into the complex interplay between protein and catalytic cofactor. *Biochimica et Biophysica Acta (BBA) - Bioenergetics* **2013**, *1827* (8-9), 974-985.
(73) Mulder, D. W.; Shepard, E. M.; Meuser, J. E.; Joshi, N.; King, P. W.; Posewitz, M. C.; Broderick, J. B.; Peters, J. W. Insights into [FeFe]-Hydrogenase Structure, Mechanism, and Maturation. *Structure* **2011**, *19* (8), 1038-1052.
(74) Lorenzi, M.; Berggren, G. [FeFe] Hydrogenases and Their Functional Models. In *Comprehensive Coordination Chemistry III*, Constable, E. C., Parkin, G., Que Jr, L. Eds.; Elsevier, 2021; pp 731-756.
(75) Knorzer, P.; Silakov, A.; Foster, C. E.; Armstrong, F. A.; Lubitz, W.; Happe, T. Importance of the protein framework for catalytic activity of [FeFe]-hydrogenases. *Journal of Biological Chemistry* **2012**, *287* (2), 1489-1499.

(76) Duan, J. F.; Mebs, S.; Laun, K.; Wittkamp, F.; Heberle, J.; Happe, T.; Hofmann, E.; Apfel, U. P.; Winkler, M.; Senger, M.; Haumann, M.; Stripp, S. T. Geometry of the Catalytic Active Site in [FeFe]-Hydrogenase Is Determined by Hydrogen Bonding and Proton Transfer. *ACS Catalysis* **2019**, *9* (10), 9140-9149.
(77) Morra, S.; Maurelli, S.; Chiesa, M.; Mulder, D. W.; Ratzloff, M. W.; Giamello, E.; King, P. W.; Gilardi, G.; Valetti, F. The effect of a C298D mutation in CaHydA [FeFe]-hydrogenase: Insights into the protein-metal cluster interaction by EPR and FTIR spectroscopic investigation. *Biochimica et Biophysica Acta (BBA) - Bioenergetics* **2016**, *1857* (1), 98-106.
(78) Gauquelin, C.; Baffert, C.; Richaud, P.; Kamionka, E.; Etienne, E.; Guieysse, D.; Girbal, L.; Fourmond, V.; Andre, I.; Guigliarelli, B.; Leger, C.; Soucaille, P.; Meynial-Salles, I. Roles of the F-domain in [FeFe] hydrogenase. *Biochimica et Biophysica Acta (BBA) - Bioenergetics* **2018**, *1859* (2), 69-77.
(79) Caserta, G.; Papini, C.; Adamska-Venkatesh, A.; Pecqueur, L.; Sommer, C.; Reijerse, E.; Lubitz, W.; Gauquelin, C.; Meynial-Salles, I.; Pramanik, D.; Artero, V.; Atta, M.; Del Barrio, M.; Faivre, B.; Fourmond, V.; Leger, C.; Fontecave, M. Engineering an [FeFe]-Hydrogenase: Do Accessory Clusters Influence O_2 Resistance and Catalytic Bias? *Journal of the American Chemical Society* **2018**, *140* (16), 5516-5526.
(80) Rodriguez-Macia, P.; Pawlak, K.; Rudiger, O.; Reijerse, E. J.; Lubitz, W.; Birrell, J. A. Intercluster Redox Coupling Influences Protonation at the H-cluster in [FeFe] Hydrogenases. *Journal of the American Chemical Society* **2017**, *139* (42), 15122-15134.
(81) Cornish, A. J.; Gartner, K.; Yang, H.; Peters, J. W.; Hegg, E. L. Mechanism of proton transfer in [FeFe]-hydrogenase from Clostridium pasteurianum. *Journal of Biological Chemistry* **2011**, *286* (44), 38341-38347.
(82) Cornish, A. J.; Ginovska, B.; Thelen, A.; da Silva, J. C.; Soares, T. A.; Raugei, S.; Dupuis, M.; Shaw, W. J.; Hegg, E. L. Single-Amino Acid Modifications Reveal Additional Controls on the Proton Pathway of [FeFe]-Hydrogenase. *Biochemistry* **2016**, *55* (22), 3165-3173.
(83) Morra, S.; Giraudo, A.; Di Nardo, G.; King, P. W.; Gilardi, G.; Valetti, F. Site saturation mutagenesis demonstrates a central role for cysteine 298 as proton donor to the catalytic site in CaHydA [FeFe]-hydrogenase. *PLOS ONE* **2012**, *7* (10), e48400.
(84) Duan, J.; Senger, M.; Esselborn, J.; Engelbrecht, V.; Wittkamp, F.; Apfel, U. P.; Hofmann, E.; Stripp, S. T.; Happe, T.; Winkler, M. Crystallographic and spectroscopic assignment of the proton transfer pathway in [FeFe]-hydrogenases. *Nature Communications* **2018**, *9* (1), 4726.
(85) Senger, M.; Eichmann, V.; Laun, K.; Duan, J.; Wittkamp, F.; Knor, G.; Apfel, U. P.; Happe, T.; Winkler, M.; Heberle, J.; Stripp, S. T. How [FeFe]-Hydrogenase Facilitates Bidirectional Proton Transfer. *Journal of the American Chemical Society* **2019**, *141* (43), 17394-17403.
(86) Kubas, A.; Orain, C.; De Sancho, D.; Saujet, L.; Sensi, M.; Gauquelin, C.; Meynial-Salles, I.; Soucaille, P.; Bottin, H.; Baffert, C.; Fourmond, V.; Best, R. B.; Blumberger, J.; Leger, C. Mechanism of O_2 diffusion and reduction in FeFe hydrogenases. *Nature Chemistry* **2017**, *9* (1), 88-95.
(87) Cohen, J.; Kim, K.; King, P.; Seibert, M.; Schulten, K. Finding gas diffusion pathways in proteins: application to O_2 and H_2 transport in CpI [FeFe]-hydrogenase and the role of packing defects. *Structure* **2005**, *13* (9), 1321-1329.
(88) Cohen, J.; Kim, K.; Posewitz, M.; Ghirardi, M. L.; Schulten, K.; Seibert, M.; King, P. Molecular dynamics and experimental investigation of H_2 and O_2

diffusion in [Fe]-hydrogenase. *Biochemical Society Transactions* **2005**, *33* (Pt 1), 80-82.
(89) Lautier, T.; Ezanno, P.; Baffert, C.; Fourmond, V.; Cournac, L.; Fontecilla-Camps, J. C.; Soucaille, P.; Bertrand, P.; Meynial-Salles, I.; Leger, C. The quest for a functional substrate access tunnel in FeFe hydrogenase. *Faraday Discussions* **2011**, *148* (0), 385-407; discussion 421-341.
(90) Mészáros, L. S.; Land, H.; Redman, H. J.; Berggren, G. Semi-synthetic hydrogenases—*in vitro* and *in vivo* applications. *Current Opinion in Green and Sustainable Chemistry* **2021**, *32*, 100521.
(91) Chongdar, N.; Birrell, J. A.; Pawlak, K.; Sommer, C.; Reijerse, E. J.; Rudiger, O.; Lubitz, W.; Ogata, H. Unique Spectroscopic Properties of the H-Cluster in a Putative Sensory [FeFe] Hydrogenase. *Journal of the American Chemical Society* **2018**, *140* (3), 1057-1068.
(92) Artz, J. H.; Mulder, D. W.; Ratzloff, M. W.; Lubner, C. E.; Zadvornyy, O. A.; LeVan, A. X.; Williams, S. G.; Adams, M. W. W.; Jones, A. K.; King, P. W.; Peters, J. W. Reduction Potentials of [FeFe]-Hydrogenase Accessory Iron-Sulfur Clusters Provide Insights into the Energetics of Proton Reduction Catalysis. *Journal of the American Chemical Society* **2017**, *139* (28), 9544-9550.
(93) Mulder, D. W.; Boyd, E. S.; Sarma, R.; Lange, R. K.; Endrizzi, J. A.; Broderick, J. B.; Peters, J. W. Stepwise [FeFe]-hydrogenase H-cluster assembly revealed in the structure of HydA(DeltaEFG). *Nature* **2010**, *465* (7295), 248-251.
(94) Laun, K.; Baranova, I.; Duan, J.; Kertess, L.; Wittkamp, F.; Apfel, U. P.; Happe, T.; Senger, M.; Stripp, S. T. Site-selective protonation of the one-electron reduced cofactor in [FeFe]-hydrogenase. *Dalton Transactions* **2021**, *50* (10), 3641-3650.
(95) Birrell, J. A.; Rodríguez-Maciá, P.; Reijerse, E. J.; Martini, M. A.; Lubitz, W. The catalytic cycle of [FeFe] hydrogenase: A tale of two sites. *Coordination Chemistry Reviews* **2021**, *449*, 214191.
(96) Artz, J. H.; Zadvornyy, O. A.; Mulder, D. W.; Keable, S. M.; Cohen, A. E.; Ratzloff, M. W.; Williams, S. G.; Ginovska, B.; Kumar, N.; Song, J.; McPhillips, S. E.; Davidson, C. M.; Lyubimov, A. Y.; Pence, N.; Schut, G. J.; Jones, A. K.; Soltis, S. M.; Adams, M. W. W.; Raugei, S.; King, P. W.; Peters, J. W. Tuning Catalytic Bias of Hydrogen Gas Producing Hydrogenases. *Journal of the American Chemical Society* **2020**, *142* (3), 1227-1235.
(97) Haumann, M.; Stripp, S. T. The Molecular Proceedings of Biological Hydrogen Turnover. *Accounts of Chemical Research* **2018**, *51* (8), 1755-1763.
(98) Senger, M.; Mebs, S.; Duan, J.; Shulenina, O.; Laun, K.; Kertess, L.; Wittkamp, F.; Apfel, U. P.; Happe, T.; Winkler, M.; Haumann, M.; Stripp, S. T. Protonation/reduction dynamics at the [4Fe-4S] cluster of the hydrogen-forming cofactor in [FeFe]-hydrogenases. *Physical Chemistry Chemical Physics* **2018**, *20* (5), 3128-3140.
(99) Roseboom, W.; De Lacey, A. L.; Fernandez, V. M.; Hatchikian, E. C.; Albracht, S. P. J. The active site of the [FeFe]-hydrogenase from Desulfovibrio desulfuricans. II. Redox properties, light sensitivity and CO-ligand exchange as observed by infrared spectroscopy. *Journal of Biological Inorganic Chemistry* **2006**, *11* (1), 102-118.
(100) Katz, S.; Noth, J.; Horch, M.; Shafaat, H. S.; Happe, T.; Hildebrandt, P.; Zebger, I. Vibrational spectroscopy reveals the initial steps of biological hydrogen evolution. *Chemical Science* **2016**, *7* (11), 6746-6752.
(101) Sommer, C.; Adamska-Venkatesh, A.; Pawlak, K.; Birrell, J. A.; Rudiger, O.; Reijerse, E. J.; Lubitz, W. Proton Coupled Electronic Rearrangement within

the H-Cluster as an Essential Step in the Catalytic Cycle of [FeFe] Hydrogenases. *Journal of the American Chemical Society* **2017**, *139* (4), 1440-1443.
(102) Winkler, M.; Senger, M.; Duan, J.; Esselborn, J.; Wittkamp, F.; Hofmann, E.; Apfel, U. P.; Stripp, S. T.; Happe, T. Accumulating the hydride state in the catalytic cycle of [FeFe]-hydrogenases. *Nature Communications* **2017**, *8* (1), 16115.
(103) Senger, M.; Kernmayr, T.; Lorenzi, M.; Redman, H. J.; Berggren, G. Hydride state accumulation in native [FeFe]-hydrogenase with the physiological reductant H_2 supports its catalytic relevance. *Chemical Communications* **2022**, *58* (51), 7184-7187.
(104) Meszaros, L. S.; Ceccaldi, P.; Lorenzi, M.; Redman, H. J.; Pfitzner, E.; Heberle, J.; Senger, M.; Stripp, S. T.; Berggren, G. Spectroscopic investigations under whole-cell conditions provide new insight into the metal hydride chemistry of [FeFe]-hydrogenase. *Chemical Science* **2020**, *11* (18), 4608-4617.
(105) Mulder, D. W.; Ratzloff, M. W.; Bruschi, M.; Greco, C.; Koonce, E.; Peters, J. W.; King, P. W. Investigations on the role of proton-coupled electron transfer in hydrogen activation by [FeFe]-hydrogenase. *Journal of the American Chemical Society* **2014**, *136* (43), 15394-15402.
(106) Wittkamp, F.; Senger, M.; Stripp, S. T.; Apfel, U. P. [FeFe]-Hydrogenases: recent developments and future perspectives. *Chemical Communications* **2018**, *54* (47), 5934-5942.
(107) Poudel, S.; Tokmina-Lukaszewska, M.; Colman, D. R.; Refai, M.; Schut, G. J.; King, P. W.; Maness, P. C.; Adams, M. W.; Peters, J. W.; Bothner, B.; Boyd, E. S. Unification of [FeFe]-hydrogenases into three structural and functional groups. *Biochimica et Biophysica Acta (BBA) - General Subjects* **2016**, *1860* (9), 1910-1921.
(108) Therien, J. B.; Artz, J. H.; Poudel, S.; Hamilton, T. L.; Liu, Z.; Noone, S. M.; Adams, M. W. W.; King, P. W.; Bryant, D. A.; Boyd, E. S.; Peters, J. W. The Physiological Functions and Structural Determinants of Catalytic Bias in the [FeFe]-Hydrogenases CpI and CpII of Clostridium pasteurianum Strain W5. *Frontiers in Microbiology* **2017**, *8*, 1305.
(109) Baffert, C.; Kpebe, A.; Avilan, L.; Brugna, M. Chapter Three - Hydrogenases and H_2 metabolism in sulfate-reducing bacteria of the Desulfovibrio genus. In *Advances in Microbial Physiology*, Poole, R. K. Ed.; Vol. 74; Academic Press, 2019; pp 143-189.
(110) Pohorelic, B. K.; Voordouw, J. K.; Lojou, E.; Dolla, A.; Harder, J.; Voordouw, G. Effects of deletion of genes encoding Fe-only hydrogenase of Desulfovibrio vulgaris Hildenborough on hydrogen and lactate metabolism. *Journal of Bacteriology* **2002**, *184* (3), 679-686.
(111) Wang, S.; Huang, H.; Kahnt, J.; Mueller, A. P.; Kopke, M.; Thauer, R. K. NADP-specific electron-bifurcating [FeFe]-hydrogenase in a functional complex with formate dehydrogenase in Clostridium autoethanogenum grown on CO. *Journal of Bacteriology* **2013**, *195* (19), 4373-4386.
(112) Schuchmann, K.; Muller, V. Direct and reversible hydrogenation of CO_2 to formate by a bacterial carbon dioxide reductase. *Science* **2013**, *342* (6164), 1382-1385.
(113) Schwarz, F. M.; Schuchmann, K.; Muller, V. Hydrogenation of CO_2 at ambient pressure catalyzed by a highly active thermostable biocatalyst. *Biotechnology for Biofuels* **2018**, *11* (1), 237.
(114) Losey, N. A.; Mus, F.; Peters, J. W.; Le, H. M.; McInerney, M. J. Syntrophomonas wolfei Uses an NADH-Dependent, Ferredoxin-Independent [FeFe]-

Hydrogenase To Reoxidize NADH. *Applied and Environmental Microbiology* **2017**, *83* (20), e01335-01317.
(115) Losey, N. A.; Poudel, S.; Boyd, E. S.; McInerney, M. J. The Beta Subunit of Non-bifurcating NADH-Dependent [FeFe]-Hydrogenases Differs From Those of Multimeric Electron-Bifurcating [FeFe]-Hydrogenases. *Frontiers in Microbiology* **2020**, *11*, 1109.
(116) Swanson, K. D.; Ratzloff, M. W.; Mulder, D. W.; Artz, J. H.; Ghose, S.; Hoffman, A.; White, S.; Zadvornyy, O. A.; Broderick, J. B.; Bothner, B.; King, P. W.; Peters, J. W. [FeFe]-hydrogenase oxygen inactivation is initiated at the H cluster 2Fe subcluster. *Journal of the American Chemical Society* **2015**, *137* (5), 1809-1816.
(117) Stripp, S. T.; Goldet, G.; Brandmayr, C.; Sanganas, O.; Vincent, K. A.; Haumann, M.; Armstrong, F. A.; Happe, T. How oxygen attacks [FeFe] hydrogenases from photosynthetic organisms. *Proceedings of the National Academy of Sciences* **2009**, *106* (41), 17331-17336.
(118) Rodriguez-Macia, P.; Galle, L. M.; Bjornsson, R.; Lorent, C.; Zebger, I.; Yoda, Y.; Cramer, S. P.; DeBeer, S.; Span, I.; Birrell, J. A. Caught in the H_{inact} : Crystal Structure and Spectroscopy Reveal a Sulfur Bound to the Active Site of an O_2-stable State of [FeFe] Hydrogenase. *Angewandte Chemie* **2020**, *59* (38), 16786-16794.
(119) Morra, S.; Arizzi, M.; Valetti, F.; Gilardi, G. Oxygen Stability in the New [FeFe]-Hydrogenase from Clostridium beijerinckii SM10 (CbA5H). *Biochemistry* **2016**, *55* (42), 5897-5900.
(120) Fasano, A.; Land, H.; Fourmond, V.; Berggren, G.; Leger, C. Reversible or Irreversible Catalysis of H^+/H_2 Conversion by FeFe Hydrogenases. *Journal of the American Chemical Society* **2021**, *143* (48), 20320-20325.
(121) Fasano, A.; Bailly, A.; Wozniak, J.; Fourmond, V.; Léger, C. Catalytic bias and redox-driven inactivation of ancestral FeFe hydrogenases from group B2. *bioRxiv* **2023**, 2023.2006.2023.541094.
(122) Shaw, A. J.; Hogsett, D. A.; Lynd, L. R. Identification of the [FeFe]-hydrogenase responsible for hydrogen generation in Thermoanaerobacterium saccharolyticum and demonstration of increased ethanol yield via hydrogenase knockout. *Journal of Bacteriology* **2009**, *191* (20), 6457-6464.
(123) Fasano, A.; Baffert, C.; Schumann, C.; Berggren, G.; Birrell, J. A.; Fourmond, V.; Leger, C. Kinetic Modeling of the Reversible or Irreversible Electrochemical Responses of FeFe-Hydrogenases. *Journal of the American Chemical Society* **2024**, *146* (2), 1455-1466.
(124) Cabotaje, P. R.; Walter, K.; Zamader, A.; Huang, P.; Ho, F.; Land, H.; Senger, M.; Berggren, G. Probing Substrate Transport Effects on Enzymatic Hydrogen Catalysis: An Alternative Proton Transfer Pathway in Putatively Sensory [FeFe] Hydrogenase. *ACS Catalysis* **2023**, *13* (15), 10435-10446.
(125) Ogata, H.; Nishikawa, K.; Lubitz, W. Hydrogens detected by subatomic resolution protein crystallography in a [NiFe] hydrogenase. *Nature* **2015**, *520* (7548), 571-574.
(126) Tai, H.; Higuchi, Y.; Hirota, S. Comprehensive reaction mechanisms at and near the Ni-Fe active sites of [NiFe] hydrogenases. *Dalton Transactions* **2018**, *47* (13), 4408-4423.
(127) Wrathall, S. L. D.; Procacci, B.; Horch, M.; Saxton, E.; Furlan, C.; Walton, J.; Rippers, Y.; Blaza, J. N.; Greetham, G. M.; Towrie, M.; Parker, A. W.; Lynam, J.; Parkin, A.; Hunt, N. T. Ultrafast 2D-IR spectroscopy of [NiFe] hydrogenase from E. coli reveals the role of the protein scaffold in controlling the active site

environment. *Physical Chemistry Chemical Physics* **2022**, *24* (40), 24767-24783.
(128) Fourmond, V.; Baffert, C.; Sybirna, K.; Dementin, S.; Abou-Hamdan, A.; Meynial-Salles, I.; Soucaille, P.; Bottin, H.; Leger, C. The mechanism of inhibition by H_2 of H_2-evolution by hydrogenases. *Chemical Communications* **2013**, *49* (61), 6840-6842.
(129) Ma, K.; Schicho, R. N.; Kelly, R. M.; Adams, M. W. W. Hydrogenase of the Hyperthermophile Pyrococcus-Furiosus Is an Elemental Sulfur Reductase or Sulfhydrogenase - Evidence for a Sulfur-Reducing Hydrogenase Ancestor. *Proceedings of the National Academy of Sciences* **1993**, *90* (11), 5341-5344.
(130) Teke, G. M.; Anye Cho, B.; Bosman, C. E.; Mapholi, Z.; Zhang, D.; Pott, R. W. M. Towards industrial biological hydrogen production: a review. *World Journal of Microbiology and Biotechnology* **2023**, *40* (1), 37.
(131) Ivanenko, A. A.; Laikova, A. A.; Zhuravleva, E. A.; Shekhurdina, S. V.; Vishnyakova, A. V.; Kovalev, A. A.; Kovalev, D. A.; Trchounian, K. A.; Litti, Y. V. Biological production of hydrogen: From basic principles to the latest advances in process improvement. *International Journal of Hydrogen Energy* **2024**, *55*, 740-755.
(132) Schumann, C.; Fernandez Mendez, J.; Berggren, G.; Lindblad, P. Novel concepts and engineering strategies for heterologous expression of efficient hydrogenases in photosynthetic microorganisms. *Frontiers in Microbiology* **2023**, *14* (1664-302X (Print)), 1179607.
(133) Siegbahn, P. E. M.; Liao, R. Z. Energetics for Proton Reduction in FeFe Hydrogenase. *The Journal of Physical Chemistry A* **2020**, *124* (50), 10540-10549.
(134) Kositzki, R.; Mebs, S.; Schuth, N.; Leidel, N.; Schwartz, L.; Karnahl, M.; Wittkamp, F.; Daunke, D.; Grohmann, A.; Apfel, U. P.; Gloaguen, F.; Ott, S.; Haumann, M. Electronic and molecular structure relations in diiron compounds mimicking the [FeFe]-hydrogenase active site studied by X-ray spectroscopy and quantum chemistry. *Dalton Transactions* **2017**, *46* (37), 12544-12557.
(135) Redman, H. J.; Huang, P.; Haumann, M.; Cheah, M. H.; Berggren, G. Lewis acid protection turns cyanide containing [FeFe]-hydrogenase mimics into proton reduction catalysts. *Dalton Transactions* **2022**, *51* (12), 4634-4643.
(136) Wang, V. C.; Esmieu, C.; Redman, H. J.; Berggren, G.; Hammarstrom, L. The reactivity of molecular oxygen and reactive oxygen species with [FeFe] hydrogenase biomimetics: reversibility and the role of the second coordination sphere. *Dalton Transactions* **2020**, *49* (3), 858-865.
(137) Gloaguen, F.; Rauchfuss, T. B. Small molecule mimics of hydrogenases: hydrides and redox. *Chemical Society Reviews* **2009**, *38* (1), 100-108.
(138) Li, Y.; Rauchfuss, T. B. Synthesis of Diiron(I) Dithiolato Carbonyl Complexes. *Chemical Reviews* **2016**, *116* (12), 7043-7077.
(139) Schilter, D.; Camara, J. M.; Huynh, M. T.; Hammes-Schiffer, S.; Rauchfuss, T. B. Hydrogenase Enzymes and Their Synthetic Models: The Role of Metal Hydrides. *Chemical Reviews* **2016**, *116* (15), 8693-8749.
(140) Armstrong, F. A.; Hirst, J. Reversibility and efficiency in electrocatalytic energy conversion and lessons from enzymes. *Proceedings of the National Academy of Sciences* **2011**, *108* (34), 14049-14054.
(141) Esmieu, C.; Raleiras, P.; Berggren, G. From protein engineering to artificial enzymes - biological and biomimetic approaches towards sustainable hydrogen production. *Sustainable Energy Fuels* **2018**, *2* (4), 724-750.
(142) Singleton, M. L.; Crouthers, D. J.; Duttweiler, R. P., III; Reibenspies, J. H.; Darensbourg, M. Y. Sulfonated Diiron Complexes as Water-Soluble Models

of the [Fe–Fe]-Hydrogenase Enzyme Active Site. *Inorganic chemistry* **2011**, *50* (11), 5015-5026.
(143) Gao, W.; Sun, J.; Åkermark, T.; Li, M.; Eriksson, L.; Sun, L.; Åkermark, B. Attachment of a Hydrogen-Bonding Carboxylate Side Chain to an [FeFe]-Hydrogenase Model Complex: Influence on the Catalytic Mechanism. *Chemistry–A European Journal* **2010**, *16* (8), 2537-2546.
(144) Apfel, U.-P.; Kowol, C. R.; Halpin, Y.; Kloss, F.; Kübel, J.; Görls, H.; Vos, J. G.; Keppler, B. K.; Morera, E.; Lucente, G.; Weigand, W. Investigation of amino acid containing [FeFe] hydrogenase models concerning pendant base effects. *Journal of Inorganic Biochemistry* **2009**, *103* (9), 1236-1244.
(145) Singleton, M. L.; Reibenspies, J. H.; Darensbourg, M. Y. A cyclodextrin host/guest approach to a hydrogenase active site biomimetic cavity. *Journal of the American Chemical Society* **2010**, *132* (26), 8870-8871.
(146) Curtis, C. J.; Miedaner, A.; Ciancanelli, R.; Ellis, W. W.; Noll, B. C.; Rakowski DuBois, M.; DuBois, D. L. $[Ni(Et_2PCH_2NMeCH_2PEt_2)_2]^{2+}$ as a functional model for hydrogenases. *Inorganic chemistry* **2003**, *42* (1), 216-227.
(147) Yang, J. Y.; Bullock, R. M.; Shaw, W. J.; Twamley, B.; Fraze, K.; DuBois, M. R.; DuBois, D. L. Mechanistic Insights into Catalytic H_2 Oxidation by Ni Complexes Containing a Diphosphine Ligand with a Positioned Amine Base. *Journal of the American Chemical Society* **2009**, *131* (16), 5935-5945.
(148) Rakowski DuBois, M.; DuBois, D. L. Development of molecular electrocatalysts for CO_2 reduction and H_2 production/oxidation. *Accounts of Chemical Research* **2009**, *42* (12), 1974-1982.
(149) Zamader, A.; Reuillard, B.; Marcasuzaa, P.; Bousquet, A.; Billon, L.; Gallart, J. J. E.; Berggren, G.; Artero, V. Electrode Integration of Synthetic Hydrogenase as Bioinspired and Noble Metal-Free Cathodes for Hydrogen Evolution. *ACS Catalysis* **2023**, *13* (2), 1246-1256.
(150) Gamache, M. T.; Charaf, R.; Kurth, L.; Filmon, D. T.; Senger, M.; Plumeré, N.; Hammarström, L.; Berggren, G. Elucidating Electron Transfer Kinetics and Optimizing System Performance for Escherichia coli-Based Semi-Artificial H_2 Production. *ACS Catalysis* **2023**, *13* (14), 9476-9486.
(151) Lorenzi, M.; Gamache, M. T.; Redman, H. J.; Land, H.; Senger, M.; Berggren, G. Light-Driven [FeFe] Hydrogenase Based H_2 Production in E. coli: A Model Reaction for Exploring E. coli Based Semiartificial Photosynthetic Systems. *ACS Sustainable Chemistry and Engineering* **2022**, *10* (33), 10760-10767.
(152) Honda, Y.; Shinohara, Y.; Fujii, H. Visible light-driven, external mediator-free H_2 production by a combination of a photosensitizer and a whole-cell biocatalyst: Escherichia coli expressing [FeFe]-hydrogenase and maturase genes. *Catalysis Science & Technology* **2020**, *10* (17), 6006-6012.
(153) Cheng, F.; Pavliuk, O.; Hardt, S.; Hunt, L. A.; Cai, B.; Kubart, T.; Hammarstrom, L.; Plumere, N.; Berggren, G.; Tian, H. Embedding biocatalysts in a redox polymer enhances the performance of dye-sensitized photocathodes in bias-free photoelectrochemical water splitting. *Nature Communications* **2024**, *15* (1), 3202.
(154) Greening, C.; Cabotaje, P. R.; Valentin Alvarado, L. E.; Leung, P. M.; Land, H.; Rodrigues-Oliveira, T.; Ponce-Toledo, R. I.; Senger, M.; Klamke, M. A.; Milton, M.; Lappan, R.; Mullen, S.; West-Roberts, J.; Mao, J.; Song, J.; Schoelmerich, M.; Stairs, C. W.; Schleper, C.; Grinter, R.; Spang, A.; Banfield, J. F.; Berggren, G. Minimal and hybrid hydrogenases are active from archaea. *Cell* **2024**, *187* (13), 3357-3372 e3319.
(155) Grinter, R.; Kropp, A.; Venugopal, H.; Senger, M.; Badley, J.; Cabotaje, P. R.; Jia, R.; Duan, Z.; Huang, P.; Stripp, S. T.; Barlow, C. K.; Belousoff, M.;

Shafaat, H. S.; Cook, G. M.; Schittenhelm, R. B.; Vincent, K. A.; Khalid, S.; Berggren, G.; Greening, C. Structural basis for bacterial energy extraction from atmospheric hydrogen. *Nature* **2023**, *615* (7952), 541-547.
(156) Francis, D. M.; Page, R. Strategies to optimize protein expression in E. coli. *Current Protocols in Protein Science* **2010**, *Chapter 5* (1), 5 24 21-25 24 29.
(157) Rosano, G. L.; Ceccarelli, E. A. Recombinant protein expression in microbial systems. *Frontiers in Microbiology* **2014**, *5* (1664-302X (Print)), 341.
(158) Freibert, S. A.; Weiler, B. D.; Bill, E.; Pierik, A. J.; Muhlenhoff, U.; Lill, R. Biochemical Reconstitution and Spectroscopic Analysis of Iron-Sulfur Proteins. *Methods in Enzymology* **2018**, *599*, 197-226.
(159) Bradford, M. M. A rapid and sensitive method for the quantitation of microgram quantities of protein utilizing the principle of protein-dye binding. *Analytical Biochemistry* **1976**, *72* (1-2), 248-254.
(160) Fish, W. W. Rapid colorimetric micromethod for the quantitation of complexed iron in biological samples. *Methods in Enzymology* **1988**, *158*, 357-364.
(161) Britt, R. D.; Rauchfuss, T. B.; Rao, G. The H-cluster of [FeFe] Hydrogenases: Its Enzymatic Synthesis and Parallel Inorganic Semisynthesis. *Accounts of Chemical Research* **2024**, *57* (14), 1941-1950.
(162) Stripp, S. T. In Situ Infrared Spectroscopy for the Analysis of Gas-processing Metalloenzymes. *ACS Catalysis* **2021**, *11* (13), 7845-7862.
(163) Ye, J. N.; Baldwin, R. P. Catalytic reduction of myoglobin and hemoglobin at chemically modified electrodes containing methylene blue. *Analytical Chemistry* **1988**, *60* (20), 2263-2268.
(164) van den Heuvel, R. H. H.; Fraaije, M. W.; van Berkel, W. J. H. [17] - Redox Properties of Vanillyl-Alcohol Oxidase. In *Methods in Enzymology*, Sen, C. K., Packer, L. Eds.; Vol. 353; Academic Press, 2002; pp 177-186.
(165) Fourmond, V.; Sabaty, M.; Arnoux, P.; Bertrand, P.; Pignol, D.; Leger, C. Reassessing the strategies for trapping catalytic intermediates during nitrate reductase turnover. *The Journal of Physical Chemistry B* **2010**, *114* (9), 3341-3347.
(166) Adams, M. W.; Mortenson, L. E. The physical and catalytic properties of hydrogenase II of Clostridium pasteurianum. A comparison with hydrogenase I. *Journal of Biological Chemistry* **1984**, *259* (11), 7045-7055.
(167) Adams, M. W.; Eccleston, E.; Howard, J. B. Iron-sulfur clusters of hydrogenase I and hydrogenase II of Clostridium pasteurianum. *Proceedings of the National Academy of Sciences* **1989**, *86* (13), 4932-4936.
(168) Bard, A. J., Faulkner, Larry R. *Electrochemical Methods: Fundamentals and Applications*; John Wiley & Sons, 2001.
(169) Fourmond, V.; Plumere, N.; Leger, C. Reversible catalysis. *Nature Reviews Chemistry* **2021**, *5* (5), 348-360.
(170) Costentin, C.; Drouet, S.; Robert, M.; Saveant, J. M. Turnover numbers, turnover frequencies, and overpotential in molecular catalysis of electrochemical reactions. Cyclic voltammetry and preparative-scale electrolysis. *Journal of the American Chemical Society* **2012**, *134* (27), 11235-11242.
(171) Rinke, C.; Schwientek, P.; Sczyrba, A.; Ivanova, N. N.; Anderson, I. J.; Cheng, J. F.; Darling, A.; Malfatti, S.; Swan, B. K.; Gies, E. A.; Dodsworth, J. A.; Hedlund, B. P.; Tsiamis, G.; Sievert, S. M.; Liu, W. T.; Eisen, J. A.; Hallam, S. J.; Kyrpides, N. C.; Stepanauskas, R.; Rubin, E. M.; Hugenholtz, P.; Woyke, T. Insights into the phylogeny and coding potential of microbial dark matter. *Nature* **2013**, *499* (7459), 431-437.

(172) Eme, L.; Spang, A.; Lombard, J.; Stairs, C. W.; Ettema, T. J. G. Archaea and the origin of eukaryotes. *Nature Reviews Microbiology* **2017**, *15* (12), 711-723.
(173) Sakai, H. D.; Nur, N.; Kato, S.; Yuki, M.; Shimizu, M.; Itoh, T.; Ohkuma, M.; Suwanto, A.; Kurosawa, N. Insight into the symbiotic lifestyle of DPANN archaea revealed by cultivation and genome analyses. *Proceedings of the National Academy of Sciences* **2022**, *119* (3), e2115449119.
(174) Zaremba-Niedzwiedzka, K.; Caceres, E. F.; Saw, J. H.; Backstrom, D.; Juzokaite, L.; Vancaester, E.; Seitz, K. W.; Anantharaman, K.; Starnawski, P.; Kjeldsen, K. U.; Stott, M. B.; Nunoura, T.; Banfield, J. F.; Schramm, A.; Baker, B. J.; Spang, A.; Ettema, T. J. Asgard archaea illuminate the origin of eukaryotic cellular complexity. *Nature* **2017**, *541* (7637), 353-358.
(175) Rodrigues-Oliveira, T.; Wollweber, F.; Ponce-Toledo, R. I.; Xu, J.; Rittmann, S. K. R.; Klingl, A.; Pilhofer, M.; Schleper, C. Actin cytoskeleton and complex cell architecture in an Asgard archaeon. *Nature* **2023**, *613* (7943), 332-339.
(176) Castelle, C. J.; Brown, C. T.; Anantharaman, K.; Probst, A. J.; Huang, R. H.; Banfield, J. F. Biosynthetic capacity, metabolic variety and unusual biology in the CPR and DPANN radiations. *Nature Reviews Microbiology* **2018**, *16* (10), 629-645.
(177) Huang, W. C.; Liu, Y.; Zhang, X.; Zhang, C. J.; Zou, D.; Zheng, S.; Xu, W.; Luo, Z.; Liu, F.; Li, M. Comparative genomic analysis reveals metabolic flexibility of Woesearchaeota. *Nature Communications* **2021**, *12* (1), 5281.
(178) Lorenzi, M.; Ceccaldi, P.; Rodriguez-Macia, P.; Redman, H. J.; Zamader, A.; Birrell, J. A.; Meszaros, L. S.; Berggren, G. Stability of the H-cluster under whole-cell conditions-formation of an H_{trans}-like state and its reactivity towards oxygen. *Journal of Biological Inorganic Chemistry* **2022**, *27* (3), 345-355.
(179) Land, H.; Ceccaldi, P.; Meszaros, L. S.; Lorenzi, M.; Redman, H. J.; Senger, M.; Stripp, S. T.; Berggren, G. Discovery of novel [FeFe]-hydrogenases for biocatalytic H_2-production. *Chemical Science* **2019**, *10* (43), 9941-9948.
(180) Adamska-Venkatesh, A.; Krawietz, D.; Siebel, J.; Weber, K.; Happe, T.; Reijerse, E.; Lubitz, W. New redox states observed in [FeFe] hydrogenases reveal redox coupling within the H-cluster. *Journal of the American Chemical Society* **2014**, *136* (32), 11339-11346.
(181) Akhtar, M. K.; Jones, P. R. Deletion of iscR stimulates recombinant clostridial Fe-Fe hydrogenase activity and H_2-accumulation in Escherichia coli BL21(DE3). *Applied Microbiology and Biotechnology* **2008**, *78* (5), 853-862.
(182) Nemeth, B.; Senger, M.; Redman, H. J.; Ceccaldi, P.; Broderick, J.; Magnuson, A.; Stripp, S. T.; Haumann, M.; Berggren, G. [FeFe]-hydrogenase maturation: H-cluster assembly intermediates tracked by electron paramagnetic resonance, infrared, and X-ray absorption spectroscopy. *Journal of Biological Inorganic Chemistry* **2020**, *25* (5), 777-788.
(183) Siebel, J. F.; Adamska-Venkatesh, A.; Weber, K.; Rumpel, S.; Reijerse, E.; Lubitz, W. Hybrid [FeFe]-hydrogenases with modified active sites show remarkable residual enzymatic activity. *Biochemistry* **2015**, *54* (7), 1474-1483.
(184) Vlasschaert, C.; Cook, D.; Xia, X.; Gray, D. A. The evolution and functional diversification of the deubiquitinating enzyme superfamily. *Genome Biology and Evolution* **2017**, *9* (3), 558-573.
(185) Tokuriki, N.; Stricher, F.; Serrano, L.; Tawfik, D. S. How protein stability and new functions trade off. *PLOS Computational Biology* **2008**, *4* (2), e1000002.
(186) Bar-Even, A.; Noor, E.; Savir, Y.; Liebermeister, W.; Davidi, D.; Tawfik, D. S.; Milo, R. The moderately efficient enzyme: evolutionary and

physicochemical trends shaping enzyme parameters. *Biochemistry* **2011**, *50* (21), 4402-4410.
(187) Saitou, N. Neutral Evolution. In *Introduction to Evolutionary Genomics*, Saitou, N. Ed.; Computational Biology, Springer International Publishing, 2018; pp 109-148.
(188) Léger, C.; Jones, A. K.; Albracht, S. P. J.; Armstrong, F. A. Effect of a Dispersion of Interfacial Electron Transfer Rates on Steady State Catalytic Electron Transport in [NiFe]-hydrogenase and Other Enzymes. *The Journal of Physical Chemistry B* **2002**, *106* (50), 13058-13063.
(189) Jones, A. K.; Lamle, S. E.; Pershad, H. R.; Vincent, K. A.; Albracht, S. P.; Armstrong, F. A. Enzyme electrokinetics: electrochemical studies of the anaerobic interconversions between active and inactive states of Allochromatium vinosum [NiFe]-hydrogenase. *Journal of the American Chemical Society* **2003**, *125* (28), 8505-8514.
(190) Winkler, M.; Duan, J.; Rutz, A.; Felbek, C.; Scholtysek, L.; Lampret, O.; Jaenecke, J.; Apfel, U. P.; Gilardi, G.; Valetti, F.; Fourmond, V.; Hofmann, E.; Leger, C.; Happe, T. A safety cap protects hydrogenase from oxygen attack. *Nature Communications* **2021**, *12* (1), 756.
(191) Corrigan, P. S.; Tirsch, J. L.; Silakov, A. Investigation of the Unusual Ability of the [FeFe] Hydrogenase from Clostridium beijerinckii to Access an O_2-Protected State. *Journal of the American Chemical Society* **2020**, *142* (28), 12409-12419.
(192) Rodriguez-Macia, P.; Reijerse, E. J.; van Gastel, M.; DeBeer, S.; Lubitz, W.; Rudiger, O.; Birrell, J. A. Sulfide Protects [FeFe] Hydrogenases From O_2. *Journal of the American Chemical Society* **2018**, *140* (30), 9346-9350.
(193) Del Barrio, M.; Sensi, M.; Fradale, L.; Bruschi, M.; Greco, C.; de Gioia, L.; Bertini, L.; Fourmond, V.; Leger, C. Interaction of the H-Cluster of FeFe Hydrogenase with Halides. *Journal of the American Chemical Society* **2018**, *140* (16), 5485-5492.
(194) Feng, X.; Schut, G. J.; Haja, D. K.; Adams, M. W. W.; Li, H. Structure and electron transfer pathways of an electron-bifurcating NiFe-hydrogenase. *Science Advances* **2022**, *8* (8), eabm7546.
(195) Wang, S.; Huang, H.; Kahnt, J.; Thauer, R. K. A reversible electron-bifurcating ferredoxin- and NAD-dependent [FeFe]-hydrogenase (HydABC) in Moorella thermoacetica. *Journal of Bacteriology* **2013**, *195* (6), 1267-1275.
(196) Kuchenreuther, J. M.; Britt, R. D.; Swartz, J. R. New insights into [FeFe] hydrogenase activation and maturase function. *PLOS ONE* **2012**, *7* (9), e45850.
(197) Nixon, J. E. J.; Filed, J.; McArthur, A. G.; Sogin, M. L.; Yarlett, N.; Loftus, B. J.; Samuelson, J. Iron-dependent hydrogenases of Entamoeba histolytica and Giardia lamblia: activity of the recombinant entamoebic enzyme and evidence for lateral gene transfer. *Biological Bulletin* **2003**, *204* (1), 1-9.
(198) Smutna, T.; Dohnalkova, A.; Sutak, R.; Narayanasamy, R. K.; Tachezy, J.; Hrdy, I. A cytosolic ferredoxin-independent hydrogenase possibly mediates hydrogen uptake in Trichomonas vaginalis. *Current Biology* **2022**, *32* (1), 124-135 e125.
(199) Stairs, C. W.; Dharamshi, J. E.; Tamarit, D.; Eme, L.; Jorgensen, S. L.; Spang, A.; Ettema, T. J. G. Chlamydial contribution to anaerobic metabolism during eukaryotic evolution. *Science Advances* **2020**, *6* (35), eabb7258.
(200) Kertess, L.; Adamska-Venkatesh, A.; Rodriguez-Macia, P.; Rudiger, O.; Lubitz, W.; Happe, T. Influence of the [4Fe-4S] cluster coordinating cysteines on active site maturation and catalytic properties of C. reinhardtii [FeFe]-hydrogenase. *Chemical Science* **2017**, *8* (12), 8127-8137.

(201) Esselborn, J.; Muraki, N.; Klein, K.; Engelbrecht, V.; Metzler-Nolte, N.; Apfel, U. P.; Hofmann, E.; Kurisu, G.; Happe, T. A structural view of synthetic cofactor integration into [FeFe]-hydrogenases. *Chemical Science* **2016**, *7* (2), 959-968.
(202) Sode, O.; Voth, G. A. Electron transfer activation of a second water channel for proton transport in [FeFe]-hydrogenase. *Journal of Chemical Physics* **2014**, *141* (22), 22D527.
(203) Long, H.; King, P. W.; Chang, C. H. Proton transport in Clostridium pasteurianum [FeFe] hydrogenase I: a computational study. *The Journal of Physical Chemistry B* **2014**, *118* (4), 890-900.
(204) Ginovska-Pangovska, B.; Ho, M. H.; Linehan, J. C.; Cheng, Y.; Dupuis, M.; Raugei, S.; Shaw, W. J. Molecular dynamics study of the proposed proton transport pathways in [FeFe]-hydrogenase. *Biochimica et Biophysica Acta (BBA) - Bioenergetics* **2014**, *1837* (1), 131-138.
(205) Sievers, F.; Wilm, A.; Dineen, D.; Gibson, T. J.; Karplus, K.; Li, W.; Lopez, R.; McWilliam, H.; Remmert, M.; Soding, J.; Thompson, J. D.; Higgins, D. G. Fast, scalable generation of high-quality protein multiple sequence alignments using Clustal Omega. *Molecular Systems Biology* **2011**, *7* (1), 539.
(206) Mulder, D. W.; Guo, Y.; Ratzloff, M. W.; King, P. W. Identification of a Catalytic Iron-Hydride at the H-Cluster of [FeFe]-Hydrogenase. *Journal of the American Chemical Society* **2017**, *139* (1), 83-86.
(207) Albracht, S. P.; Roseboom, W.; Hatchikian, E. C. The active site of the [FeFe]-hydrogenase from Desulfovibrio desulfuricans. I. Light sensitivity and magnetic hyperfine interactions as observed by electron paramagnetic resonance. *Journal of Biological Inorganic Chemistry* **2006**, *11* (1), 88-101.
(208) Cao, Z.; Hall, M. B. Modeling the active sites in metalloenzymes. 3. Density functional calculations on models for [Fe]-hydrogenase: structures and vibrational frequencies of the observed redox forms and the reaction mechanism at the Diiron Active Center. *Journal of the American Chemical Society* **2001**, *123* (16), 3734-3742.
(209) Liu, Z. P.; Hu, P. A density functional theory study on the active center of Fe-only hydrogenase: characterization and electronic structure of the redox states. *Journal of the American Chemical Society* **2002**, *124* (18), 5175-5182.
(210) Pandey, A. S.; Harris, T. V.; Giles, L. J.; Peters, J. W.; Szilagyi, R. K. Dithiomethylether as a ligand in the hydrogenase h-cluster. *Journal of the American Chemical Society* **2008**, *130* (13), 4533-4540.
(211) Budria, J. G.; Raugei, S.; Cavallo, L. Structure and bonding in monomeric iron(III) complexes with terminal oxo and hydroxo ligands. *Inorganic chemistry* **2006**, *45* (4), 1732-1738.
(212) Mukherjee, J.; Lucas, R. L.; Zart, M. K.; Powell, D. R.; Day, V. W.; Borovik, A. S. Synthesis, structure, and physical properties for a series of monomeric iron(III) hydroxo complexes with varying hydrogen-bond networks. *Inorganic chemistry* **2008**, *47* (13), 5780-5786.
(213) Corrigan, P. S.; Majer, S. H.; Silakov, A. Evidence of Atypical Structural Flexibility of the Active Site Surrounding of an [FeFe] Hydrogenase from Clostridium beijerinkii. *Journal of the American Chemical Society* **2023**, *145* (20), 11033-11044.
(214) Kamp, C.; Silakov, A.; Winkler, M.; Reijerse, E. J.; Lubitz, W.; Happe, T. Isolation and first EPR characterization of the [FeFe]-hydrogenases from green algae. *Biochimica et Biophysica Acta (BBA) - Bioenergetics* **2008**, *1777* (5), 410-416.

(215) Adamska, A.; Silakov, A.; Lambertz, C.; Rudiger, O.; Happe, T.; Reijerse, E.; Lubitz, W. Identification and characterization of the "super-reduced" state of the H-cluster in [FeFe] hydrogenase: a new building block for the catalytic cycle? *Angewandte Chemie* **2012**, *51* (46), 11458-11462.
(216) Lorent, C.; Katz, S.; Duan, J.; Kulka, C. J.; Caserta, G.; Teutloff, C.; Yadav, S.; Apfel, U. P.; Winkler, M.; Happe, T.; Horch, M.; Zebger, I. Shedding Light on Proton and Electron Dynamics in [FeFe] Hydrogenases. *Journal of the American Chemical Society* **2020**, *142* (12), 5493-5497.
(217) Meszaros, L. S.; Nemeth, B.; Esmieu, C.; Ceccaldi, P.; Berggren, G. *In Vivo* EPR Characterization of Semi-Synthetic [FeFe] Hydrogenases. *Angewandte Chemie* **2018**, *57* (10), 2596-2599.
(218) Bennett, B.; Lemon, B. J.; Peters, J. W. Reversible carbon monoxide binding and inhibition at the active site of the Fe-only hydrogenase. *Biochemistry* **2000**, *39* (25), 7455-7460.
(219) Martini, M. A.; Bikbaev, K.; Pang, Y.; Lorent, C.; Wiemann, C.; Breuer, N.; Zebger, I.; DeBeer, S.; Span, I.; Bjornsson, R.; Birrell, J. A.; Rodriguez-Macia, P. Binding of exogenous cyanide reveals new active-site states in [FeFe] hydrogenases. *Chemical Science* **2023**, *14* (11), 2826-2838.
(220) Rodriguez-Macia, P.; Kertess, L.; Burnik, J.; Birrell, J. A.; Hofmann, E.; Lubitz, W.; Happe, T.; Rudiger, O. His-Ligation to the [4Fe-4S] Subcluster Tunes the Catalytic Bias of [FeFe] Hydrogenase. *Journal of the American Chemical Society* **2019**, *141* (1), 472-481.
(221) Abou Hamdan, A.; Dementin, S.; Liebgott, P. P.; Gutierrez-Sanz, O.; Richaud, P.; De Lacey, A. L.; Rousset, M.; Bertrand, P.; Cournac, L.; Leger, C. Understanding and tuning the catalytic bias of hydrogenase. *Journal of the American Chemical Society* **2012**, *134* (20), 8368-8371.
(222) Hexter, S. V.; Esterle, T. F.; Armstrong, F. A. A unified model for surface electrocatalysis based on observations with enzymes. *Physical Chemistry Chemical Physics* **2014**, *16* (24), 11822-11833.
(223) Kisgeropoulos, E. C.; Bharadwaj, V. S.; Mulder, D. W.; King, P. W. The Contribution of Proton-Donor pKa on Reactivity Profiles of [FeFe]-hydrogenases. *Frontiers in Microbiology* **2022**, *13*, 903951.
(224) Lee, H. J.; Reimann, J.; Huang, Y.; Adelroth, P. Functional proton transfer pathways in the heme-copper oxidase superfamily. *Biochimica et Biophysica Acta (BBA) - Bioenergetics* **2012**, *1817* (4), 537-544.
(225) Fdez Galvan, I.; Volbeda, A.; Fontecilla-Camps, J. C.; Field, M. J. A QM/MM study of proton transport pathways in a [NiFe] hydrogenase. *Proteins* **2008**, *73* (1), 195-203.
(226) Teixeira, V. H.; Soares, C. M.; Baptista, A. M. Proton pathways in a [NiFe]-hydrogenase: A theoretical study. *Proteins* **2008**, *70* (3), 1010-1022.
(227) Matias, P. M.; Soares, C. M.; Saraiva, L. M.; Coelho, R.; Morais, J.; Le Gall, J.; Carrondo, M. A. [NiFe] hydrogenase from Desulfovibrio desulfuricans ATCC 27774: gene sequencing, three-dimensional structure determination and refinement at 1.8 A and modelling studies of its interaction with the tetrahaem cytochrome c3. *Journal of Biological Inorganic Chemistry* **2001**, *6* (1), 63-81.
(228) Greco, C.; Fourmond, V.; Baffert, C.; Wang, P. H.; Dementin, S.; Bertrand, P.; Bruschi, M.; Blumberger, J.; de Gioia, L.; Léger, C. Combining experimental and theoretical methods to learn about the reactivity of gas-processing metalloenzymes. *Energy & Environmental Science* **2014**, *7* (11), 3543-3573.
(229) Vansuch, G. E.; Wu, C. H.; Haja, D. K.; Blair, S. A.; Chica, B.; Johnson, M. K.; Adams, M. W. W.; Dyer, R. B. Metal-ligand cooperativity in the soluble

hydrogenase-1 from Pyrococcus furiosus. *Chemical Science* **2020**, *11* (32), 8572-8581.
(230) Rumpel, S.; Sommer, C.; Reijerse, E.; Fares, C.; Lubitz, W. Direct Detection of the Terminal Hydride Intermediate in [FeFe] Hydrogenase by NMR Spectroscopy. *Journal of the American Chemical Society* **2018**, *140* (11), 3863-3866.
(231) Gutierrez-Sanchez, C.; Olea, D.; Marques, M.; Fernandez, V. M.; Pereira, I. A.; Velez, M.; De Lacey, A. L. Oriented immobilization of a membrane-bound hydrogenase onto an electrode for direct electron transfer. *Langmuir* **2011**, *27* (10), 6449-6457.
(232) Chongdar, N.; Rodriguez-Macia, P.; Reijerse, E. J.; Lubitz, W.; Ogata, H.; Birrell, J. A. Redox tuning of the H-cluster by second coordination sphere amino acids in the sensory [FeFe] hydrogenase from Thermotoga maritima. *Chemical Science* **2023**, *14* (13), 3682-3692.
(233) Goris, T.; Wait, A. F.; Saggu, M.; Fritsch, J.; Heidary, N.; Stein, M.; Zebger, I.; Lendzian, F.; Armstrong, F. A.; Friedrich, B.; Lenz, O. A unique iron-sulfur cluster is crucial for oxygen tolerance of a [NiFe]-hydrogenase. *Nature Chemical Biology* **2011**, *7* (5), 310-318.
(234) Fritsch, J.; Scheerer, P.; Frielingsdorf, S.; Kroschinsky, S.; Friedrich, B.; Lenz, O.; Spahn, C. M. The crystal structure of an oxygen-tolerant hydrogenase uncovers a novel iron-sulphur centre. *Nature* **2011**, *479* (7372), 249-252.
(235) Schafer, C.; Bommer, M.; Hennig, S. E.; Jeoung, J. H.; Dobbek, H.; Lenz, O. Structure of an Actinobacterial-Type [NiFe]-Hydrogenase Reveals Insight into O_2-Tolerant H_2 Oxidation. *Structure* **2016**, *24* (2), 285-292.
(236) Bleijlevens, B.; van Broekhuizen, F. A.; De Lacey, A. L.; Roseboom, W.; Fernandez, V. M.; Albracht, S. P. The activation of the [NiFe]-hydrogenase from Allochromatium vinosum. An infrared spectro-electrochemical study. *Journal of Biological Inorganic Chemistry* **2004**, *9* (6), 743-752.
(237) Gellman, S. H. On the role of methionine residues in the sequence-independent recognition of nonpolar protein surfaces. *Biochemistry* **1991**, *30* (27), 6633-6636.
(238) Tsou, C. L. The role of active site flexibility in enzyme catalysis. *Biochemistry (Mosc)* **1998**, *63* (3), 253-258.
(239) Luo, G.; Ono, S.; Beukes, N. J.; Wang, D. T.; Xie, S.; Summons, R. E. Rapid oxygenation of Earth's atmosphere 2.33 billion years ago. *Science Advances* **2016**, *2* (5), e1600134.
(240) Catling, D. C.; Zahnle, K. J.; McKay, C. Biogenic methane, hydrogen escape, and the irreversible oxidation of early Earth. *Science* **2001**, *293* (5531), 839-843.
(241) Greening, C.; Grinter, R. Microbial oxidation of atmospheric trace gases. *Nature Reviews Microbiology* **2022**, *20* (9), 513-528.
(242) Berney, M.; Greening, C.; Hards, K.; Collins, D.; Cook, G. M. Three different [NiFe] hydrogenases confer metabolic flexibility in the obligate aerobe Mycobacterium smegmatis. *Environmental Microbiology* **2014**, *16* (1), 318-330.
(243) Greening, C.; Villas-Boas, S. G.; Robson, J. R.; Berney, M.; Cook, G. M. The growth and survival of Mycobacterium smegmatis is enhanced by co-metabolism of atmospheric H_2. *PLOS ONE* **2014**, *9* (7), e103034.
(244) Greening, C.; Berney, M.; Hards, K.; Cook, G. M.; Conrad, R. A soil actinobacterium scavenges atmospheric H_2 using two membrane-associated, oxygen-dependent [NiFe] hydrogenases. *Proceedings of the National Academy of Sciences* **2014**, *111* (11), 4257-4261.
(245) Reeve, H. A.; Ash, P. A.; Park, H.; Huang, A.; Posidias, M.; Tomlinson, C.; Lenz, O.; Vincent, K. A. Enzymes as modular catalysts for redox half-reactions

in H_2-powered chemical synthesis: from biology to technology. *Biochemical Journal* **2017**, *474* (2), 215-230.
(246) Cordero, P. R. F.; Grinter, R.; Hards, K.; Cryle, M. J.; Warr, C. G.; Cook, G. M.; Greening, C. Two uptake hydrogenases differentially interact with the aerobic respiratory chain during mycobacterial growth and persistence. *Journal of Biological Chemistry* **2019**, *294* (50), 18980-18991.
(247) Siebert, E.; Schmidt, A.; Frielingsdorf, S.; Kalms, J.; Kuhlmann, U.; Lenz, O.; Scheerer, P.; Zebger, I.; Hildebrandt, P. Resonance Raman spectroscopic analysis of the iron–sulfur cluster redox chain of the Ralstonia eutropha membrane-bound [NiFe]-hydrogenase. *Journal of Raman Spectroscopy* **2021**, *52* (12), 2621-2632.
(248) Pandelia, M. E.; Nitschke, W.; Infossi, P.; Giudici-Orticoni, M. T.; Bill, E.; Lubitz, W. Characterization of a unique [FeS] cluster in the electron transfer chain of the oxygen tolerant [NiFe] hydrogenase from Aquifex aeolicus. *Proceedings of the National Academy of Sciences* **2011**, *108* (15), 6097-6102.
(249) Zanello, P. Structure and electrochemistry of proteins harboring iron-sulfur clusters of different nuclearities. Part II. [4Fe-4S] and [3Fe-4S] iron-sulfur proteins. *Journal of Structural Biology* **2018**, *202* (3), 250-263.
(250) Li, H.; Rauchfuss, T. B. Iron carbonyl sulfides, formaldehyde, and amines condense to give the proposed azadithiolate cofactor of the Fe-only hydrogenases. *Journal of the American Chemical Society* **2002**, *124* (5), 726-727.
(251) Cloirec, A. L.; Davies, S. C.; Evans, D. J.; Hughes, D. L.; Pickett, C. J.; Best, S. P.; Borg, S. A di-iron dithiolate possessing structural elements of the carbonyl/cyanide sub-site of the H-centre of Fe-only hydrogenase. *Chemical Communications* **1999**, (22), 2285-2286.
(252) Lyon, E. J.; Georgakaki, I. P.; Reibenspies, J. H.; Darensbourg, M. Y. Carbon Monoxide and Cyanide Ligands in a Classical Organometallic Complex Model for Fe-Only Hydrogenase. *Angewandte Chemie* **1999**, *38* (21), 3178-3180.
(253) Schmidt, M.; Contakes, S. M.; Rauchfuss, T. B. First Generation Analogues of the Binuclear Site in the Fe-Only Hydrogenases: $Fe_2(\mu\text{-}SR)_2(CO)_4(CN)_2^{2-}$. *Journal of the American Chemical Society* **1999**, *121* (41), 9736-9737.

Appendix I: Classification of [FeFe] hydrogenases

H2 oxidation and production specific activity of native (N) and recombinant (R) [FeFe] hydrogenases characterized to date.
One unit. U, is defined as an activity catalysing the evolution of 1 µmol H2/min. nr = not reported/not determined

GROUP	Organism	Sub-class	Acronym	Proposed function	N/R	whole cell or lysate H2 uptake/release	H2 oxidation (U/mg)	H2 production (U/mg)	References	Structure
A	*Acetobacterium woodii*									
		M3	*AwHydABCD*	Electron bifurcation	N		760	nr	Schuchmann and Muller, 2012	
		M2	*Aw HydA2*	CO_2 reduction	N		10,800	14	Schuchmann and Muller, 2013	
		M2	*Aw HydA2*	CO_2 reduction	R		0.14	nr	Leo et al., 2021	
A	*Caldanaerobacter subterraneus*									
		M3	*CasHydABCD*		R		38	5	Kelly et al., 2015	
A	*Caldicellulosiruptor bescii*									
		M3	*CbHydABCD*				nr	nr	Poudel et al., 2016	
A	*Chlamydomonas moewusii*									
		M1	*CmHydA1*		N		nr	1,598	Kamp et al., 2008	
A	***Chlamydomonas reinhardtii***									3C8Y, 3LX4 (Mulder et al., 2010)
		M1	*CrHydA1*	H_2 production	N		nr	935	Happe and Naber, 1993;	
		M1	*CrHydA1*	H_2 production	R		nr	760	Girbal et al., 2005	
		M1	*CrHydA1*	H_2 production	R	61 ++	nr	150	King et al., 2006	
		M1	*CrHydA1*	H_2 production	N		nr	741	Kamp et al., 2008	
		M1	*CrHydA1*	H_2 production	R		nr	740±56	Sybirna et al., 2008	
		M1	*CrHydA1*	H_2 production	R		nr	625	von Abendroth et al., 2008	
		M1	*CrHydA1*	H_2 production	R		nr	730	Winkler et al., 2009	
		M1	*CrHydA1*	H_2 production	R		251±49	641±88	Kuchenrenther et al., 2010;	
		M1	*CrHydA1*	H_2 production	R		nr	400	Yacoby et al., 2011	
		M1	*CrHydA1*	H_2 production	R		nr	1,000	Yacoby et al., 2012	
		M1	*CrHydA1*	H_2 production	R		6.1 ± 1.2*	nr	Knörzer et al., 2012	
		M1	*CrHydA1*	H_2 production	R		nr	308 ± 40	Esselborn et al., 2013	
		M1	*CrHydA1*	H_2 production	R		nr	700-800	Berggren et al., 2013	
		M1	*CrHydA1*	H_2 production	R		~180	~600	Siebel et al., 2015	
		M1	*CrHydA1*	H_2 production	R		150 ± 7	854 ± 130	Engelbrecht et al., 2017	
		M1	*CrHydA1*	H_2 production	R		nr	782 ± 14	Engelbrecht et al., 2021	
		M1	*CrHydA2*	H_2 production	R	108 +++	nr	116.1	King et al., 2006	
		M1	*CrHydA2*	H_2 production	R		27 ± 0.5	166 ± 11	Engelbrecht et al., 2017	
		M1	*CrHydA2*	H_2 production	R		nr	189 ± 7	Engelbrecht et al., 2021	
A	*Chlorella fusca*									
		M1	*CfHydA*		N			1,000	Winkler et al., 2012	
		M1	*CfHydA*		N			450	Winkler et al., 2012	
A	*Chlorella variabilis*									
		M3	*CvHydA1*		R		11 ± 2	152 ± 13	Engelbrecht et al., 2017	
A	*Chlorococcum submarinum*									
		M1	*CsHydA1*		N		nr	639	Kamp et al., 2008	
A	*Clostridium acetobutylicum*									
		M3	*CaHydA1*	H_2 production	R		5,522	10	Girbal et al., 2005	
		M3	*CaHydA*		R	96 ++	nr	75.2	King et al., 2006	
		M3	*CaHydA* ΔN		R	6 +	nr	31.6	King et al., 2006	
		M3	*CaHydA1*	H_2 production	R		720,000	162±4	Demuez et al., 2007	
		M3	*CaHydA1*	H_2 production	R		nr	1,750	von Abendroth et al., 2008	
		M3	*CaHydA1*	H_2 production	R		nr	1880 ± 108	Morra et al., 2015	
A	*Clostridium autoethanogenum*									
		M2	*CaHytA-E/FdhA*	H_2-dependent formate oxidation	N		18,000	40	Wang et al., 2013b	
A	***Clostridium beijerinckii***									6TTL (Winkler et al., 2021)
		M2c	*CbHydA1/CbA5H*		R		158±34	751±91	Morra et al., 2016	
		M2c	*CbHydA1/CbA5H*		R		218±50	nr	Corrigan et al., 2020	

A	***Clostridium pasteurianum***								1FEH (Peters et al., 1998), 1C4A (Lemon and Peters, 1999), 4XDC (Esselborn et al., 2016, Esselborn et al., 2019) variants: 6GLY, 6GLZ, 6GM0, 6GM1, 6GM2, 6GM3, 6GM4, 6GM5, 6GM6, 6GM7, and 6GM8 (Duan et al., 2018)	
		M3	*CpI*	H_2 production	N		3,000	nr	Nakos and Mortenson 1971	
		M3	*CpI*	H_2 production	N		15000*	nr	Nakos and Mortenson 1971	
		M3	*CpI*	H_2 production	N		nr	1,380	Chen and Mortenson 1974	
		M3	*CpI*	H_2 production	N		nr	2,530	Chen and Mortenson 1974	
		M3	*CpI*	H_2 production	N		nr	4,000	Chen and Blanchard 1978	
		M3	*CpI*	H_2 production	N		nr	1,480	Chen and Blanchard 1978	
		M3	*CpI*	H_2 production	N		17,500*	nr	Adams and Mortenson, 1984	
		M3	*CpI*	H_2 production	N		24,000*	5,500	Adams 1990	
		M3	*CpI*	H_2 production	R		476±39	1,087±146	Kuchenreuther et al., 2010	
		M3	*CpI*	H_2 production	R		3.1 ± 0.4*	1598±103	Knörzer et al., 2012	
		M3	*CpI*	H_2 production	R		nr	2,037 ± 616	Esselborn et al., 2013	
		M3	*CpI*	H_2 production	R			3648 ± 194	Engelbrecht et al., 2017	
		M2	*CpII*	H_2 uptake	N		400-800*	nr	Chen and Blanchard 1978	
		M2	*CpII*	H_2 uptake	N		3000*	5.9	Adams and Mortenson, 1984	
		M2	*CpII*	H_2 uptake	N		25,800*	7.6	Adams and Mortenson, 1984	
		M2	*CpII*	H_2 uptake	N		25,800*	28	Adams and Mortenson, 1984	
		M2	*CpII*	H_2 uptake	N		34,000	10	Adams 1990	
		M2	*CpII*	H_2 uptake	R		110,000*	16.2±0.14	Artz et al., 2020	
A	*Clostridium perfringens*									
		M3	*CpHydA*		R		nr	~4,000	Morra et al., 2015	
		M3	*CpHydA*		R		nr	1645 ± 16	Morra et al., 2016	
A	*Desulfovibrio fructosovorans*									
		M2(D)	*DfHydAB*		N		17,000	nr	Casalot et al., 1998	
		M3	*DfHnd*	Electron bifurcation	N		2,500±200	155±15	Kpebe et al., 2018	
A	***Desulfovibrio vulgaris (DvH)/Desulfovibrio desulfuricans (DdH/DdHydAB)***								1HFE (Nicolet et al., 1999, Nicolet et al., 2001, Rodriguez-Macia et al., 2020	
		M2(D)	*DvH Miyazaki*	H_2 uptake	N		nr	200	Yagi et al., 1970	
		M2(D)	*DvH Hildenborough*	H_2 uptake	N		15,400	nr	Haschke and Campbell 1971	
		M2(D)	*DvH Hildenborough*	H_2 uptake	N		53	nr	Legall et al., 1971	
		M2(D)	*DvH Miyazaki*	H_2 uptake	N		nr	610	Yagi et al., 1976	
		M2(D)	*DvH Hildenborough*	H_2 uptake	N		38,000	3,800	van der Westen et al., 1978	
		M2(D)	*DvH Hildenborough*	H_2 uptake	N		50,000	10,400	Adams 1990	
		M2(D)	*DdH*	H_2 uptake	N		62,200	8,200	Hatchikian et al., 1992;	
		M2(D)	*DvH Hildenborough*	H_2 uptake	R		12.5	nr	Laffly et al., 2010	
		M2(D)	*DdH*	H_2 uptake	R		~80,000	~4,700	Birrell et al., 2016	
A	*Megasphaera elsdenii*									
		M2	*MeHydA*		N		nr	510	Vandijk et al., 1979	
		M2	*MeHydA*		N		nr	4,200	Vandijk et al., 1981	
		M2	*MeHydA*		N		9,000	7,000	Adams 1990	
		M2	*MeHydA*		R		nr	308±40	Esselborn et al., 2013	
		M2	*MeHydA*		R		nr	600±50	Caserta et al., 2016	
		M2	*MeH-HydA*		R		nr	135 ± 10	Caserta et al., 2018	
A	*Moorella thermoacetica*									
		M3	*MtHydABC*	Electron bifurcation	N		195	5-10"	Wang et al., 2013a	
A	*Peptoclostridium acidaminophilum*	M3	*PaHymABCD*			0.8 +	nr	nr	Graentzdoerffer et al., 2003	
A	*Ruminococcus albus*									
		M3	*RaHydABC*	Electron bifurcation	N		60"	0.3-0.6	Zheng et al., 2014	
A	*Solobacterium moorei*	M2	*SmHydA*		R	1.5 +	nr	nr	Land et al., 2019	

A	*Syntrophomonas wolfei*	M3	*SwHyd1ABC*	Non-electron bifurcation	R		571	24	Losey et al., 2017	
A	*Syntrophus aciditrophicus*	M3	*SaHydAB*	Non-electron bifurcation	R		13	0.4	Losey et al., 2020	
A	*Thermoanaerobacter kivui*	M2	*TkHydA2*	CO_2 reduction	N		14,400	930	Schwarz et al., 2018	
A	*Thermoanaerobacterium saccharolyticum*	M3	*TsHydABCD*		N	0.02 +	nr	nr	Shaw et al., 2009	
A	***Thermotoga maritima***									7P5H D2 tetramer, 7P8N (Bridge closed forward), 7P91 (Bridge closed reverse), and 7P92 (Open bridge) (Furlan et al., 2022)
		M4	*TmHydABC*	Electron bifurcation	N		70	15	Verhagen et al., 1999	
		M4	*TmHydABC*	Electron bifurcation	N		nr	1.2	Schut and Adams, 2009	
		M4	*TmHydABC*	Electron bifurcation	R		1300 ± 140	550 ± 50	Chongdar et al., 2020	
		M4	*TmHydA*		R		2000 ± 200	475 ± 60	Chongdar et al., 2020	
A	*Tetradesmus obliquus*	M1	*ToHydA*		N		nr	700	Florin et al., 2001	
A	*Volvox carteri*	M1	*VcHydA1*				nr	108	Cornish et al., 2015	
		M1	*VcHydA2*				nr	2	Cornish et al., 2015	
B	*Clostridium acetobutylicum*	M2a	*CaHydB/CaHydA2*		R	13 +	nr	8.6	King et al., 2006	
B	*Clostridium pasteurianum*	M2a	*CpIII*		R		15±3.8	305±58	Artz et al., 2020	
		M2a	*CpIII*		R		15±3.8	650±73	Artz et al., 2020	
B	*Ruminococcus albus*	M3a	*RaHydA2*		N		nr	nr	Zheng et al., 2014	
B	*Thermoanaerobacterium saccharolyticum*	M3a	*TsHfsD*		N	0.09 +			Shaw et al., 2009	
C	*Ruminococcus albus*	M2f	*RaHydS*	H_2 sensing	N		nr	nr	Zheng et al., 2014	
C	*Thermoanaerobacterium saccharolyticum*	M2f	*TsHfsB*	H_2 sensing	N	0.04 +	2.10	nr	Shaw et al., 2009	
C	*Thermotoga maritima*	M2f	*TmHydS*	H_2 sensing	R		~58	~6	Chongdar et al., 2018	
D	*Thermoanaerobacter mathranii*	M2e	*TamHydS*	H_2 sensing	R	0.5 +			Land et al., 2019	
		M2e	*TamHydS*	H_2 sensing	R		nr	0.09±0.005	Land et al., 2020	
D	*Thermoanaerobacterium saccharolyticum*	M2e	*TsHyd2*		N	0.6 +			Shaw et al., 2009	

Appendix II: Classification of [NiFe] hydrogenases

GROUP	Organism	Sub-group	Gene names commonly used	Acronym	Proposed function	growth H2 uptake/release	H2 oxidation (U/mg)	H2 production (U/mg)	Km	Structure
Group 1: membrane-bound H2-uptake [NiFe]-hydrogenases			hupSL, hydAB, hupAB, hyaAB, hoxKG, mbhSL, hybOC, hynSL, hysAB, vhtGA, vhoGA							
	Desulfovibrio vulgaris *Desulfomicrobium baculatum* *Methanosarcina mazei*	1a: ancestral			Liberates electrons for sulphate, metal, organohalide and methanogenic heterodisulphide respiration. Includes [NiFeSe] variants.					2WPN 1CC1
	Desulfovibrio gigas *Wolinella succinogenes* *Helicobacter pylori*	1b: prototypical		HynAB HydABC	Liberates electrons for sulphate, fumarate and nitrate respiration.	 +	1500* (Faque et al., 1988) 4.2	440 (Faque et al., 1988)		1FRV
	Escherichia coli *Salmonella enterica*	1c: Hyb type		Hyd-2	Liberates electrons primarily for fumarate respiration. Possibly bidirectional.	 +	34	2.5	Km 17 µM (McDowall et al., 2014)	
	Ralstonia eutropha *Escherichia coli* *Aquifex aeolicus*	1d: oxygen tolerant		Hya/ReMBH Hyd-1 Hyd-I/II Hyd-M/Hyd-1-Cytb	Electron input for aerobic respiration and oxygen-tolerant anaerobic respiration. Low-affinity, oxygen-tolerant hydrogenases that support growth of Proteobacteria and others	 	 1 13	 nr nr	Km 6 µM (McDowall et al., 2014) Km 9 µM (McDowall et al., 2014)	3RGW 4GD3
	Allochromatium vinosum *Aquifex aeolicus* *Thiocapsa roseopersicina*	1e: Isp type		 Hyd-I/II? HynSL	Liberates electrons primarily for sulphur respiration. Possibly bidirectional.	 +				3MYR
	Geobacter sulfurreducens *Frankia sp.*	1f: oxygen protecting		Hya	Unresolved. May liberate electrons to reduce reactive oxygen species.	+				
	*Pyrodictium brockii** *Acidianus ambivalens**	1g: Crenarchaeota type			Unresolved. May liberate electrons primarily for sulphur respiration.		1238 833*	nr nr		
	Ralstonia eutropha *Mycobacterium smegmatis* *Streptomyces avermitilis*	1h/5: Actinobacteria type		Hhy/AH Hyd2 Hyd-B-like	Scavenges electrons from tropospheric H2 to sustain aerobic respiration during starvation. High-affinity, O_2-insensitive enzyme shown to oxidize atmospheric H_2 in Actinobacteria and four other phyla.	 +	0.3*	nr	3.6 ± 0.5 µM Km(app) = 0.05 µM Km(app) = 0.04 µM	5AA5
	Uncharacterised.	1i		Hyl	Implicated in atmospheric H_2 oxidation in Bacteriodetes					
Group 2: Cytosolic H2-uptake [NiFe]-hydrogenases										
	Anabaena sp.	2a: Cyanobacteria type	HupSL, MbhSL		Electron input for aerobic respiration and recycling H2 produced by cellular processes (for example, nitrogenase, fermentation). Huc: High-affinity, O_2-insensitive enzyme shown to oxidize atmospheric H_2 in Actinobacteria and five other phyla.	+				
	Mycobacterium smegmatis *Nitrospira moscoviensis**			Hyd1/Huc Hup		 +			Km(app) = 0.180 µM; Km 0.129 µM (Grinter et al., 2023)	7UUS
	Alcaligenes eutrophus *Ralstonia eutropha* *Rhodobacter capsulatus*	2b: HK linked, H_2-sensing	HupUV, HoxBC	 RH Hup	Senses H2 and activates two-component cascade controlling hydrogenase expression.	+				
	Uncharacterised.	2c: DGC linked (putative)			Unknown. Predicted to sense H2 and induce cyclic di-GMP production.					
	Aquifex aeolicus	2d: Aquificae type		Hyd-I/II	Unknown. May generate reductant for carbon fixation or have a regulatory role.		100	nr		
	Uncharacterised.	2e		Hys	Uncharacterized enzyme implicated in atmospheric H_2 oxidation in archaea					
Group 3: Cytosolic bidirectional [NiFe]-hydrogenases										
	Methanothermobacter marburgensis *Methanosarcina barkeri*	3a: F420 coupled	frhAG, fruAH, freAG	Frh	Directly couples oxidation of H2 to reduction of F420 during methanogenesis. Reverse reaction may also occur. Includes [NiFeSe] variants.	 +				4OMF
	Pyrococcus furiosus *Thermococcus kodakarensis* *Mycobacterium smegmatis*	3b: NADP coupled	hydDA, shyDA, hyjSL, hyhSL, hydDA,hydoa, cytc3DA, shyDA	 Hyh Hyd3	Directly couples oxidation of NADPH to evolution of H2. May be reversible. Some complexes are proposed to have sulfhydrogenase activity. Disposal of excess reducing equivalents in the form of H_2 Adopt fermentative hydrogen production in response to oxygen limitation	 + +	44	nr	 Km(app) < 0.20 µM	
	Methanothermobacter marburgensis	3c: HDR linked	mvhGA, vhcGA, vhuGA, mvhSL	MvhADG/HdrABC	Bifurcates electrons from H2 to heterodisulphide and ferredoxin in methanogens without cytochromes.	+	50*			
	Anabaena sp. *Ralstonia eutropha* *Thiocapsa roseopersicina*	3d: NAD coupled	hoxYH	 SH Hox	Directly interconverts electrons between H2 and NAD depending on redox state.	+ +	 35.1	 nr		
Group 4: Membrane-bound H2-evolving [NiFe]-hydrogenases			hyfIG, hycGE, cooLH, echFE, ehaNO, ehbMN							
	Escherichia coli *Salmonella enterica*	4a: formate hydrogenlyases		FHL Hyd-3	Couples oxidation of formate to fermentative evolution of H2. Hyf-type complexes may translocate protons via antiporter modules.	+ +			Km 34 µM	

Pyrococcus furiosus *Thermococcus onnurineus* *Thermococcus kodakarensis*	4b: Mrp linked	Mbh	Couples oxidation of formate or carbon monoxide to proton reduction. Generates sodium-motive force via Mrp antiporter modules.	+ +	0.07 (845 Adams 1990)	2.5 (2900 Adams 1990)
Carboxydothermus hydrogenoformans *Rhodospirillum rubrum*	4c: CODH linked		Forms complex with carbon monoxide dehydrogenase to anaerobically respire CO using protons as terminal electron acceptors.	+ +	180	450
Methanococcus maripaludis	4d: Eha/Ehb type	Eha/Ehb	Multimeric complexes that couple H2 oxidation to ferredoxin reduction for anaplerotic (Eha) and anabolic (Ehb) purposes. H+/Na+ driven.	+		
Methanosarcina barkeri *Desulfovibrio gigas* *Thermoanaerobacter tengcongensis*	4e: Ech type	Ech Ech Ech	Couples ferredoxin oxidation to H2 evolution. This process is physiologically reversible via H+/Na+ translocation.	+ + +		
Uncharacterised.	4f: Ehf type (putative)		Unknown. May couple oxidation of a one-carbon compound to proton reduction concurrent with proton translocation. Related to Ehr complexes.			

Appendix III: Supplementary information for Chapter 3

Experimental methods for the characterization of **Mu**

General

All chemicals were purchased from Sigma-Aldrich or VWR and used as received unless otherwise stated. Protein expression was analyzed by 12% SDS-PAGE mini gels in a BIO-RAD Mini PROTEAN® system. The proteins were stained with Page Blue protein staining solution (Thermo Fisher Scientific) according to the supplier instructions. All anaerobic work was performed in an MBRAUN glovebox ([O2] < 5 ppm). The $[2Fe]^{ADT}$ and $[2Fe]^{PDT}$ were synthesized following literature protocols with minor modifications and verified by FTIR spectroscopy.[250-253] UV-Vis spectra were obtained using a Model Infinite 200 Pro – Infinite M Nano spectrophotometer using a 1-mm pathlength absorption cuvette for reconstitution.

Codon-optimized gene sequence of **Mu**

The gene encoding **Mu** was codon optimized for expression in *E. coli*, synthesized, and cloned in pET-11a(+) by Genscript using restriction sites *Nde*I and *Bam*HI (see **Tab. S5** from **Paper I**[154] for the full sequence).

Whole cell EPR sample preparation from small-scale cultures

Expression constructs were transformed in chemically competent *E. coli* BL21(DE3) to express the *apo* forms of the hydrogenases lacking the diiron subsite of the H-cluster. Starting cultures were grown overnight in 5 mL LB medium containing 100 µg/mL ampicillin at 37°C. These cultures were subsequently used to inoculate 80 mL of M9 medium (22 mM Na_2HPO_4, 22 mM KH_2PO_4, 85 mM NaCl, 18 mM NH_4Cl, 0.2 mM $MgSO_4$, 0.1 mM $CaCl_2$, 0.4% (v/v) glucose) containing 100 µg/mL ampicillin. Cultures were grown at 37°C and 150 rpm until an optical density (OD_{600}) of approximately 0.4 to 0.6 was reached. Protein expression was induced by the addition of 0.1 mM $FeSO_4$ and 1 mM IPTG. Induced cultures were incubated at 20°C and 150 rpm for approximately 16 h. Cells were thereafter harvested by centrifugation at 4,930 × *g* for 10 mins at 4°C.

The 2 mL dense cell suspension generated via the *in vivo* artificial activation protocol reported previously[179] was centrifuged, and the cell pellet was washed with 1 mL Tris-HCl buffer (100 mM Tris, 150 mM NaCl, pH 8.0) three times under anaerobic conditions. After the washing protocol, the cells were resuspended with 100 µL Tris buffer pH 8.0 and then transferred into EPR tubes. The tubes were capped and directly frozen in liquid N_2. X-band EPR measurements were performed on a Bruker ELEXYS E500 spectrometer equipped with a SuperX EPR049 microwave bridge and a cylindrical TE011 ER 4122SHQE cavity in connection with an Oxford Instruments continuous flow cryostat. Measuring temperatures were achieved using liquid helium flow through an ITC 503 temperature controller (Oxford Instruments).

Lysate preparation from large-scale cultures

Expression constructs were transformed in chemically competent *E. coli* BL21(DE3) and *E. coli* BL21(DE3) ΔiscR cells. Starter cultures were grown overnight in 10 mL LB medium containing 100 µg mL^{-1} ampicillin at 37°C. These cultures were subsequently used to inoculate 1 L of M9 medium (22 mM Na_2HPO_4, 22 mM KH_2PO_4, 85 mM NaCl, 18 mM NH_4Cl, 0.2 mM $MgSO_4$, 0.1 mM $CaCl_2$, 0.4% (v/v) glucose) containing 100 µg mL^{-1} ampicillin. Cultures were grown at 37°C and 150 rpm until an optical density (OD_{600}) of approximately 0.4 to 0.6 was reached. Protein expression was induced by the addition of 0.1 mM $FeSO_4$ and 1 mM IPTG. Induced cultures were incubated at 20°C and 150 rpm for approximately 16 h. Cells were thereafter harvested by centrifugation at 4,930 × *g* for 10 mins at 4°C. All subsequent operations were carried out under anaerobic conditions to prevent hydrogenase inactivation by atmospheric oxygen in an MBRAUN glovebox. The cell pellet was resuspended in 100 mM Tris-HCl pH 8.0, with NaCl (150 mM), $MgCl_2$ (10 mM), lysozyme from chicken egg white (1 mg/mL), DNAse I from bovine pancreas (0.05 mg/mL), RNase A from bovine pancreas (0.05 mg/mL), and a tablet of cOmplete™ EDTA-free protease inhibitor cocktail, and was incubated inside the glovebox for 30 min. Cell lysis was performed by sonication (50% amplitude, 3 x 5 sec with 15 sec intervals; 60 sec rest and repeated 3x). The supernatant was recovered by centrifugation (29,080 × *g*, 10 mins, 4°C). Cell debris was removed by centrifugation in a Beckman Coulter Optima L-90K Ultracentrifuge (222,592 × *g*, 60 min). The supernatant was collected and filtered (0.45 µm syringe filter).

Purification, reconstitution of [4Fe-4S] cluster, and activation with $[2Fe]^{ADT}$ of the BL21(DE3)-expressed **Mu**

The filtered supernatant was loaded in a StrepTrap™ XT (Cytiva) affinity column using a BioLogic DuoFlow™ FPLC system (Bio-Rad) and purified

according to the manufacturer´s instructions. Products eluted by 50 mM biotin were concentrated using Amicon®Ultra 30 kDa molecular weight cut-off (MWCO) centrifugal filters (Merck Millipore Ltd.). Samples were stored anaerobically at −80 °C. Coomassie-stained SDS-PAGE was used to assess purity. Protein estimations were performed via Bradford assay using bovine serum albumin as a standard.[159] Quantification of Fe-content was performed using a previously reported assay using a commercially available Fe^{2+} standard for AAS TraceCERT (Sigma Aldrich) for the calibration curve.[160]

To semi-enzymatically reconstitute the iron-sulfur clusters, a solution of 110 µM *apo* protein in 100 mM Tris-HCl, 150 mM NaCl pH 8.0 was incubated with 500 µM dithiothreitol (DTT) under strictly anaerobic conditions for 10 min at room temperature. The iron and sulfur sources were ferrous ammonium sulfate and L-cysteine, respectively, both added in 1.5-fold molar excess to the desired number of Fe-atoms to be added. Reconstitution was initiated by adding a 1% molar equivalent of recombinant cysteine desulfurase (*E. coli* IscS), slowly releasing sulfide *in situ* from cysteine. Reaction mixtures were incubated at room temperature up to 2 hours. At the same time, the increase of absorbance around 405 nm was monitored by UV/Vis. The reconstitution process was stopped by running the reaction mixture through a PD-10 column (GE Healthcare), equilibrated in 10 mM Tris-HCl, 15 mM NaCl pH 8.0.

To activate **Mu** with $[2Fe]^{ADT}$, under strictly anaerobic conditions, the reconstituted enzyme (50 µM) was mixed with sodium dithionite (1 mM, 20× excess) in 100 mM phosphate buffer, pH 6.8 and incubated in room temperature for 10 minutes. Cofactor incorporation started with the addition of $[2Fe]^{ADT}$ (600 µM, 12× excess), and the reaction mixture was incubated for 1 h. The mixture was loaded onto a PD-10 desalting column (GE Healthcare) equilibrated with 10 mM Tris-HCl pH 8.0. The sample was concentrated using Amicon®Ultra 30 kDa MWCO centrifugal filters (Merck Millipore Ltd.), aliquoted into PCR tubes, and transferred into airtight serum vials (3-5 µL each) before they were flash-frozen in liquid N_2 and stored at -80°C until further use.

Purification and activation with $[2Fe]^{ADT}$ of the BL21(DE3) ΔiscR-expressed **Mu** in lysates

The filtered supernatant (approximately 100 mL) from the BL21(DE3) ΔiscR-expressed **Mu** was added with 100 µL of $[2Fe]^{ADT}$ and incubated for 1 hour prior to loading in a StrepTrap™ XT column. Products eluted by 50 mM biotin were loaded onto a PD-10 desalting column (GE Healthcare) equilibrated with 10 mM Tris-HCl pH 8.0, then concentrated using Amicon®Ultra 30 kDa molecular weight cut-off (MWCO) centrifugal filters (Merck Millipore Ltd.).

Samples were stored anaerobically at −80 °C. Coomassie-stained SDS-PAGE was used to assess purity. Protein estimations were performed via Bradford assay using bovine serum albumin as a standard.[159] Quantification of Fe-content was performed using a previously reported assay using a commercially available Fe^{2+} standard for AAS TraceCERT (Sigma Aldrich) for the calibration curve.[160]

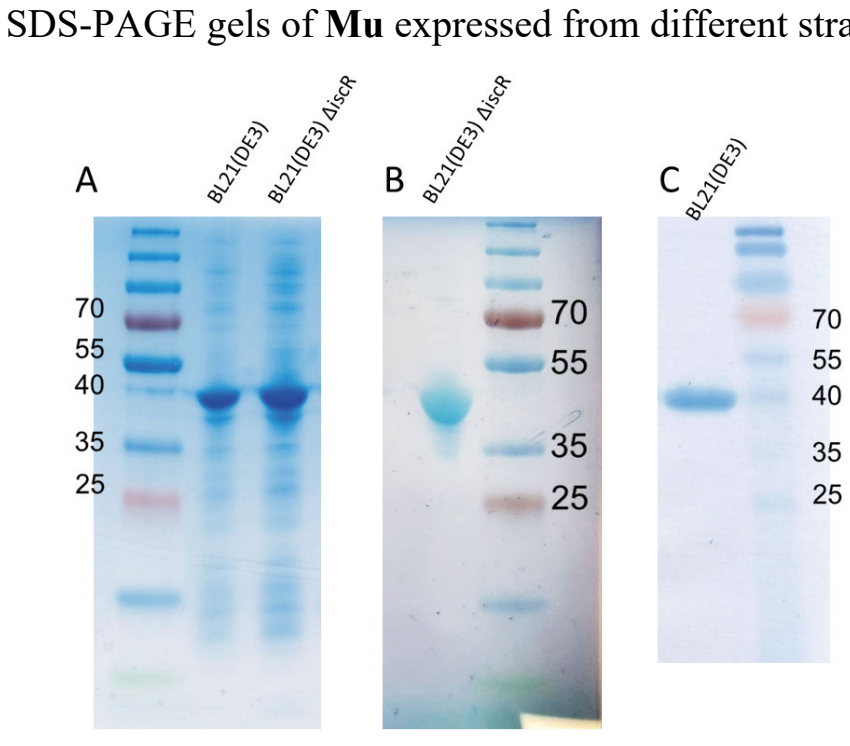

Figure A3.1. **SDS-PAGE analysis of purified Mu under different expression and activation conditions. (A)** Comparison of **Mu** expression levels in Bl21 and Bl21ΔiscR strains. No significant difference in expression levels is observed. **(B)** Purified **Mu** from Bl21ΔiscR activated with $[2Fe]^{ADT}$ prior to purification. **(C)** Purified **Mu** from Bl21 without prior activation with $[2Fe]^{ADT}$.

Sequence alignment and structural models of **Mu**

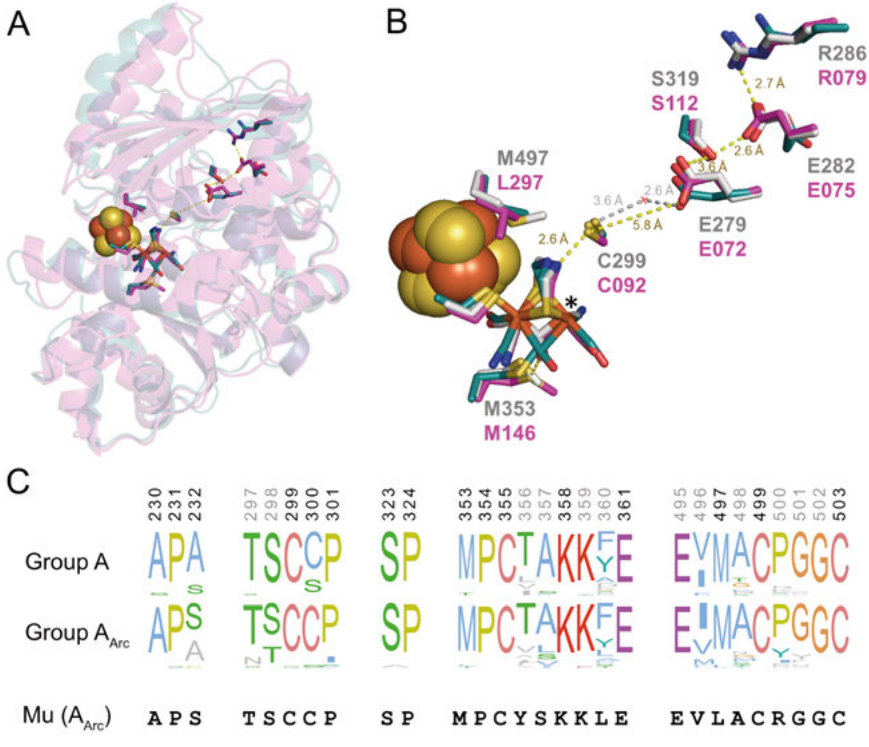

Figure A3.2. Structural models of Mu. (A) Comparision of **Mu** Alphafold model[154] (magenta cartoon) and YASARA-generated homology model of **Mu** (dark cyan cartoon), aligned with the crystal structure of *Cp*I (PDB ID: 4XDC[201]). **(B)** For *Cp*I residues, the atoms are color-coded as: C: grey, O: red, N: blue, Fe: orange, S: yellow. The Fe_d is indicated with an asterisk (*). The proton transfer pathway (PTP) of Group A (grey sticks) is proposed to include C299, E279, S319, E282, and R286 (grey sticks). The corresponding residues in **Mu** (C: magenta and dark cyan for Alphafold and YASARA models, respectively), emphasizing the conserved second and outer coordination sphere residues with the exception of $M497_{CpI}$, which is replaced with a leucine in **Mu** ($L297_{Mu}$). The distances labelled in yellow are between the amine bridgehead of the ADT ligand and $C092_{Mu}$, $E072_{Mu}$, $S112_{Mu}$, $E072_{Mu}$, and $R079_{Mu}$. The distances labelled in grey are between $C299_{CpI}$, a water molecule, and $E279_{CpI}$ **(C)** Normalized consensus sequence logos generated for Group A and A_{Arc} using Jalview and a ClustalΩ multiple sequence alignment of sequences obtained from refs[15, 154]. The numbering is based on *Cp*I, and the key residue positions are indicated in the top panel. The amino acid sequence of **Mu** is also presented in the bottom panel.

Acta Universitatis Upsaliensis

Digital Comprehensive Summaries of Uppsala Dissertations from the Faculty of Science and Technology 2436

Editor: The Dean of the Faculty of Science and Technology

A doctoral dissertation from the Faculty of Science and Technology, Uppsala University, is usually a summary of a number of papers. A few copies of the complete dissertation are kept at major Swedish research libraries, while the summary alone is distributed internationally through the series Digital Comprehensive Summaries of Uppsala Dissertations from the Faculty of Science and Technology. (Prior to January, 2005, the series was published under the title "Comprehensive Summaries of Uppsala Dissertations from the Faculty of Science and Technology".)

Distribution: publications.uu.se
urn:nbn:se:uu:diva-536472

ACTA UNIVERSITATIS
UPSALIENSIS
2024